# Dark Matter Indirect Detection and Phenomenology of Flavored Dark Matter Models

Von der Fakultät für Mathematik, Informatik und Naturwissenschaften der RWTH Aachen University zur Erlangung des akademischen Grades einer Doktorin der Naturwissenschaften genehmigte Dissertation

vorgelegt von

Lena Maria Rathmann, M.Sc.

aus

Hamburg

Berichter: Univ.-Prof. Dr. rer. nat. Michael Krämer
Jun.-Prof. Dr. rer. nat. Felix Kahlhöfer

Tag der mündlichen Prüfung: 23. Mai 2025

Diese Dissertation ist auf den Internetseiten der Universitätsbibliothek verfügbar.

RWTH Aachen University

Doctoral Thesis

# Dark Matter Indirect Detection and Phenomenology of Flavored Dark Matter Models

*Author:*
Lena Maria Rathmann

*Supervisor:*
Prof. Dr. Michael Krämer,
Prof. Dr. Felix Kahlhoefer

*This thesis was realized at the*

Institute for Theoretical Particle Physics and Cosmology

Department of Physics

Faculty of Mathematics, Computer Science and Natural Sciences

May 28, 2025

# Abstract

Dark matter remains one of the most fascinating puzzles in modern physics, with its existence being well established through a variety of astrophysical observations. However, despite extensive experimental and theoretical efforts, the properties of dark matter remain largely unknown. In this thesis, we contribute to the search for dark matter by studying two different strategies: First, we study indirect detection with cosmic ray antideuterons which can provide insights into the interactions of dark matter with Standard Model particles. Second, we develop dark matter models to help explain the observational evidence and study specifically the phenomenology of flavored dark matter models.

In the first part, we investigate the indirect detection of dark matter with cosmic ray antideuterons which are expected to have a much lower background compared to other antiparticles, making them a promising target for dark matter searches. We compute their injection spectrum using Monte Carlo simulations, taking into account the uncertainties that arise from the modeling of the production of antideuterons. We simulate the propagation of antideuterons through the Galaxy using two different propagation models and include the uncertainties of the propagation parameters. The computed antideuteron fluxes are used to develop and train a neural network emulator to predict the antideuteron flux with a significant speed-up compared to simulations. Using the emulator, we investigate the sensitivity of current and future experiments to antideuterons produced in dark matter annihilations. We find that our tool is accurate and efficient and can be used for the interpretation of future antideuteron data in the context of dark matter.

In the second part of the thesis we focus on the phenomenology of flavored dark matter models. These models offer a rich phenomenology that can evade current constraints and allow for a more dynamic freeze-out phenomenology. First, we study a flavored Majorana dark matter model with couplings to up-type quarks and focus on more general freeze-out scenarios. We perform detailed scans over the parameter space to obtain viable points that are not excluded by current constraints and find that including coannihilation and conversion processes significantly increases the viable parameter space of the model. The parameter space is then confronted with constraints from a variety of LHC searches, and we discuss possible signatures to distinguish the Majorana dark matter model from the Dirac case. We find that the charge asymmetry in the production of a top quark and a jet is a promising signature.

Lastly, we expand the study to include a variety of flavored dark matter models and develop a framework to perform an automated study of the phenomenology of these models. This framework includes all relevant constraints from the relic abundance, direct and indirect detection experiments as well as flavor and collider constraints and allows for a systematic study of the viable parameter space of flavored dark matter models. To demonstrate the capabilities of the framework, we perform a study of a model with couplings to right-handed leptons. We conclude that the phenomenology of the model can be studied very efficiently with this framework and find that it is mostly constrained by the relic abundance and flavor observables.

# Zusammenfassung

Die dunkle Materie ist nach wie vor eines der faszinierendsten Rätsel der modernen Physik. Ihre Existenz ist durch viele astrophysikalische Beobachtungen gut belegt. Trotz umfangreicher experimenteller und theoretischer Bemühungen sind ihre Eigenschaften jedoch noch weitgehend unbekannt. In dieser Arbeit leisten wir einen Beitrag zur Suche nach dunkler Materie, indem wir zwei verschiedene Strategien untersuchen: Erstens untersuchen wir den indirekten Nachweis mit kosmischen Antideuteronen, die Einblicke in die Wechselwirkungen der dunklen Materie mit dem Standardmodell geben können. Zweitens entwickeln wir Modelle für dunkle Materie, und untersuchen insbesondere die Phänomenologie von Modellen für flavored dunkle Materie.

Im ersten Teil untersuchen wir den indirekten Nachweis von dunkler Materie mit kosmischen Antideuteronen, welche im Vergleich zu anderen Antiteilchen einen sehr geringeren Hintergrund haben. Dies macht sie zu einem guten Kandidaten für die Suche nach dunkler Materie. Wir berechnen ihr Injektionsspektrum mit Hilfe von Monte-Carlo-Simulationen und berücksichtigen dabei die Unsicherheiten aus der Modellierung der Produktion. Wir simulieren die Propagation von Antideuteronen durch die Galaxis mit zwei verschiedenen Modellen unter Berücksichtigung der Unsicherheiten. Die berechneten Flüsse werden zur Entwicklung eines Emulators verwendet, um den Fluss schneller zu berechnen im Vergleich zu den Simulationen. Mit Hilfe des Emulators untersuchen wir die Antideuteron Sensitivität aktueller und zukünftiger Experimente. Wir stellen fest, dass unser Emulator effizient für die Interpretation zukünftiger Daten im Zusammenhang mit dunkler Materie ist.

Der zweite Teil der Arbeit befasst sich mit der Phänomenologie von flavored dunkler Materie Modellen. Diese Modelle bieten eine reichhaltige Phänomenologie, die sich den derzeitigen Beschränkungen entziehen kann. Zunächst untersuchen wir ein Majorana-Modell mit Kopplungen an up-Typ-Quarks und konzentrieren uns auf allgemeinere Freeze-out-Szenarien. Wir führen detaillierte Scans über den Parameterraum durch, um Regionen zu finden, die nicht durch Experimente ausgeschlossen sind. Wir stellen fest, dass die Einbeziehung von Koannihilations- und Konversionsprozessen den validen Parameterraum erheblich erweitert. Anschließend konfrontieren wir den Parameterraum mit einer Reihe von LHC-Suchen und diskutieren mögliche Signaturen, um das Majorana-Modell von dem Dirac-Modell zu unterscheiden. Wir finden, dass eine Ladungsasymmetrie im Endzustand eine aussichtsvolle Signatur ist.

Schließlich erweitern wir die Studie um eine Vielzahl von flavored dunkle Materie Modelle und entwickeln ein Framework, um eine Studie der Phänomenologie dieser Modelle durchzuführen. Dieser Framework umfasst alle relevanten Beschränkungen aus der Reliktdichte, direkten und indirekten Nachweisen sowie Flavor- und Beschleuniger-Experimenten und ermöglicht eine systematische Untersuchung des möglichen Parameterraums von diesen Modellen. Um unseren Framework zu demonstrieren, führen wir eine Studie eines Modells mit Kopplungen an rechtshändige Leptonen durch. Wir stellen fest, dass wir die Phänomenologie mit diesem Framework sehr effizient untersuchen können und dass es hauptsächlich Einschränkungen durch die Reliktdichte und die Flavor-Observablen gibt.

# Declaration of Authorship

I, Lena Maria Rathmann, declare this thesis and the work presented in it are my own and have been generated by me as the result of my own original research. Hiermit erkläre ich an Eides statt / I do solemnly swear that:

1. This work was done wholly or mainly while in candidature for the doctoral degree at this faculty and university.
2. Where any part of this thesis has previously been submitted for a degree or any other qualification at this university or any other institution, this has been clearly stated.
3. Where I have consulted the published work of others or myself, this is always clearly attributed.
4. Where I have quoted from the work of others or myself, the source is always given. This thesis is entirely my own work, with the exception of such quotations.
5. I have acknowledged all major sources of assistance.
6. Where the thesis is based on work done by myself jointly with others, I have made clear exactly what was done by others and what I have contributed myself.
7. The research carried out during this thesis and described in this work has led to several scientific publications, listed on the following page.

---

Date, Signature

# List of Publications

This thesis is founded on the research I conducted during my doctoral studies at the Institute for Theoretical Particle Physics and Cosmology at RWTH Aachen University. The following publications are derived from this research:

**Published**

1. H. Acaroğlu, M. Blanke, J. Heisig, M. Krämer, and **L. Rathmann**, *"Flavoured Majorana Dark Matter then and now: From freeze-out scenarios to LHC signatures"*, published in JHEP 06 (2024) 179 [1]

2. J. Heisig, M. Korsmeier, M. Krämer, K. Nippel, and **L. Rathmann**, *"$\bar{\text{D}}$ARKRAYNET: Emulation of cosmic-ray antideuteron fluxes from dark matter"*, published in JCAP 11 (2024) 017 [2]

# Acknowledgements

This thesis represents the culmination of years of work, and it would not have been possible without the support, guidance, and encouragement of many individuals and institutions.

First and foremost, I would like to express my deepest gratitude to my supervisor Prof. Dr. Michael Krämer for his invaluable mentorship, continuous support and guidance throughout my doctoral studies. I am grateful for the opportunity to work in such a stimulating research environment and for the freedom to explore my own ideas. Furthermore, I am thankful for getting the ability to attend numerous conferences and workshops, which have broadened my horizons and allowed me to meet many inspiring researchers.

I would also like to extend my sincere thanks to my second supervisor Prof. Dr. Felix Kahlhoefer for his support and advice during my doctoral studies. I am grateful for his great hospitality when I visited the Karlsruhe Institute of Technology and for the many fruitful discussions we had. Furthermore, I very much look forward to continuing and expanding our collaboration in the future.

I am also very thankful for the support and guidance of Dr. Jan Heisig starting during my Bachelor's and continuing during my doctoral studies. Without his expertise and advice, this thesis would not have been possible. I have learned a lot from him, and I am grateful for the many productive discussions we had.

Additionally, I am grateful for my collaboration with Dr. Monika Blanke who was always very supportive and helpful even though we mostly saw each other online. She was also a great host during my visit to Karlsruhe, and I am looking forward to continuing our collaboration in the future.

I would also like to thank all my collaborators, namely Dr. Harun Acaroğlu, Dr. Michael Korsmeier, Dr. Kathrin Nippel, and Dr. Felix Wilsch for the great collaboration. I am grateful for the many great discussions we had and the work that has come out of it.

I would like to thank Dr. Monika Blanke, Dr. Jan Heisig, Dr. Hanno Jacobs, Lukas Lang, and Dr. Felix Wilsch for proofreading this thesis and providing valuable feedback. I am grateful for their time and effort, which have significantly improved the quality of this thesis.

Being a part of the Institute for Theoretical Particle Physics and Cosmology at RWTH Aachen University has been a great experience, and I am grateful for having had the opportunity to work in such a stimulating research environment. I am particularly thankful for my office mates, Marie Hein, and Dr. Kathrin Nippel, for being great colleagues and friends with whom I have shared many great moments. Among these moments are the many coffee breaks, book club evenings, and movie nights together with all of our friends and colleagues at the institute, which I will always remember fondly.

My heartfelt thanks go to my family for their unconditional love, encouragement, and belief in me. I am grateful for their support and understanding, which have

been invaluable to me throughout my studies. A very special thanks goes to Dr. Hanno Jacobs for his unwavering love, patience, and encouragement throughout this journey. His understanding, support, and ability to make me laugh, even in the most stressful moments, have meant more to me than words can express. I would also like to thank my friends for their support and encouragement, which have helped me to stay motivated and focused during challenging times.

Finally, I would like to express my deepest gratitude to the Deutsche Forschungsgemeinschaft (DFG, German Research Foundation) for funding my doctoral studies through the Collaborative Research Center TTR 257 "Particle Physics Phenomenology after the Higgs Discovery".

# Contents

**Abstract** **i**

**Zusammenfassung** **iii**

**Declaration of Authorship** **v**

**List of Publications** **vii**

**Acknowledgements** **ix**

**Introduction** **1**

**1 Overview of Dark Matter** **5**
1.1 Evidence for dark matter . . . . . 5
1.1.1 Galaxy rotation curves . . . . . 5
1.1.2 Galaxy clusters . . . . . 8
1.1.3 Large scale structures . . . . . 9
1.1.4 Cosmic microwave background . . . . . 10
1.2 Properties of dark matter . . . . . 10
1.3 Production in the Early Universe . . . . . 11
1.4 Searches for dark matter . . . . . 16
1.4.1 Direct searches . . . . . 17
1.4.2 Collider searches . . . . . 19
1.4.3 Indirect searches . . . . . 21
1.5 Dark matter candidates . . . . . 25
1.5.1 Scalar singlet Higgs portal model . . . . . 25
1.5.2 Dark minimal flavor violation . . . . . 26

**I Dark Matter Indirect Detection**

**2 Dark Matter Indirect Detection with Antideuterons** **31**
2.1 Introduction . . . . . 31
2.2 Cosmic ray antideuterons . . . . . 32
2.2.1 Production with the coalescence mechanism . . . . . 33
2.2.2 Spectra from Dark Matter annihilation . . . . . 36
2.2.3 Propagation . . . . . 38
2.2.4 Detection . . . . . 43
2.3 Neural emulation of antideuteron flux . . . . . 46
2.3.1 Training sample . . . . . 47
2.3.2 Network setup and performance . . . . . 48
2.3.3 Marginalized spectra and sensitivity factor . . . . . 52
2.4 Projections for experimental sensitivities . . . . . 54

2.5 Summary . . . . . 58

## II Phenomenology of Flavored Dark Matter Models

**3 Flavored Majorana Dark Matter 63**
3.1 Introduction . . . . . 63
3.2 Model description . . . . . 64
3.2.1 Field content and interactions . . . . . 64
3.2.2 Parameterization of the coupling matrix . . . . . 64
3.2.3 Dark matter mass spectrum . . . . . 66
3.3 Phenomenology . . . . . 66
3.3.1 Dark matter relic density . . . . . 67
3.3.2 Direct detection . . . . . 71
3.3.3 Indirect detection . . . . . 73
3.3.4 Flavor constraints . . . . . 73
3.4 Scans and results . . . . . 74
3.4.1 Scan setups . . . . . 75
3.4.2 Combined results . . . . . 78
3.5 Collider searches . . . . . 82
3.5.1 LHC simplified model constraints . . . . . 82
3.5.2 Model-specific signatures . . . . . 86
3.6 Summary . . . . . 90

**4 General Framework for Studying Flavored Dark Matter 93**
4.1 Introduction . . . . . 93
4.2 Flavored dark matter models . . . . . 93
4.2.1 Real scalar dark matter . . . . . 95
4.2.2 Complex scalar dark matter . . . . . 97
4.2.3 Majorana fermion dark matter . . . . . 99
4.2.4 Dirac fermion dark matter . . . . . 101
4.3 Flavored dark matter phenomenology . . . . . 102
4.3.1 Relic density . . . . . 102
4.3.2 Direct detection . . . . . 103
4.3.3 Indirect detection . . . . . 103
4.3.4 Collider constraints . . . . . 105
4.3.5 Flavor constraints . . . . . 105
4.4 Example: Majorana dark matter coupling to right-handed leptons . . 106
4.4.1 Scan setup . . . . . 106
4.4.2 Results . . . . . 107
4.5 Summary . . . . . 112

## III Conclusions and Appendices

**5 Conclusions 117**

**A Sensitivity Factor for the SSHP Model 121**

**B Cross Sections and Rates for Flavored Majorana Dark Matter 123**
B.1 Cross sections for annihilation processes . . . . . 123
B.2 Cross sections for conversion processes (scatterings) . . . . . 126

B.3 Decay rates . . . . . 127

**Bibliography** **129**

# Introduction

One of the biggest mysteries in modern science is the nature of a still unknown form of matter which seems to only interact gravitationally with visible matter and not electromagnetically. Because of the lack of interaction with light, this form of matter referred to as dark matter [3–5]. The theory of dark matter helps to explain the observed motions of stars and galaxies, observations of colliding galaxy clusters, the formation of large scale structures, and the anisotropies in the cosmic microwave background (CMB) which would otherwise be impossible if only the visible matter were present. By investigating the anisotropies in the CMB with the Planck satellite, the amount of dark matter can even been measured to be about 84% of the entire cosmological matter density [6]. To summarize, the evidence for its existence is overwhelming but so far the exact properties and interactions with ordinary matter are still unknown. Therefore, a promising candidate for dark matter is needed to explain the observed phenomena.

So far, the Standard Model (SM) of particles provides no fitting dark matter candidate even though the SM is the most successful quantum field theory to this day. There are many theories beyond the SM as to what dark matter is made of. Popular theories are that dark matter is made out of additional new particles which are expected to be interacting weakly, not electrically charged and stable [7–10]. The particles proposed in these dark matter models can potentially be detected by looking for missing energy at colliders and elastic or inelastic scatters of dark matter with atomic nuclei, called direct detection. Another possibility is to look for SM particles produced by dark matter annihilation in the form of an excess in cosmic ray (CR) fluxes, called indirect detection, which is what we will focus on in the first part of this thesis.

A promising target for detecting dark matter indirectly through annihilations are antiparticles as their production in astrophysical sources is very rare compared to particles and dark matter annihilation would produce an equal amount of particles and antiparticles [11–13]. Established targets for indirect detection are positrons and antiprotons. The background for these particles from astrophysical sources however is still high compared to the flux expected from dark matter annihilation. Therefore, we want to study the production of antideuterons in this thesis as their production from CR interactions in the energy range relevant for dark matter annihilation is very suppressed [14–19]. This makes them a very promising target for indirect detection of dark matter.

There are many models that aim to explain the nature of dark matter and that are currently being tested by various experiments. Probably the most popular model for particle dark matter are weakly interacting massive particles (WIMPs). Their popularity arises from the fact that the prospects to detect them with current and future experiments are very promising and that they can easily predict the observed relic abundance of dark matter by assuming that dark matter interacts weakly and that the dark matter mass is around the electroweak scale [20]. Unfortunately, there has not been a conclusive detection signal that can confirm the validity of any WIMP

candidate yet and the constraints for most WIMP models are getting tighter with upcoming experiments [21]. Therefore, it is necessary to look for alternative dark matter models which have a less constrained parameter space.

One example of such an alternative model is a flavored dark matter model which is based on the idea that dark matter comes in multiple generations and has a non-trivial flavor structure in their couplings to SM fermions [22–29]. This additional flavor structure is well motivated as the existence of multiple generations of particles is a well established fact in the SM. The flavored dark matter model allows for a more complex phenomenology such that the correct relic abundance can be achieved while still being consistent with current constraints from various experiments. However, because of the non-trivial flavor structure, models of flavored dark matter are heavily constrained by flavor observables. Therefore, the models have been restricted to models with minimal flavor violation (MFV) where the only source of flavor violation stems from the SM Yukawa couplings [30–33]. This assumption is very restrictive in terms of the flavor structure of the models and therefore a more general framework was introduced in [34] called dark minimal flavor violation (DMFV) which allows for a single new source of flavor violation in the dark sector. As a result, the models can have a more complex flavor structure while still having a manageable amount of new parameters. In this framework, the dark matter particles are introduced as a triplet under a new global flavor symmetry group and couple to SM fermions through a new mediator particle. There are many options as to what fundamental properties the dark matter flavor triplet and the mediator can have. The phenomenology of various models has been studied in the literature with models for Dirac fermion dark matter [34–40], Majorana fermion dark matter [41] and complex scalar dark matter [42–44].

In this thesis, we will first focus on a case where the dark matter triplet consists of Majorana fermions and the mediator is a scalar particle coupling to up-type quarks. We will extend the phenomenological study of [41] to include a more complex freeze-out scenario which takes into account the coannihilations of the dark matter particles and the mediator. By assuming that the conversions between the dark matter particles and the mediator do not have to be in equilibrium at freeze-out, we can open up the viable parameter space for the model in the conversion-driven freeze-out scenario. In addition, we revisit the constraints from LHC searches and perform a broader analysis of the parameter space using a larger number of LHC searches. Lastly, we will identify promising searches to distinguish between Majorana and Dirac fermion dark matter models that couple to up-type quarks.

Because of the many possibilities for constructing a flavored dark matter model in the DMFV framework, we will furthermore develop a general analysis pipeline for studying the phenomenology of various possible flavored dark matter models. This is especially important since only a handful of the possible models have been studied in the literature so far. We will first discuss 20 possible models and their parameters and then develop a general framework for the calculation of the relic abundance and the constraints from direct and indirect detection, collider searches and flavor observables. We will then apply this framework to the case of a Majorana fermion dark matter triplet coupling to right-handed leptons and show the results of the analysis.

This thesis is structured in the following way: In chapter 1, we will give an overview of the evidence for dark matter and review the currently known properties of dark matter. We will also discuss the thermal production of dark matter in the early universe. Furthermore, we summarize the current experimental status of dark matter detection and list a few relevant dark matter candidates that we will consider in this

thesis.

The thesis is then split into two main parts. In part I, we will focus on the indirect detection of dark matter using antideuterons produced in dark matter annihilation. We will start with a review of the production of antideuterons in dark matter annihilation and the propagation of antideuterons together with the experimental status of antideuteron searches in section 2.2. We will then present a neural emulator that is able to compute the antideuteron flux from dark matter annihilation and validate it against the results of a full numerical calculation in section 2.3. In section 2.4, we will present the sensitivity projections for AMS-02 and the future GAPS and AMS-100 experiments to the antideuteron flux from dark matter annihilation.

In part II, we will focus on the phenomenology of flavored dark matter models. We will first discuss one specific model in chapter 3 where the dark matter particle is a Majorana fermion and the mediator is a scalar particle coupling to up-type quarks. The full description of the model will be discussed in section 3.2 and the phenomenology of the model will be studied in section 3.3 where we discuss the thermal production of the dark matter particles and the constraints from direct and indirect searches as well as flavor observables. We then discuss the phenomenological scans we perform to constrain the parameter space and show the results of the scans in section 3.4. The last section of the chapter, section 3.5, will focus on the constraints from LHC searches and the prospects for distinguishing between Majorana and Dirac fermion dark matter models that couple to up-type quarks. In chapter 4, we adopt a broader perspective and consider various possible flavored dark matter models. We will first discuss the possible models and their parameters in section 4.2 and then develop a general framework for the calculation of the relic abundance and the constraints from direct and indirect detection, collider searches and flavor observables in section 4.3. To demonstrate the applicability of the framework, we will apply it to the case of a Majorana fermion dark matter triplet coupling to right-handed SM leptons in section 4.4.

Finally, we will conclude in chapter 5 with a summary of the most important results and an outlook on future work.

# Chapter 1

# Overview of Dark Matter

The Universe is a vast and complex system, governed by forces and phenomena that are not yet fully understood. Among the most compelling mysteries in modern cosmology is the existence of dark matter, a form of matter that neither emits nor interacts with electromagnetic radiation but whose gravitational effects shape the cosmos on both large and small scales. Even though there are other possible explanations for the observed phenomena, the theory of dark matter is the most widely accepted explanation. Because of its very weak interaction with the Standard Model (SM) particles, dark matter is difficult to detect in experiments and so far, no direct or indirect detection of an interaction between dark matter and the SM has been successful. This is why the nature of dark matter remains one of the most important open questions in particle physics and cosmology.

In this chapter we summarize the current status of dark matter research. For recent reviews on dark matter see e.g. [3–5, 8, 45, 46]. Here, we discuss some of the most important evidences for dark matter and the properties that have been inferred so far. We then continue with reviewing the thermal production of dark matter in the early Universe. We also discuss the different search strategies for particle dark matter and some resulting current constraints on the dark matter cross section. Lastly, we discuss the relevant dark matter models that we will consider in this thesis which can account for the observed evidence of dark matter.

## 1.1 Evidence for dark matter

Even though we have not detected the effects of dark matter interactions with SM particles in any experiment, we can see its gravitational interaction effects at different scales in the Universe: on the galactic scale, on the scale of galaxy clusters and on cosmological scales, which we will discuss in the following. Historically, one of the first and most important evidences for dark matter came from the study of galaxy rotation curves by Fritz Zwicky in 1933 [47], which also provides the most direct evidence for dark matter.

### 1.1.1 Galaxy rotation curves

In spiral galaxies, the rotation curves of the stars and gas in the galaxy are measured by observing the Doppler shift of the light emitted by the stars and gas. The rotation curve is the velocity of the stars and gas as a function of the distance to the center of the galaxy. The visible mass in spiral galaxies is mostly concentrated in a central bulge and a disc. At large enough distances, the entire mass is inside the radius of

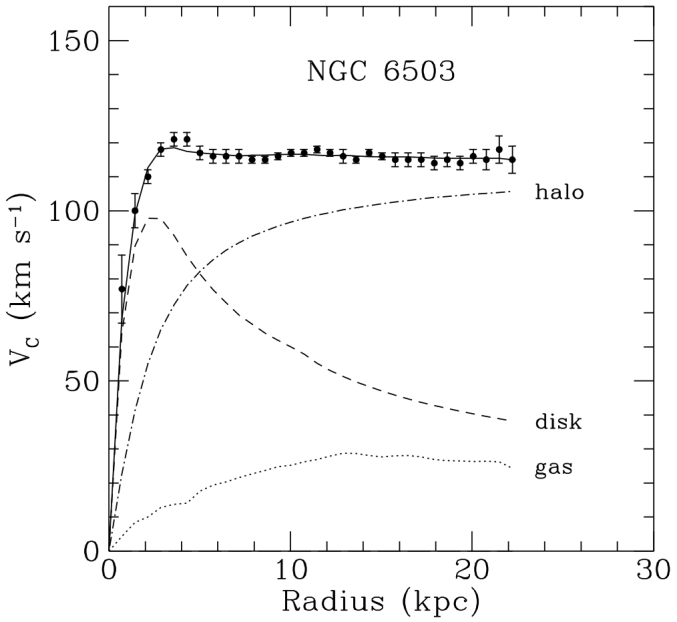


**Figure 1.1:** Galaxy rotation curve of NGC 6503. The dotted, dashed and dash-dotted lines represent the contributions of gas, the galactic disc and the dark matter halo, respectively. The solid line shows the best-fit to the data. Figure taken from [4].

the galaxy and the velocity $v$ can be computed as a function of the distance $R$ to the center with Gauss' theorem:

$$v(R) = \sqrt{\frac{GM(R)}{R}}\,, \tag{1.1}$$

where $M(R)$ is the mass captured in a sphere of radius $R$ and $G$ is the gravitational constant. The resulting rotation curve assuming that there is only the visible galactic disc and gas can be seen in fig. 1.1, represented by the dashed line, where we show as an example the galaxy rotation curve measured for NGC 6503 [48].

In contrast to the prediction of the rotation curve for the galactic disc, the observed velocity does not decrease with $1/\sqrt{R}$ but stays constant at large distances. This implies that there is more mass in the galaxy than can not be seen. Instead, a constant velocity $v_0$ as indicated by the dash-dotted line in fig. 1.1 implies that there is an additional spherical halo with $M(R) \propto R$ leading to a mass density distribution $\rho$ that decreases with $R^{-2}$ instead of an exponential decrease:

$$\rho(R) = \frac{v_0^2}{4\pi G R^2} \tag{1.2}$$

Due to the fact that the halo cannot be seen, it is considered to be mostly made out of dark matter. This behavior of the rotation curve was found in all galaxies that have been studied meaning that dark matter is present in all of them.

In practice, the modeling of the dark matter density distribution is more complex than indicated in eq. (1.2). Popular models which describe the observations well are the Navarro-Frenk-White (NFW) profile [49], the isothermal sphere (ISO) profile [48], the

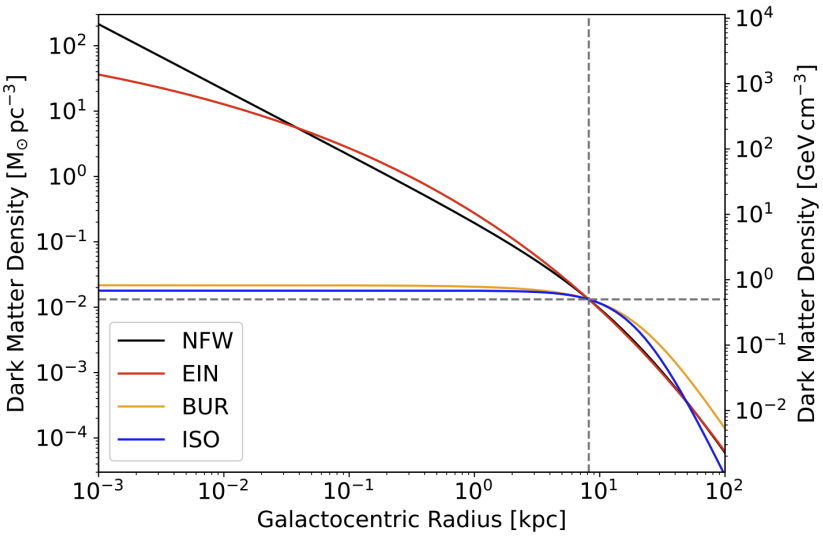


**Figure 1.2:** Different dark matter density profiles. We show the Navarro-Frenk-White (NFW), Einasto (EIN), Burkert (BUR) and isothermal sphere (ISO) profiles in black, red, yellow and blue, respectively. The values at the distance of the Solar System to the Galactic center are indicated by the dashed gray lines. Figure taken from [52].

Burkert (BUR) profile [50], and the Einasto (EIN) profile [51]. The density profiles of these models are given by

$$\rho_{\mathrm{NFW}}(R) = \frac{\rho_0}{\frac{R}{R_s}\left(1+\frac{R}{R_s}\right)^2}\,, \tag{1.3}$$

$$\rho_{\mathrm{ISO}}(R) = \frac{\rho_0}{\left(1+\left(\frac{R}{R_s}\right)^2\right)^2}\,, \tag{1.4}$$

$$\rho_{\mathrm{BUR}}(R) = \frac{\rho_0 R_s^3}{(R_s+R)\,(R_s^2+R^2)}\,, \tag{1.5}$$

$$\rho_{\mathrm{EIN}}(R) = \rho_0 \exp\left(-\frac{2}{\alpha}\left[\left(\frac{R}{R_s}\right)^{\alpha}-1\right]\right), \tag{1.6}$$

where $R_s$ is a characteristic scale and $\rho_0$ is the dark matter density at the distance of the Solar System to the Galactic center. All profiles are shown in fig. 1.2 where the NFW, EIN, BUR and ISO profiles are shown in black, red, yellow and blue, respectively. The BUR and ISO profiles display a core in the center of the galaxy in contrast to the NFW and EIN profiles which are cuspy. In fig. 1.1, an ISO profile has been used to fit the data.

As an alternative to the dark matter hypothesis explaining the rotation curves, one could also modify the theory of gravity. This is done in the theory of Modified Newtonian dynamics (MOND) which assumes that the gravitational force changes for small accelerations [53]. However, MOND has been shown to be inconsistent with other observations like the Bullet Cluster which we will discuss to next.



**Figure 1.3:** Composite image of the Bullet Cluster. The optical image shows galaxies in the background. The X-ray image in pink shows the hot gas of the two galaxies. Measurements of the position of the majority of the mass reconstructed from gravitational lensing are shown in blue. Credit: NASA/CXC/CfA/M.Markevitch; NASA/STScI, Magellan/U.Arizona/D.Clowe; ESO WFI

### 1.1.2 Galaxy clusters

Galaxy clusters have formed from the gravitational collapse of over-dense regions in the early Universe and are now the largest gravitationally bound systems. These over-dense regions have formed from the gravitational collapse of dark matter halos which have attracted baryonic matter and later on formed galaxies. Therefore, galaxy clusters are a great probe to study dark matter as they still contain a large amount of dark matter.

To estimate the amount of dark matter in these galaxy clusters, the visible mass is compared to the invisible mass. The amount of visible mass can be estimated by using the X-ray emission of the hot gas in the cluster. Furthermore, since galaxy clusters are extremely massive, light traveling past the cluster will be influenced by the gravitational field of the cluster. This leads to distorted images of galaxies in the background as the light coming from background galaxies will be bent by the galaxy cluster in front. This is called gravitational lensing. The distorted images can then be used to infer the total amount of mass needed to cause such a distortion of light [54].

One of the most famous examples for the evidence of dark matter is the observation of the Bullet Cluster studied in [55, 56] and shown in fig. 1.3. It shows two galaxy clusters which have most likely collided in the past and passed through one another. In red, the X-ray measurement of the hot gas of the two galaxy clusters shows a characteristic bullet shape from the interactions between the clusters when they crossed one another. Hence, this part also shows where the visible mass is located. The blue part shows the distribution of mass reconstructed from gravitational lensing measurements. This shows that the majority of the mass is not located at the same place as the hot gas because the majority of the mass has passed through one another without interacting. The best explanation for this phenomenon is that the majority of the total mass

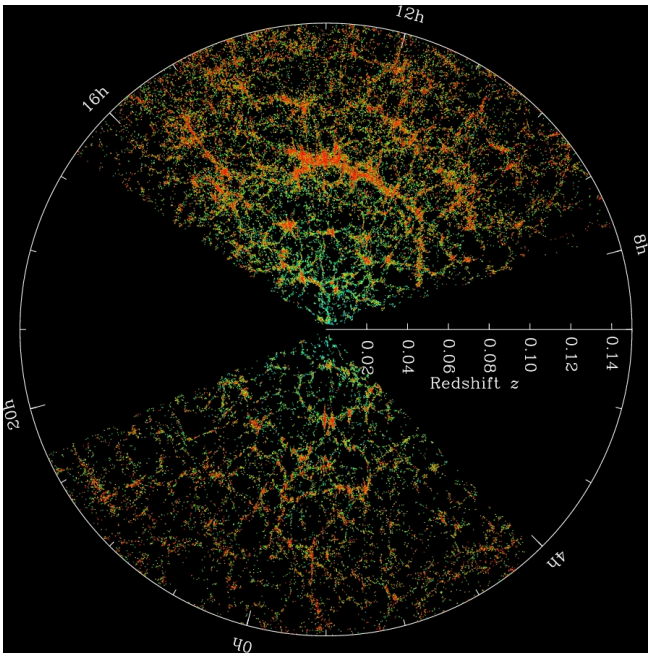


**Figure 1.4:** Slices through a 3-dimensional map of the distribution of galaxies measured by the Sloan Digital Sky Survey. Credit: M. Blanton and the SDSS

consists of mostly dark matter since dark matter did not interact with itself or the hot gas during the collision.

After the observation of the Bullet Cluster, many other similar systems have been studied and from all of them, it can be concluded that the existence of dark matter can be established with a significance of more than $7\sigma$ [57]. These observations have also been very important for the evidence for dark matter as this phenomenon cannot be explained by the theory of MOND since the theory fails to explain the separation of the visible and invisible mass [58].

### 1.1.3 Large scale structures

Instead of studying individual galaxy clusters, one can also study a large number of them and find that they form structures which are correlated. This is called the large scale structure of the Universe and is depicted in fig. 1.4 which shows slices through a 3-dimensional map of the distribution of galaxies measured by the Sloan Digital Sky Survey (SDSS) [59].

These structures have formed because of small inhomogeneities in the density field of the early Universe which caused small gravitational wells. In contrast to baryons and photons which were interacting rapidly when the Universe was still very hot, dark matter is interacting at most very weakly and non-relativistic (cold) which lead to dark matter clumping together in the gravitational wells. This would not have happened if dark matter was relativistic (hot) because it would simply stream out of the structures. Later, when the Universe has cooled enough for the formation of neutral hydrogen atoms, baryons began to concentrate in the now larger gravitational wells formed by dark matter. These heavy clusters of dark matter and baryons became heavier and finally formed the first stars and galaxies. Without the existence of cold dark matter, the formation of structures as we observe them today would have not

been possible.

This was verified by performing large N-body simulations where the gravitational motion of a large number of massive particles is simulated numerically. With these simulations, it is possible to simulate the clustering of dark matter and baryons and the resulting formation of correlated structures. One of the largest N-body simulation is the Millennium Run [60] with $2160^3$ particles in a cube with a length of $500\,h^{-1}$Mpc.

### 1.1.4 Cosmic microwave background

The imprints of dark matter can also be observed in the anisotropies of the cosmic microwave background (CMB). The CMB consists of the photons that have decoupled from baryonic matter in the early Universe and have been free-streaming through the expanding Universe without further interactions ever since. As described before, dark matter created gravitational wells and because the baryons and photons were tightly coupled in the early Universe, they are pulled into these wells together. This leads to an increased pressure and the photon pressure acts against the gravitational pull. This creates temperature fluctuations around dark matter clumps which can be observed through the CMB photons today. The position of the temperature fluctuations in the CMB depends on the dark matter density and the size of the fluctuations is determined by the amount of dark matter with respect to baryonic matter. The CMB anisotropies have been measured with high precision by the PLANCK satellite [6] and determine the amount of dark matter very accurately. The measured the energy density of cold dark matter is given by

$$\Omega_{\mathrm{DM}}h^2 = \frac{\rho_{\mathrm{DM}}}{\rho_{\mathrm{cr}}} = 0.1200 \pm 0.0012\,, \tag{1.7}$$

where $\Omega_{\mathrm{DM}}$ is the energy density of cold dark matter. It is given in units of the critical density $\rho_{\mathrm{cr}} = 3H^2/8\pi G$ and where $G$ is the Newtonian constant of gravitation and $h$ is the Hubble parameter $H$ in units of 100 km/s/Mpc. This corresponds to 26.4% of the total energy density of the Universe and 84.4% of the overall matter content in the Universe.

Using the different types of evidences for dark matter, we will now discuss the properties of dark matter that have been inferred from these observations.

## 1.2 Properties of dark matter

One can extract a few characteristics that dark matter should have from the observations of the effects of dark matter on different scales of the Universe: dark matter should be cold (non-relativistic), have no or extremely small electric charge, interact mostly through gravity, be stable over the lifetime of the Universe, and have small self-interactions [61]. An upper bound on the electric charge can be set to $3.5 \times 10^{-7}(m_{\mathrm{DM}}/1\,\mathrm{GeV})^{0.58}$ for $m_{\mathrm{DM}} > 1\,\mathrm{GeV}$ and to $4.0 \times 10^{-7}(m_{\mathrm{DM}}/1\,\mathrm{GeV})^{0.35}$ for $m_{\mathrm{DM}} < 1\,\mathrm{GeV}$ [62]. Merging clusters and the ellipticity of certain galaxies can place an upper bound on the self-interaction cross section of dark matter which is $\sigma_{\mathrm{DM-DM}}/m_{\mathrm{DM}} < 0.47\,\mathrm{cm}^2/\mathrm{g}$ at 95% C.L. [57]. A bound on the mass of dark matter can also be placed, although the allowed mass range is very large. The lower bound is set by the De Broglie wavelength of dark matter particles which has to fit the size of the smallest gravitationally bound dwarf galaxies. This leads to a lower bound of

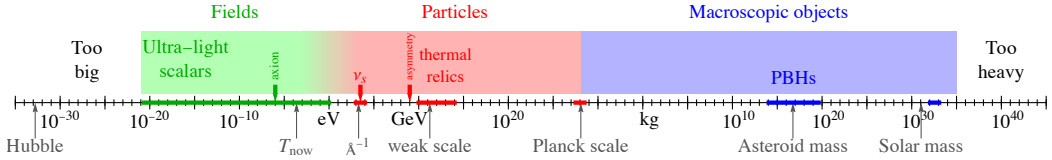


**Figure 1.5:** The entire mass range of possible dark matter candidates. Figure taken from [5].

$m_{\rm DM} \gtrsim 10^{-21}$ eV (note that fermionic dark matter has a higher lower bound because of the Pauli exclusion principle which results in $m_{\rm DM} \gtrsim 100\,\text{eV}$ [63]). An upper bound can be derived from the requirement that the dark matter mass has to be smaller than the mass of typical small dwarf galaxies which leads to an upper bound of $m_{\rm DM} \lesssim 10^4 M_\odot$ where $M_\odot$ is a solar mass [5].

These characteristics can be met either by a new or existing particle species or unknown massive objects like primordial black holes (PBHs). The entire allowed mass range and possible dark matter candidates are shown in fig. 1.5. Particles with very light masses are usually described by a classical field as long as they are lighter than the inverse Bohr radius (the most probable distance between the nucleus and the electron in a hydrogen atom) which is of the order of a keV. In this range, the de Broglie wavelength is larger than the size of atoms which means that dark matter will interact collectively with ordinary matter. For masses above the keV scale, dark matter is described as a particle as the de Broglie wavelength is smaller than the size of an atom and dark matter will interact with atoms individually. The largest possible mass of a particle is the Planck mass $M_P$ so above the Planck scale, dark matter is described as macroscopic objects which can be ordinary astrophysical objects like large planets or PBHs.

In the SM, the candidate that fulfills most of the requirements is the neutrino. Unfortunately, neutrinos can not make up all of dark matter because of their light mass which makes them a hot dark matter candidate which does not fulfill the requirement of cold dark matter. Therefore, a new candidate outside the SM is needed to explain the nature of dark matter.

## 1.3 Production in the Early Universe

For the remainder of the thesis, we focus on particle dark matter. Specifically, we consider weakly interacting massive particles (WIMPs) which is a well motivated and popular dark matter candidate [20, 21]. Particles that fall into that category are only weakly interacting with the SM where weakly means either through the weak force or with a small coupling comparable to the weak coupling strength. The typical mass range of WIMPs is of the order of $\sim 10\,\text{GeV} - \text{TeV}$ and the particles are stable or extremely long-lived. The popularity of WIMPs motivated many experiments to search for them which we will discuss in section 1.4. Before that, we will discuss the thermal production of dark matter in the early Universe which is a common production mechanism for WIMPs.

The energy density of dark matter has been measured by the PLANCK satellite and is given in eq. (1.7). Therefore, a proposed dark matter model has to predict the correct relic abundance to match the observation. In general, particle dark matter can be produced via thermal or non-thermal production or through a particle-antiparticle

asymmetry [61]. Non-thermal production means that the dark matter particles were not in thermal equilibrium in the early Universe. Examples for non-thermal relics are axion-like particles and dark matter produced via freeze-in. In contrast, thermal relics (meaning that dark matter was produced thermally) have been in thermal equilibrium with the SM in the early Universe.

Thermally produced dark matter interacts very frequently with the thermal bath in the early Universe because of the hot and dense conditions, meaning that all particles are in thermal equilibrium. As the Universe expands and cools down, interactions between dark matter and the SM become less likely and the dark matter particles decouple chemically. Because dark matter can not be produced efficiently anymore, their abundance drops until the annihilation rate of dark matter particles falls below the expansion rate of the Universe and their number density becomes constant. This process is referred to as the standard freeze-out mechanism. We will describe more complex freeze-out mechanisms for thermalized dark matter, like freeze-out with coannihilations and conversion-driven freeze-out, in section 3.3.1.

The relic abundance of dark matter produced through freeze-out can be calculated by solving a Boltzmann equation which relates the Liouville operator $\boldsymbol{L}$ describing the time rate of change to the collision operator $\boldsymbol{C}$ acting on the phase space distribution function $f(\boldsymbol{p}, \boldsymbol{x})$ which depends on the momentum $\boldsymbol{p}$ and the position $\boldsymbol{x}$ of the particles. The Boltzmann equation is given by

$$\boldsymbol{L}[f] = \boldsymbol{C}[f]\,. \tag{1.8}$$

This equation describes the interactions of the particles and therefore the change in their phase-space distribution. By assuming that the phase space distribution is homogeneous and isotropic, this equation can be simplified to an equation describing the change in the number density $n$ over time of the particles by integrating over the momentum space. Inserting expressions for the Liouville and collision operators, the Boltzmann equation for the number density $n$ is given by

$$\frac{\mathrm{d}n}{\mathrm{d}t} + 3Hn = -\langle\sigma v\rangle \left(n^2 - (n_{\mathrm{eq}})^2\right)\,, \tag{1.9}$$

where $H = \dot{R}/R$ is the Hubble rate in terms of the scale factor $R$ which describes the expansion of the Universe and $\langle\sigma v\rangle$ is the thermally averaged annihilation cross section $\sigma$ times the velocity $v$. The number density the particles would have in thermal equilibrium is described with $n_{\mathrm{eq}}$. The value of the Hubble parameter can be computed using the Friedmann equation [10]

$$H^2 = \frac{8\pi G}{3}\rho\,, \tag{1.10}$$

where $G$ is the gravitational constant. During freeze-out, the energy density $\rho$ is given by the energy density of radiation

$$\rho = \rho_{\mathrm{rad}} = \frac{\pi^2}{30} g_{\mathrm{eff}} T^4\,. \tag{1.11}$$

Inserting this expression into eq. (1.10) and using the relation $G = 1/M_P^2$ with the reduced Planck mass $M_P \approx 1.2 \times 10^{19}$ GeV, we get

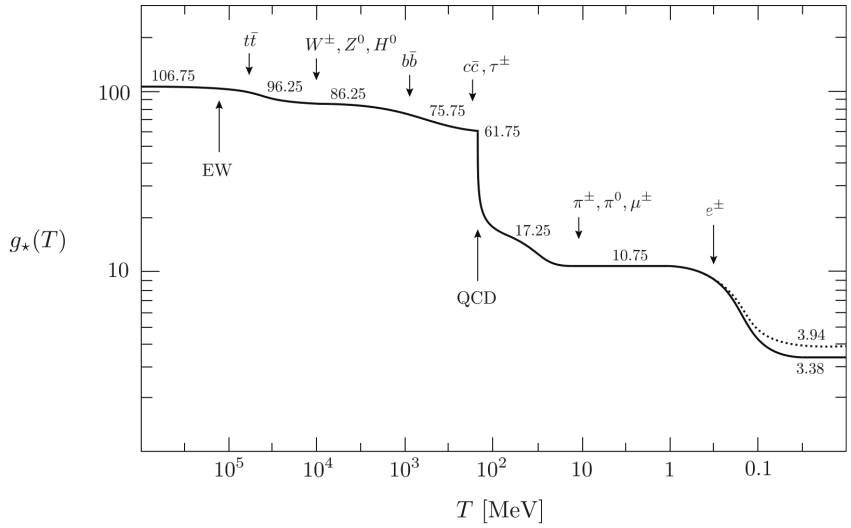


**Figure 1.6:** Evolution of relativistic degrees of freedom. The solid line shows the degrees of freedom for the energy density $g_{\text{eff}}(T)$ and the dashed line shows the degrees of freedom for the entropy density $h_{\text{eff}}(T)$. From [64].

$$H = \sqrt{\frac{8\pi^3}{90}} \sqrt{g_{\text{eff}}} \frac{T^2}{M_P} \,. \tag{1.12}$$

The effective number of relativistic degrees of freedom $g_{\text{eff}}$ depends on the temperature and varies as the Universe cools down, and heavier particles become non-relativistic. It is described by the sum over all boson and fermion degrees of freedom $g_{b/f}$ where each contribution is weighted by the temperature $T_{b/f}$ of the individual species

$$g_{\text{eff}}(T) = \sum_{\text{bosons}} g_b \frac{T_b^4}{T^4} + \sum_{\text{fermions}} \frac{7}{8} g_f \frac{T_f^4}{T^4} \,. \tag{1.13}$$

The evolution of $g_{\text{eff}}$ is shown in fig. 1.6. For very high temperatures, all particles are relativistic and $g_{\text{eff}}$ is given by the sum of internal degrees of freedom of all SM particles $g_{\text{eff}} = g_b + \frac{7}{8} g_f = 106.75$. As the Universe cools down, the number of relativistic degrees of freedom decreases because particles become non-relativistic, indicated by the arrows shown in the figure.

The equilibrium number density $n_{\text{eq}}$ can be expressed using the Maxwell-Boltzmann distribution as the equilibrium distribution function

$$n_{\text{eq}} = \frac{g}{(2\pi)^3} \int e^{-E/T} \mathrm{d}^3 p = \frac{gTm^2}{2\pi^2} K_2 \left( \frac{m}{T} \right) \,, \tag{1.14}$$

where $m$ is the mass of the particle and $g$ is the number of internal degrees of freedom. The function $K_i$ is the modified Bessel functions of second kind and order $i$. The Maxwell-Boltzmann distribution is valid for non-relativistic particles which is a good approximation for dark matter particles during freeze-out.

The general thermally averaged cross section for any annihilation process of two particles (particle 1 and particle 2) is defined as

$$\langle \sigma v \rangle = \frac{\int \sigma v e^{-E_1/T} e^{-E_2/T} \mathrm{d}^3 p_1 \mathrm{d}^3 p_2}{\int e^{-E_1/T} e^{-E_2/T} \mathrm{d}^3 p_1 \mathrm{d}^3 p_2}\,, \tag{1.15}$$

where $E_1$ and $E_2$ are the energies of the particles and $p_1$ and $p_2$ their momenta. $v$ is the Møller velocity which is covariant when written in terms of the interaction rate $\Gamma = n_1 n_2 \sigma v$ [65] and is defined as

$$v = \frac{\sqrt{(p_1 \cdot p_2)^2 - m_1^2 m_2^2}}{E_1 E_2}\,. \tag{1.16}$$

This expression can be used to evaluate the integrals in eq. (1.15) assuming that dark matter is made out of one particle species ($m_1 = m_2 = m$) which reduces the expression to one integral over the squared center of mass energy $s$:

$$\langle \sigma v \rangle = \frac{1}{8 m^4 T K_2^2(m/T)} \int_{4m^2}^{\infty} \sigma \sqrt{s} (s - 4m^2) K_1(\sqrt{s}/T) \mathrm{d}s \tag{1.17}$$

It is convenient to express eq. (1.9) in terms of the co-moving number density $Y = n/\rho_s$ where $\rho_s$ is the entropy density which is given by $\rho_s = S/R^3$ where $S$ is the entropy. The entropy density can be rewritten in terms of the energy density $\rho$ and the pressure $P$ of the particles in the thermal bath. The energy density is given by the energy density during radiation domination $\rho_{\mathrm{rad}}$ as in eq. (1.11) and using $P = \rho/3$, the entropy density can be expressed as

$$\rho_s = \sum_i \frac{\rho_i + P_i}{T_i} = \frac{2\pi^2}{45} h_{\mathrm{eff}} T^3\,. \tag{1.18}$$

The effective number of degrees of freedom in entropy $h_{\mathrm{eff}}$ depends again on the temperature through

$$h_{\mathrm{eff}}(T) = \sum_{\mathrm{bosons}} g_b \frac{T_b^3}{T^3} + \sum_{\mathrm{fermions}} \frac{7}{8} g_f \frac{T_f^3}{T^3}\,. \tag{1.19}$$

The evolution of $h_{\mathrm{eff}}(T)$ is shown in fig. 1.6. For high temperatures, all relativistic particles are in thermal equilibrium and $h_{\mathrm{eff}} = g_{\mathrm{eff}}$. Because of the different temperature dependence of decoupled particles, $h_{\mathrm{eff}}$ and $g_{\mathrm{eff}}$ begin to deviate at lower temperatures leading to larger values of $h_{\mathrm{eff}}$ compared to $g_{\mathrm{eff}}$.

The Boltzmann equation in terms of the co-moving number density $Y$ is then given by

$$\frac{\mathrm{d}Y}{\mathrm{d}t} = \frac{\mathrm{d}}{\mathrm{d}t}\left(\frac{n}{\rho_s}\right) = \frac{1}{\rho_s}\frac{\mathrm{d}n}{\mathrm{d}t} - \frac{n}{\rho_s^2}\frac{\mathrm{d}\rho_s}{\mathrm{d}t}\,. \tag{1.20}$$

In the absence of entropy production, $S$ is constant and the time derivative of $\rho_s$ is given by

$$\frac{\mathrm{d}\rho_s}{\mathrm{d}t} = -3\frac{\dot{R}}{R}\rho_s = -3H\rho_s\,, \tag{1.21}$$

which leads to

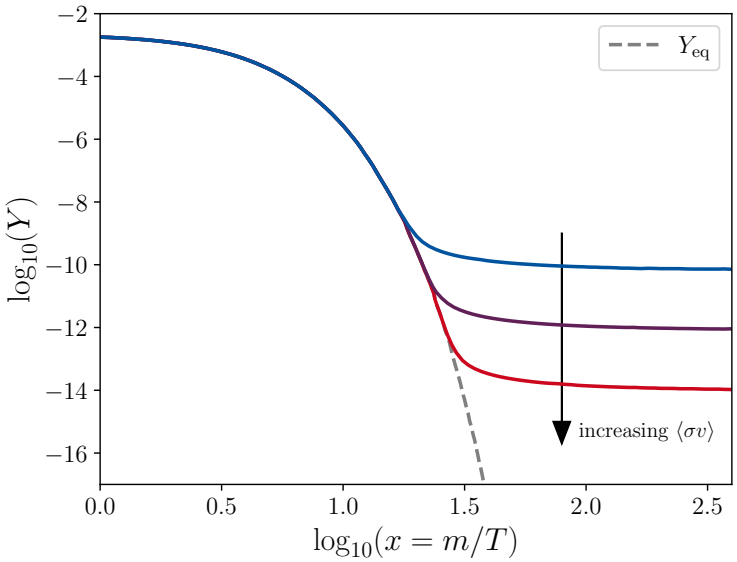


**Figure 1.7:** Evolution of the co-moving number density $Y$ as a function of the temperature $T$ of the Universe. The final relic abundance decreases with increasing annihilation rate as shown by the different colored lines. Adapted from [66].

$$\frac{\mathrm{d}Y}{\mathrm{d}t} = -\rho_s \langle\sigma v\rangle \left(Y^2 - (Y_{\mathrm{eq}})^2\right) . \tag{1.22}$$

The next convenient step is to express eq. (1.22) in terms of the dimension-less quantity $x = m/T$ as the right-hand side of the equation depends only on the temperature. The derivative of $Y$ with respect to $x$ is then given by

$$\frac{\mathrm{d}Y}{\mathrm{d}x} = \frac{\mathrm{d}t}{\mathrm{d}x}\frac{\mathrm{d}Y}{\mathrm{d}t} = -\frac{1}{3H}\frac{\mathrm{d}\rho_s}{\mathrm{d}x}\frac{\mathrm{d}Y}{\mathrm{d}t} = \frac{1}{Hx}\frac{\mathrm{d}\rho_s}{\mathrm{d}x}\langle\sigma v\rangle \left(Y^2 - (Y_{\mathrm{eq}})^2\right) , \tag{1.23}$$

where we have used the result for the time derivative of $\rho_s$ from eq. (1.21).

The evolution of the co-moving number density as a function of $x = m/T$ described by eq. (1.23) is shown in fig. 1.7 for different annihilation cross sections indicated by different colors. For large temperatures, the number density still follows the equilibrium number density as the interaction rate is much larger than the Hubble rate. At some point, $Y$ decouples from the equilibrium density as the interaction rate gets closer to the Hubble rate. The final relic abundance stays constant when the interaction rate becomes much smaller than the Hubble rate and its value depends on the size of the annihilation rate.

Once the present-day number density $Y_0$ has been determined through solving eq. (1.23), the relic density can be calculated with

$$\Omega h^2 = \frac{m_{\mathrm{DM}}\rho_{s,0}Y_0}{\rho_c}, \tag{1.24}$$

where $\rho_{s,0}$ is the present-day entropy density and $\rho_c = 3H^2/8\pi G$ is the critical density. In order to obtain the relic abundance predicted by a specific dark matter model, one usually has to solve the entire Boltzmann equation in eq. (1.23). However, the

calculation can be simplified by making a few assumptions which leads to an estimate of the value for $\langle\sigma v\rangle$ which can be used to estimate the relic abundance [7, 10].

To first get an estimate of $\Omega h^2$, we first rewrite eq. (1.24) in terms of the number density $n$ and introduce a factor $T_0^3/T_0^3$ where $T_0$ is the present-day temperature of the Universe. This leads to

$$\Omega h^2 = \frac{m_{\mathrm{DM}} T_0^3}{\rho_c} \frac{n_0}{T_0^3} \,. \tag{1.25}$$

Assuming again that the entropy density is conserved so that $RT = \text{constant}$, we can relate the present-day temperature $T_0$ and number density $n_0$ to the freeze-out temperature $T_{\mathrm{fo}}$ and number density $n_{\mathrm{fo}}$ with $n_0/T_0^3 \approx n_{\mathrm{fo}}/T_{\mathrm{fo}}^3$. During freeze-out, the interaction rate is approximately equal to the Hubble rate $n_{\mathrm{fo}}\langle\sigma v\rangle \approx H_{\mathrm{fo}}$ which we can use to obtain the number density at freeze-out $n_{\mathrm{fo}}$. Using eq. (1.12), we can approximate the Hubble rate at freeze-out with $H_{\mathrm{fo}} \approx m_{\mathrm{DM}}^2/x_{\mathrm{fo}}^2 M_P$ which then gives us the following expression for the relic abundance

$$\Omega h^2 \approx \frac{m_{\mathrm{DM}} T_0^3}{\rho_c} \frac{m_{\mathrm{DM}}^2}{x_{\mathrm{fo}}^2 M_P \langle\sigma v\rangle} = \frac{x_{\mathrm{fo}} T_0^3}{\rho_c M_P} \frac{1}{\langle\sigma v\rangle} \,. \tag{1.26}$$

Using $x_{\mathrm{fo}} \approx 25$ which is a typical value for when freeze-out occurs that has been obtained by solving the Boltzmann equation numerically, we can estimate the value of $\Omega h^2$:

$$\Omega h^2 \approx \frac{3.8 \times 10^{-27}\,\mathrm{cm}^3/\mathrm{s}}{\langle\sigma v\rangle} \,. \tag{1.27}$$

This expression can be used to estimate the value of $\langle\sigma v\rangle$ by using the measured value of $\Omega h^2$ from PLANCK in eq. (1.7). The typical annihilation cross section for a thermal relic is thus

$$\langle\sigma v\rangle \approx 3 \times 10^{-26}\,\mathrm{cm}^3/\mathrm{s} \,, \tag{1.28}$$

which is the benchmark value for a thermal relic. This value can be used to estimate the relic abundance of a dark matter model without solving the full Boltzmann equation by computing the thermally averaged annihilation rate for the dark matter model and comparing it to the benchmark value.

## 1.4 Searches for dark matter

Because of the popularity of WIMPs as a dark matter candidate, many experiments have been designed to search for them which lead to numerous approaches to detect dark matter particles. They can be categorized by either indirect searches, direct searches or collider searches. The three different types of searches are shown in fig. 1.8. In indirect detection experiments, scientists search for SM particles that are produced during annihilation dark matter which is depicted by the green arrow. Direct detection experiments use the signal produced by dark matter scattering with SM particles as it is shown with the blue arrow. Colliders try to produce dark matter directly by

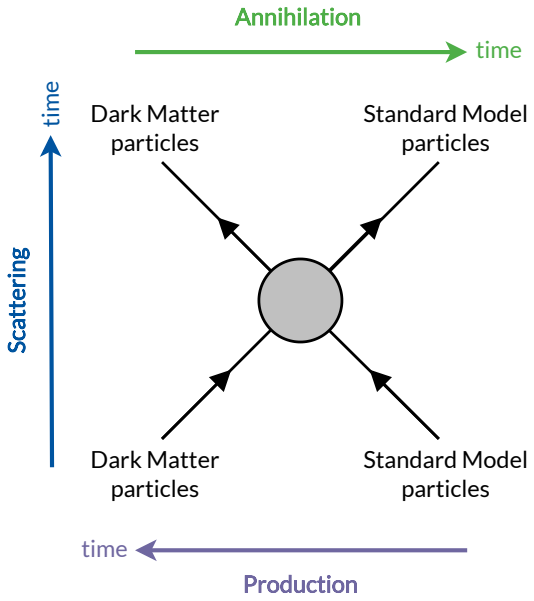


**Figure 1.8:** Schematic diagram explaining direct and indirect detection and collider searches. The green arrow shows the indirect detection through dark matter annihilation, the blue arrow shows the direct detection through dark matter scattering and the purple arrow shows the collider searches for dark matter produced in particle collisions.

colliding SM particles which is shown by the purple arrow. In the following, we will discuss the different search strategies in more detail.

### 1.4.1 Direct searches

In direct searches, experiments look for the recoil of SM particles when dark matter particles scatter on the detector material, see for example [67, 68] for recent reviews. Even though dark matter particles should pass through the detector very frequently, the scattering rate is expected to be extremely low because of the small cross section of dark matter particles, and the energy deposited in the detector is very small. To overcome these challenges, the detectors have to be highly sensitive and have a low background. In order to suppress the background, the detectors are usually placed deep underground to shield them from cosmic rays and the detector material is chosen to be ultrapure. The sensitivity is increased by using large detector volumes and long exposure times. If a dark matter scattering event happens, the energy that is deposited in the detector can then be measured in terms of heat (thermal phonons in crystals), scintillation light or ionization.

Nowadays, most of the very sensitive experiments use noble gases like xenon or argon as the detector material because they can reach a high level of radiopurity and the detector volume can be increased easily. The three largest xenon-based detectors are currently XENONnT [69], LUX-ZEPLIN (LZ) [70] and PandaX-4t [71]. Xenon-based detectors have an advantage with respect to argon-based detectors as xenon has a higher atomic number which leads to an optimal self-shielding against external background. The most sensitive argon detectors are DarkSide-50 [72] and DEAP-3600 [73]. An even larger argon detector is going to be the DarkSide-20k detector which is currently under construction [74].

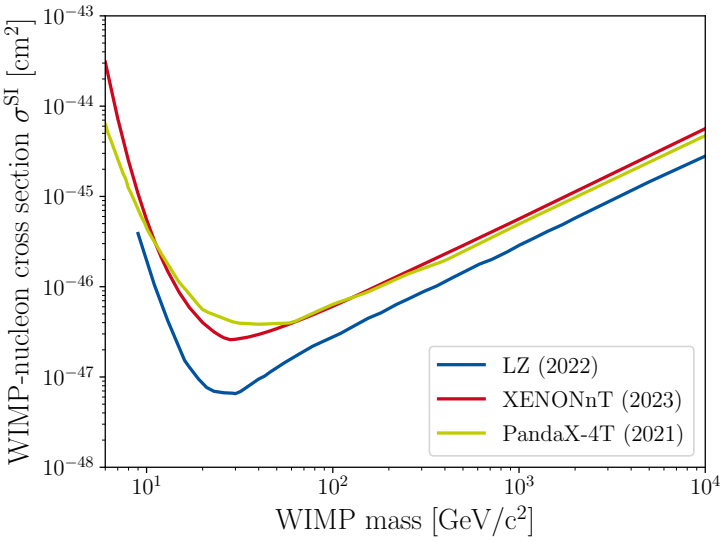


**Figure 1.9:** Current constraints on the SI WIMP-nucleon cross section from xenon-based experiments. The strongest limits are obtained with XENONnT [79] (red), LZ [80] (blue) and PandaX-4t [81] (green).

Other experimental techniques for direct detection are the use of cryogenic detectors, scintillating crystals or superheated liquids. Cryogenic detectors are cooled down to very low temperatures and measure the energy deposited in the detector through heat, ionization and/or scintillation. Among the most sensitive cryogenic detectors are the CDMS experiment [75] and the CRESST experiment [76]. Scintillating crystals are based on mostly NaI or less commonly CsI crystals that are doped with thalium. The energy deposited in the crystal is measured through the scintillation light that is produced. To reject backgrounds, the energy that is deposited is not measured on an event by event basis but rather by using the fact that the dark matter signal should produce a nuclear recoil signal with an annual modulation. The DAMA/LIBRA experiment [77] is the most famous experiment using this technique. Lastly, detectors using superheated liquid are usually operated as bubble chambers. The energy deposited in the liquid triggers a phase transition that leads to the formation of a bubble. The PICO-60 experiment [78] is the most sensitive experiment in this category.

In general, there are two types of interactions that can be detected in direct detection experiments: dark matter scattering on nuclei (nuclear recoil) or electrons (electronic recoil) [5]. The nuclear recoil signal is more sensitive to dark matter masses in the tens of GeV mass range while the electronic recoil signal is more sensitive to dark matter masses in the few MeV mass range. This is because the energy transfer in a scattering event is the largest when the mass of the dark matter particle is similar to the mass of the target particle. Here, we are not interested in dark matter masses in the few MeV mass range, so we will focus on the nuclear recoil signal.

Usually, the cross section of dark matter scattering on a nucleus $\sigma_A$ is converted into the dark matter-nucleon cross section $\sigma_N$. The scattering is further split into a spin-independent (SI) and a spin-dependent (SD) part. Typically, the constraints from SI scattering are stronger than the constraints from SD scattering as the SI cross section is enhanced by the coherent scattering of the dark matter particles on the nucleus. The SD cross section can be further separated into the cross section for scattering on protons and neutrons.

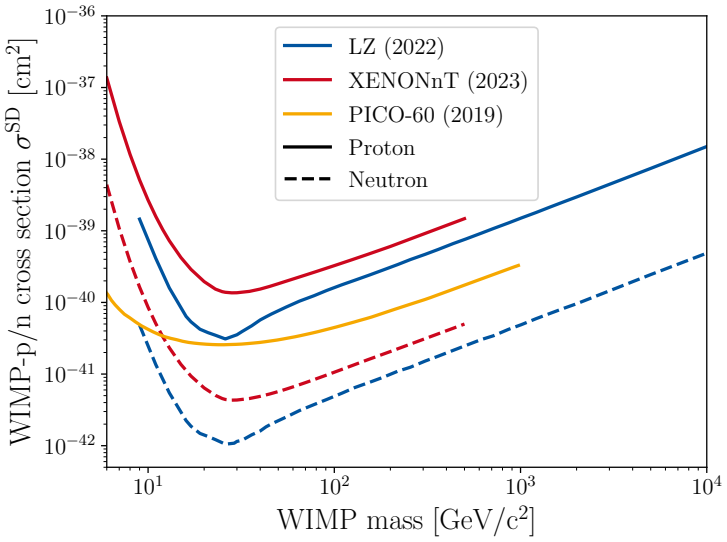


**Figure 1.10:** Current constraints on the SD WIMP-proton and WIMP-neutron cross section from xenon-based experiments. The strongest limits are obtained with XENONnT [79] (red), LZ [80] (blue) and PICO-60 [78] (orange).

The strongest limits on the SI WIMP-nucleon cross section $\sigma^{SI}$ for dark matter masses above 10 GeV come from xenon-based experiments. The current constraints are shown in fig. 1.9 with limits from XENONnT [79], LZ [80] and PandaX-4t [81]. For the SD cross section, the corresponding limits for WIMP-proton and WIMP-neutron scattering are shown in fig. 1.10. In this case, PandaX-4t has not published any results yet and the strongest limits for WIMP-proton scatterings are not obtained with a xenon based experiment but with PICO-60 [78].

### 1.4.2 Collider searches

The next search strategy we want to discuss is collider searches. In collider searches, the aim is to produce dark matter particles directly in the experiment by colliding SM particles. If dark matter is a thermal relic with a TeV-scale mass, then it may be produced at current and future colliders [5]. The most difficult part of collider searches is that the dark matter particle is invisible to the detector and leaves no trace. Therefore, if dark matter is produced, it will manifest itself as missing energy in the detector. In order to reconstruct the amount of missing energy, other visible particles that are also created in the collision have to be detected, such as initial state radiation particles or particles that are produced in the decay of the mediator.

The two main types of colliders are electron-positron colliders and hadron colliders that collide protons with protons or antiprotons. The largest electron-positron collider that has been used for dark matter searches is the LEP collider at CERN with a maximum center-of-mass energy of $\sqrt{s} \approx 200$ GeV [82]. With current hadron colliders, it is possible to go to even higher center-of-mass energies. For example, the LHC $pp$ collider at CERN has a center-of-mass energy of $\sqrt{s} = 14$ TeV [83]. A disadvantage of these colliders is however, that in contrast to electrons, protons are not elementary particles and are made out of quarks and gluons. This means that the elementary particles inside the proton only carry a fraction of the total proton energy and the collisions produce a large quantum chromodynamics (QCD) background. Additionally,

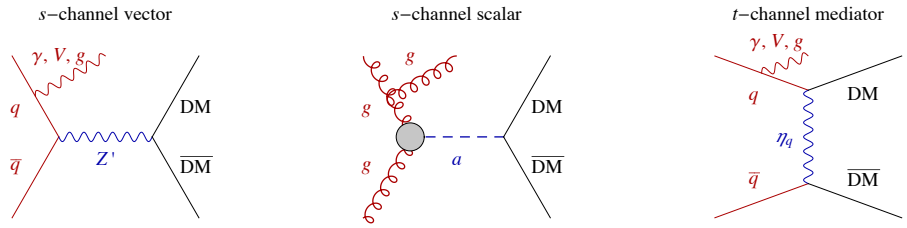


**Figure 1.11:** Examples for Feynman diagrams for the $s$-channel simplified model with a vector mediator (left), the $s$-channel simplified model with a scalar mediator (middle) and the $t$-channel simplified model with a colored mediator (right). Figure taken from [5].

the LHC is only able to measure the missing transverse energy $\not{E}_T$ as the total energy of the particular partonic event is unknown. Therefore, LHC searches also have to rely on additional particles that are detected in the detector to determine the missing transverse energy.

So far, no significant excess over the SM background has been observed in all collider experiments even though specific searches have been performed in order to detect a dark matter signal. This can either mean that the dark matter particle is too heavy to be produced with current colliders or the coupling to the SM particles is too small. These searches can nevertheless be used to constrain the parameter space of dark matter models.

Here, we want to focus on constraints from searches at the LHC as these searches are the most constraining for the dark matter models considered in this thesis, see e.g. [84–86] for recent reviews on LHC searches. In order to interpret the results from the LHC in terms of dark matter models, the most straightforward way is to study the phenomenology of every single model. This is however very time-consuming and not feasible for all models. A model-independent alternative is to use effective field theories (EFTs) which are a general framework to describe physical phenomena at a given energy scale by systematically incorporating all possible interactions consistent with the symmetries of the system, while higher-energy effects are encoded in suppressed operators. However, because hadron colliders can go to very high energies, the EFT approach is not always valid as the mediator mass can be in the TeV range. Therefore, simplified models have been developed to interpret the LHC results for a given dark matter model as a bridge between the two ends of the spectrum [87, 88].

The goal of these simplified models is to capture the main features of the dark matter model and to provide a simple and general framework to interpret the LHC results. Simplified models typically introduce two new particles: the dark matter field and the mediator. They can be divided into two classes: models where the mediator is a singlet under the SM gauge group and models where the mediator is charged under the SM gauge group. Models that belong into the first class will generally lead to $s$-channel simplified models where the mediator is in the $s$-channel and can be either a spin-0 or a spin-1 particle. Models that belong into the second class will generally lead to $t$-channel simplified models which are well motivated by supersymmetric models. A representative diagram for each of these models is shown in fig. 1.11.

The phenomenology for $s$-channel simplified models varies depending on the spin of the mediator. A typical choice for the mediator is a vector or an axial vector particle as the phenomenology is simpler in this case. In case the mediator is a scalar or

pseudoscalar, the most sensitive searches are for two tops plus missing energy $t\bar{t} + \not{E}_T$ signatures as well as two bottom quarks plus missing energy $b\bar{b} + \not{E}_T$ signatures. Searches for mono-jet plus missing energy $\not{E}_T + j$ are not easily accessible as the calculation of the mono-jet cross section is not straightforward. For the vector and axial vector mediator, the strongest signal comes from the decay of the mediator. If this decay is invisible, then the strongest constraints come from the mono-jet plus missing energy signature. If the mediator decays predominantly into SM particles, then the strongest constraints come from di-jet resonances.

In the case of $t$-channel simplified models with a colored mediator that couples to quarks, the simplified models are often similar to the ones for squark searches where a squarks is the supersymmetric partner of a quark. Therefore the results can often be easily translated to the simplified model as the phenomenology is similar to the pair production of the mediator which leads to a $\not{E}_T + jj$ signature. An important difference to squark searches is however, that the cross section for the pair production of the mediator through a $t$-channel dark matter exchange is not necessarily negligible as it is the case for squarks. This cross section also depends on whether the dark matter particle is a Dirac or Majorana fermion. In addition, these simplified models can be constrained with $\not{E}_T + j$ searches through either the emission of an initial state gluon or through the production and decay of the mediator.

Even more exotic signatures that are also covered by the simplified models can be used to search for long-lived particles (LLPs) which are unstable particles with a sizable lifetime [86, 89]. The existence of LLPs is motivated in beyond Standard Model (BSM) models as the decay rate of a particle can be suppressed by very small couplings or if the mass difference between the decaying particle and the decay products is small which are both often the case in dark matter models. These LLPs can then travel a macroscopic distance before decaying inside or even outside the detector. If the decay happens inside the detector and produces SM particles, the signature is a displaced vertex. Another signature is the disappearing track signature where a charged LLP decays into an invisible particle and a charged particle which has too little energy to be detected. If the LLP caries color charge, it can hadronize prior to its decay and form a so called R-hadron bound state which consists of a colored LLP and SM particles. These R-hadrons can potentially be detected in the detector as they leave distinct signatures due to their high mass, low velocity and large ionization energy loss.

### 1.4.3 Indirect searches

Indirect detection experiments look for dark matter decay or annihilation inside or outside the Galaxy by looking for an excess in the flux of SM particles that arrive as cosmic rays on Earth, see [5, 11–13] for recent reviews on indirect detection. The flux of cosmic rays produced by dark matter depends primarily on the dark matter annihilation cross section or decay rate. A benchmark for the annihilation cross section for a canonical WIMP scenario is the thermal cross section $\langle \sigma v \rangle \approx 3 \times 10^{-26} \mathrm{cm}^3 \mathrm{s}^{-1}$ which is the cross section needed to produce the correct relic abundance of dark matter, as discussed in section 1.3.

The flux also depends on the distribution of dark matter. The higher the density, the higher the flux. The most promising targets for indirect detection with a high dark matter density are the Galactic Center, the inner halo of the Milky Way, dwarf spheroidal galaxies and galaxy clusters. As these targets can have very complicated

underlying astrophysical processes, it can be difficult to estimate the astrophysical background, and it can be very large compared to the dark matter signal. Therefore, the best targets are those with a good signal to background ratio. This is for example the case when focusing on antimatter particles like positrons and antiprotons as they are less likely to be produced by astrophysical processes than their matter counterparts whereas particles and antiparticles are produced in equal amounts in most dark matter models where there is no dark matter-antimatter asymmetry.

Lastly, the flux is also determined by the energy spectrum of the particle produced in the annihilation or decay. This depends on the mass of the dark matter particle and the corresponding annihilation or decay channel. In order to be able to compute the energy spectra model-independently, the decay or annihilation energy spectrum for each channel is often computed separately, see e.g. [90, 91] for a detailed discussion and computation of the energy spectra. Possible channels are for example the annihilation into quarks, leptons, gauge bosons or Higgs bosons. These final state particles can then decay and hadronize into stable SM particles like (anti)protons, electrons, positrons, neutrinos and photons that propagate through the Galaxy and can be detected on Earth. When considering a specific dark matter model, the energy spectra for the dominant annihilation or decay channels are weighted by the branching fraction of that channel which is determined by the model and then summed up to get the total energy spectrum.

As mentioned before, antiparticles like positrons and antiprotons are good targets for indirect detection. Furthermore, antinuclei like antideuterons have also been proposed to be used for the search for dark matter. Other promising targets are gamma-rays and neutrinos. Each of these targets has its own properties and detection potentiality that comes with advantages and disadvantages when it comes to indirect detection. We will list the most important advantages and disadvantages for each target in the following.

**High-energy photons ($\gamma$-rays)** Photons are not deflected by the magnetic fields in our Galaxy and can therefore be traced back to their source. They have been the first particle considered as a probe for dark matter annihilation in e.g. [92]. The background is however mostly very high as photons are produced by many astrophysical processes. Therefore, the most promising regions for $\gamma$-ray detection are around the Galactic Center, other nearby galaxies or galaxy clusters where the dark matter density is very high or using the entire distribution of dark matter in our Universe. Dark matter can potentially produce $\gamma$-rays through the annihilation of dark matter particles into quarks or leptons which then produce $\gamma$-rays through hadronization or decay, through radiation or by annihilating into $\gamma$-rays directly. The latter is however often one-loop suppressed as dark matter is not charged. Many experiments are able to detect $\gamma$-rays where the most important experiments for dark matter indirect detection are Fermi-LAT [93] on the International Space Station (ISS) and MAGIC [94, 95], VERITAS [96], HESS [97, 98], HAWC [99] and LHAASO [100] which are ground-based telescopes.

**Low-energy photons (X-rays)** Low-energy photons are produced by dark matter annihilation into electrons or positrons which then produce photons through inverse Compton scattering, synchrotron radiation or bremsstrahlung. These processes depend on the astrophysical environment which introduces additional uncertainties. They can also be produced directly by decays of light dark matter particles in the keV

to MeV mass range. Low-energy photons can be detected by X-ray telescopes like XMM-Newton [101, 102], INTEGRAL [103], Chandra [104], Suzaku [105] and NuSTAR [106].

**Neutrinos** Like photons, neutrinos are neutral and can therefore propagate through the Galaxy without being deflected by magnetic fields. In addition, because of their small interaction cross sections, they can propagate through dense regions like the Galactic Center and even through the Sun and Earth with a low probability of being absorbed or deflected [107]. This is also the reason why neutrinos are hard to detect and are measured indirectly by detecting a charged particle produced in a neutrino interaction. Therefore, the energy of the neutrino can only be reconstructed partly. Experiments capable of detecting neutrinos are IceCube [108], ANTARES [109], Super-Kamiokande [110] and Baikal-GVD [111]. Some of these experiments can also be used to look for neutrinos produced by dark matter interactions in the Sun or Earth as neutrinos can escape these dense regions. This allows to place constraints on the SD and SI scattering cross section of dark matter as the amount of dark matter captured in the Sun or Earth depends on the scattering cross section and influences the neutrino flux.

**Positrons** In contrast to neutrinos and photons, positrons are deflected by the magnetic fields in our Galaxy which makes it impossible to trace them back to their source [112]. Therefore, the only information about the dark matter signal comes from the energy spectrum. However, positrons interact with the interstellar medium and lose energy through synchrotron radiation, Coulomb scattering, ionization, bremsstrahlung and inverse Compton scattering. In addition to that, low-energy positrons with energies below $\sim$ 1 GeV are deflected by the solar wind and do not reach Earth. High-energy positrons coming from nearby sources are however less affected by these issues and are therefore a good target for indirect detection as they are much less abundant than electrons. Positrons can be detected by for example AMS-02 [113] and PAMELA [114] which can distinguish between electrons and positrons and DAMPE [115] and CALET [116] which can only measure the total flux of both. High-energy positrons have also been measured on Earth by HESS [97, 98] and VERITAS [96]. Some experiments like AMS-02 [117, 118] and PAMELA [119, 120] have even detected an excess of positrons which could be a hint for dark matter, see e.g. [121–123] for a discussion of the positron excess.

**Antiprotons** Like positrons, antiprotons diffuse in the galactic magnetic fields and can not be traced back to their source [124]. On the other hand, they are much less affected by energy loss processes than positrons as they only lose energy through scattering with the interstellar medium [125]. Because of this, also antiprotons from far-away regions of our Galaxy can reach Earth. This however makes the background from astrophysical processes larger and more uncertain. As it is the case for positrons, low-energy antiprotons with energies below a fraction of a GeV can not enter the solar system. Antiprotons are mainly detected by AMS-02 [113] and PAMELA [114].

**Antideuterons** Antideuterons are produced when an antiproton and an antineutron coalesce which can happen in the hadronic shower of a dark matter annihilation or decay. Antideuterons are very rare in the Universe as they are only produced through cosmic ray interactions and not directly by astrophysical processes. This makes them

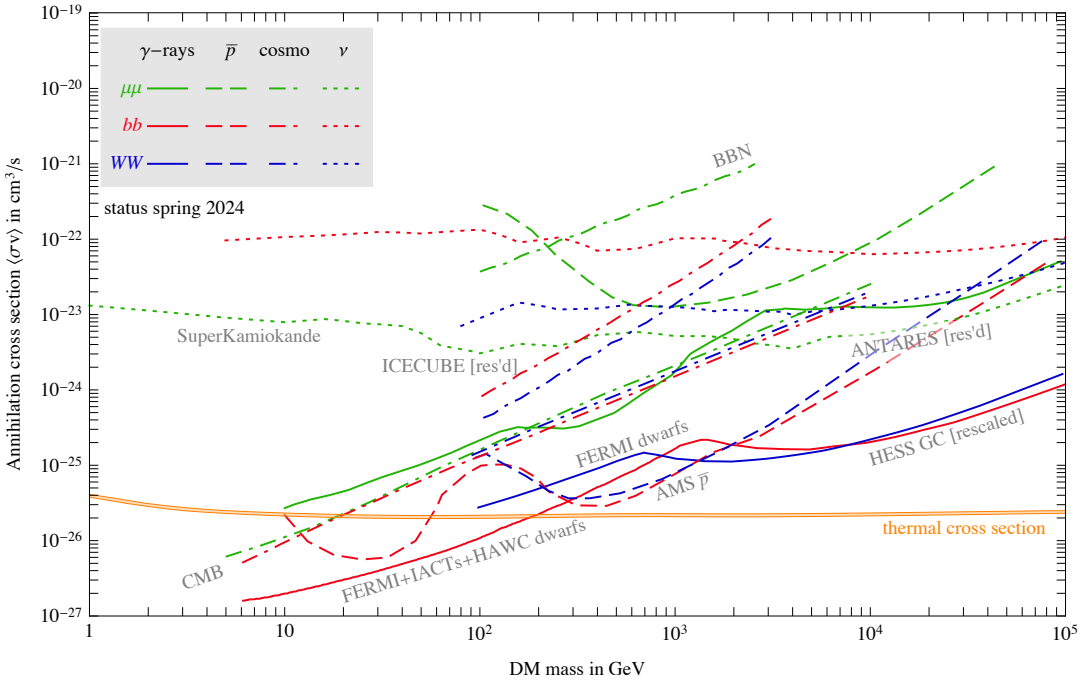


**Figure 1.12:** Current constraints on the dark matter annihilation cross section for different annihilation channels from indirect detection experiments. The area above the lines is ruled out by the experiments. The different colors represent the different annihilation channels into $\mu^+\mu^-$ (green), $b\bar{b}$ (red) and $W^+W^-$ (blue). Some constraints have been rescaled in terms of the dark matter density profile to bring them to the standard NFW profile. Figure taken from [5].

a very good target for dark matter indirect detection with the additional benefit that antideuterons from cosmic rays peak at a different energy range than from dark matter because of the different kinematics in the production process [14]. This is why we will consider antideuterons as a target for indirect detection in chapter 2. Antideuterons can potentially be detected by AMS-02 [113] and BESS Polar-II [126] although so far there has been no bublication of an antideuteron signal that has been detected. In the future, the upcoming GAPS experiment [127] may be able to detect the first antideuteron signal.

Using all of these messengers, indirect detection experiments can place constraints on the dark matter annihilation or decay rate assuming that there is no excess in the data. Some of current constraints on the dark matter thermally averaged annihilation cross section as a function of the dark matter mass for different annihilation channels are shown in fig. 1.12. The constraints are presented for the annihilation channels into $\mu^+\mu^-$ (green), $b\bar{b}$ (red) and $W^+W^-$ (blue). The considered messengers are $\gamma$-rays, antiprotons and neutrinos. The last source of constraints called "cosmo" is a combination of the constraints from the CMB and Big Bang nucleosynthesis (BBN). In orange, the benchmark thermal cross section is shown that is obtained from the relic abundance of dark matter. The area above the lines is ruled out by the different experiments.

The strongest constraints are mostly obtained using $\gamma$-rays, but also neutrinos and charged particles can be the most constraining messenger for some dark matter models. The thermal annihilation cross section is excluded for dark matter masses up $\sim 200$ GeV for the $b\bar{b}$ annihilation channel and up to $\sim 20$ GeV for the $\mu^+\mu^-$ channel. The

strongest constraints for the different channels lie between $\sim 10^{-24}$ and $\sim 10^{-27}\text{cm}^3\text{s}^{-1}$, depending on the channel and the dark matter mass.

## 1.5 Dark matter candidates

After having discussed the different search strategies for dark matter, we now want to introduce some WIMP dark matter candidates that we will consider in this thesis. The most popular WIMP models are based on supersymmetric extensions of the Standard Model. However, because these models have been studied extensively in the literature and have not been discovered yet, we will focus on alternative models that have been proposed in the literature. In the following, we will introduce the scalar singlet Higgs portal model and models with an additional flavor structure in the dark sector.

### 1.5.1 Scalar singlet Higgs portal model

One of the most simplistic dark matter models is the scalar singlet Higgs portal (SSHP) model [128–130] which falls into the category of WIMP models. The only new particle that is introduced is a real neutral scalar singlet $S$ that couples to the SM Higgs boson $h$ through the Higgs portal. The particle is rendered stable by introducing an ad-hoc global symmetry $S \to -S$. The Lagrangian for this model is given by

$$\mathcal{L} = \mathcal{L}_{\text{SM}} + \frac{1}{2}\partial_\mu S \partial^\mu S - \frac{1}{2}m_{S,0}^2 S^2 - \frac{\lambda_S}{4}S^4 - \lambda_{HS} S^2 H^\dagger H \,, \tag{1.29}$$

where $H$ is the SM Higgs doublet and $m_S$ and $\lambda_S$ are the mass and self-coupling of the scalar singlet. The coupling $\lambda_{HS}$ is the Higgs portal coupling. After electroweak symmetry breaking, the interaction term with the Higgs boson becomes

$$\mathcal{L}_{\text{int}} = -\lambda_{HS} v S h - \frac{\lambda_{HS}}{2} S^2 h^2 \,. \tag{1.30}$$

The mass of the scalar singlet is then given by $m_S^2 = m_{S,0}^2 + 2\lambda_{HS}\, v^2$ where $v$ is the vacuum expectation value of the Higgs field.

Various aspects of the phenomenology of the model have been studied in detail in the literature, see for example [131–133] for detailed studies of the combined phenomenological aspects. Because of the simplicity of the model, there are only two relevant parameters: the mass of the scalar singlet $m_S$ and the Higgs portal coupling $\lambda_{HS}$. By requiring that the dark matter particle makes up the entire relic abundance, the coupling $\lambda_{HS}$ is set for any dark matter mass. The relic abundance is computed using the annihilation cross section which can be easily calculated as the only processes contributing are $SS \to h \to f\bar{f}$ where $f$ is any kinematically allowed SM final state and $SS \to hh$ for $m_S > m_h$. The region where the correct relic abundance is obtained is shown in fig. 1.13 as the green band where we show the Higgs portal coupling $\lambda_{HS}$ as a function of the dark matter mass.

Direct detection experiments place strong constraints on the model. The spin-independent scattering cross section can be easily calculated with [134]

$$\sigma_{\text{SI}} = \frac{\lambda_{HS}^2 m_N^2 f_N^2}{\pi m_h^4 m_S^2} \,, \tag{1.31}$$

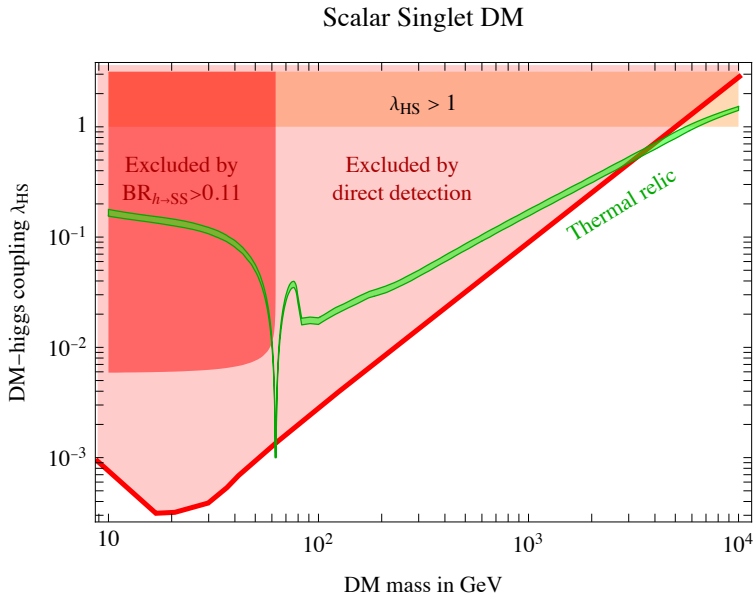


**Figure 1.13:** Current constraints on the Higgs portal coupling $\lambda_{HS}$ as a function of the dark matter mass $m_S$ for the scalar singlet Higgs portal model. The constraints are obtained from direct detection experiments and shown in the lighter red shaded area. The green band shows the region where the correct relic abundance is obtained. Figure taken from [5].

where $m_N$ is the nucleon mass and $f_N$ is the nucleon matrix element. For simplicity and to shorten the expression, $m_S \gg m_N$ is assumed. The constraints obtained by direct detection experiments can then be translated into constraints on the Higgs portal coupling $\lambda_{HS}$ as a function of the dark matter mass $m_S$, shown by the red line in fig. 1.13. Most of the parameter space is already excluded by direct detection experiments, except for a small region around half the Higgs mass where the annihilation cross section is resonantly enhanced and for very heavy dark matter masses of $\sim 3$ TeV. The Higgs resonance region is particularly interesting as it can evade the strong constraints from direct detection experiments. Therefore, this region has gained particular interest in the literature as it also coincides with the preferred region to explain the Fermi-LAT Galactic Center excess [135].

The SSHP model has also been studied in terms of indirect detection constraints using $\gamma$-rays and antiprotons [136, 137] and at the LHC [138]. The constraints from indirect detection and the LHC are however much weaker than the constraints from direct detection experiments. Because the model has been significantly constrained, extensions of the model have been proposed in the literature [139, 140]. Even though the model is already strongly constrained, we still consider it in this thesis in chapter 2 as it is a very simple model that can easily be studied in the context of indirect searches with antideuterons.

### 1.5.2 Dark minimal flavor violation

A more complex model which serves as an alternative to supersymmetric WIMP models are models where a non-trivial flavor structure in the dark sector is introduced. This is motivated by the fact that the SM has a rich flavor structure, and it is natural to ask whether the dark sector could have a similar structure. These flavored dark

matter (FDM) models have three matter generations in the dark sector and a flavor-violating coupling to the quarks and leptons in the SM [22–29]. These models have then been restricted to the minimal flavor violation (MFV) hypothesis, where flavor changing neutral currents are suppressed [30–33], with specific models studied in for example [141–145]. This had the advantage of agreeing well with experimental data on flavor physics, but had the disadvantage of eliminating the interesting effects in the flavor sector. Therefore, the concept of dark minimal flavor violation (DMFV) was introduced [34], where a new single source of flavor and CP violation is introduced beyond the SM Yukawa couplings. This allows for a richer phenomenology in the flavor sector while still keeping the amount of new parameters minimal. Additionally, the new source of flavor and CP violation is potentially able to explain anomalies in flavor physics.

In the DMFV framework, the dark matter flavor triplet $\chi = (\chi_1, \chi_2, \chi_3)^T$ couples to SM fermions $f$ with a corresponding mediator $\phi$ and a coupling strength parameterized by a complex $3 \times 3$ matrix $\lambda$. The interaction is given by the Lagrangian

$$\mathcal{L}^{\text{DMFV}} \supset \lambda_{ij} \overline{f}_i \chi_j \phi + \text{h.c.}\,. \tag{1.32}$$

The SM fermion can be right-handed up- or down-type quarks ($u_R$ or $d_R$), right-handed leptons ($e_R$), left-handed quarks ($q_L$), or left-handed leptons ($\ell_L$). The dark matter triplet can either be a real or complex scalar, a Majorana fermion or a Dirac fermion while the lightest state of the triplet is assumed to account for the observed dark matter relic density. Here, we call the heaviest state $\chi_1$, while the lightest state is $\chi_3$. The corresponding particle type and charges of the mediator then depend on the dark matter particle type and the SM fermion it couples to. Here, we consider a complex scalar and a Dirac fermion as candidates for the mediator. The new flavor symmetry $\mathcal{G}_\chi$ depends on the particle type of the dark matter triplet. A self-conjugate particle introduces a $\text{O}(3)_\chi$ symmetry group while for a non-self-conjugate particle the symmetry group is a $\text{U}(3)_\chi$ group. Together with the SM flavor symmetry, this leads to the global flavor symmetry

$$\mathcal{G}_{\text{flavour}} = \text{U}(3)_q \times \text{U}(3)_u \times \text{U}(3)_d \times \text{U}(3)_e \times \text{U}(3)_\ell \times \mathcal{G}_\chi\,, \tag{1.33}$$

which is broken only by the SM Yukawa couplings $Y_u$, $Y_d$ and $Y_\ell$ and the dark matter coupling $\lambda$.

Numerous configurations in the DMFV framework have been studied already in the literature. For Dirac fermionic dark matter, models with couplings to right-handed up-type quarks ($u_R$) [35–37], right-handed down-type quarks ($d_R$) [34, 38], right-handed leptons ($e_R$) [40], as well as left-handed quarks ($q_L$) [37, 39] have been studied in detail. The only model with a Majorana dark matter particle that has been studied is a model which couples to $u_R$ [41]. Complex scalar dark matter has been studied in the context of couplings to $e_R$ [42–44], and $\ell_L$ [43].

# Part I

# Dark Matter Indirect Detection

# Chapter 2

# Dark Matter Indirect Detection with Antideuterons

This chapter is based on ref. [2]. Here, we will consider the indirect detection of dark matter with cosmic ray antideuterons. In order to explore the potential of antideuterons as a dark matter signal, we will first discuss the production using the coalescence model and propagation of cosmic ray antideuterons for two different cosmic ray propagation models. Using a large number of different antideuteron fluxes we obtain using a set of different values for the coalescence and propagation parameter, as well as different dark matter masses, we train a recurrent neural network called $\bar{\text{D}}$arkRayNet in order to speed up the computation of the fluxes. We then use the neural network to test the sensitivity of the cosmic ray experiment AMS-02 and future experiments GAPS and AMS-100 to the antideuteron flux produced by dark matter annihilation.

In this work, I implemented the coalescence mechanism and computed the antideuteron injection spectra from dark matter annihilation. I also finished the developed and training of the neural network and contributed to the calculation of the sensitivity of the experiments to a dark matter signal.

## 2.1 Introduction

Cosmic rays are made out of high-energy charged particles that originate from our Galaxy or extragalactic sources and propagate through the Universe. They are one of the most important ingredients to study different processes in the Universe like the acceleration of particles in astrophysical sources, the structure of the Galaxy, and the nature of dark matter as their composition and energy spectra are sensitive to these processes, as discussed in section 1.4.3. Cosmic rays produced by astrophysical sources or potentially dark matter annihilation are called primary cosmic rays. Secondary cosmic rays are produced by the interaction of primary cosmic rays with the interstellar medium (ISM), or decay of primary cosmic rays. The main contribution of cosmic rays are protons with about 90% which make them a great target to study astrophysical processes [146]. Because protons are so abundant, it is currently impossible to detect a signal from dark matter annihilation over the background as astrophysical processes produce a lot more protons than dark matter annihilation.

Antiparticles like antiprotons or positrons are produced much less frequently by astrophysical sources and are therefore a great target for dark matter searches, see [147–152] for recent analyses of cosmic ray antiproton fluxes. However, sizable uncertainties in the background predictions still complicate the search for a dark matter signal over

the astrophysical background [153–158]. These uncertainties are however irrelevant for antinuclei like antideuterons as their background is several orders of magnitude smaller than a possible signal at sub-GeV energies. Therefore, antideuterons are a great target for dark matter searches which is why we consider them as an indirect probe of dark matter by studying the production and propagation of cosmic ray antideuterons in the following.

## 2.2 Cosmic ray antideuterons

Cosmic ray antideuterons can be produced through different processes in the Universe. There is no known primary astrophysical source of antideuterons so the only possible primary production is through dark matter annihilation. This contribution can be clearly distinguished from secondary antideuterons which are produced through interactions of primary cosmic rays like protons with the ISM as this leads to a kinematic suppression of the production of secondary antideuterons at lower energies. The production through dark matter annihilations however is not suppressed at lower energies which leads to a background-free search in this energy region (see e.g. [14, 15] and [16–19] for early and more recent discussions of antideuterons from dark matter annihilation, respectively).

The common model to describe the production of primary and secondary antideuterons is the coalescence mechanism which we will focus on in this work. In this model an antiproton and an antineutron can coalesce and form an antideuteron if they have small relative momenta and are close enough in space. The production of secondary antideuterons has first been described in [159] with an analytic formalism to describe coalescence mechanism where it is assumed that the production of antiprotons and antineutrons is not correlated. This approach has since then been developed further in [160–165].

However, the assumption that the production of antiprotons and antineutrons is uncorrelated does not hold for e.g. dark matter annihilation into $W^+W^-$. In this case the particles are correlated as they are produced and concentrated in two back-to-back jets which enhanced the probability of producing an antideuteron [166]. This can be addressed correctly by introducing an event-by-event based coalescence mechanism [166–170] using Monte Carlo (MC) event generators Pythia [171] and Herwig [172]. Others have used QGSJET [173, 174] in ref. [175] and EPOS-LHC [176] and Geant4's FTFP-BERT [177] in ref. [18] for the MC simulations. Both the analytic and the event-by-event based approach are described in more detail in the next section.

MC generators are not tuned to the correlation of antiproton and antineutron production as this has not been measured. Therefore, different MC generators will give different results regarding the antideuteron production when using the coalescence mechanism. An alternative and more elaborate model has been proposed later in [175, 178, 179] following an idea described in [180] which uses a quantum mechanical coalescence criterion based on the overlap of the wave functions of antiprotons and antineutrons using the Wigner formalism. However, in the analysis of [175] the MC generator QGSJET is used, so the problem of an inaccurate modeling of the antiproton and antineutron correlations in the event generator remains. In ref. [181], the authors have extended the Wigner formalism by implementing the Argonne nucleon-nucleon potential which is entirely fixed by proton and neutron scattering data and does not have to be tuned to antideuteron data.

### 2.2.1 Production with the coalescence mechanism

We will focus on the analytic and event-by-event based approaches to the coalescence mechanism which we will use for the rest of the analysis. The following introduction to the coalescence mechanism is largely based on [168].

The amount of antideuterons produced in an event can be determined in terms of the phase-space distributions of the individual particles $f(\sqrt{s}, \vec{k})$ which depends on the center-of-mass energy $\sqrt{s}$ and the momentum $\vec{k}$

$$dN_{\bar{d}} = f_{\bar{d}}(\sqrt{s}, \vec{k})\; d^3\vec{k}_{\bar{d}}\,. \tag{2.1}$$

The phase-space distribution of the antideuteron depends on the momentum distribution of the $\bar{p}\bar{n}$ pair $f_{(\bar{p}\bar{n})}(\sqrt{s}, \vec{k}_{\bar{p}}, \vec{k}_{\bar{n}})$ and the probability (also called the coalescence function) $C(\vec{k}_{\bar{p}}, \vec{k}_{\bar{n}}|\vec{k}_{\bar{d}}) = C(\vec{k}_{\bar{p}}, \vec{k}_{\bar{n}})\; \delta^3(\vec{k}_{\bar{d}} - \vec{k}_{\bar{p}} - \vec{k}_{\bar{n}})$ of an antiproton with momentum $\vec{k}_{\bar{p}}$ and an antineutron with momentum $\vec{k}_{\bar{n}}$ will form an antideuteron:

$$f_{\bar{d}}(\sqrt{s}, \vec{k}_{\bar{d}}) = \int f_{(\bar{p}\bar{n})}(\sqrt{s}, \vec{k}_{\bar{p}}, \vec{k}_{\bar{n}})\; C(\vec{k}_{\bar{p}}, \vec{k}_{\bar{n}})\; \delta^3(\vec{k}_{\bar{d}} - \vec{k}_{\bar{p}} - \vec{k}_{\bar{n}})\; d^3\vec{k}_{\bar{n}}\; d^3\vec{k}_{\bar{p}}\,. \tag{2.2}$$

Momentum conservation requires that the total momentum is $\vec{k}_{\bar{d}} = \vec{k}_{\bar{p}} + \vec{k}_{\bar{n}}$. Using this and the relative momentum $\vec{\Delta} = \vec{k}_{\bar{p}} - \vec{k}_{\bar{n}}$, eq. (2.2) can be rewritten in terms of $\vec{k}_{\bar{d}}$ and $\vec{\Delta}$:

$$f_{\bar{d}}(\sqrt{s}, \vec{k}_{\bar{d}}) = \frac{1}{8} \int f_{(\bar{p}\bar{n})}(\sqrt{s}, (\vec{k}_{\bar{d}} + \vec{\Delta})/2, (\vec{k}_{\bar{d}} - \vec{\Delta})/2)\; C(\vec{\Delta})\; d^3\vec{\Delta}\,, \tag{2.3}$$

where we have integrated over $\vec{k}_{\bar{d}}$ using the $\delta$-function. The factor $1/8$ arises from the Jacobian of the transformation $\{\vec{k}_{\bar{p}}, \vec{k}_{\bar{n}}\} \to \{\vec{k}_{\bar{d}}, \vec{\Delta}\}$.

So far the phase space is not written in a Lorentz-invariant form. This can be done by multiplying the phase space with the corresponding Lorentz-factor $\gamma_i$. This allows us to reformulate eq. (2.3) in a Lorentz-invariant form

$$\gamma_{\bar{d}}\; f_{\bar{d}}(\sqrt{s}, \vec{k}_{\bar{d}}) \approx \frac{1}{8} \left( \frac{\gamma_{\bar{d}}}{\gamma_{\bar{p}}\gamma_{\bar{n}}} \int C(\vec{\Delta})\; d^3\vec{\Delta} \right) \gamma_{\bar{p}}\gamma_{\bar{n}}\; f_{(\bar{p}\bar{n})}(\sqrt{s}, \vec{k}_{\bar{d}}/2, \vec{k}_{\bar{d}}/2)\,, \tag{2.4}$$

where we have also used that the relative momentum of the $\bar{p}$ and $\bar{n}$ pair has to be small in order to form an antideuteron. This means that the coalescence function $C(\vec{\Delta})$ has to be 0 for large relative momenta. In practice, the coalescence function is approximated with a step function

$$C(\vec{\Delta}) = \theta(\Delta^2 - p_c^2)\,, \tag{2.5}$$

where $p_c$ is the so-called coalescence momentum which determines the maximum relative momentum that a $\bar{p}$ and $\bar{n}$ pair can have in order to still form a $\bar{d}$. The value of the coalescence momentum is not known a priori but must be determined by fitting to experiments that have produced antideuterons like LEP [182] or ALICE [183].

Equation (2.4) can be simplified by going to the $\bar{d}$ rest-frame where the Lorentz factors are approximately unity and the term in the bracket can be evaluated using the expression for the coalescence function in eq. (2.5) to be $4\pi p_c^3/3$. Plugging this

back into eq. (2.4) we get the following expression for the antideuteron distribution

$$\frac{dN_{\bar{d}}}{d^3\vec{k}_{\bar{d}}} = \frac{1}{8}\frac{4\pi p_c^3}{3} f_{(\bar{p}\bar{n})}(\sqrt{s}, \vec{k}_{\bar{d}}/2, \vec{k}_{\bar{d}}/2)\,. \tag{2.6}$$

One way to obtain the distribution of antideuterons is to evaluate eq. (2.6) analytically which is called the spherical approximation. In this approach, one assumes that the production of $\bar{p}$ and $\bar{n}$ is uncorrelated and that their distribution is isotropic. This allows for a factorization of the phase space distribution of the $\bar{p}$ and $\bar{n}$ pair $f_{(\bar{p}\bar{n})}(\sqrt{s}, \vec{k}_{\bar{p}}, \vec{k}_{\bar{n}}) = f_{(\bar{p})}(\sqrt{s}, \vec{k}_{\bar{p}}) \cdot f_{(\bar{n})}(\sqrt{s}, \vec{k}_{\bar{n}})$ assuming that $2m_{\mathrm{DM}}$ is much larger than the antideuteron mass. The individual phase space distributions can then be expressed in terms of the amount of particles as in eq. (2.1). As in [166], we can rewrite eq. (2.6) in terms of the dimensionless quantity $x = E_{\mathrm{kin}}/m_{\mathrm{DM}}$ where $E_{\mathrm{kin}}$ is the kinetic energy and assuming $m_{\bar{p}} = m_{\bar{n}} = m_{\bar{d}}/2$:

$$\frac{dN_{\bar{d}}}{dx_{\bar{d}}} = \frac{p_c^3}{3m_{\mathrm{DM}}^2 m_{\bar{p}}} \frac{1}{\sqrt{x_{\bar{d}}^2 + 4m_{\bar{p}}x_{\bar{d}}/m_{\mathrm{DM}}}} \frac{dN_{\bar{p}}}{dx_{\bar{p}}} \frac{dN_{\bar{n}}}{dx_{\bar{n}}}\,. \tag{2.7}$$

The $\bar{p}$ and $\bar{n}$ spectra need to be evaluated at $x_{\bar{p}} = x_{\bar{n}} = x_{\bar{d}}/2$.

In this spherical approximation, the antideuteron spectrum is suppressed by $1/m_{\mathrm{DM}}^2$ for large dark matter masses. However, this does not describe the antideuteron production correctly for higher dark matter masses. In this case, the annihilation products are boosted and the resulting SM particles are concentrated in two back-to-back jets which can no longer be described by a spherical distribution. Because of the jet structure, the antideuteron production probability is enhanced and using the spherical approximation will underestimate the antideuteron yield.

Another issue with the spherical approximation is that it does not take the spatial separation of an antiproton and antineutron pair into account. If the two particles are again produced in two different back-to-back jets then the probability of them coalescing is suppressed as the distance between the two particles is too large for the nuclear forces to act.

To solve these issues, the condition in eq. (2.5) is used in the event-by-event based approach of the coalescence mechanism which takes the spatial distribution of the particles correctly into account. This is done by using a Monte Carlo event generator and checking for every produced $(\bar{p}, \bar{n})$ pair in each event if their relative momentum is smaller than the coalescence momentum $p_c$ and if their spatial separation is smaller than 2 fm which is of the order of the spatial extension of the antideuteron wave-function.

Furthermore, the authors of [184] have shown that the production of antideuterons can be enhanced by the decay of a $\bar{\Lambda}_b$ baryon. This particle will decay at a displaced vertex into multi-nucleon states with small relative momenta due to its rest-mass of 5.6 GeV. Because of this, antiproton and antineutron pairs produced in this decay will likely form an antideuteron. It was also shown that the $b \to \Lambda_b$ transition ratio in Pythia does not match the measured value by LEP which is about 3 times higher. Indeed, the $\Lambda_b$ production cross section is subject to large uncertainties which need to be taken into account when working with the coalescence model.

Another uncertainty comes from the fit of the coalescence momentum $p_c$ to experimental data. Many experiments have measured antideuterons produced in various

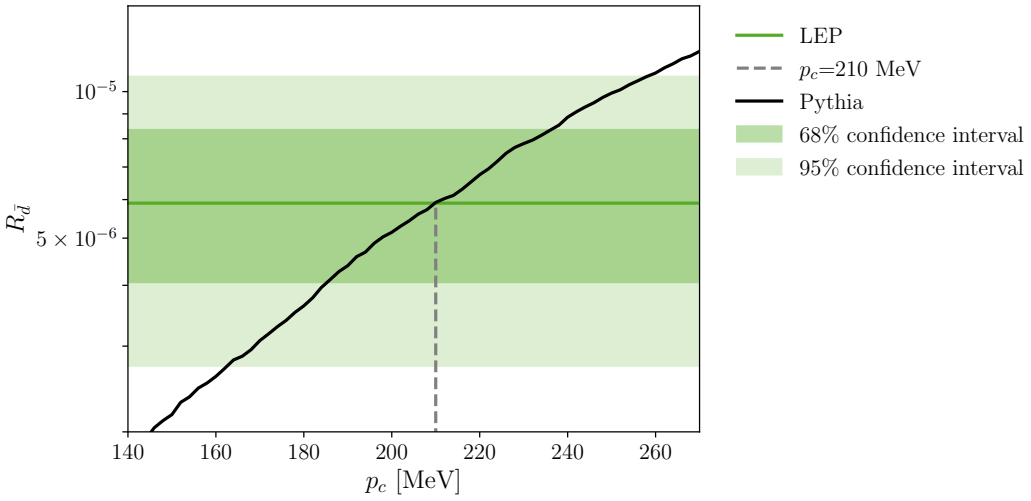


**Figure 2.1:** Antideuteron production rate from hadronic Z decays measured by LEP (green line) and simulated with Pythia (black line) as a function of coalescence momentum to determine the upper and lower bounds on the coalescence momentum. The shaded regions show the 68% and 95% confidence intervals. The best-fit value indicated by the gray dashed line is $p_c = 210\,\text{MeV}$.

processes. An example for a hadronic process is protons colliding and producing antideuterons at the LHC or $e^+e^-$ annihilation at LEP as an example for a leptonic process [168]. Because we want to mimic the conditions of dark matter annihilations as closely as possible we use the data from $e^+e^-$ annihilations producing antideuterons as there are no hadronic initial states. At LEP, the number of antideuterons in $e^+e^-$ collisions at the Z resonance per hadronic Z decay has been measured to be $R_{\bar{d}} = \left(5.9 \pm 0.5\,(\text{sys.})\right) \times 10^{-6}$ in the momentum range $0.62\,\text{GeV} < p < 1.03\,\text{GeV}$ and a polar angle in the interval $|\cos\theta| < 0.95$ [182]. The systematic error arises from the uncertainty in the efficiency of antideuteron detection.

To estimate the statistical error we assume Poisson statistics to compute the upper and lower bounds of the corresponding 68% and 95% confidence intervals as shown in [61] for the 11 antideuterons that have been measured. In order to obtain the error on the production rate we divide the resulting bounds by the observed number of hadronic $Z$ decays and the antideuteron detection efficiency. For the 68% and 95% confidence intervals we thus obtain $R_{\bar{d}} = \left(5.9\,^{+2.5}_{-1.8}\,(\text{stat.}) \pm 0.5\,(\text{sys.})\right) \times 10^{-6}$.

To simulate the production of antideuterons, we use MadGraph_aMC@NLO [185] to generate $10^8$ events for the process $e^+e^- \to Z \to q\bar{q}$ at the Z resonance and Pythia 8.2 [171] for the showering and hadronization. For each event, we select all antiprotons and antineutrons that have been produced at the initial vertex as well as those coming from $\Lambda_b$-decays and compute the relative momentum $\Delta^\mu = p^\mu_{\bar{p}} - p^\mu_{\bar{n}}$ and spacial separation for each pairing. According to the condition in eq. (2.5) an antideuteron is formed if the relative momentum is smaller than the coalescence momentum. We therefore select the paring with the smallest relative momentum and check the condition of eq. (2.5) while varying $p_c$, as well as if their spatial separation is smaller than 2 fm. Note that there is usually only one or no pairing that satisfies these conditions per event. The resulting antideuteron production rate as a function of $p_c$ is shown in fig. 2.1 in black and compared to the LEP measurement in green. The best-fit coalescence momentum is obtained when the simulated production rate matches the measured one. This is the case for

$$p_c = 210\,^{+27}_{-25}\ (^{+48}_{-47})\ \text{MeV}\,, \tag{2.8}$$

where we also obtain the 68% (95%) confidence level intervals from the uncertainty on the production rate measurement shown in the shaded green regions. This result matches the one found in ref. [184] with $p_c = 215\,^{+19}_{-23}\,\text{MeV}$.

### 2.2.2 Spectra from Dark Matter annihilation

For the simulation of dark matter annihilating into dark matter particles we use MadDM 3 [186] and once again Pythia 8.2 to simulate the production of antideuterons from the hadronization and showering of the annihilation products. We generate at least $10^8$ events per annihilation channel and dark matter mass to compute the dark matter annihilation source spectra $\mathrm{d}N/\mathrm{d}E_{\text{kin}}$ for 37 dark matter masses between 2 GeV and 10 TeV. We have considered the annihilation channels $q\bar{q}$, $c\bar{c}$, $b\bar{b}$, $t\bar{t}$, $gg$, $hh$, $W^+W^{-(*)}$, and $ZZ^{(*)}$, where the asterisk denotes an off-shell gauge boson relevant for dark matter masses below the respective pair-production threshold and $q$ corresponds to the three light quark flavors, $u, d, s$, as their annihilation spectra are almost indistinguishable. For the computation of the dark matter annihilation source spectra, we assume that dark matter annihilates purely into the annihilation channel considered, and the annihilation products are produced at a center of mass energy of two times the dark matter mass. We use the same treatment of obtaining the antideuterons from the events as for the fit to LEP data which is described above. We use the coalescence momentum in eq. (2.8) and account for the discrepancy in the $b \to \Lambda_b$ transition ratio between Pythia and the measurement from LEP with an extra free parameter $r_{\Lambda_b}$ that resales the $\Lambda_b$ production rate. To match the factor found in [184] we set its fiducial value to 3.

The source spectra for the annihilation channels $b\bar{b}$, $q\bar{q}$, and $W^+W^-$ and a dark matter mass of $m_{\text{DM}} = 100\,\text{GeV}$ are shown in fig. 2.2 with the dark blue solid line. We used the best-fit value in eq. (2.8) for the coalescence momentum and set $r_{\Lambda_b}$ equal to 3. The darker shaded blue region shows the $1\sigma$ uncertainty range for $p_c$ while the lighter shaded blue region shows the variation of $r_{\Lambda_b}$ by a factor of 2. Note that the lighter shaded blue region is only visible in the $b\bar{b}$ channel as the $\Lambda_b$ boson is produced from $b$ quarks and therefore does not affect the other channels. We compare our spectra to previous results by also presenting the spectra from Cirelli *et al.* [90] (dashdotted yellow), Ibarra and Wild [187] (dotted purple), Fornengo *et al.* [168] (dashed green), and Kadastik *et al.* [166] (dashdotdotted red).

There are several differences in the spectra presented in the figure, which result from differences in the computation of the injection spectra. The primary difference is the use of various versions of the shower algorithm Pythia. Most of the spectra shown were generated using Pythia 8.1 (with the exception of ref.[168], which used Pythia 6.4), while we use a more recent version, Pythia 8.2. The use of an older version in ref.[168] may explain why their spectra are consistently higher than the others. The impact of using different shower algorithms has also been discussed in ref. [91].

The version of Pythia and the MC event generator used also has an impact on the exact value of the coalescence momentum, as well as the experiment used to determine the value. This leads to different values of $p_c$ in the various references we present. As the spectra are roughly proportional to $p_c^3$, this can explain an overall off-sets when comparing different spectra.

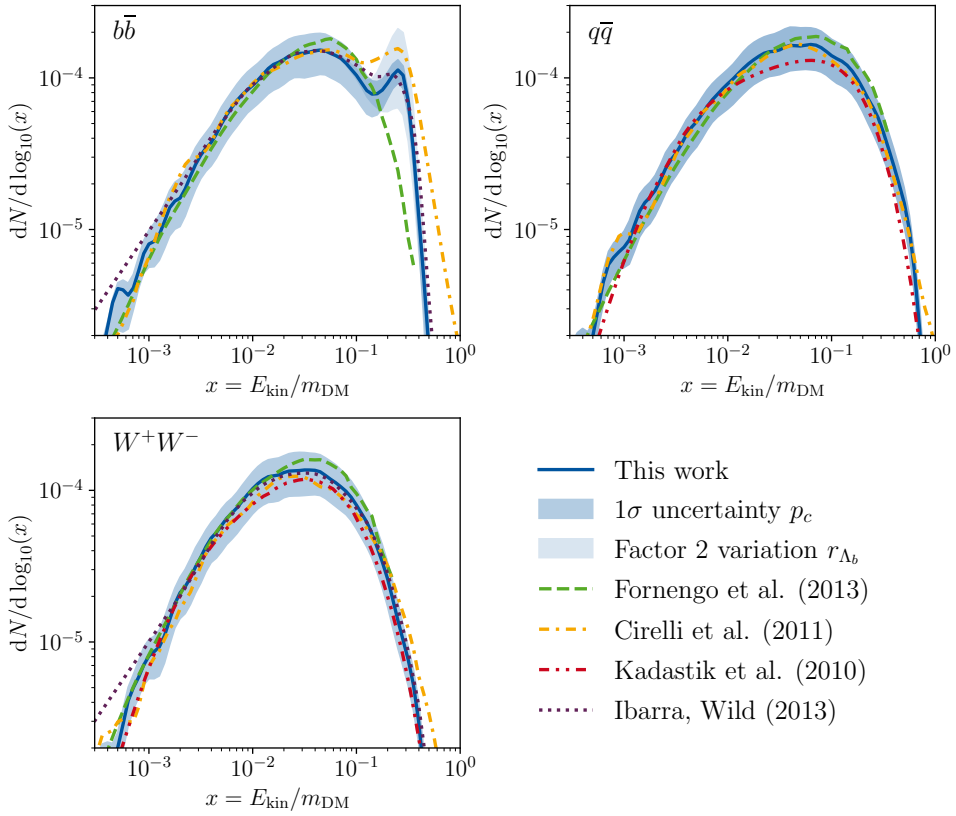


**Figure 2.2:** Comparison of $m_{\mathrm{DM}} = 100\,\mathrm{GeV}$ dark matter annihilation spectra for different annihilation channels. The panels show annihilation via the $b\bar{b}$ (top left), $q\bar{q}$ (top right) and $W^+W^-$ (bottom left) channels. The darker shaded blue region shows the $1\sigma$ uncertainty range of the coalescence parameter $p_c$. The lighter shaded blue region in the $b\bar{b}$ spectrum shows the region of a factor 2 increase and decrease in the production rate of $\Lambda_b$ baryons from $b$ quarks. The spectra are compared to previous results by Cirelli *et al.* [90] (dashdotted yellow), Ibarra and Wild [187] (dotted purple), Fornengo *et al.* [168] (dashed green), and Kadastik *et al.* [166] (dashdotdotted red).

The most prominent difference in the source spectra is visible in the $b\bar{b}$ channel where most but not all spectra display a bump between $x = 0.1$ and 1. The bump is produced when antideuterons coming from the decay of long-lived particles are taken into account. The antiprotons and antineutrons are then produced at a displaced vertex as the long-lived particle has time to travel away from the initial vertex before the decay. The distance of these particles to the particles produced in prompt decays is too large for the formation of an antideuteron because of the finite range of the nuclear forces. Only if the distance between the antiproton and the antineutron is below a few fm can they coalesce and form an antideuteron [187]. This can only happen if all particles are produced directly at the initial vertex or through the off-vertex production of a $\bar{\Lambda}_b$ particle as described in [184]. Therefore, if particles produced by long-lived particles are not taken into account then there is no bump between $x = 0.1$ and 1. In contrast to that, if the spatial separation of the produced antiprotons and antineutrons is not checked, then the amount of antideuterons is overestimated, and the bump is too large as in [90]. Here, we take the off-vertex production of antideuterons from $\bar{\Lambda}_b$ particles into account and check whether the spatial separation of the antiproton and antineutron is below 2 fm.

Another difference which should however be negligible is the difference in the light quark content, denoted by $q$, as these particles are still very light compared to all dark matter masses considered. In Fornengo *et al.* [168] this includes only the lightest quark $u$ while we, Cirelli *et al.* [90], and Kadastik *et al.* [166] also include down and charm quarks.

### 2.2.3 Propagation

Because we are not interested in antideuterons produced at the source but rather in the antideuteron flux at Earth, we have to model the propagation of antideuterons through our Galaxy and Solar System. Cosmic ray propagation can be described by a set of coupled diffusion equations which model the effects of diffusion and reacceleration in the galactic magnetic fields, convection from galactic winds, energy gains and losses, fragmentation and decay [188]. These equations describe the evolution of the particle density $\psi_i(\boldsymbol{x}, p, t)$ of particle species $i$ as a function of its momentum $p$, position $\boldsymbol{x}$ and time $t$:

$$\begin{aligned}\frac{\partial \psi_i(\boldsymbol{x}, p, t)}{\partial t} = q_i(\boldsymbol{x}, p) + \boldsymbol{\nabla} \cdot (D_{xx} \boldsymbol{\nabla} \psi_i - \boldsymbol{V} \psi_i) + \frac{\partial}{\partial p} p^2 D_{pp} \frac{\partial}{\partial p} \frac{1}{p^2} \psi_i \\ - \frac{\partial}{\partial p} \left[ \frac{\mathrm{d}p}{\mathrm{d}t} \psi_i - \frac{p}{3} (\boldsymbol{\nabla} \cdot \boldsymbol{V}) \psi_i \right] - \frac{1}{\tau_{f,i}} \psi_i - \frac{1}{\tau_{r,i}} \psi_i \,.\end{aligned} \tag{2.9}$$

We will discuss each term of eq. (2.9) and their effect separately in the following, including the parameters used in cosmic ray propagation. Please note that the following is only one possible way to describe cosmic ray propagation and that there are other possible setups that can also describe the propagation, see for example [189] for a review.

**Source term** The first term in eq. (2.9) is the source term $q_i(\boldsymbol{x}, p)$ for the particle type $i$ that describes the injection of cosmic rays at the Galactic position $\boldsymbol{x}$. The term varies for every species depending on what the source of the species is and describes

the injection of primary cosmic rays separately from the secondary injection. Primary sources can be astrophysical processes such as supernova remnants or pulsars, as well as dark matter annihilation into standard model particles.

The dark matter annihilation source term for antideuterons is given by

$$q_{\bar{d}}^{(\mathrm{DM})}(\boldsymbol{x}, E_{\mathrm{kin},\bar{d}}) = \frac{1}{2}\left(\frac{\rho(\boldsymbol{x})}{m_{\mathrm{DM}}}\right)^2 \langle\sigma v\rangle_{\mathrm{tot}} \sum_f \mathcal{B}_f \frac{\mathrm{d}N_{\bar{d}}^f}{\mathrm{d}E_{\mathrm{kin},\bar{d}}} \,. \tag{2.10}$$

Here, $m_{\mathrm{DM}}$ represents the dark matter mass, while $\rho(\boldsymbol{x})$ denotes the energy density profile. The quantity $\langle\sigma v\rangle_{\mathrm{tot}}$ is the velocity-averaged annihilation cross section times velocity. The summation includes all relevant annihilation channels $f$, each contributing with a relative fraction $\mathcal{B}_f = \langle\sigma v\rangle_f / \langle\sigma v\rangle_{\mathrm{tot}}$ and energy spectrum $\mathrm{d}N_{\bar{d}}^f/\mathrm{d}E_{\mathrm{kin}}$ at the source. For the energy density profile, we assume a Navarro-Frenk-White (NFW) distribution [49], with a scale radius of $r_h = 20\,\mathrm{kpc}$ and a local dark matter density of $0.43\ \mathrm{GeV/cm^3}$ at the solar position. In this analysis, both $m_{\mathrm{DM}}$ and $\mathcal{B}_f$ are treated as free parameters of the dark matter model.

Secondary antideuterons can be produced by cosmic ray protons which collide with hydrogen atoms. The source term for secondary antideuterons can be written as [159, 161]:

$$q_{\bar{d}}^{(\mathrm{sec})}(\boldsymbol{x}, E_{\mathrm{kin},\bar{d}}) = \int \frac{\mathrm{d}\sigma_{pH\to\bar{d}X}}{\mathrm{d}E_{\mathrm{kin},\bar{d}}}(E_{\mathrm{kin},p}, E_{\mathrm{kin},\bar{d}})\, 4\pi\, n_H(\boldsymbol{x})\, \Phi_p(E_{\mathrm{kin},p})\, \mathrm{d}E_{\mathrm{kin},p} \,. \tag{2.11}$$

Here, $\Phi_p(E_{\mathrm{kin},p})$ is the flux of primary protons and $n_H(\boldsymbol{x})$ is the hydrogen density in the ISM. The differential production cross section for antideuterons $\mathrm{d}\sigma_{pH\to\bar{d}X}/\mathrm{d}E_{\mathrm{kin},\bar{d}}$ is computed using the spherical approximation of the coalescence mechanism.

Other primary cosmic rays are assumed to be accelerated by astrophysical sources through diffusive shock acceleration and are then released into the Galaxy [190]. From simulations, it has been shown that this mechanism produces a power law spectrum for the accelerated particles [191]. In addition, a break in the spectrum at low energies is needed to explain AMS-02 data at around a few GeV [192]. We therefore model the primary source term for all other cosmic rays as a smoothly broken power law:

$$q_i(R) \propto \left(\frac{R}{R_0}\right)^{-\gamma_1} \left(\frac{R_0^{1/s} + R^{1/s}}{2R_0^{1/s}}\right)^{-s(\gamma_2-\gamma_1)} \,, \tag{2.12}$$

where $R$ is the rigidity of the particle which depends on the momentum $p$ and its charge $Z$ and is defined as $R = p/|Z|$. The term with the smoothing parameter $s$ can be removed to obtain a power law without a break. The parameter $R_0$ determines the position of the break and $\gamma_1$ and $\gamma_2$ are the spectral indices above and below the break. In this work we assume that all primary nuclei have the same injection spectrum except for protons where we allow for a different spectral behavior.

**Spatial diffusion** The next term, $\boldsymbol{\nabla}\cdot(D_{xx}\boldsymbol{\nabla}\psi_i)$, accounts for the interaction of the cosmic rays with the turbulent magnetic fields in our Galaxy which is described by spatial diffusion. This is the dominant process for cosmic ray nuclei, especially at high energies. The diffusion term depends on the diffusion tensor which we model with a

diffusion coefficient times a unity matrix as we assume that the turbulent magnetic fields are isotropic. The diffusion coefficient is modeled with a double-broken power law with smooth breaks as a function of rigidity $R$ and no spatial dependence as we assume that the diffusion coefficient is constant throughout the Galaxy. The diffusion coefficient is given by:

$$D_{xx}(R) \propto \beta R^{\delta_l} \left[1 + \left(\frac{R}{R_{D,0}}\right)^{\frac{1}{s_{D,0}}}\right]^{s_{D,0}\,(\delta-\delta_l)} \left[1 + \left(\frac{R}{R_{D,1}}\right)^{\frac{1}{s_{D,1}}}\right]^{s_{D,1}\,(\delta_h-\delta)} . \quad (2.13)$$

$R_{D,0}$ and $R_{D,1}$ set the positions of the two breaks and the smoothing is controlled by the smoothing parameters $s_{D,0}$ and $s_{D,1}$, respectively. The spectral indices below, between and above the breaks are parameterized by $\delta_l$, $\delta$ and $\delta_h$. The velocity of the particle in units of the speed of light $c$ is given by $\beta$ and the diffusion coefficient is normalized to $D_{xx}(R{=}4\,\mathrm{GV}) = D_0$, where $D_0$ is another parameter of the propagation model.

We choose this parameterization for the diffusion coefficient as a break in the diffusion coefficient is expected when the turbulence changes between a regime where the turbulence is self-generated to a regime with externally generated turbulence [193, 194]. The second break around 300 GV can be directly observed in the AMS-02 data [146]. Since the break in the cosmic ray spectrum is more pronounced in secondaries than in primaries [195], it suggests a change in the diffusion coefficient rather than in the injection spectrum [196]. The break at lower rigidities is however more speculative as other processes like convection and reacceleration can have an impact on the cosmic rays as well [155, 197]. We will therefore consider two different approaches to the modeling of the diffusion coefficient, one with a break at low energies and one without. The two approaches will be further discussed below.

**Convection** The term $-\boldsymbol{\nabla} \cdot (\boldsymbol{V}\psi_i)$ describes the transportation of the cosmic rays by convective winds which have the velocity $\boldsymbol{V}$. An increase in the convection velocity decreases the cosmic ray flux below $\sim 10$ GV. We assume that the velocity is constant and always perpendicular to the Galactic plane, $\boldsymbol{V} = v_{0,\mathrm{c}}\,\mathrm{sign}(z)\,\boldsymbol{e}_z$. The value of the velocity is left as a free parameter in our model.

**Reacceleration** Cosmic rays can be reaccelerated by scattering on Alfvèn magnetic waves which is modeled by diffusion in momentum space with $\partial/\partial p\; p^2 D_{pp}\; \partial/\partial p\; 1/p^2 \psi_i$. The diffusion coefficient $D_{pp}$ can be parameterized in terms of the spatial diffusion coefficient $D_{xx}$ and the velocity of the Alfvèn magnetic waves $v_\mathrm{A}$ in the following way [198]:

$$D_{pp} = \frac{4(p\,v_\mathrm{A})^2}{3(2-\delta)(2+\delta)(4-\delta)\delta\, D_{xx}} \quad (2.14)$$

Here, $\delta$ is the same spectral index parameter as already mentioned in the discussion of the diffusion coefficient in eq. (2.13).

**Continuous energy losses and adiabatic momentum change** Continuous energy losses are described by the term $-\partial/\partial p\,[\mathrm{d}p/\mathrm{d}t\;\psi_i]$. This term includes processes

such as synchrotron radiation, (inverse) Compton scattering, Bremsstrahlung and ionization losses [125]. The term $\partial/\partial p\,[p/3(\boldsymbol{\nabla}\cdot\boldsymbol{V})\psi_i]$ describes adiabatic momentum gain or loss which is caused by a non-zero divergence of $\boldsymbol{V}$.

**Fragmentation and decay** The last two terms in the propagation equation describe catastrophic energy losses due to fragmentation $-\psi_i/\tau_{f,i}$ and radioactive decay $-\psi_i/\tau_{r,i}$ of cosmic ray particles. The mean fragmentation time $\tau_{f,i}$ depends on the density of the ISM and on the inelastic cross section of the respective process. The decay time $\tau_{r,i}$ depends only on energy [188].

The particle density $\psi_i(\boldsymbol{x}, p, t)$ as given in the propagation equation can also be expressed as a flux of particles $\Phi_i$ which is defined as the number of particles $N$ per area $A$, time $t$, solid angle $\Omega$ and energy $E$:

$$\Phi = \frac{\mathrm{d}^4 N}{\mathrm{d}A\mathrm{d}t\mathrm{d}\Omega\mathrm{d}E} = \frac{c}{4\pi}\psi\,, \tag{2.15}$$

where $c$ is the speed of light. The flux is the commonly used quantity in cosmic ray measurements, hence we will focus on computing the antideuteron flux from dark matter annihilation.

In our analysis we consider two different cosmic ray propagation models which are both based on eq. (2.9) called diffusion break (DIFF.BRK) and injection break (INJ.BRK) model. The parameters used in both models and their ranges that we explored are displayed in table 2.1. The ranges for the parameters were obtained by using MultiNest scans that were performed in [151]. In the following, we will describe the two models in more detail.

In the INJ.BRK model it is assumed that the injection spectra of primary astrophysical cosmic rays is modeled by a broken power law as in eq. (2.12). We allow for different values for the slopes for protons ($\gamma_{1,p}$ and $\gamma_{2,p}$) and Helium ($\gamma_1$ and $\gamma_2$) to account for the observed difference in the two fluxes. The reason for this difference is still unclear and subject to research. Some ideas are for example different source populations [199–201] or a Z/A-dependence of the efficiency of Fermi shock acceleration [202, 203]. The diffusion coefficient is modeled as a single power law which is achieved by setting $\delta_l = \delta$ in eq. (2.13). We therefore neglect the parameters $\delta_l, R_{D,0}$ and $s_D$ in this model. We also include reacceleration and convection with the parameters $v_A$ and $v_{0,c}$. This model has been studied in detail in other publications [125, 204–208].

The DIFF.BRK model assumes a single power law for the primary injection spectra which means setting $\gamma_1 = \gamma_2$ in eq. (2.12) while still allowing for different slopes for different values for protons and Helium. This model also assumes that there is no reacceleration term. In contrast to the INJ.BRK model, the diffusion coefficient is modeled as a double-broken power law which includes the parameters $\delta_l, R_{D,0}$ and $s_D$ again. The additional break has been attributed to a damping effect on turbulence at low energies, caused by the interaction between cosmic rays and turbulent magnetic fields [209]. This model has also been studied in [207] and tested against data from AMS-02 in [192, 197, 210].

The last parameter in both models is the half-height of the diffusion model which we fix to $z_h = 4\,\mathrm{kpc}$. This corresponds roughly to the lower bound obtained from beryllium data from AMS-02 [197, 208, 211–213]. Note however that a precise determination of the halo height is not possible so far because of significant systematic uncertainties in the fragmentation cross sections of secondaries [197, 211, 214] which allow for larger

**Table 2.1:** Parameters and their respective ranges in the INJ.BRK and DIFF.BRK models. Parameters that are not used in the respective model are marked with a dash.

| Parameters | DIFF.BRK | INJ.BRK |
|---|---|---|
| $\gamma_{1,p}$ | – | $\{1.60, 1.85\}$ |
| $\gamma_1$ | – | $\{1.60, 1.85\}$ |
| $\gamma_{2,p}$ | $\{2.25, 2.37\}$ | $\{2.41, 2.50\}$ |
| $\gamma_2$ | $\{2.19, 2.31\}$ | $\{2.36, 2.44\}$ |
| $R_0$ [GV] | – | $\{4939, 8765\}$ |
| $s$ | – | $\{0.22, 0.46\}$ |
| $D_0$ [$10^{28}$ cm$^2$/s] | $\{3.41, 4.45\}$ | $\{3.53, 5.47\}$ |
| $\delta_l$ | $\{-0.97, -0.37\}$ | – |
| $\delta$ | $\{0.48, 0.60\}$ | $\{0.30, 0.42\}$ |
| $\delta_h - \delta$ | $\{-0.20, -0.08\}$ | $\{-0.17, -0.04\}$ |
| $R_{D,0}$ [GV] | $\{3044, 4928\}$ | – |
| $s_D$ | $\{0.31, 0.51\}$ | – |
| $R_{D,1}$ [$10^3$ GV] | $\{122, 315\}$ | $\{126, 414\}$ |
| $v_\mathrm{A}$ [km/s] | – | $\{14.3, 29.2\}$ |
| $v_{0,\mathrm{c}}$ [km/s] | $\{0, 14.5\}$ | $\{0, 8.61\}$ |

values for $z_h$. This also has a direct impact on the cosmic ray fluxes and results in sizable uncertainties, see for example [215]. To be conservative, we have chosen the small value from above following the reasoning of [151].

The coupled transport equations in eq. (2.9) are usually solved numerically for each species assuming that the cosmic rays to be in steady state meaning that the time derivative in eq. (2.9) vanishes. The equations are then solved on a 3-dimensional grid where two dimensions are used to account for the spatial distribution of the cosmic rays in cylindrical coordinates. The radial distance to the Galactic center is described by $r$ and the distance perpendicular to the plane by $z$. The last dimension is used for the kinetic energy.

Tools that can be used to solve the equations are for example DRAGON [216, 217], PICARD [218] or the semi-analytical tool USINE [219]. In this work we use Galprop version 56 [220] and Galtoollibs 885[1]. We have modified the standard version of Galprop in the following way to implement antideuterons and our propagation model: we included the source terms for secondary and tertiary antideuterons with the analytic coalescence model as described in [166] and in section 2.2.1. We also included the inelastic and tertiary cross sections for antideuterons. Furthermore, we added the antideuteron primary source term from dark matter annihilation according to section 2.2.3 using the annihilation spectra we computed in section 2.2.2. In terms of implementing the propagation model, we have included the smoothly broken power law for the injection spectra as in eq. (2.12) and the diffusion coefficient as in eq. (2.13). Lastly, we have improved the antiproton production cross sections

[1] `https://galprop.stanford.edu`

according to ref. [221].

**Solar modulation** Cosmic rays that arrive at our Solar System have to travel through the heliosphere to get to Earth. During that process, the cosmic rays are deflected and decelerated by the solar winds. This effect is called solar modulation and is strongest for low energy cosmic rays. It is almost negligible for cosmic rays with rigidities above a few tens of GV. The strength of this effect varies with the activity of the sun which changes in a 22-year cycle. Solar modulation can be modeled by an equation similar to the galactic propagation equation in eq. (2.9) which are typically solved numerically, see for example [222–225]. A simplified approach is however more common which is called the force-field approximation [226]. In this approach, the local interstellar (LIS) flux is modified with

$$\Phi_{\mathrm{TOA},i}(E_{\mathrm{TOA},i}) = \frac{E_{\mathrm{TOA},i}^2 - m_i^2}{E_{\mathrm{LIS},i}^2 - m_i^2} \Phi_{\mathrm{LIS},i}(E_{\mathrm{LIS},i})\,, \tag{2.16}$$

$$E_{\mathrm{TOA},i} = E_{\mathrm{LIS},i} - e|Z_i|\varphi_i\,. \tag{2.17}$$

Here, $\Phi$ is the cosmic ray flux as defined in eq. (2.15) and $E$ is the kinetic energy. The subscripts denote whether the flux is the LIS flux with the corresponding energy or the top of the atmosphere (TOA) flux. The mass of the cosmic ray particle is given by $m_i$, its charge number by $Z_i$ and $e$ is the elementary charge. The solar modulation potential $\varphi_i$ is time and charge-sign dependent and needs to be matched to the solar potential at the time of the experiment.

We consider three different experiments, AMS-02, GAPS and AMS-100, which we will describe in more detail below. For AMS-02, we treat the force-field potential as a nuisance parameter which we can vary and marginalize over just like the propagation parameters. This can only be done because we already have data from AMS-02. For future experiments we fix the force-field potential to a value that we estimate. GAPS is scheduled to take data in the winter of 2024/2025[2]. During this time, the solar potential will be near its maximum [227], so we set the potential to $\phi = 700\,\mathrm{MV}$. The solar potential for AMS-100 however can not be predicted as it is still unclear if and when it will operate. We therefore set its value to $\phi = 600\,\mathrm{MV}$.

### 2.2.4 Detection

There are currently two experiments in operation which have the capability to detect cosmic ray antideuterons: AMS-02 [113] and BESS-Polar II [126]. Both experiments use magnetic spectrometers to distinguish antiparticles. Because the antideuteron sensitivity of AMS-02 is better than the sensitivity of BESS by more than an order of magnitude [228], we will not focus on BESS in this work.

AMS stands for Alpha Magnetic Spectrometer, and it is installed on the ISS since May 2011 [113, 146]. The detector is able to measure and identify the flux of elementary particles and antiparticles like electrons, positrons, protons and antiprotons as well as nuclei and antinuclei. AMS-02 can also determine the sign and value of the charge, the momentum and rigidity of these particles.

The structure of the AMS-02 detector is shown in fig. 2.3. The detector consists of a transition radiation detector (TRD), a time-of-flight (TOF) system, a silicon tracker,

[2] `https://gaps1.astro.ucla.edu/gaps/`

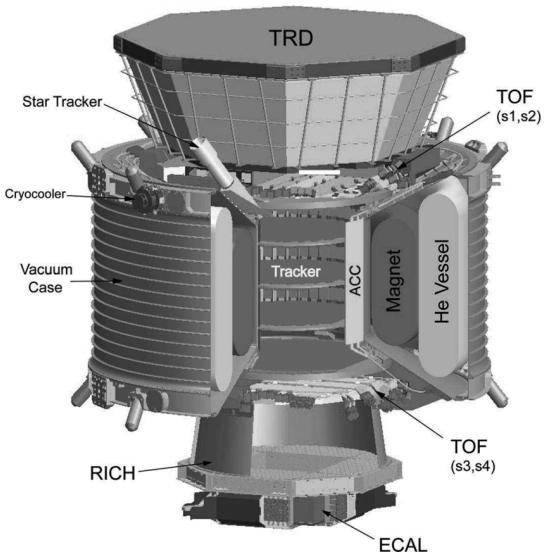


**Figure 2.3:** Schematic view of the components of the AMS-02 detector. It consists of a transition radiation detector (TRD), a time-of-flight (TOF) system, a silicon tracker, a ring imaging Cherenkov detector (RICH), a permanent magnet, an electromagnetic calorimeter (ECAL) and an anti-coincidence counter (ACC). From [229].

a ring imaging Cherenkov detector (RICH), a permanent magnet, an electromagnetic calorimeter (ECAL) and an anti-coincidence counter (ACC). The TRD is used to identify electrons and positrons by transition radiation, as well as to reject protons and distinguish nuclei by their energy loss rate. Below the TRD is the TOF system which can measure the direction and velocity of the particles and their charge. The silicon tracker together with the permanent magnet are used to determine the charge and momentum of the particles by measuring its trajectory. The RICH can identify the velocity and charge of the particles which are inferred from the geometrical shapes generated by the Cherenkov effect. At the bottom of the detector is the ECAL which is a three-dimensional imaging instrument that is used to measure the energy of specifically high-energy electrons and positrons. Finally, the ACC is used to identify particles that are not of interest by rejecting particles that enter or exit the tracker transversely. In general, the detector is able to measure particles with energies between hundreds of MeV and a few TeV. AMS-02 has already collected a large amount of data and has published several results on various cosmic rays [146].

Antideuterons can be detected by AMS-02 in the RICH detector and the TOF system

**Table 2.2:** Expected antideuteron flux sensitivities and energy ranges of the three considered experiments.

| **Experiment** | **Energy range** [GeV/nuc] | $\boldsymbol{\Phi_{\mathrm{sens},E_{\mathrm{exp}}}}$ $[\mathrm{cm}^{-2}\,\mathrm{s}^{-1}\,\mathrm{sr}^{-1}\,(\mathrm{GeV/nuc})^{-1}]$ | **Ref.** |
|---|---|---|---|
| GAPS | $[0.05, 0.25]$ | $2 \times 10^{-6}$ | [230] |
| AMS-02 | [0.2, 0.8] and [2.2, 4.2] | $4.5 \times 10^{-7}$ | [231] |
| AMS-100 | $[0.1, 8.0]$ | $3 \times 10^{-11}$ | [232] |

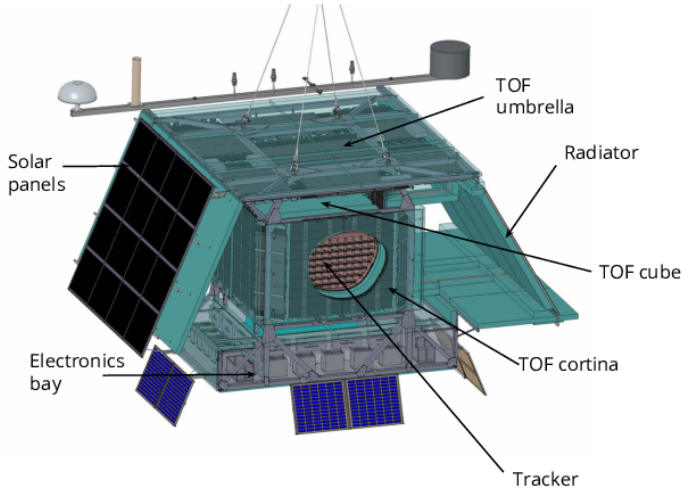


**Figure 2.4:** Schematic view of the GAPS detector. From [234].

[16]. They are identified and separated from other particles by determining the mass and charge of the particle. The TOF system is able to detect antideuterons in the lowest energy region while the RICH detector is used for higher energies. The experimental antideuteron flux sensitivity for AMS-02 is given in section 2.2.4. So far, no antideuterons have been detected officially, but there are reports of a few antideuterons detected by AMS-02 in preliminary analyses [233].

The next generation of magnetic spectrometers in space is AMS-100 which is planned to be installed on the ISS in the far future [232]. The detector will be able to measure antideuterons in an even larger energy range with a sensitivity that is expected to be about three orders of magnitude smaller than the AMS-02 sensitivity. The expected sensitivity for AMS-100 is given in section 2.2.4.

Another upcoming detector is the General Antiparticle Spectrometer (GAPS) [127] which is a balloon-borne experiment that is designed to measure low-energy antideuterons and other antinuclei [230]. In contrast to the AMS-02 experiment that uses a magnetic spectrometer to distinguish antiparticles from particles, the GAPS experiment will use a new exotic atom capture and decay technique. Its launch is planned for the winter of 2024/2025[3]. A schematic view of the experiment is shown in fig. 2.4. It consists of an inner and outer time-of-flight (TOF) system which is able to measure the velocity and direction of the antiparticle. The TOF system surrounds a tracker system made out of Si detectors where the particle loses energy and is stopped in the tracker. An antiparticle will be trapped by a nucleus in the Si detector and form an exotic atom (an atom where an antiparticle replaces an electron) in its excited state. The exotic atom will then de-excite through a series of atomic transitions with the emission of X-rays. The measured energies of the X-rays are used to determine the mass of the captured antiparticle which is used to distinguish different antinuclei from one another. Afterwards, the antiparticle will annihilate with the nucleus and produce a shower of mainly pions and protons. The amount of pions and protons produced can also be used to determine the mass of the antiparticle. The expected sensitivity to antideuteron fluxes for GAPS is also given in section 2.2.4.

[3] `https://gaps1.astro.ucla.edu/gaps/`

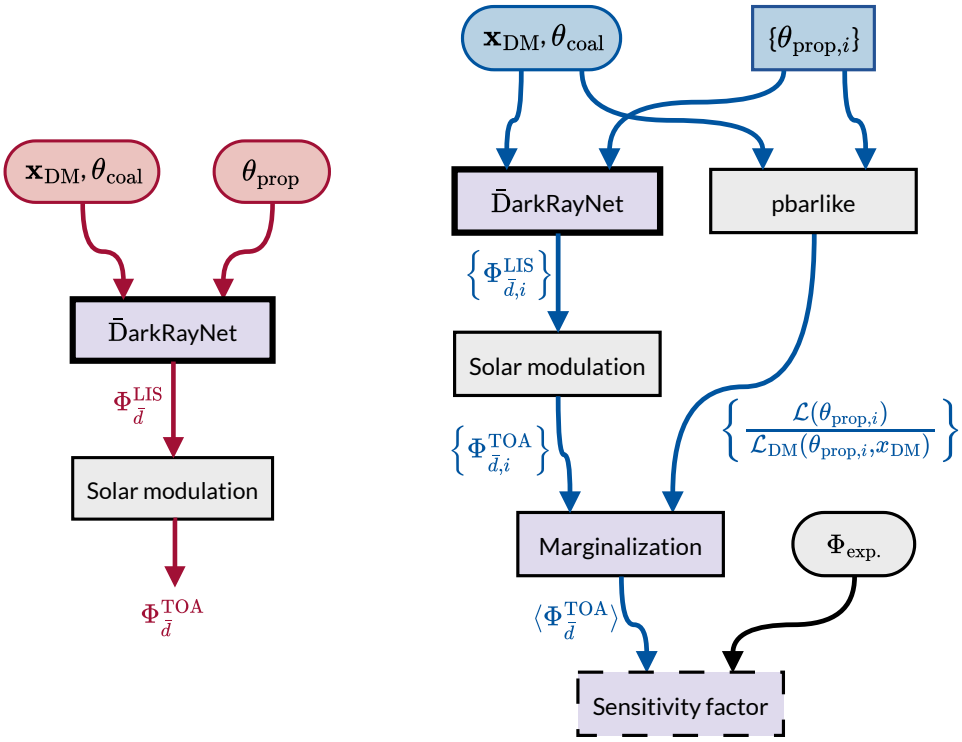


**(a)** Single flux **(b)** Marginalized flux

**Figure 2.5:** Tool-chain for obtaining a single antideuteron flux and the sensitivity factor. The rounded boxes show the input and the rectangular boxes correspond to different steps in our analysis. In purple, we show our new contributions. The left diagram shows the tool-chain for obtaining a single antideuteron flux on Earth. The right diagram shows the tool-chain for obtaining the sensitivity factor for a given experiment including uncertainties from the propagation model by marginalizing over the propagation parameters.

## 2.3 Neural emulation of antideuteron flux

The production of antideuterons from dark matter annihilation is a very rare process. Obtaining a smooth spectrum requires simulating $\mathcal{O}(10^8)$ events for each dark matter parameter point of interest. We therefore need a lot of computational power to simulate the antideuteron annihilation spectra as presented in fig. 2.2. In addition, we also need to simulate the propagation of the antideuterons through the Galaxy using Galprop and the propagation model described in section 2.2.3. Computing only one flux for a given set of propagation parameters is fairly fast and only takes $\mathcal{O}(10)$ seconds. However, we want to take the uncertainties in the propagation model into account which means that we have to compute the flux for numerous parameter points to marginalize over them which is again computationally expensive. We therefore developed a neural network trained on our simulated antideuteron fluxes to speed up the computation of new fluxes. In addition to that, we train a separate network to predict the secondary antideuteron flux which we also obtain using Galprop.

In this section we will describe the architecture of the neural network, as well as the tool-chain to predict the experimental sensitivities to the antideuteron flux as shown in fig. 2.5. The diagram of the left of fig. 2.5 depicts the tool-chain for obtaining a single antideuteron flux on Earth for a given set of parameters. The central tool is

the neural emulator $\bar{\text{D}}$arkRayNet, which predicts the local interstellar antideuteron flux $\Phi_{\bar{d}}^{\text{LIS}}$ for a set of dark matter parameters $\vec{x}_{\text{DM}} = \{m_{\text{DM}}, \mathcal{B}_f, \langle\sigma v\rangle_{\text{tot}}\}$ including the mass $m_{\text{DM}}$, the branching fractions into SM particles $\mathcal{B}_f$ and the total thermally averaged annihilation cross section $\langle\sigma v\rangle_{\text{tot}}$, as well as the coalescence parameters $\vec{\theta}_{\text{coal}} = \{p_c, r_{\Lambda_b}\}$, and propagation parameters $\vec{\theta}_{\text{prop}}$. We describe the training sample used to train the network in section 2.3.1 and the network architecture in section 2.3.2. The network is published as an extension to the DarkRayNet presented in [149, 151] and is available on GitHub. To account for the influence of our solar system on the flux, we then compute the top-of-atmosphere flux $\Phi_{\bar{d}}^{\text{TOA}}$ using the force-field approximation as described in section 2.2.3.

The diagram on the right of fig. 2.5 shows the tool-chain for obtaining the sensitivity factor for a given experiment including uncertainties from the propagation model by marginalizing over the propagation parameters. The marginalized flux $\langle\Phi\rangle_{\bar{d}}$ is obtained by using a set of propagation parameters $\{\theta_{\text{prop},i}\}$ to compute a set of LIS fluxes $\{\Phi_{\bar{d},i}^{\text{LIS}}\}$ using the $\bar{\text{D}}$arkRayNet as well as the likelihood of the propagation parameters using the antiproton likelihood calculator pbarlike [151]. The sensitivity factor is then computed by comparing the marginalized flux to the experimental sensitivity $\Phi_{\text{exp}}$ of the respective experiment. The marginalization routine as well as the exact computation of the sensitivity factor is described in section 2.3.3.

### 2.3.1 Training sample

The neural network to predict the antideuteron flux from dark matter annihilation is trained on a set of approximately 250000 antideuteron fluxes. The training sample is generated by randomly sampling the dark matter parameters $\vec{x}_{\text{DM}}$ and the coalescence parameters $\vec{\theta}_{\text{coal}}$ from their respective prior distributions. The dark matter mass is sampled logarithmically in the range $m_{\text{DM}} \in [2, 1000]\,\text{GeV}$ and each branching fraction is sampled logarithmically in the range $\mathcal{B}_f \in [10^{-5}, 1]$. We consider the annihilation channels $q\bar{q}$, $c\bar{c}$, $b\bar{b}$, $t\bar{t}$, $gg$, $hh$, $W^+W^{-(*)}$, and $ZZ^{(*)}$, as already mentioned in section 2.2.2. After sampling the branching fractions, we renormalize them so that their sum is equal to 1. The coalescence momentum is sampled from a flat prior in the range $p_c \in [148, 300]\,\text{MeV}$ which covers the 95% confidence level interval and the rescaling of the $\Lambda_b$ production rate is sampled logarithmically in the range $r_{\Lambda_b} \in [0.3, 20]$.

The remaining input parameters are the propagation parameters $\vec{\theta}_{\text{prop}}$ for both propagation models we consider which are sampled from their posterior distribution computed from a fit to proton, antiproton and Helium data from AMS-02 [146] under the assumption of no additional dark matter signal. This approach has been adopted from [151] where the posterior distributions have been identified using MultiNest scans. We use the result from [156, 157] to account for the error correlations of the AMS-02 measurements.

We then generate a set of injection spectra using the randomly sampled dark matter and coalescence parameters as described in section 2.2.2. The injection spectra are then propagated through the Galaxy using Galprop and the two propagation models described in section 2.2.3 with the aforementioned set of propagation parameters. For the annihilation channels $W^+W^{-(*)}$ and $ZZ^{(*)}$ we simulate the propagation using a separate network trained on the propagation of the remaining channels to save computational resources. The same set of propagation parameters is also used to

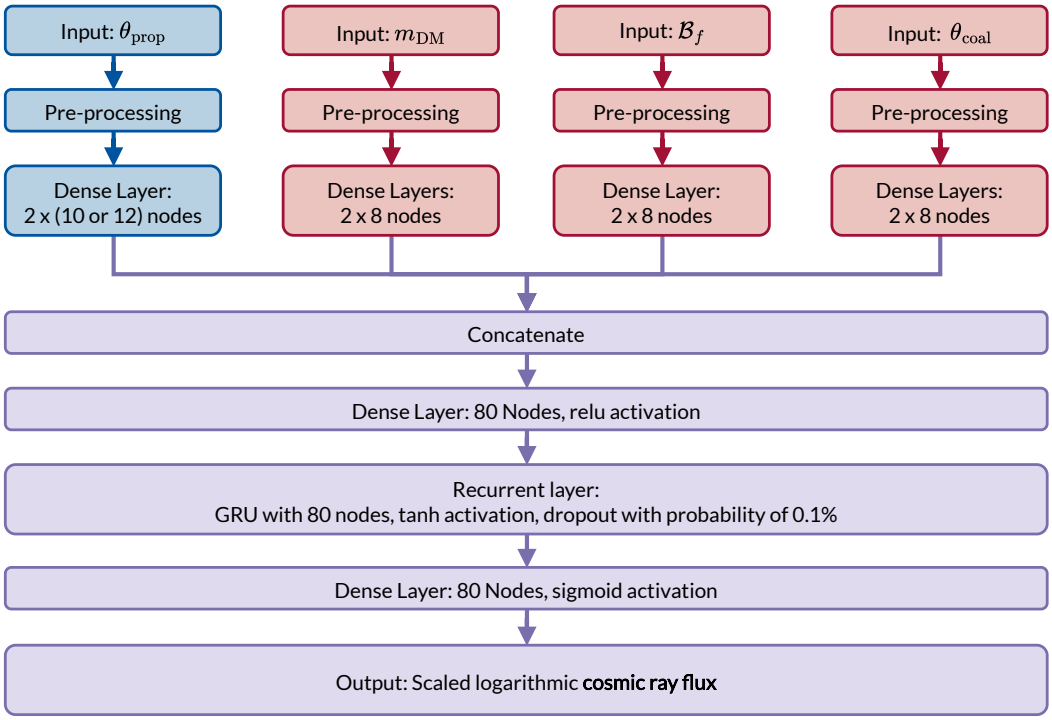


**Figure 2.6:** Sketch of the network setup to predict the flux of antideuterons from dark matter annihilation. The number of nodes for the propagation parameter input depends on the propagation model (12 for INJ.BRK and 10 for DIFF.BRK).

generate a set of secondary antideuteron fluxes. The resulting fluxes are then used to train the neural network.

### 2.3.2 Network setup and performance

We use the antideuteron fluxes obtained from dark matter annihilation and secondary production for the two considered propagation models to train four individual networks. This way, we are able to predict the primary and secondary antideuterons separately for each propagation model. For all networks, we use the API Keras [235] which is based on Tensorflow [236].

The network architecture for the antideuteron flux from dark matter annihilation is shown in fig. 2.6. In order to improve the performance of the network when predicting the different physical effects of the input parameters, we first set up four individual feed-forward neural networks for the propagation parameters $\vec{\theta}_{\mathrm{prop}}$, the dark matter mass $m_{\mathrm{DM}}$, the 8 branching fractions $\mathcal{B}_f$, and the coalescence parameters $\vec{\theta}_{\mathrm{coal}}$. We use different pre-processing procedures for the individual input parameters: we map $p_c$ and the logarithms of $m_{\mathrm{DM}}$, $r_{\Lambda_b}$ and the branching fractions to the range $[0, 1]$. The propagation parameters are individually mapped to a distribution with a mean of 0 and a standard deviation of 1. As the flux of antideuterons spans over several orders of magnitude, we map the flux onto 80 bins and transform the fluxes with

$$\tilde{\Phi}_{\bar{d}} = 1 + \frac{1}{10} \log \left( \frac{\Phi_{\bar{d}}}{\mathrm{GeV}^{-1}\,\mathrm{cm}^{-2}\,\mathrm{s}^{-1}\,\mathrm{sr}^{-1}} \left( \frac{m_{\mathrm{DM}}}{\mathrm{GeV}} \right)^2 \left( \frac{p_{c,0}}{p_c} \right)^3 \frac{E/\mathrm{n}}{\mathrm{GeV}} \right) , \tag{2.18}$$

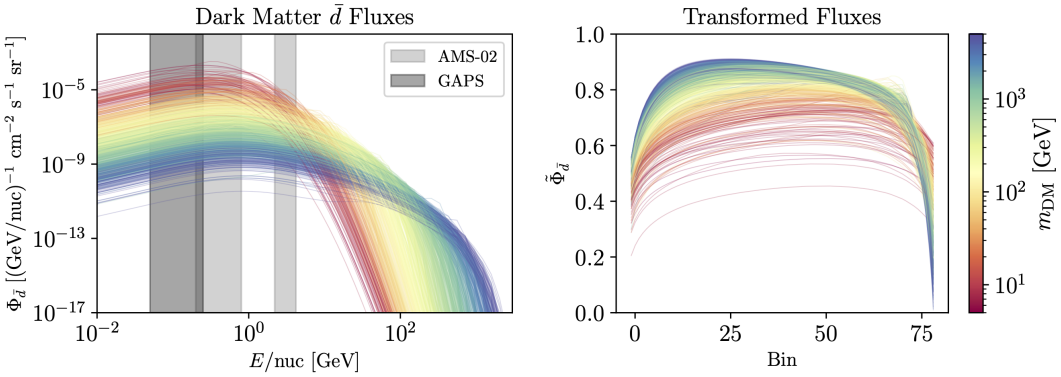


**Figure 2.7:** Examples of local interstellar antideuteron fluxes in the INJ.BRK model (left) and their transformation (right). The network is trained on the transformed fluxes. The color sale indicates the dark matter mass. The shaded gray regions indicate the energy ranges of GAPS and AMS-02 in which the experiments are sensitive to antideuterons.

so that almost all fluxes are mapped onto the range $[0, 1]$. Here, $p_{c,0}$ is the best-fit value for the coalescence momentum (see section 2.2.1) and $E/\mathrm{n}$ is the kinetic energy per nucleon. This transformation maps parts of some fluxes with very small values to values smaller than 0. Because these are way below any future sensitivity of the experiments, we do not consider this a problem and set these values to 0 in the transformation. To obtain the actual flux from the rescaled flux, one can easily invert the transformation. We show the transformation for a set of randomly selected fluxes in the INJ.BRK model in fig. 2.7 to visualize how the transformation works. The left plot shows the original fluxes for different dark matter masses indicated by the color scale and the right plot shows the corresponding transformed fluxes. We also show the energy ranges of the GAPS and AMS-02 experiments in which the experiments are sensitive to antideuterons with the shaded gray regions.

We then concatenate the output of the four networks and feed them into a recurrent network consisting of a dense layer with 80 nodes, a recurrent layer with 80 nodes and finally another dense layer with 80 nodes which represents the rescaled antideuteron flux. We also added a small dropout probability of 0.1% to the input of the recurrent layer. The network is trained using the mean absolute error loss function and the Adam optimizer. We use a `ReduceLROnPlateau` schedule to reduce the learning rate during the training, starting from a learning rate of $10^{-2}$. The training is stopped early if the validation loss does not decrease for 20 epochs using an `EarlyStopping` callback. We use approximately 250000 antideuteron fluxes for each propagation model to train the network.

The network trained on the secondary production of antideuterons has only one type of input which consists of the propagation parameters which have been preprocessed in the same way as for the network predicting the antideuteron flux from dark matter annihilation. We preprocess the secondary fluxes by mapping the logarithm of the fluxes onto a distribution of 0 mean and a standard deviation of 1. The network architecture consists of three dense layers with ReLU activations, followed by a recurrent layer and another hidden layer. We again implement a `ReduceLROnPlateau` schedule and an `EarlyStopping` callback. The network is trained using the mean squared error loss function and the Adam optimizer. We again use approximately 250000 secondary antideuteron fluxes for each propagation model for the training.

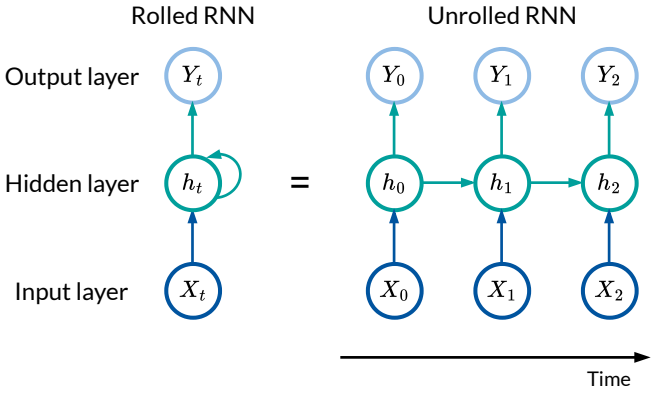


**Figure 2.8:** Visualization of a recurrent neural network by unrolling the network for a fixed number of time steps. The input layer contains the sequential data, the hidden layer processes the data across multiple time steps and the output layer produces the output of the network.

Both network architectures use a recurrent layer which allows us to take into account the correlation between energy bins in the flux. This significantly improves the performance of our network as the flux of antideuterons is not expected to change drastically between neighboring energy bins. Recurrent neural networks (RNNs) are usually used for sequential data by processing data across multiple time steps which uses the output of a recurrent layer as an input of the same layer in the next time step [237]. This hidden vector acts as a memory component that is updated between time steps. A visualization of an RNN is shown in fig. 2.8. On the left, a rolled RNN is shown with an input layer containing sequential data, a hidden layer that takes its output as an input for the next time step and an output layer. On the right, the unrolled version of the RNN is shown which shows the network for a fixed number of time steps. The hidden layer is updated at each time step with the output of the hidden state of the previous time step and the input of the current time step. The output of the hidden layer is then used as an input for the next time step.

An RNN is usually trained using backpropagation through time as the same parameters are shared between each time step [238]. In this case, the gradient of the loss function which is used to update the weights is calculated by using the chain rule to compute the gradient of the loss at each time step and summing them up. This however can become problematic when dealing with long term dependencies as the gradient can vanish or explode. This problem has been solved by introducing a Gated Recurrent Unit or a Long Short-Term Memory cell.

The Long Short-Term Memory (LSTM) introduced in [239] replaces the simple hidden cell by a hidden state and cell state that acts as long-term memory and three gates that update the cell state: a forget gate, an input gate and an output gate. The forget gate decides which information to discard from the cell state, the input gate decides which information to add to the cell state and the output gate decides which information is passed onto the next time step. The LSTM has been shown to be able to learn long-term dependencies without the vanishing gradient problem.

The Gated Recurrent Unit (GRU) [240] is a simplified version of the LSTM. It combines the forget and input gate into a single update gate and merges the cell state and hidden state. The GRU has been shown to perform similarly to the LSTM while

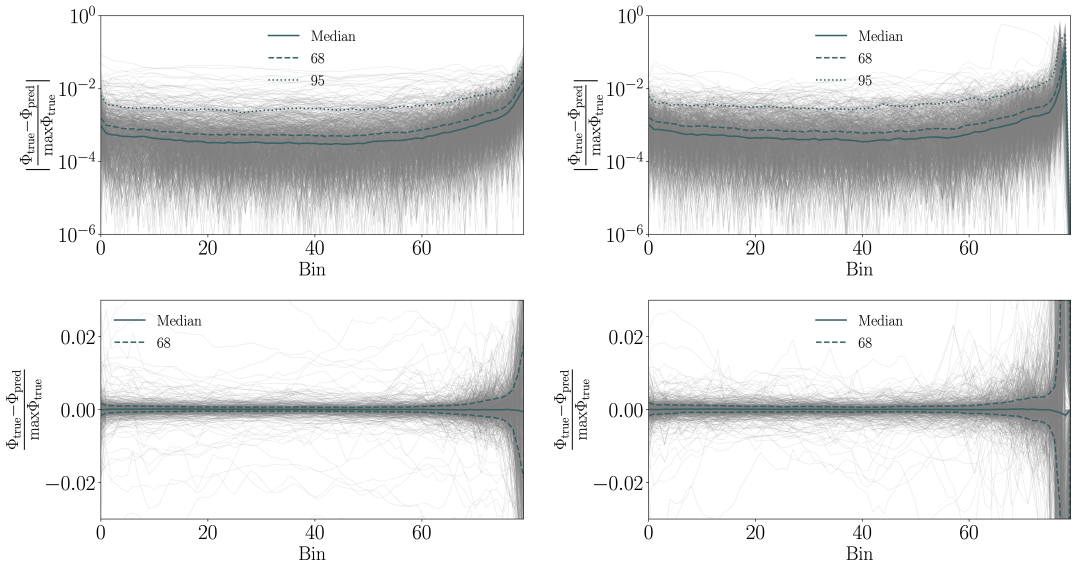


**(a)** INJ.BRK **(b)** DIFF.BRK

**Figure 2.9:** Comparison of the predicted transformed flux and the true transformed flux in both propagation models for 1000 randomly selected antideuteron fluxes from dark matter annihilation. The upper panels show the absolute value of the difference between the predicted and true fluxes while the lower panels show the total difference.The solid blue line shows the median relative deviation of all spectra while the dashed and dotted lines show the 68 and 95 percentile of the deviations, respectively.

being computationally more efficient due to fewer parameters that have to be trained. Therefore, we use a GRU in our dark matter annihilation and secondary production networks.

To evaluate the accuracy of our networks we use a test sample of 1000 antideuteron fluxes for each propagation model that have not been used for training. We then compare the predicted fluxes to the true fluxes by computing the difference between them, normalized by the maximum of the true flux. For the antideuteron flux from dark matter annihilation we use the transformed flux for the comparison which is shown in fig. 2.9. The top panels show the absolute value of the difference between the predicted and true fluxes while the bottom panels show the total difference.

We find that the network is able to predict 68 % of all transformed fluxes in the majority of the bins with a relative deviation of less than $6 \times 10^{-4}$. The largest uncertainties are in the last few bins. This is expected as the fluxes in these bins are very small, and therefore the network has difficulties in predicting them accurately. This however is not a problem as the respective fluxes in these bins are way below the expected sensitivity of the experiments and not of relevance for us. The accuracy in predicting the transformed spectra translates into a relative error of $\mathcal{O}(10^{-2})$ in the actual flux.

The network trained on the secondary antideuteron flux performs similarly well. We compute the accuracy in the same way as before but now taking the actual flux instead of the transformed flux. We find that the network is able to predict all fluxes with a relative deviation of less than $5 \times 10^{-3}$ for both propagation models in all energy bins. The performance of the secondary antideuteron network is even better than for

the dark matter annihilation network. This is expected as the dimensionality of the parameter space is much smaller for the secondary antideuteron flux than for the dark matter annihilation flux. As both accuracies are sufficient for our purposes, we use the networks to predict the antideuteron fluxes for the sensitivity calculations.

### 2.3.3 Marginalized spectra and sensitivity factor

To assess the capability of the experiments to detect antideuterons from dark matter annihilation, we follow the tool-chain as shown in fig. 2.5b to marginalize over the propagation parameters and compute the projected sensitivity. We use the DarkRayNet to predict the LIS antideuteron flux for a set of propagation parameters obtained from the posterior sample which was also used for the training sample and a set of dark matter and coalescence parameters. The TOA fluxes are then obtained by using the force-field approximation as described in section 2.2.3. The marginalized flux is computed in the following way:

$$\langle \Phi \rangle_{\bar{d},E_{\mathrm{exp}}}(x_{\mathrm{DM}}) = \int \mathrm{d}\theta_{\mathrm{prop}}\; p_{\mathrm{DM}}(\theta_{\mathrm{prop},i}, x_{\mathrm{DM}})\, \Phi_{\bar{d},E_{\mathrm{exp}}}(\theta_{\mathrm{prop}}, x_{\mathrm{DM}}) \tag{2.19}$$

$$= \int \mathrm{d}\theta_{\mathrm{prop}}\; p_{\mathrm{DM}}(\theta_{\mathrm{prop}}, x_{\mathrm{DM}})\, \frac{p(\theta_{\mathrm{prop}})}{p(\theta_{\mathrm{prop}})}\, \Phi_{\bar{d},E_{\mathrm{exp}}}(\theta_{\mathrm{prop}}, x_{\mathrm{DM}}) \tag{2.20}$$

$$= \underbrace{\int \mathrm{d}\theta_{\mathrm{prop}}\; p(\theta_{\mathrm{prop}})}_{\sim \sum_i}\; \underbrace{\frac{p_{\mathrm{DM}}(\theta_{\mathrm{prop}}, x_{\mathrm{DM}})}{p(\theta_{\mathrm{prop}})}}_{(*)}\; \Phi_{\bar{d},E_{\mathrm{exp}}}(\theta_{\mathrm{prop}}, x_{\mathrm{DM}}) \tag{2.21}$$

$$\approx \underbrace{\frac{Z}{Z_{\mathrm{DM}}}}_{(**)} \sum_i \Phi_{\bar{d},E_{\mathrm{exp}}}(\theta_{\mathrm{prop},i}, x_{\mathrm{DM}})\, \frac{\mathcal{L}_{\mathrm{DM}}(\theta_{\mathrm{prop},i}, x_{\mathrm{DM}})}{\mathcal{L}(\theta_{\mathrm{prop},i})} \tag{2.22}$$

$$= \left( \sum_i \frac{\mathcal{L}_{\mathrm{DM}}(\theta_{\mathrm{prop},i}, x_{\mathrm{DM}})}{\mathcal{L}(\theta_{\mathrm{prop},i})} \right)^{-1} \sum_i \Phi_{\bar{d},E_{\mathrm{exp}}}(\theta_{\mathrm{prop},i}, x_{\mathrm{DM}})\, \frac{\mathcal{L}_{\mathrm{DM}}(\theta_{\mathrm{prop},i}, x_{\mathrm{DM}})}{\mathcal{L}(\theta_{\mathrm{prop},i})}\,. \tag{2.23}$$

Here, $p$ denotes the posterior, $\pi$ the prior, and $Z$ the evidence, i.e., the normalization of the posterior. In the third step, we approximate the integral by a sum over the sample of propagation parameters. We can also rewrite the posterior ratio using Bayes' theorem as follows:

$$(*) = \frac{p_{\mathrm{DM}}(\theta_{\mathrm{prop}}, x_{\mathrm{DM}})}{p(\theta_{\mathrm{prop}})} = \frac{Z}{Z_{\mathrm{DM}}}\, \frac{\pi(\theta_{\mathrm{prop}})}{\pi(\theta_{\mathrm{prop}})}\, \frac{\mathcal{L}_{\mathrm{DM}}(\theta_{\mathrm{prop}}, x_{\mathrm{DM}})}{\mathcal{L}_{\mathrm{DM}}(\theta_{\mathrm{prop}})}\,. \tag{2.24}$$

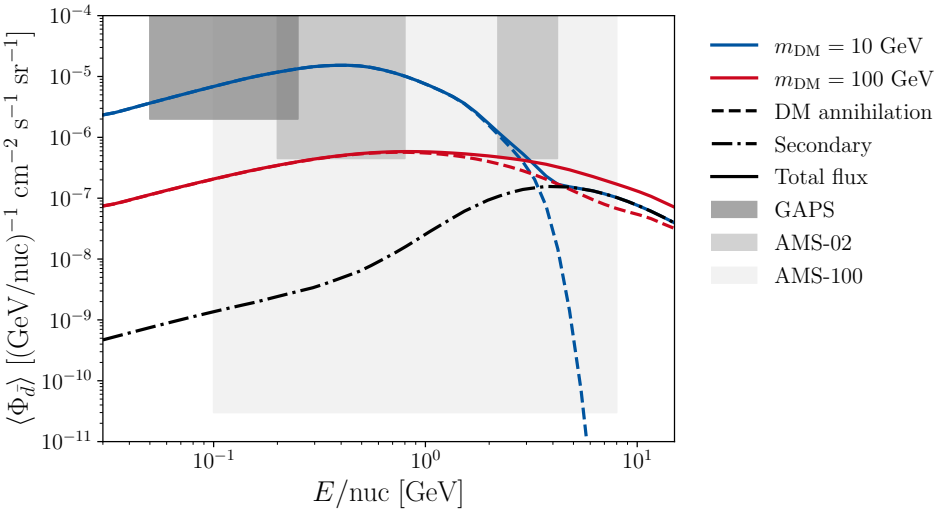


**Figure 2.10:** Two flux examples for annihilation into $b\bar{b}$ in the INJ.BRK model for dark matter masses of 10 and 100 GeV. The fluxes are marginalized over all propagation parameters and the solar potential of GAPS was assumed. The fluxes are calculated assuming a thermal cross section of $\langle\sigma v\rangle = 3\times10^{-26}\,\mathrm{cm^3 s^{-1}}$. Secondary antideuterons are shown with the dashed-dotted line. The shaded regions indicate the antideuteron flux sensitivities of GAPS, AMS-02 and AMS-100.

The evidence ratio can be expressed as

$$(**) = \frac{Z_{\mathrm{DM}}}{Z} \tag{2.25}$$

$$= \frac{\int \mathrm{d}\theta_{\mathrm{prop}} \pi(\theta_{\mathrm{prop}}) \mathcal{L}_{\mathrm{DM}}(\theta_{\mathrm{prop}}, x_{\mathrm{DM}})}{Z} \tag{2.26}$$

$$= \int \mathrm{d}\theta_{\mathrm{prop}} \frac{\pi(\theta_{\mathrm{prop}})\mathcal{L}(\theta_{\mathrm{prop}})}{Z} \frac{\mathcal{L}_{\mathrm{DM}}(\theta_{\mathrm{prop}}, x_{\mathrm{DM}})}{\mathcal{L}(\theta_{\mathrm{prop}})} \tag{2.27}$$

$$= \int \mathrm{d}\theta_{\mathrm{prop}} p(\theta_{\mathrm{prop}}) \frac{\mathcal{L}_{\mathrm{DM}}(\theta_{\mathrm{prop}}, x_{\mathrm{DM}})}{\mathcal{L}(\theta_{\mathrm{prop}})} \tag{2.28}$$

$$\approx \sum_i \frac{\mathcal{L}_{\mathrm{DM}}(\theta_{\mathrm{prop},i}, x_{\mathrm{DM}})}{\mathcal{L}(\theta_{\mathrm{prop},i})} \,. \tag{2.29}$$

We compute the likelihood ratio $\mathcal{L}_{\mathrm{DM}}(\theta_{\mathrm{prop},i}, x_{\mathrm{DM}})/\mathcal{L}(\theta_{\mathrm{prop},i})$ of the propagation parameters using the antiproton likelihood calculator pbarlike [151]. The marginalized secondary antideuteron flux can be computed in the same way using the network trained on the secondary antideuteron flux. Marginalizing over the propagation parameters allows us to take the uncertainties in the propagation model into account.

We show two examples of the marginalized fluxes for annihilation into $b\bar{b}$ in the INJ.BRK model in fig. 2.10 for dark matter masses of 10 GeV in the dashed blue line and 100 GeV in the dashed red line. The fluxes are marginalized over all propagation parameters and the solar potential of GAPS was assumed. We computed the fluxes assuming a thermal cross section of $\langle\sigma v\rangle = 3\times10^{-26}\,\mathrm{cm^3 s^{-1}}$ as given in eq. (1.28) and using the best-fit value for $p_c$ and $r_{\Lambda_b} = 3$. The secondary antideuterons are shown with the dashed-dotted line. Additionally, the shaded regions show the antideuteron flux sensitivities of GAPS, AMS-02 and AMS-100 as given in section 2.2.4. This

also shows that the secondary antideuteron flux is not relevant for the sensitivity of AMS-02 and GAPS as the flux is suppressed in the energy range of the experiments. In contrast to that, the antideuteron fluxes from dark matter annihilation peak in the energy range of the experiments.

The sensitivity factor is then computed by comparing the marginalized flux for given dark matter and coalescence parameters to the experimental sensitivity $\Phi_{\text{sens},E_{\text{exp}}}$ of the respective experiment. The sensitivity factor is then given by

$$\text{Sensitivity factor} := \frac{\langle\Phi\rangle_{\bar{d},E_{\text{exp}}}}{\Phi_{\text{sens},E_{\text{exp}}}}\,, \tag{2.30}$$

where $\langle\Phi\rangle_{\bar{d},E_{\text{exp}}}$ is the marginalized antideuteron flux in the energy range of the experiment. Therefore, a sensitivity factor larger than one indicates that the experiment is sensitive to the antideuteron flux from dark matter annihilation as it would be the case for $m_{\text{DM}} = 10\,\text{GeV}$ flux in fig. 2.10. A sensitivity factor smaller than one indicates that the experiment is not sensitive to the antideuteron flux.

## 2.4 Projections for experimental sensitivities

In this section, we compute the sensitivity factor for the three considered experiments using the tool-chain as described in section 2.3.3 for two different dark matter model scenarios in the INJ.BRK and DIFF.BRK propagation models. The first scenario is dark matter annihilating purely into $b\bar{b}$. For the second scenario we consider the singlet scalar Higgs portal (SSHP) model as described in section 1.5.1 where we fix the coupling to the Higgs so that the correct relic density is obtained, see for example [135, 136]. This fixes the branching fractions into the SM particles above the Higgs production threshold. Below $m_{\text{DM}} = m_h$ the branching fractions are fixed by the dark matter mass and the coupling of the Higgs to SM particles. We also consider two different assumptions for the total annihilation cross section $\langle\sigma v\rangle_{\text{tot}}$. In the first case we fix the annihilation cross section to the thermal value of $\langle\sigma v\rangle_{\text{tot}} = 3\times10^{-26}\,\text{cm}^3\text{s}^{-1}$ which is required by thermal freeze-out, see section 1.3, while in the second case we use the annihilation cross section obtained from the antiproton exclusion limit as described in ref. [151] for the respective propagation model. Note that the limits from antiprotons do not reach below a dark matter mass of 10 GeV as the uncertainties in the modeling of solar modulation and propagation at these low energies are very large [149].

We show the resulting sensitivity factors for the annihilation into $b\bar{b}$ and the Higgs portal model in fig. 2.11 for AMS-02 and for the annihilation into $b\bar{b}$ only in fig. 2.12 for GAPS and AMS-100 in the left and right panels, respectively. The sensitivity to the SSHP model for GAPS and AMS-100 is very similar to the one for the annihilation into $b\bar{b}$. Therefore, we do not show the sensitivity factor for the SSHP model for GAPS and AMS-100 here but show the results in appendix A. For all sensitivity factors we consider dark matter masses between 5 GeV and 4 TeV for the thermal cross section in red and between 10 GeV and 4 TeV for the antiproton cross section limits in blue. The solid lines and shaded bands around them denote the results for a $\Lambda_b$ rescaling parameter of $r_{\Lambda_b} = 3$ and the $1\sigma$ uncertainty from the determination of the coalescence momentum, respectively, while the dashed curves correspond to $r_{\Lambda_b} = 1$. The sensitivity factors are shown for the INJ.BRK model in the left panels and for the DIFF.BRK model in the right panels.

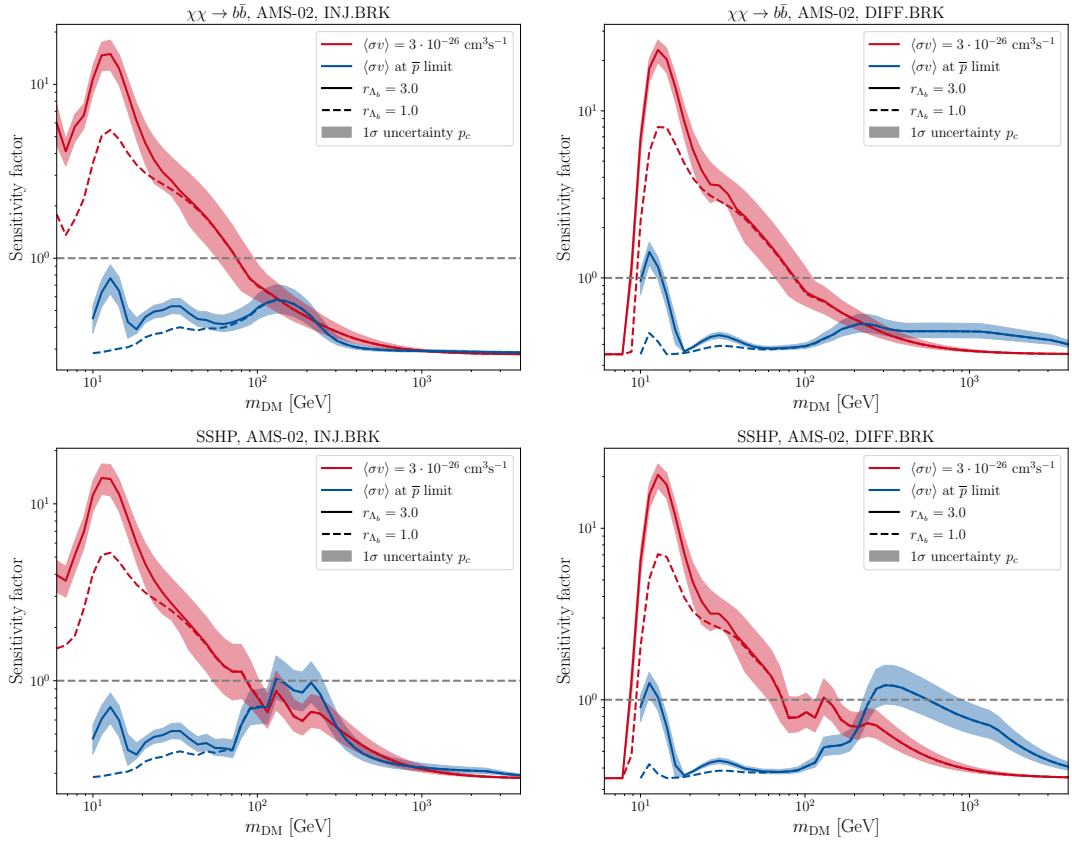


**Figure 2.11:** Sensitivity factor of AMS-02 experiment for annihilation into $b\bar{b}$ (upper panels) and the scalar singlet Higgs portal model (lower panels) within the propagation models INJ.BRK (left panels) and DIFF.BRK (right panels). The solid lines and shaded bands around them denote the results for a $\Lambda_b$ rescaling parameter of $r_{\Lambda_b} = 3$ and the $1\sigma$ uncertainty from the determination of the coalescence momentum, respectively, while the dashed curves correspond to $r_{\Lambda_b} = 1$. The red lines correspond to a fixed annihilation cross section while we use the annihilation cross section obtained from the antiproton exclusion limit for the blue lines. The dashed gray line corresponds to the threshold of where the corresponding experiment is sensitive to an antideuteron flux.

Within the assumptions of the analysis for the antiproton limits, we can exclude the region above the blue line for dark matter masses larger than 10 GeV. This exclusion depends strongly on the propagation model. In the DIFF.BRK model the thermal cross section is excluded up to masses of approximately 200 GeV while in the INJ.BRK model this exclusion reaches up to masses of around one TeV. There is however an intermediate section between roughly 100 and 200 GeV where the limits are not as strong as for the thermal cross section. This region is smaller for the annihilation into $b\bar{b}$ than for the Higgs portal model as the annihilation into $W^+W^-, ZZ$, and $hh$ is dominant in the Higgs portal model for these dark matter masses.

First, we want to discuss the sensitivity factor for AMS-02 in fig. 2.11. Assuming the antiproton exclusion and $r_{\Lambda_b} = 3$, we find that AMS-02 is sensitive to a dark matter signal in three distinct mass regions, depending on the propagation model and assumptions on the annihilation channels: in the DIFF.BRK model we find a sensitivity factor larger than one for dark matter masses between 10 and 20 GeV for both dark matter models. In the Higgs portal model we find two different regions depending on the propagation model. The INJ.BRK model results in a detectable mass range between 100 and 200 GeV while in the DIFF.BRK model the region starts at 200 GeV. This difference comes from the fact that the antiproton limit in the DIFF.BRK model is weakened above a mass of 200 GeV which allows for a larger annihilation rate. For even higher masses, the antideuteron flux decreases more drastically in the energy regions of AMS-02 even though both antiproton limits in both propagation models are weaker. Also note that the sensitivity factor for the Higgs portal model and for annihilation into $b\bar{b}$ looks almost identical for dark matter masses below 50 GeV. This is because the branching fraction into $b\bar{b}$ is dominant for this mass range in the Higgs portal model.

Regarding the possible detection of around 7 antideuteron events in AMS-02 [233], we find that we can only reproduce this signal for dark matter masses below 10 GeV, assuming the thermal cross section and the sensitivity of AMS-02 as given in section 2.2.4. However, the sensitivity was computed assuming that the detector was built using a superconducting magnet [231] while in reality, a permanent magnet was used [232]. In addition to that, a publication of the possible measurement is still pending such that this observation is not conclusive.

Next, we will focus on the sensitivity to dark matter annihilation into $b\bar{b}$ of the upcoming experiments GAPS and AMS-100 as shown in fig. 2.12. The upper two plots show the sensitivity factor for GAPS while the lower two plots show the sensitivity factor for AMS-100 for both propagation models. In the low mass region ($m_{\mathrm{DM}} < 10$ GeV) the sensitivity of GAPS can compete with the one of AMS-02 which provides a great independent test of the existence of low-energy antideuterons. For dark matter masses above 10 GeV, the sensitivity of GAPS is worse than the one of AMS-02. This is due to the fact that GAPS is optimized for low-energy antideuterons and is therefore not sensitive to high-energy antideuterons.

The sensitivity of AMS-100 is significantly better than the one of AMS-02 and GAPS by several orders of magnitude. Due to this improved sensitivity, AMS-100 will also be sensitive to the flux of secondary antideuterons which is not the case for the other experiments. This can be seen by the constant value of the sensitivity factor at large dark matter masses. This also means that in the case of AMS-100, the sensitivity factor does not represent the sensitivity to dark matter annihilation into antideuterons but rather the sensitivity to the total antideuteron flux.

In our analysis we also focus on the impact of the coalescence parameters to the

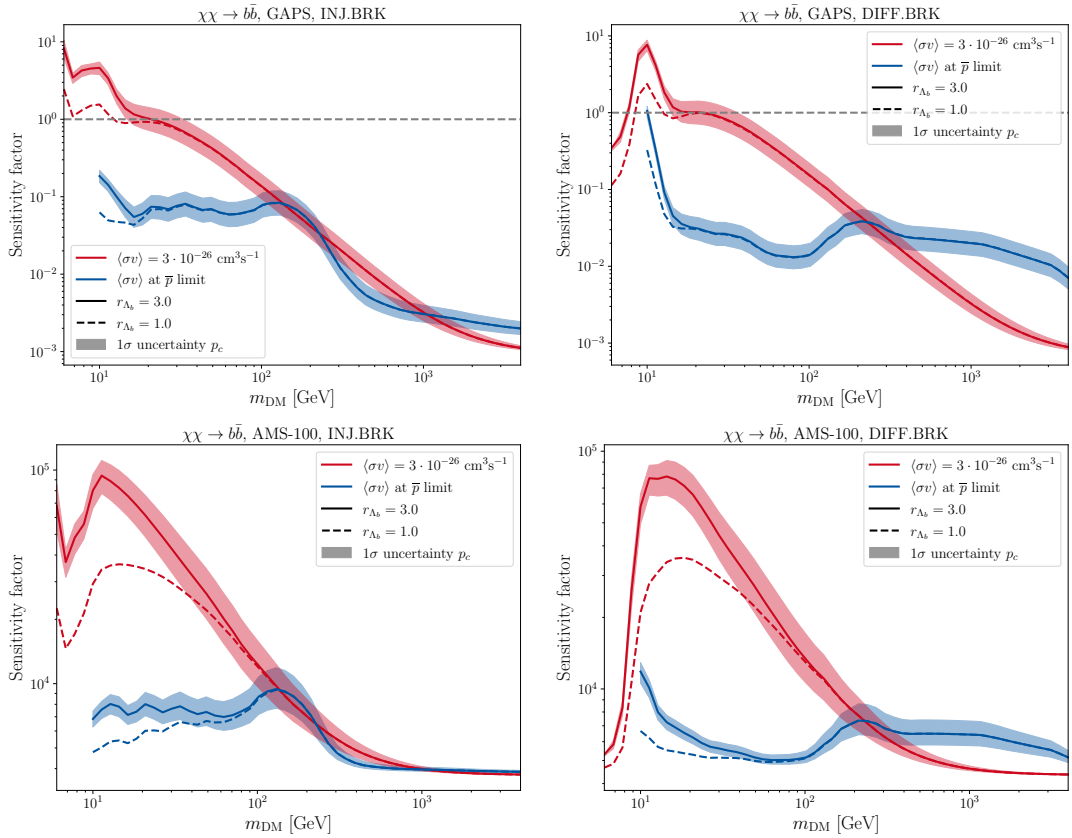


**Figure 2.12:** Sensitivity factor for GAPS (upper panels) and AMS-100 (lower panels) within the propagation models INJ.BRK (left panels) and DIFF.BRK (right panels). Here we consider annihilation into $b\bar{b}$ only. As in fig. 2.11, the solid lines and shaded bands denote the results for $r_{\Lambda_b} = 3$ and the $1\sigma$ coalescence momentum uncertainty, respectively, while the dashed curves correspond to $r_{\Lambda_b} = 1$.

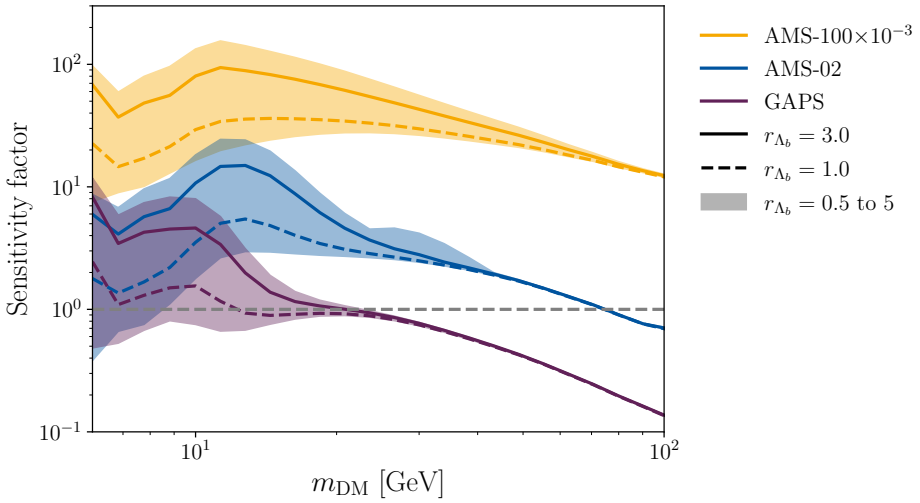


**Figure 2.13:** Sensitivity factor of all experiments in the INJ.BRK model for dark matter annihilation into $b\bar{b}$ with varying rescaling of the $\Lambda_b$ production rate $r_{\Lambda_b}$ assuming a thermal cross section of $\langle\sigma v\rangle = 3 \times 10^{-26}\,\mathrm{cm^3 s^{-1}}$. We show the sensitivity of AMS-100 in yellow, the one of AMS-02 in blue and the one of GAPS in purple. Note that for better display the result for AMS-100 is scaled down by a factor of $10^{-3}$. The solid lines correspond to $r_{\Lambda_b} = 3$ while the dashed lines correspond to $r_{\Lambda_b} = 1$. The shaded bands show the variation of $r_{\Lambda_b}$ from 0.5 to 5.

sensitivity factor. The impact of the $1\sigma$ uncertainty on the coalescence momentum can be seen in figs. 2.11 and 2.12 by the shaded bands around the solid lines. The bands are not of constant size as they get smaller towards higher dark matter masses and also towards smaller masses. The former is due to the fact that the secondary antideuteron flux is more important for higher dark matter masses as the flux from dark matter annihilation decreases for larger dark matter masses. For the secondary emission, we did not consider the impact of varying the coalescence momentum. The latter effect comes from the contribution of antideuterons produced by the decay of $\Lambda_b$ baryons which has a much weaker dependence on $p_c$. For lower dark matter masses, the bump in the flux that is produced by the decay of $\Lambda_b$ baryons lies in the energy range of the experiments and therefore has a large impact on the sensitivity factor. The fact that the contribution from $\Lambda_b$ baryons is more important for low dark matter masses can also be seen in fig. 2.13 where we show the sensitivity factor for all experiments in the INJ.BRK model for dark matter annihilation into $b\bar{b}$ with varying rescaling of the $\Lambda_b$ production rate $r_{\Lambda_b}$. The shaded bands show the variation of $r_{\Lambda_b}$ from 0.5 to 5. The sensitivity factor increases with increasing $r_{\Lambda_b}$ for small dark matter masses. For higher dark matter masses, the sensitivity factor is almost constant as the contribution from $\Lambda_b$ baryons becomes less important.

## 2.5 Summary

In this chapter, we have considered low-energy antideuterons as a promising indirect detection probe for the annihilation of dark matter. We have carefully analyzed the sensitivity of the currently running AMS-02 experiment, the upcoming GAPS experiment and the future AMS-100 mission to a potential signal from dark matter

annihilation. This entailed simulating the production of antideuterons with Monte Carlo simulations, including the uncertainties of the coalescence model used to describe the production of antideuterons. These consisted of the uncertainty on the coalescence momentum which we obtained by fitting to LEP data, as well as a rescaling of the $\bar{\Lambda}_b$ production rate which affects antideuterons produced in $b\bar{b}$ annihilation. Additionally, we included uncertainties from the propagation of antideuterons through our Galaxy by using two different propagation models and varying the corresponding propagation parameters.

To speed up the computation of the antideuteron fluxes and enable a fast computation of the marginalized antideuteron flux, we developed a neural network to predict the antideuteron fluxes from dark matter annihilation and secondary production called $\bar{\text{D}}$arkRayNet. For this, we used a recurrent neural network to account for the correlation between neighboring energy bins. The tool computes the propagated antideuteron flux directly from the dark matter mass, the coalescence parameters and the propagation parameters within a few seconds. We have shown that the network is able to predict the majority of antideuteron fluxes with a relative deviation of less than $10^{-2}$ for the dark matter annihilation flux and less than $5 \times 10^{-3}$ for the secondary antideuteron flux.

The development of this tool enables the study of a wide range of dark matter models and propagation parameters in a fast and efficient way which would otherwise be computationally very expensive. This is due to two reasons: first, the computation of the antideuteron injection spectra using Monte Carlo event generators like Pythia requires $\mathcal{O}(10^8)$ events per dark matter mass and annihilation channel to obtain a sufficiently smooth spectrum. Second, the propagation of antideuterons through the Galaxy requires the solution of a diffusion equation using tools like Galprop. This becomes especially computationally expensive when varying the propagation parameters to account for uncertainties in the propagation. The neural network allows us to compute the antideuteron fluxes in a few seconds which makes it possible to compute the marginalized antideuteron flux for a large number of dark matter models and propagation parameters. As this is orders of magnitudes faster than the full simulations, we concluded that the $\bar{\text{D}}$arkRayNet is a powerful tool for the study of large dark matter parameter spaces.

To demonstrate the capabilities of our tool, we computed the sensitivity of AMS-02, GAPS and AMS-100 to a dark matter annihilation signal using two different propagation models and two different dark matter models: dark matter annihilating purely into $b\bar{b}$ and the singlet scalar Higgs portal model. We also considered two different assumptions for the total annihilation cross section: the thermal cross section and the annihilation cross section obtained from the antiproton exclusion limit from [151]. For AMS-02, we found that the experiment is sensitive to dark matter annihilating into $b\bar{b}$ for dark matter masses smaller than 20 GeV assuming the antiproton exclusion limit. For the Higgs portal model, we found a second region of sensitivity at around 200 GeV in the INJ.BRK model and above 200 GeV in the DIFF.BRK model. When addressing the potential detection of a few antideuterons by AMS-02, we found that this could only be reproduced for dark matter masses below 10 GeV assuming the thermal cross section. Fortunately, the GAPS experiment shows sensitivity to a dark matter annihilation signal in this mass region as well, allowing for an independent test of AMS-02 results. Although the sensitivity of antideuteron searches in both experiments does not substantially surpass that of current antiproton searches, they offer a vital independent probe due to their notably lower background. Lastly, because of its significantly improved predicted sensitivity,

AMS-100 will be able to test the entire dark matter mass range considered in this work. However, for higher dark matter masses, the sensitivity factor does not represent the sensitivity to dark matter annihilation into antideuterons but rather the sensitivity to the total antideuteron flux as the contribution from secondary antideuterons becomes important.

# Part II

# Phenomenology of Flavored Dark Matter Models

# Chapter 3

# Flavored Majorana Dark Matter

This chapter is based on the work presented in [1]. Here, we discuss the phenomenology of a Majorana dark matter flavor triplet coupled to right-handed up-type quarks in the DMFV framework. We extend the analysis of [41] by focusing on a more general freeze-out mechanism, including conversion-driven freeze-out. In order to study the phenomenology of the model, we perform detailed scans over the parameter space to find viable areas in parameter space that are consistent with the observed dark matter relic abundance and constraints from direct and indirect detection experiments and flavor physics. We further test the allowed parameter regions by reinterpreting LHC searches for dark matter using simplified dark matter models. Lastly, we discuss model-specific signatures that can be used to distinguish the model from a Dirac dark matter model.

My contribution to this project was the implementation of the different freeze-out scenarios together with computing the relevant cross sections and performing the numerical scans to determine the regions in the parameter space that are consistent with the observed dark matter relic density.

## 3.1 Introduction

As discussed in section 1.5, a popular candidate for solving the dark matter problem is the WIMP with a mass in the GeV to TeV range. Despite numerous searches that have been performed to detect WIMPs, no conclusive evidence has been found so far and the parameter space for WIMPs has been significantly constrained. This has led to a shift in focus towards more exotic dark matter candidates with non-standard properties. One such candidate is flavored dark matter which can be realized in the DMFV framework as introduced in section 1.5.2. In this framework, the dark matter particle comes in three different flavors which couple to the SM particles with a flavor-dependent coupling matrix. This flavor structure can lead to a rich phenomenology with implications for dark matter detection experiments, flavor physics and collider searches. Some analyses have already been performed in the literature where the phenomenology of specific realizations of dark matter models in the DMFV framework has been studied (see section 1.5.2 for a complete list).

In the following, we will focus on Majorana dark matter coupling to right-handed up-type quarks where a general analysis has been performed in [41]. Here, we put emphasis on the conversion-driven freeze-out mechanism, which is a novel mechanism for dark matter freeze-out that can be realized in the DMFV framework and has not been studied in the previous analysis. Furthermore, we reinterpret current LHC searches for dark matter in this context.

## 3.2 Model description

In this section, we introduce the model setup for the Majorana dark matter flavor triplet coupled to right-handed up-type quarks and discuss the field content, interactions and the parameterization of the coupling matrix. We will also discuss the resulting mass spectrum of the dark matter particles.

### 3.2.1 Field content and interactions

We introduce a Majorana flavor triplet $\chi = (\chi_1, \chi_2, \chi_3)^T$ that couples to right-handed up-type quarks $u_R$ via a complex scalar mediator $\phi$ with the coupling matrix $\lambda$. The Majorana fermion is a singlet under the SM gauge group but transforms as a triplet under a new approximate flavor symmetry group of the dark sector $\mathrm{O}(3)_\chi$. The mediator $\phi$ carries the same quantum numbers as the up-type quarks $\phi \sim (\mathbf{3}, \mathbf{1}, 2/3)$ where we have used the notation $(\mathrm{SU}(3)_C, \mathrm{SU}(2)_L, \mathrm{U}(1)_Y)$. We stabilize the dark matter triplet by introducing a $\mathbb{Z}_2$ symmetry under which all new fields are odd while all SM particles are even. The Lagrangian of this model is given by

$$\begin{aligned}\mathcal{L} &= \mathcal{L}_{\mathrm{SM}} + \frac{1}{2}\left(i\bar{\chi}\partial\!\!\!/\chi - M_\chi\bar{\chi}\chi\right) - \left(\lambda_{ij}\bar{u}_{Ri}\chi_j\phi + \mathrm{h.c.}\right) \\ &\quad + (D_\mu\phi)^\dagger(D^\mu\phi) - m_\phi^2\phi^\dagger\phi + \lambda_{H\phi}\phi^\dagger\phi H^\dagger H + \lambda_{\phi\phi}\left(\phi^\dagger\phi\right)^2 , \end{aligned} \tag{3.1}$$

where $\chi$ is expressed as a four-component Majorana spinor $\chi = (\chi_L, i\sigma_2\chi_L^*)^T$ and $\chi_L$ is a two-component Weyl spinor. The coupling strength of the Higgs portal coupling is parameterized with $\lambda_{H\phi}$ and the self-interaction of the mediator is given by $\lambda_{\phi\phi}$. In this analysis however, we neglect the impact of $\lambda_{H\phi}$ and $\lambda_{\phi\phi}$ on the dark matter phenomenology. While neglecting $\lambda_{\phi\phi}$ does not have an impact on the analysis, neglecting $\lambda_{H\phi}$ needs a more careful consideration. The Higgs portal coupling influences the effective coupling of the Higgs to gluons and photons through loop processes. However, the impact on the effective coupling is expected to be small for the mediator masses allowed by LHC searches as the contribution from the mediator is suppressed by $m_\phi^2$. In addition, the coupling $\lambda_{H\phi}$ produces a $\bar{\chi}_3\chi_3 h$ coupling between dark matter and the Higgs at one-loop. This has potential implications for direct detection experiments and the relic abundance of dark matter. However, here we want to focus on the impact of the flavor structure on the dark matter phenomenology and therefore neglect the impact of $\lambda_{H\phi}$.

### 3.2.2 Parameterization of the coupling matrix

In the DMFV framework, the coupling matrix $\lambda$ is a generic complex $3 \times 3$ matrix with 9 real parameters and 9 complex phases. Here, we can use the flavor symmetry $\mathrm{O}(3)_\chi$ to simplify the parameterization of the coupling matrix to the physical degrees of freedom. To do this, we can make use of the singular value decomposition and write the coupling matrix as

$$\lambda = U \cdot \mathrm{diag}(D_1, D_2, D_3) \cdot V \,, \tag{3.2}$$

where $U$ and $V$ are unitary matrices and $D_i$ are the positive and real entries of the diagonal matrix. With this ansatz, we introduce more parameters since $U$ and $V$ have 9 free parameters each which leads to 21 free parameters in total. However, we can remove the redundant parameters by using a diagonal rephrasing of $U$ and $V$

$$U' = U \,\mathrm{diag}(e^{i\alpha_1}, e^{i\alpha_2}, e^{i\alpha_3})\,, \tag{3.3}$$
$$V' = \mathrm{diag}(e^{-i\alpha_1}, e^{-i\alpha_2}, e^{-i\alpha_3})\, V\,, \tag{3.4}$$

which removes 3 redundant parameters. We can now remove 3 additional degrees of freedom from $V$ by using the flavor symmetry $\mathrm{O}(3)_\chi$. Using the factorization of [241], we can write $V$ as

$$V = O\, d\, P\,, \tag{3.5}$$

where $O$ and $P$ are orthogonal matrices with 3 real degrees of freedom and $d$ is a diagonal unitary matrix $d = \mathrm{diag}(e^{i\gamma_1}, e^{i\gamma_2}, e^{i\gamma_3})$. Since $\bar{\chi}\chi = i(\chi_L^\dagger \sigma_2 \chi_L^* - \chi_L^T \sigma_2 \chi_L)$ is invariant under orthogonal transformations, we can use the transformation $\chi_L \to P^{-1}\chi_L$ to remove $P$ from the factorization of $V$. This leaves us with the following for the coupling matrix with a total of 15 physical degrees of freedom

$$\lambda = U \,\mathrm{diag}(D_1, D_2, D_3)\, O \,\mathrm{diag}(e^{i\gamma_1}, e^{i\gamma_2}, e^{i\gamma_3})\,. \tag{3.6}$$

For the parameterization of $U$, we choose the same parameterization as in [35, 242]:

$$\begin{aligned} U &= U_{23}\, U_{13}\, U_{12} \\ &= \begin{pmatrix} 1 & 0 & 0 \\ 0 & c_{23}^\theta & s_{23}^\theta e^{-i\delta_{23}} \\ 0 & -s_{23}^\theta e^{i\delta_{23}} & c_{23}^\theta \end{pmatrix} \begin{pmatrix} c_{13}^\theta & 0 & s_{13}^\theta e^{-i\delta_{13}} \\ 0 & 1 & 0 \\ -s_{13}^\theta e^{i\delta_{13}} & 0 & c_{13}^\theta \end{pmatrix} \begin{pmatrix} c_{12}^\theta & s_{12}^\theta e^{-i\delta_{12}} & 0 \\ -s_{12}^\theta e^{i\delta_{12}} & c_{12}^\theta & 0 \\ 0 & 0 & 1 \end{pmatrix}, \end{aligned} \tag{3.7}$$

where $c_{ij}^\theta = \cos(\theta_{ij})$ and $s_{ij}^\theta = \sin(\theta_{ij})$. The angles $\theta_{ij}$ and the phases $\delta_{ij}$ are the only physical degrees of freedom in the parameterization of $U$ as we have already removed three phases with the diagonal rephrasing of eq. (3.3). The orthogonal matrix $O$ is parameterized as

$$O = O_{23}\, O_{13}\, O_{12} = \begin{pmatrix} 1 & 0 & 0 \\ 0 & c_{23}^\phi & s_{23}^\phi \\ 0 & -s_{23}^\phi & c_{23}^\phi \end{pmatrix} \begin{pmatrix} c_{13}^\phi & 0 & s_{13}^\phi \\ 0 & 1 & 0 \\ -s_{13}^\phi & 0 & c_{13}^\phi \end{pmatrix} \begin{pmatrix} c_{12}^\phi & s_{12}^\phi & 0 \\ -s_{12}^\phi & c_{12}^\phi & 0 \\ 0 & 0 & 1 \end{pmatrix}, \tag{3.8}$$

where we have used the notation $c_{ij}^\phi = \cos(\phi_{ij})$ and $s_{ij}^\phi = \sin(\phi_{ij})$ again. Together with the diagonal matrices $D$ and $d$, this gives us the full parameterization of the coupling matrix $\lambda$ with 15 physical degrees of freedom:

$$\theta_{23}, \theta_{13}, \theta_{12}, \phi_{23}, \phi_{13}, \phi_{12}, \delta_{23}, \delta_{13}, \delta_{12}, \gamma_1, \gamma_2, \gamma_3, D_1, D_2, D_3\,. \tag{3.9}$$

In our analysis, we will look at the following ranges for the parameters:

$$\theta_{ij} \in [0, \frac{\pi}{4}], \quad \phi_{ij} \in [0, \frac{\pi}{4}], \quad \delta_{ij} \in [0, 2\pi), \quad \gamma_i \in [0, 2\pi), \quad D_i \in [0, 2]\,. \tag{3.10}$$

We choose the ranges of $\theta_{ij}$ and $\phi_{ij}$ to avoid double counting of the parameter space. The upper limit of $D$ is chosen to guarantee perturbativity.

### 3.2.3 Dark matter mass spectrum

According to the DMFV, the mass term of the dark matter triplet $M_\chi$ can not be a generic $3\times3$ matrix as this would be an additional source of flavor violation. Therefore, we use the spurion expansion of MFV [31] to parameterize the mass matrix in powers of the flavor-violating coupling $\lambda$

$$M_\chi = m_\chi \left[\mathbb{1} + \frac{\eta}{2}(\lambda^\dagger\lambda + \lambda^T\lambda^*) + \mathcal{O}(\lambda^4)\right], \tag{3.11}$$

where $m_\chi$ is the universal mass term and $\eta$ accounts for our ignorance of the ultraviolet completion of the theory. This parameter is expected to be at most of the order one for DMFV if the contribution to the mass matrix arises at tree level [34]. For higher order effects however, $\eta$ is expected to be suppressed by loop factors and is therefore much smaller.

In general, the mass matrix in eq. (3.11) is not diagonal which leads to a misalignment between the mass eigenstates and the flavor eigenstates. Therefore, we can diagonalize $M_\chi$ with an Autonne-Takagi factorization [243, 244] to obtain the mass eigenstates

$$M_\chi = W^T M_\chi^D W\,, \tag{3.12}$$

where $M_\chi^D$ is a diagonal matrix with the mass eigenvalues $m_{\chi_i}$ and $W$ is an orthogonal matrix that diagonalizes $M_\chi$ where we arrange the rows so that $m_{\chi_1} > m_{\chi_2} > m_{\chi_3}$. With this diagonalization, we need to redefine the dark matter fields as $\chi_L \to W\chi_L$ to work in the mass basis. This transforms the coupling matrix $\lambda$ to

$$\tilde{\lambda} = \lambda W^T\,. \tag{3.13}$$

As an analytical expression for $W$ is not possible due to the complexity of the mass corrections, we need to perform a numerical diagonalization of $M_\chi$ to obtain the mass eigenstates. Additionally, we want to ensure that the lightest flavor eigenstate $\chi_3$ is stable and therefore impose the condition $m_{\chi_3} < m_\phi$.

## 3.3 Phenomenology

After having discussed the model setup, we now want to discuss the phenomenology of the model. We will first discuss the dark matter relic density together with the conversion-driven freeze-out mechanism. After that, we discuss constraints from direct and indirect detection experiments and flavor physics. The constraints obtained with collider searches are discussed separately in section 3.5.

### 3.3.1 Dark matter relic density

The relic density of dark matter is measured to be $\Omega_{\rm DM}h^2 = 0.12$ [6] and is determined by the annihilation processes of thermally produced dark matter particles in the early universe. In the standard thermal WIMP scenario with a single dark matter particle, the dark matter relic density is determined using the freeze-out mechanism as described in section 1.3. In our flavored dark matter scenario however, we have introduced a dark matter triplet and a mediator which leads to a more complex freeze-out scenario where coannihilations and conversions between the different dark matter particles and the mediator have to be taken into account. This can be done using different methods depending on the efficiency of the conversions between the different dark matter particles which we will discuss in the following.

**Freeze-out with coannihilations** The calculation of the relic abundance including coannihilations between different dark sector particles has been addressed in [245] for the first time and has been further discussed in [246]. To include the effect of coannihilations, we have to go beyond the standard freeze-out Boltzmann equation as presented in eq. (1.23) and consider a set of coupled Boltzmann equations which trace the abundances all dark sector particles. The Boltzmann equation for the evolution of the number density $n_i$ for any particle $\chi_i$ in the dark sector containing $N$ different particles is generally given by [245]

$$\begin{aligned}\frac{\mathrm{d}n_i}{\mathrm{d}t} =& -3Hn_i - \sum_j^N \langle\sigma_{ij}v_{ij}\rangle(n_i n_j - n_i^{\rm eq}n_j^{\rm eq}) \\ &- \sum_{j\neq i}\Big[\langle\sigma'_{Xij}v_{ij}\rangle(n_i n_X - n_i^{\rm eq}n_X^{\rm eq}) - \langle\sigma'_{Xji}v_{ij}\rangle(n_j n_X - n_j^{\rm eq}n_X^{\rm eq})\Big] \\ &- \sum_{j\neq i}\Big[\Gamma_{ij}(n_i - n_i^{\rm eq}) - \Gamma_{ji}(n_j - n_j^{\rm eq})\Big]\,.\end{aligned} \tag{3.14}$$

Here, the first term on the right-hand side describes the dilution of the number density due to the expansion of the universe with $H$ being the Hubble parameter. The second term describes the coannihilation of particles $\chi_i$ and $\chi_j$ into SM particles with the total annihilation cross section

$$\sigma_{ij} = \sum_X \sigma_{\chi_i\chi_j\to X}\,, \tag{3.15}$$

where we sum over all possible SM final states. The terms in the next line accounts for the conversions between different particles in the dark sector $\chi_i \to \chi_j$ by interacting with SM particles with the total scattering cross section

$$\sigma'_{Xij} = \sum_Y \sigma_{\chi_i X\to\chi_j Y}\,. \tag{3.16}$$

The last term describes the decay of particles $\chi_i$ into other particles in the dark sector and SM particles with the decay rate

$$\Gamma_{ij} = \sum_X \Gamma_{\chi_i\to\chi_j X}\,. \tag{3.17}$$

In our model, the Boltzmann equations include all $\chi_i$ states, as well as the mediator.

To simplify this system of equations, we can make use of the fact that all dark sector particles eventually decay into the stable lightest state with a decay rate that is much faster than the age of the universe. This allows us to describe the final abundance of the lightest state (which in our model we choose to be $\chi_3$) by the sum over all particles in the dark sector with $n = \sum_i^N n_i$. Because in this approach the second and third lines of eq. (3.14) cancel in the sum, we can rewrite the Boltzmann equation as

$$\frac{\mathrm{d}n}{\mathrm{d}t} = -3Hn - \sum_{i,j=1}^{N} \langle \sigma_{ij} v_{ij} \rangle (n_i n_j - n_i^{\mathrm{eq}} n_j^{\mathrm{eq}}) \,. \tag{3.18}$$

If the conversion rate $\Gamma_{\chi_i \to \chi_j} = \sum_X \langle \sigma'_{Xij} v_{ij} \rangle n_X^{\mathrm{eq}}$ between different particles in the dark sector is much faster than the Hubble rate then dark sector particles stay in thermal equilibrium with each other and their ratios are equal to the ratio of their equilibrium values

$$\frac{n_i}{n} = \frac{n_i^{\mathrm{eq}}}{n^{\mathrm{eq}}} \,. \tag{3.19}$$

This assumption is justified in most cases as the conversion rate depends on the background particle densities of SM particles which is much larger than the particle densities of the dark sector particles. This allows us to simplify the Boltzmann equation to

$$\frac{\mathrm{d}n}{\mathrm{d}t} = -3Hn - \langle \sigma_{\mathrm{eff}} v \rangle (n^2 - n_{\mathrm{eq}}^2) \,, \tag{3.20}$$

where the effective annihilation cross section is given by

$$\langle \sigma_{\mathrm{eff}} v \rangle = \sum_{i,j=1}^{N} \langle \sigma_{ij} v_{ij} \rangle \frac{n_i^{\mathrm{eq}}}{n^{\mathrm{eq}}} \frac{n_j^{\mathrm{eq}}}{n^{\mathrm{eq}}} \,. \tag{3.21}$$

The Boltzmann equation can then be reformulated again in terms of the yield $Y$ and the dimensionless quantity $x = m_{\chi_3}/T$ as in section 1.3

$$\frac{\mathrm{d}Y}{\mathrm{d}x} = \frac{1}{Hx} \frac{\mathrm{d}\rho_s}{\mathrm{d}x} \langle \sigma_{\mathrm{eff}} v \rangle \left( Y^2 - Y_{\mathrm{eq}}^2 \right) \,. \tag{3.22}$$

Note that here we have multiple masses $m_i$ of different dark sector particles $\chi_i$, so we choose to parameterize the equation in terms of the lightest mass $m_{\chi_3}$.

Because of the simplifications obtained by assuming that the conversions between different dark sector particles are very efficient, we can use the same formalism as in the standard freeze-out scenario. The only difference is that the effective annihilation cross section is now a sum over all particles in the dark sector. We refer to this scenario as the *canonical freeze-out* scenario and use this formalism to calculate the relic abundance whenever the conversion rate is much faster than the Hubble rate. For the phenomenological scans in this work, we will split this scenario into three sub-scenarios which we will present in section 3.4.1.

However, if the conversions become very inefficient because of very small couplings and the conversion rate is of the same order as the Hubble rate during freeze-out, we have

to solve the full set of coupled Boltzmann equations. This is called conversion-driven freeze-out scenario and has been discussed in [247, 248].

**Conversion-driven freeze-out** In the conversion-driven freeze-out scenario, the assumption that the dark sector particles are in thermal equilibrium is not true anymore and the simplification using eq. (3.19) does not hold. This means that the coupled Boltzmann equations have to be solved for each particle in the dark sector explicitly. In our case, we have to solve the Boltzmann equations for each particle of the Majorana triplet $\chi_i$ and the mediator $\phi$ which are given by

$$\begin{aligned}\frac{\mathrm{d}Y_{\chi_i}}{\mathrm{d}x} = \frac{1}{3H}\frac{\mathrm{d}\rho_s}{\mathrm{d}x}\Bigg[ &\sum_{j=1}^{3}\langle\sigma v\rangle_{\chi_i\chi_j\to qq'}\left(Y_{\chi_i}Y_{\chi_j} - Y_{\chi_i}^{\mathrm{eq}}Y_{\chi_j}^{\mathrm{eq}}\right) + \langle\sigma v\rangle_{\phi\chi_i\to qg}\left(Y_{\chi_i}Y_{\phi} - Y_{\chi_i}^{\mathrm{eq}}Y_{\phi}^{\mathrm{eq}}\right)\\ &+ \frac{1}{\rho_s}\sum_{j\neq i}\left(\Gamma_{\chi_i q\to\chi_j q'} + \widetilde{\Gamma}_{\chi_i\to\chi_j qq'}\right)\left(Y_{\chi_i} - Y_{\chi_j}\frac{Y_{\chi_i}^{\mathrm{eq}}}{Y_{\chi_j}^{\mathrm{eq}}}\right)\\ &- \frac{1}{\rho_s}\left(\widetilde{\Gamma}_{\phi\to\chi_i q} + \Gamma_{\phi g\to\chi_i q} + \Gamma_{\phi q\to\chi_i g}\right)\left(Y_{\phi} - Y_{\chi_i}\frac{Y_{\phi}^{eq}}{Y_{\chi_i}^{eq}}\right)\Bigg]\,,\end{aligned} \tag{3.23}$$

$$\begin{aligned}\frac{\mathrm{d}Y_{\phi}}{\mathrm{d}x} = \frac{1}{3H}\frac{\mathrm{d}\rho_s}{\mathrm{d}x}\Bigg[ &\frac{1}{2}\langle\sigma v\rangle_{\phi\phi\to gg,qq'}\left(Y_{\phi}^2 - Y_{\phi}^{\mathrm{eq}2}\right) + \sum_i\langle\sigma v\rangle_{\phi\chi_i\to qg}\left(Y_{\phi}Y_{\chi_i} - Y_{\phi}^{\mathrm{eq}}Y_{\chi_i}^{\mathrm{eq}}\right)\\ &+ \frac{1}{\rho_s}\sum_{i=1}^{3}\left(\widetilde{\Gamma}_{\phi\to\chi_i q} + \Gamma_{\phi g\to\chi_i q} + \Gamma_{\phi q\to\chi_i g}\right)\left(Y_{\phi} - Y_{\chi_i}\frac{Y_{\phi}^{\mathrm{eq}}}{Y_{\chi_i}^{\mathrm{eq}}}\right)\Bigg]\,.\end{aligned} \tag{3.24}$$

Here, the Boltzmann equations are parameterized in terms of the dark matter mass with $x = m_{\chi_3}/T$ and $Y_\phi$ described the sum of the abundances of the mediator and its antiparticle. The right-hand side of the first lines in both equations describe the coannihilations of the particles with the thermally averaged cross section $\langle\sigma v\rangle_{ij\to kl}$ for the process $ij \to kl$ where $k, l$ can be either right-handed up-type quarks $q$ or gluons $g$. The term $\langle\sigma v\rangle_{\phi\phi\to gg,qq'}$ describes the sum over the cross sections of the processes $\phi\phi^\dagger \to gg$, $\phi\phi^\dagger \to qq'^\dagger$ and $\phi\phi \to qq'$. For each process, we sum over the different quark flavors in the final state.

The remaining terms describe the conversions between different particles in the dark sector through either scattering processes with the rate $\Gamma_{ij\to kl} = \langle\sigma v\rangle_{ij\to kl}\, n_j^{\mathrm{eq}}$ or decays with the thermally averaged decay rate $\widetilde{\Gamma}_{i\to\{k\}} = \Gamma_{i\to\{k\}}K_1(m_i/T)/K_2(m_i/T)$. Here, $K_n$ are the modified Bessel functions of the second kind and order $n$. The equilibrium number density is defined analogously to eq. (1.14) for each species $i$ with internal degrees of freedom $g_i$ and mass $m_i$ as

$$Y_i^{\mathrm{eq}} = \frac{n_i^{\mathrm{eq}}}{\rho_s} = \frac{g_i T m_i^2}{2\pi^2\rho_s}K_2(m_i/T)\,. \tag{3.25}$$

The analytical expressions for the relevant annihilation and conversion processes in this model are presented in appendix B.

Sometimes some particles in the dark sector can still be in thermal equilibrium with each other while others are not. In this case, we can reduce the number of Boltzmann

**Table 3.1:** Scenarios within the conversion-driven freeze-out regime considered in this thesis and their corresponding naming scheme. The upper part of the table collects scenarios where the freeze-out is driven by conversions between different $\chi_i$ states, while the lower part shows scenarios where the freeze-out is driven by conversions between $\chi_i$ and $\phi$. The '$\ll$' symbol used in the mass hierarchy column is used to indicate a sufficient mass splitting to suppress a significant contribution from coannihilation effects. In our analysis, we focus on the three scenarios marked with an asterisk.

| | Name | Mass hierarchy | Weakly coupled | Dominant coupling |
|---|---|---|---|---|
| $\star$ | $\mathrm{C}_\chi 1_u$ | $m_{\chi_3} < m_{\chi_{1,2}} \ll m_\phi$ | $\chi_3$ | $\tilde{\lambda}_{u3}$ |
| | $\mathrm{C}_\chi 1_t$ | $m_{\chi_3} < m_{\chi_{1,2}} \ll m_\phi$ | $\chi_3$ | $\tilde{\lambda}_{t3}$ |
| | $\mathrm{C}_\chi 2_u$ | $m_{\chi_{2,3}} < m_{\chi_1} \ll m_\phi$ | $\chi_2, \chi_3$ | $\tilde{\lambda}_{u3}$ |
| $\star$ | $\mathrm{C}_\phi 1_u$ | $m_{\chi_3} < m_\phi \ll m_{\chi_{1,2}}$ | $\chi_3$ | $\tilde{\lambda}_{u3}$ |
| | $\mathrm{C}_\phi 1_t$ | $m_{\chi_3} < m_\phi \ll m_{\chi_{1,2}}$ | $\chi_3$ | $\tilde{\lambda}_{t3}$ |
| $\star$ | $\mathrm{C}_\phi 2_u$ | $m_{\chi_{2,3}} < m_\phi \ll m_{\chi_1}$ | $\chi_2, \chi_3$ | $\tilde{\lambda}_{u3}$ |

equations that need to be solved by considering the sum over a subset of states among which we can assume chemical equilibrium due to highly efficient conversions. This subset is then described by a single Boltzmann equation with an effective annihilation cross section and an effective conversion rate into each particle that does not belong to this subset. An example for this procedure was presented in [249].

Here, we want to focus on specific scenarios where the conversion-driven freeze-out mechanism is relevant by identifying a dominant coannihilator which can be either the heavier $\chi_i$ states or the mediator $\phi$ and choosing a specific flavor structure. In case the heavier $\chi_i$ states are the dominant coannihilators, the coupling matrix $\tilde{\lambda}$ needs to have a specific hierarchy to meet the conditions for the conversion-driven freeze-out scenario. The coupling of the coannihilating states to the SM particles has to be large while the coupling of $\chi_3$ needs to be very small to ensure that the conversion rate is suppressed. We restrict ourselves to the cases where $\chi_3$ couples predominantly to either the up quark where the coupling strength is of the order of $10^{-6}$ [247] or the top quark where typical couplings are slightly larger [250]. In general, not only $\chi_3$ can have a very small coupling, so we also consider two weakly coupled states.

We classify the scenarios we consider with a naming convention to specify the dominant coannihilator, the number of weakly coupled states and the flavor structure. The naming convention we introduce is as follows: $\mathrm{C}_X n_f$ where $X$ is the dominant coannihilator, $n$ is the number of weakly coupled states and $f$ is the quark flavor to which the weakly coupled states couple predominantly. In table 3.1, we present the different possible scenarios and illustrate the use of this naming convention. We highlight the scenarios where we perform a detailed analysis with an asterisk. Note that the list of scenarios is not exhaustive and other scenarios can be considered as well.

Two examples of the evolution of the abundances of the different particles in the dark sector for the scenarios $\mathrm{C}_\chi 1_u$ (left) and $\mathrm{C}_\phi 1_u$ (right) are shown in fig. 3.1 for randomly chosen parameter points. To calculate the abundance as a function of $x = m_{\chi_3}/T$, we explicitly solve the coupled Boltzmann equations for the different particles as

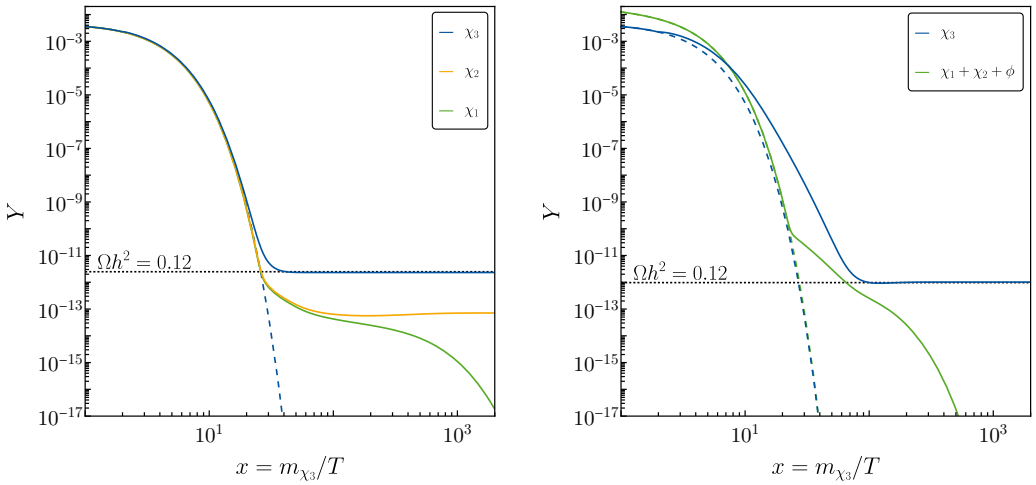


**Figure 3.1:** Example of the evolution of the abundances of different particles in two conversion-driven freeze-out scenarios. The left panel shows the abundances of $\chi_1$, $\chi_2$ and $\chi_3$ in green, yellow and blue respectively in the $C_\chi 1_u$ scenario. The blue dashed line shows the equilibrium abundance of $\chi_3$. The right panel shows the abundance of $\chi_3$ in blue and the sum of the abundances of $\chi_1$, $\chi_2$ and $\phi$ in green in the $C_\phi 1_u$ scenario. The dashed lines represent the corresponding equilibrium abundances.

presented in eq. (3.23) and eq. (3.24). For the $C_\chi 1_u$ scenario, we set the masses to $m_{\chi_1} = 285.3\,\text{GeV}$, $m_{\chi_2} = 279.8\,\text{GeV}$, $m_{\chi_3} = 278.8\,\text{GeV}$, $m_\phi \simeq 570\,\text{GeV}$ and the dark matter coupling to up quarks to $|\tilde{\lambda}_{u3}| = 4.1 \times 10^{-5}$. Because the mediator is much heavier than the $\chi_i$ states, we only solve the evolution of the abundances of the dark matter particles. We show the abundance of $\chi_1$, $\chi_2$ and $\chi_3$ in green, yellow and blue, respectively. The dilution of the abundance is driven by $\chi_1$ annihilations as it has a sizable coupling to the top, $|\tilde{\lambda}_{t1}| = 0.8$. At around $x \simeq 100$, the abundance of $\chi_1$ drops significantly as the particle starts to decay into the lighter $\chi_i$ states. Note that in this example, $\chi_2$ appears to be stable on the considered timescale because of the very small mass splitting to $\chi_3$ and the small coupling. Eventually, the $\chi_2$ particles will decay into $\chi_3$ at a later time.

For the $C_\phi 1_u$ scenario shown on the right, we choose the masses $m_{\chi_3} = 451.1\,\text{GeV}$ and $m_\phi = 462.0\,\text{GeV}$. The masses of the remaining $\chi_i$ states are much heavier and the corresponding couplings large. Therefore, the conversions between the heavier $\chi_i$ states and the mediator are efficient, and we can consider the sum of their abundances shown in green. The coupling of $\chi_3$ to the up quark is set to $|\tilde{\lambda}_{u3}| = 1.4 \times 10^{-7}$. In this scenario, the dark matter abundance shown in blue starts to depart from its equilibrium value already at $x \simeq 3$. At around $x \simeq 100$, the $\chi_3$ abundance starts to become constant as the remaining mediator particles start to decay into $\chi_3$. The evolution is very similar to the one computed in ref. [247] where only one $\chi$ state was considered.

### 3.3.2 Direct detection

As discussed in section 1.4.1, direct detection experiments can set strong constraints on the dark matter parameter space with the strongest constraints coming usually from SI dark matter-nucleon interactions. In our model however, the leading contribution

to the SI cross section corresponding to the interaction types $\bar{\chi}\chi\bar{q}q$ and $(\bar{\chi}\gamma^\mu\chi)(\bar{q}\gamma_\mu q)$ vanish due to the Majorana nature of the dark matter particle and the chiral coupling structure. Therefore, it is necessary to consider subleading contributions to the SI cross section which includes the contribution from loop-induced dark matter-gluon scattering processes as well as considering the SD cross section as well.

A detained analysis of the direct detection constraints in this model has been performed in [41] where the SI and SD dark matter-nucleon interaction cross sections have been computed and data from XENON1T and PICO-60 were used to constrain the model. Here, we want to summarize the outline of the calculation. We then use the results for the cross sections together with the updated limits on the SI and SD cross sections from LZ [80] as shown in fig. 1.9 and fig. 1.10 to constrain the parameter space of the model.

The dark matter-nucleon scattering cross section for the SI ($\sigma^N_{\text{SI}}$) and SD ($\sigma^N_{\text{SD}}$) case are computed with

$$\sigma^N_{\text{SI}} = \frac{4}{\pi}\left(\frac{m_N m_\chi}{m_N + m_\chi}\right)^2 |f_N|^2 \,, \tag{3.26}$$

$$\sigma^N_{\text{SD}} = \frac{3}{16\pi}\left(\frac{m_N m_\chi}{m_N + m_\chi}\right)^2 \left(\sum_{q=u,d,s} \Delta q^N a_q\right)^2 \,, \tag{3.27}$$

where $N = p, n$ denotes the nucleon, $m_N$ is the mass of the nucleon and $m_\chi$ is the mass of the dark matter particle. In the SI case, $f_N$ is the matrix element of the SI quark-nucleon interaction which takes into account the next-to-leading order (NLO) interactions between dark matter and quarks and the loop-induced scattering between gluons and dark matter. For the SD case, the sum over the light quarks is reduced to only one term as $\chi_3$ couples only to up-type quarks in our model. In the remaining term, $\Delta u^N$ describes the spin content of the nucleon in terms of the up quark and $a_u$ is the Wilson coefficient of the SD quark-nucleon interaction which is given by

$$a_u = \frac{|\tilde{\lambda}_{u3}|^2}{m_\phi^2 - (m_\chi + m_u)^2} \,. \tag{3.28}$$

The Feynman diagrams for the tree-level dark matter-quark scattering and the loop-induced dark matter-gluon scattering taken into account here are shown in fig. 3.2. Note that for the SI case, the propagator in the tree-level diagram is expanded to NLO.

In order to compare the direct detection limits from LZ with the theoretical predictions for the SI cross sections, we need to sum over the contributions from the proton and the neutron in the nucleus to obtain the total SI cross section

$$\sigma_{\text{SI}} = \frac{4\mu^2}{\pi A^2} |Z f_p + (A - Z) f_n|^2 \,, \tag{3.29}$$

where $A$ is the atomic mass number of xenon, $Z$ is the atomic number and $\mu$ is the reduced mass of the dark matter particle and the nucleus $\mu = m_N m_\chi/(m_N + m_\chi)$. For the SD cross section, we only use the limits on the SD WIMP-neutron cross section from LZ as it is more constraining than the SD WIMP-proton cross section. Therefore,

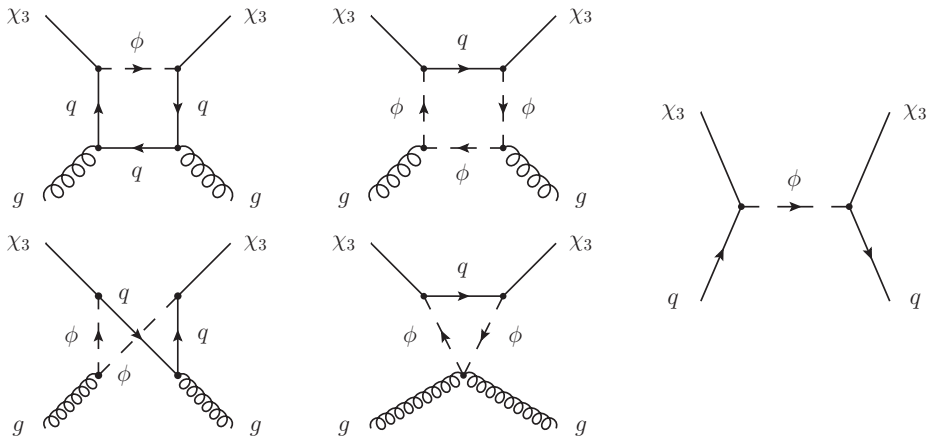


**Figure 3.2:** Feynman diagrams for the loop induced dark matter-gluon scattering processes (left) and the tree-level dark matter-quark scattering processes (right). Diagrams taken from [41].

we use the following SD cross section to compare with the limits from LZ

$$\sigma_{\mathrm{SD}} = \frac{3}{16\pi} \frac{m_n^2 m_\chi^2}{(m_n + m_\chi)^2} \left(\Delta u^n a_u\right)^2 . \tag{3.30}$$

Using these results, we can exclude regions in the parameter space of the model where one or both of the cross sections exceed the limits from LZ.

### 3.3.3 Indirect detection

We improve on the analysis in [41] by additionally including the constraints from indirect detection experiments. The strongest constraints on our model arise from measurements of cosmic-ray antiprotons measured by AMS-02 [251]. Since the s-wave annihilation cross section of the process $\chi_3\chi_3 \to q\bar{q}$ is helicity suppressed, we only take annihilations into $t\bar{t}$ into account. The p-wave annihilation cross section is proportional to $v^2 \sim 10^{-6}$ which is too small to produce a significant signal. Hence, we compute the cross section for the process $\chi_3\chi_3 \to t\bar{t}$ and compare it to the limits obtained in ref. [147] which were obtained by fitting to AMS-02 proton, antiproton and helium data [251–253] together with proton and helium data from CREAM [254] and VOYAGER [255]. We exclude regions in the parameter space where the predicted annihilation cross section exceeds the limits of ref. [147].

### 3.3.4 Flavor constraints

The introduction of a new flavor and CP-violating coupling matrix $\lambda$ in the dark sector can generally lead to large flavor-changing neutral current (FCNC) effects which are strongly constrained by flavor physics observables. Since the dark matter flavor triplet couples to up-type quarks in our model, the most constraining process is the $D^0 - \bar{D}^0$ mixing to which the dark matter particles can contribute at loop level. The contributing processes are shown in fig. 3.3. The diagrams can interfere destructively which allows for a larger viable parameter space. On the other hand, outside the interference region the couplings $D_1$ and $D_2$ of the coupling matrix $\lambda$ are constrained

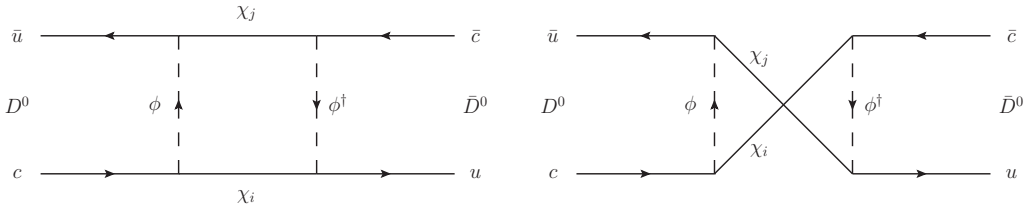


**Figure 3.3:** Feynman diagrams contributing to the $D^0 - \bar{D}^0$ mixing processes. Diagrams taken from [41].

even in the flavor-conserving case where $\theta_{ij} = \phi_{ij} = 0$. These effects have also been discussed in detail in [41]. Here, we summarize and use the results from this work to apply the constraints from the $D^0 - \bar{D}^0$ mixing using the results from the references [61, 256–259] to the parameter space of the model.

To obtain the additional contributions to the $D^0 - \bar{D}^0$ mixing, the authors of [41] have used the formalism of effective Hamiltonians. Using this formalism and neglecting the mass splittings between different $\chi_i$, the authors have computed the off-diagonal element of the $D^0 - \bar{D}^0$ mass matrix from new physics (NP) introduced by our model which is given by

$$M_{12}^{D,\mathrm{NP}} = \frac{\eta_D m_D f_D^2 \hat{B}_D}{384\pi^2 m_\phi^2} \left[ \left(\lambda\lambda^\dagger\right)_{cu}^2 \cdot f(x) - \left(\lambda\lambda^T\right)_{cc} \left(\lambda\lambda^T\right)_{uu}^* \cdot g(x) \right] . \tag{3.31}$$

Here, $\eta_D$ accounts for NLO contributions from the renormalization group running and $m_D$ is the mass of the $D$ meson. $f_D$ and $\hat{B}_D$ are the decay constant and the bag parameter of the $D$ meson respectively which are obtained from lattice QCD. The functions $f(x)$ and $g(x)$ are loop functions which are explicitly given in [41]. Using this, we can compute the NP contribution to the $D^0$ mixing parameter $x_{12}^D$ and the weak phase responsible for CP-violation in the mixing $\phi_{12}^D$:

$$x_{12}^D = 2\tau_{D^0} \left| M_{12}^{D,\mathrm{SM}} + M_{12}^{D,\mathrm{NP}} \right| , \tag{3.32}$$

$$\phi_{12}^D = \arg\left( M_{12}^{D,\mathrm{SM}} + M_{12}^{D,\mathrm{NP}} \right) . \tag{3.33}$$

The parameter $\tau_{D^0}$ is the lifetime of the $D^0$ meson. The numerical values of $x_{12}^D$ and $\phi_{12}^D$ are then compared to the experimental values obtained from the Heavy Flavor Averaging Group (HFLAV) [259] by demanding that their values are within the 95% confidence level interval of the experimental values. The intervals are given by $x_{12}^D = [0.21\%, 0.63\%]$ and $\phi_{12}^D = [-2.8^\circ, 1.7^\circ]$.

## 3.4 Scans and results

In this section, we describe the phenomenological scan we perform to determine the viable parameter space of the model. We will first discuss the scan setups for the different scenarios we consider and then present the combined results from the different constraints.

### 3.4.1 Scan setups

In our scans, we use the constraints from direct detection experiments, indirect searches and flavor observables as described in sections 3.3.2 to 3.3.4, respectively, to determine the viable parameter space of the model. We further compute the relic density in the canonical freeze-out scenario and the conversion-driven freeze-out scenario as described in section 3.3.1. We require that the relic density matches the measured value of $\Omega_{\rm DM}h^2 = 0.12$ [6] within an assumed theoretical uncertainty of 10%. Constraints from collider searches are considered separately in section 3.5.

With these scans, we want to constrain the parameter space of the model which are the 15 parameters that define the coupling matrix $\lambda$ in eq. (3.9), the mass of the mediator $m_\phi$, the mass term of the dark matter particles $m_\chi$ and the parameter $\eta$ from eq. (3.11). In order to specifically target different freeze-out scenarios and flavor structures, we perform different scans with different ranges for the individual parameters and different assumptions on the flavor structure. Within these scenarios, we randomly generate points in the parameter space and use them to compute the dark matter mass matrix as given in eq. (3.11). We then diagonalize the mass matrix to obtain the mass eigenstates and use the transformation matrix to compute the coupling matrix $\tilde{\lambda}$ in the mass basis as in eq. (3.13). Using this, we compute the all relevant observables as described above and apply the constraints to the parameter space. In the following, we present the different scenarios we consider in our scans, as well as the scan ranges for the individual parameters.

**Canonical freeze-out scenario** To be in the canonical freeze-out scenario, we require that the conversion rate between the different dark matter particles is much faster than the Hubble rate during freeze-out. This is the case when the couplings are large enough to keep the dark sector particles in thermal equilibrium with each other. Because of this, we can compute the relic abundance using only one Boltzmann equation as in eq. (3.22). This can be done by using standard tools like MICROMEGAS [260] which is what we use in this work. This is an improvement compared to the work in [41] where the dark matter annihilation rate was computed using the partial wave expansion $\langle\sigma v\rangle = a + b\langle v^2\rangle$ and the result was compared to the value from the literature.

Here, we consider three different canonical freeze-out scenarios for which we will present the results separately. They are defined in the following:

- The **Quasi-Degenerate Freeze-Out (QDF)** scenario, where the mass splittings between $\chi_3$ and the heavier flavors $\chi_{1,2}$

$$\Delta m_{i3} = \frac{m_{\chi_i}}{m_{\chi_3}} - 1 \tag{3.34}$$

  are smaller than 1% such that they can be considered as quasi-degenerate. In this scenario, the decay of the heavier states into the lightest state is kinematically suppressed, and all three flavors contribute to the relic density.

- The **Single Flavor Freeze-Out (SFF)** scenario, where the mass splittings $\Delta m_{i3}$ are larger than 10% such that the heavier states are extremely Boltzmann suppressed and only the lightest state contributes to the relic density. Still, the conversion rate between the different states is large enough to keep them in thermal equilibrium with each other.

- The **Generic Canonical Freeze-Out (GCF)** scenario, where the mass splittings are between 1% and 10%. In this case, the heavier states are still relevant for the relic density but are not as suppressed as in the SFF scenario. This includes all other points that do not fall into the QDF or SFF scenarios.

The first two scenarios have already been considered in [41] with the additional assumptions that the mass corrections of the $\chi_i$ states are always negative ($\eta < 0$) and that the mass splitting of the heaviest state and the mediator is larger than 10%. Here, we relax these assumptions and consider the full parameter space of the model in the GCF scenario.

We perform the scans by randomly sampling the parameters in the scan ranges with their respective priors as shown in table 3.2. After applying the aforementioned constraints, we keep the points that are not excluded until we have gathered $10^4$ points for each scenario. The fraction of points allowed by all constraints is of the order of $10^{-4}$.

**Table 3.2:** Scan ranges and priors for the parameters in the canonical freeze-out scenarios. The priors indicate whether the scan range is sampled linearly (lin) or logarithmically (log). The upper part of the table shows the parameters of the coupling matrix $\tilde{\lambda}$ and the lower part shows the mass parameters.

| **Parameter** | **Range** | **Prior** |
|---|---|---|
| $D_i$ | $[0, 2]$ | lin |
| $\theta_{ij}$ | $[0, \pi/4]$ | lin |
| $\phi_{ij}$ | $[0, \pi/4]$ | lin |
| $\delta_{ij}$ | $[0, 2\pi)$ | lin |
| $\gamma_i$ | $[0, 2\pi)$ | lin |
| $\eta$ | $[-1, -0.01] \cup [0.01, 1]$ | log |
| $m_\chi$ [GeV] | $[100, 2000]$ | lin |
| $m_\phi$ [GeV] | $[m_{\chi_3}, m_{\chi_3} + 2000]$ | lin |

**Conversion-driven freeze-out scenario** For the conversion-driven freeze-out scenario, we define specific scenarios in order to suppress the conversion rate between the different dark matter particles. We consider the scenarios marked with an asterisk in table 3.1 where the freeze-out is driven by conversions between different $\chi_i$ states or between $\chi_i$ and $\phi$. In the $C_\chi 1_u$ scenario, the dominant coannihilators are the heavier $\chi_i$ states and $\chi_3$ couples predominantly to the up quark. In the $C_\phi 1_u$ and $C_\phi 2_u$ scenarios, the freeze-out is driven by conversions between $\chi_i$ and $\phi$ and $\chi_3$ couples again predominantly to the up quark. The difference in these two scenarios is that in the second scenario, we consider two weakly coupled states instead of one.

Here, we focus on scenarios where $\chi_3$ couples to the up quark and not the top quark as the latter scenario is disfavored in the conversion-driven freeze-out regime. This is due to two different reasons: First, the annihilation cross section of a $\chi_i\chi_j$ pair into a fermion is helicity suppressed and therefore the annihilation into top quarks results in the largest cross section. In the conversion-driven freeze-out scenario, the annihilation cross section of the heavier states needs to be sufficiently large which is given, if the

**Table 3.3:** Scan ranges and priors for the parameters in the conversion-driven freeze-out scenarios. The three columns correspond to the scenarios $C_\chi 1_u$, $C_\phi 1_u$ and $C_\phi 2_u$ respectively. The parameters in the upper part of the table define the coupling matrix $\tilde{\lambda}$ and the lower part shows the mass parameters. Note that we have set $\phi_{ij} = 0$ in all cases for simplicity as non-zero values only dilute the splitting between different couplings and do not induce new effects.

| **Parameter** | **Range, prior** | | |
|---|---|---|---|
| | $C_\chi 1_u$ | $C_\phi 1_u$ | $C_\phi 2_u$ |
| $D_1$ | $[10^{-7}, 10^{-5}]$, log | $[10^{-7}, 10^{-5}]$, log | $[10^{-7}, 10^{-5}]$, log |
| $D_2$ | $[0.1, 2]$, lin | $[0.2, 2]$, lin | $[10^{-7}, 10^{-5}]$, log |
| $D_3$ | $[0.1, 2]$, lin | $[0.2, 2]$, lin | $[0.2, 2]$, log |
| $\theta_{12}$ | $[10^{-8}, 10^{-5}]$, log | $[10^{-9}, 10^{-7}]$, log | $[0, \pi/4]$, lin |
| $\theta_{13}$ | $[10^{-8}, 10^{-5}]$, log | $[10^{-9}, 10^{-7}]$ log | $[10^{-10}, 10^{-8}]$, log |
| $\theta_{23}$ | $[0, \pi/4]$, lin | $[0, \pi/4]$, lin | $[10^{-10}, 10^{-8}]$, log |
| $\phi_{ij}$ | 0 | 0 | 0 |
| $\delta_{ij}$ | $[0, 2\pi)$, lin | $[0, 2\pi)$, lin | $[0, 2\pi)$, lin |
| $\gamma_i$ | $[0, 2\pi)$, lin | $[0, 2\pi)$, lin | $[0, 2\pi)$, lin |
| $\eta$ | $[0.005, 0.1]$, lin | $[0.5, 1]$, lin | $[0.5, 1]$, lin |
| $m_\chi$ [GeV] | $[100, 2000]$, lin | $[100, 2000]$, lin | $[100, 2000]$, lin |
| $m_\phi$ [GeV] | $[1.2\, m_{\chi_1}, 3\, m_{\chi_1}]$, lin | $[m_{\chi_3}, 1.1\, m_{\chi_3}]$, lin | $[m_{\chi_2}, 1.1\, m_{\chi_2}]$, lin |

annihilation into top quarks is allowed. This is not the case in the $C_\chi 1_t$ scenario by definition which leads to very few points allowed by the correct relic abundance. The second reason is that in the $C_\phi 1_t$ scenario, the mass splitting between $\chi_3$ and the heavier states needs to be large which is achieved by choosing large couplings for $\chi_1$ and $\chi_2$. This is however disfavored by the constraints from flavor physics if $\chi_1$ and $\chi_2$ couple only to light quarks. Therefore, this leads to very few viable points in this scenario as well.

To find the viable parameter space in the conversion-driven freeze-out scenarios, we proceed differently than in the canonical freeze-out scenarios as in this case, we need to explicitly solve the coupled Boltzmann equations for the different dark matter particles which can not be done with micrOMEGAs. Hence, we use our own code to solve the Boltzmann equations numerically which is computationally more expensive. In addition, there is a complex interplay between the different parameters that makes it non-trivial to satisfy the relic density constraint. Therefore, performing random scans will not be efficient in this case.

To be more efficient, we first perform scans where we randomly sample the parameter space in the ranges given in table 3.3 and then apply the constraints from direct detection, indirect detection and flavor physics. We then use micrOMEGAs to compute the relic density, falsely assuming chemical equilibrium between the different dark matter particles. As inefficient conversion rates only increase the computed relic density using the coupled Boltzmann equations compared to the equilibrium case, we can use the results from micrOMEGAs to identify the regions in the parameter space

where the relic density is too small to obtain potential solutions in the conversion-driven freeze-out scenario. We specifically select the results where the relic density is at least 30% below the measured value. Using these selected points, we then vary for each point the respective weak coupling(s) ($D_1$ in the $C_\chi 1_u$ and $C_\phi 1_u$ scenarios and $D_1, D_2$ in the $C_\phi 2_u$ scenario) and compute the relic abundance using our own code until the measured relic abundance is reached within a 10% theoretical uncertainty. During this process, we keep the remaining parameters fixed. In the $C_\phi 2_u$ scenario, we also keep the ratio of the two weak couplings $D_1/D_2$ fixed, meaning that both couplings are rescaled by the same factor. Note that the scan ranges as given in table 3.3 do not apply during this process.

An example of how this process works is shown in fig. 3.4 for the $C_\chi 1_u$ scenario. On the left, we show the relic density as a function of the coupling $|\tilde{\lambda}_{u3}|$ for a randomly sampled point in the parameter space. The blue line shows the relic density obtained with micrOMEGAs assuming chemical equilibrium which does not change with the coupling. The initially obtained relic density is too low as it lies below the measured value indicated with the cyan dashed line. The cyan band corresponds to the 10% assumed theoretical uncertainty. In red, we show the result obtained by solving the coupled Boltzmann equations, and it shows an increase of the relic density with lower couplings. In our rescaling routine, we then vary the coupling until the relic density matches the measured value within the theoretical uncertainty. Here, this is the case for $|\tilde{\lambda}_{u3}| \approx 4 \times 10^{-5}$. In the right plot, we show the relic abundance of the full set of points for the $C_\chi 1_u$ scenario for the result obtained with micrOMEGAs (blue) and the result obtained by solving the Boltzmann equations after the coupling has been rescaled (red). After the rescaling, we find typical couplings in the range of approximately $10^{-7}$ to $10^{-4}$. For the other two cases, the weak couplings are typically of the order of $10^{-7}$.

### 3.4.2 Combined results

The points in our scan that are still allowed by all considered constraints for the different scenarios in the canonical freeze-out regime are shown in fig. 3.5. In blue, green and yellow we show the points that are allowed in the GCF, QDF and SFF scenarios respectively. As expected, by not restricting ourselves to the QDF and SFF scenarios, we find a larger viable parameter space with respect to the one found in [41]. Specifically, we find more allowed parameter points for smaller mass splittings between the dark matter particle and the mediator $\Delta m_{\phi 3} = (m_\phi - m_{\chi_3})/m_{\chi_3}$ (see upper left panel) and for intermediate mass splittings $\Delta m_{13} = (m_{\chi_1} - m_{\chi_3})/m_{\chi_3}$ (see upper right panel). For these points, coannihilation effects between $\chi_3$ and the heavier states or the mediator become important. However, in the lower left region of the plot showing the mass splitting $\Delta m_{\phi 3}$, we find no viable points. This is due to the effect of $\phi$ pair annihilations diluting the dark matter number density for efficient conversion rates which lowers the relic density below the measured value. This region will therefore become important when considering the conversion-driven freeze-out scenarios. Note that the unpopulated regions in the upper right corners of both panels are due to our chosen scan ranges.

In the lower two panels of fig. 3.5, we show the mass splitting parameter $\eta$ as a function of the coupling $|\tilde{\lambda}_{u3}|$ (left) and $|\tilde{\lambda}_{t3}|$ (right). By construction, the QDF and SFF scenarios are restricted to only negative values of $\eta$ which is why we find no points in the upper regions of both plots. The GCF scenario is not restricted to negative values of $\eta$, and we find a larger viable parameter space in this case where $\chi_3$ can

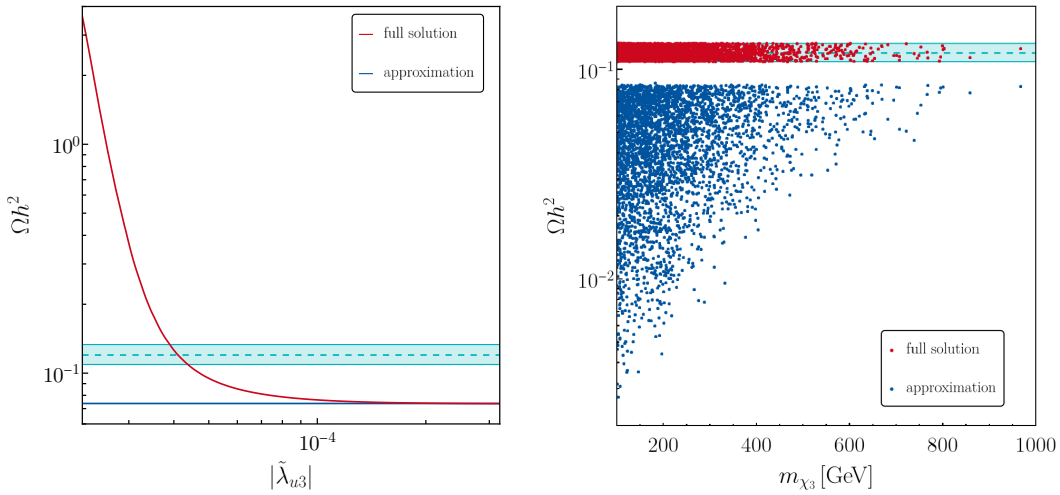


**Figure 3.4:** Example of the rescaling routine for the $C_\chi 1_u$ scenario. The left plot shows the relic density as a function of the coupling $|\tilde{\lambda}_{u3}|$. The blue line shows the relic density obtained with MICROMEGAs assuming chemical equilibrium. The red line shows the result obtained by solving the coupled Boltzmann equations. The cyan line and band show the measured relic density and the 10% theoretical uncertainty respectively. The right plot shows the relic abundance of the full set of points for the $C_\chi 1_u$ scenario obtained with the approximation from MICROMEGAs (blue) and the full solution after the coupling has been rescaled (red).

also have the weakest coupling to the SM. There are also differences in the allowed range for $\eta$ in the QDF and SFF scenarios. In the QDF scenario, the mass splittings between the different dark matter particles are small which requires a small value for $\eta$, unless the couplings are very small. In the SFF scenario, the mass splittings are large which requires larger values of $\eta$ and of the couplings. This is particularly visible in the plot of $|\tilde{\lambda}_{t3}|$ where larger values for the coupling are still allowed. This was also observed in [41], and we can confirm that the SFF scenario is predominantly top-flavored here.

The results for the conversion-driven freeze-out scenarios are shown in fig. 3.6, analogous to the upper panels of fig. 3.5. The points that are allowed in the $C_\chi 1_u$, $C_\phi 1_u$ and $C_\phi 2_u$ scenarios are shown in red, turquoise and purple respectively. For comparison, we show all allowed points of the canonical freeze-out scenarios in gray. We find that in the left plot of fig. 3.6, the $C_\phi 1_u$ and $C_\phi 2_u$ scenarios populate the lower left region where the relic density is too low in the canonical freeze-out scenarios. This result is similar to the one found in ref. [247] where only one Majorana fermion $\chi$ was considered. In contrast to this more minimal model where the regions of the canonical and conversion-driven freeze-out scenarios were sharply separated, we observe an overlap of these regions for our case, specifically towards large $\chi_3$ masses and for the intermediate mass splitting region. This is because of the additional contributions from $t$-channel processes involving $\chi_1$ and/or $\chi_2$ to the $\phi$ pair annihilation cross section which can increase the cross section if the corresponding couplings are large. We also find that the $C_\phi 1_u$ scenario allows for slightly larger mass splittings between $\chi_3$ and the mediator $\phi$ compared to the $C_\phi 2_u$ scenario which can be explained by the following. In the $C_\phi 2_u$ scenario, the number of particles lighter than $\phi$ is doubled. These particles can only deplete through the conversion process into $\phi$ and because

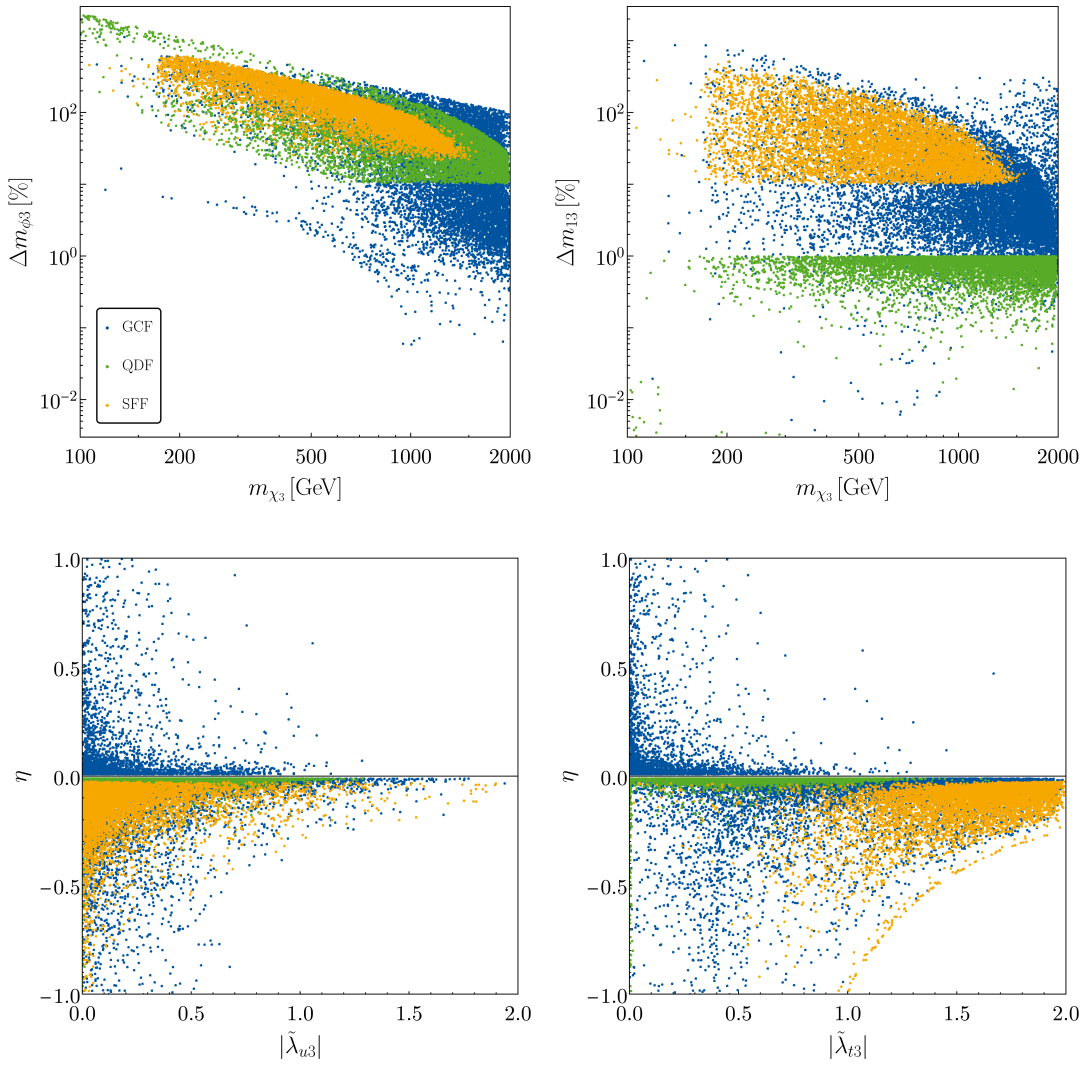


**Figure 3.5:** Viable parameter space in the canonical freeze-out scenarios. The green and yellow points correspond to the QDF and SFF scenarios, respectively. The remaining points belonging to the GCF scenario are shown in blue. The upper left panel shows the mass splitting between $\chi_3$ and the mediator $m_\phi$ and the upper right panel shows the mass splitting between $\chi_3$ and the heaviest state $m_{\chi_1}$ as a function of the dark matter mass $m_{\chi_3}$. The lower panels show the mass splitting parameter $\eta$ as a function of the coupling $|\tilde{\lambda}_{u3}|$ (left) and $|\tilde{\lambda}_{t3}|$ (right).

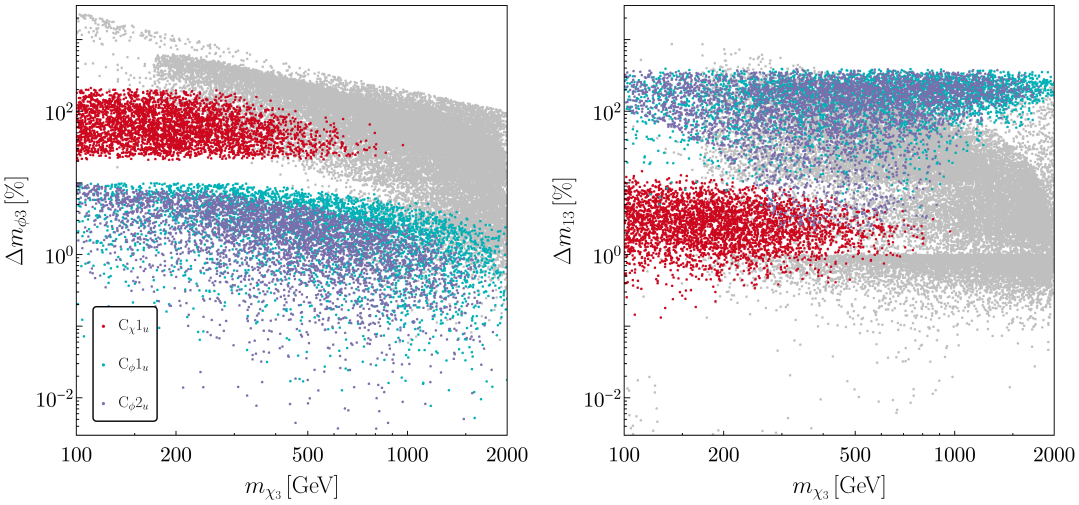


**Figure 3.6:** Same as the upper two panels of fig. 3.5 but for the conversion-driven freeze-out scenarios. The results for the $C_\chi 1_u$, $C_\phi 1_u$ and $C_\phi 2_u$ scenarios are shown in red, turquoise and purple respectively. In order to compare to the canonical freeze-out scenarios, we also show the allowed points of these scenarios in gray.

of that, the rate of depletion is limited to that of $\phi$ pair annihilation. Therefore, the number density of the very weakly interacting sector for a point in the $C_\phi 2_u$ scenario is larger than for a similar point in the $C_\phi 1_u$ scenario where $\chi_2$ is significantly heavier than $\phi$. Hence, a larger $\Delta m_{\phi 3}$ for a given dark matter mass that produces the correct relic abundance in the $C_\phi 1_u$ scenario would overshoot the relic abundance in the $C_\phi 2_u$ scenario as a smaller $\Delta m_{\phi 3}$ is required to effectively enhance the dilution rate in the dark sector.

We now focus on the result for the $C_\chi 1_u$ scenario in fig. 3.6. In this scenario, we require the mass of $\phi$ to be at least 1.2 times the mass of $\chi_1$ to ensure that the dominant contribution to the annihilation rate is from $\chi_1$ and $\chi_2$ annihilations. This is why we find viable parameter points in this scenario only in the upper region of the left plot and all $\Delta m_{13}$ mass splittings shown in the right plot are small. This is also the region where the canonical freeze-out scenario overlaps with the $C_\chi 1_u$ scenario. Small $\Delta m_{13}$ mass splittings are still allowed in the canonical freeze-out scenarios as the $\chi_i$ pair annihilation cross section can become arbitrarily small for small couplings. Additionally, we find that the $C_\chi 1_u$ scenario favors relatively small values for $\eta$. This is because in order to maximize the coannihilation effects, the mass splittings between $\chi_1$ and $\chi_3$ needs to be small. At the same time, the annihilation rate of the heavier $\chi_i$ states must be large and therefore requires large couplings meaning that $\eta$ has to be small to obtain a small mass splitting.

Lastly, we want to comment on two simplifications we have made in our calculation of the relic density. First, we have assumed kinetic equilibrium when solving the Boltzmann equations in eqs. (3.23) and (3.24) which means that we assume that momentum dependence of the distribution functions is proportional to the thermal distribution. In the conversion-driven freeze-out regime, this assumption is not necessarily valid as the couplings needed in this scenario are very small and therefore elastic scattering of dark matter with the thermal bath is not necessarily efficient. However, the authors of [247] have shown that due to the small mass splittings

between the different $\chi_i$ particles, dark matter inherits a (nearly) thermal distribution from the annihilating particle. Therefore, we can justify the use of the integrated Boltzmann equations in this case with corrections smaller than $\sim 10\%$. Second, we have neglected corrections coming from non-relativistic effects of the colored mediator $\phi$, i.e. the Sommerfeld enhancement and bound state formation effects (see ref. [261] for a description of these bound state effects). The latter has been shown to lead to sizable contributions to the annihilation cross section in the conversion-driven freeze-out regime and can therefore significantly increase the viable parameter space [262]. Especially in the $C_\phi 1_u$ and $C_\phi 2_u$ scenarios, the bound state formation effects are expected to extend the viable parameter space towards larger dark matter masses. The study of these effects is however beyond the scope of this work and will be considered in future work.

## 3.5 Collider searches

In this section, we discuss the constraints from LHC searches on the parameter space of the model. As the mediator in our model is colored, we can use the results obtained with $t$-channel simplified models which are already heavily constrained by LHC searches [263]. In order to improve on the analysis done in [41] where a simple recast of the most relevant LHC search for supersymmetric squarks was performed, we include a larger number of searches by using the SModelS tool [264, 265]. Through that, we also identify promising future search strategies for our model at the LHC. In addition, ref. [41] found that the Majorana-specific $t$-channel exchange of the $\chi_i$ states in the pair production of the mediator $uu \to \phi\phi$ significantly contributes to the total cross section. This is strongly enhanced by the up quark parton distribution function for the process. This leads to a significant rate of the same-sign process $pp \to tt + \not{E}_T$ which is not present in the case of Dirac dark matter. As no dedicated search for this signature has been performed yet, we want to discuss other model specific signatures that can be used to distinguish between Majorana and Dirac dark matter.

### 3.5.1 LHC simplified model constraints

To obtain the constraints from LHC searches, we use SModelS [264, 265] which decomposes the results of a large number of LHC searches into simplified models. The tool then uses the simplified models to compute the constraints on the parameter space of a given model. We use SModelS through the interface to MicrOMEGAs to obtain the LHC production cross sections and decay tables and compute the constraints on the parameter space of the different scenarios we considered in section 3.4. The relevant searches that place constraints on our model are listed in table 3.4.

The main results of the SModelS analysis are shown in fig. 3.7. The upper left panel shows the constraints from $\not{E}_T$ searches on the canonical freeze-out scenarios in the $m_\phi$-$m_{\chi_3}$ plane. Here, we do not distinguish between the QDF, SSF and GCF scenarios and show the combined result. All points that are still allowed by all constraints discussed in the previous section, as well as LHC constraints are shown in dark shading. The lighter shaded points are excluded by LHC searches at 95% CL. When comparing our results to the ones found in [41], we find similar constraints for the canonical freeze-out scenarios. Our results also match the ones obtained for the simplified models used in the original interpretation of the $\not{E}_T$ searches by the LHC collaborations for a large fraction of the points in the region extending up to mediator and dark matter

**Table 3.4:** Relevant LHC searches for each scenario identified in our SModelS [264, 265] analysis. The freeze-out scenario is listed in the first column, the search report number in the second, the center-of-mass energy of the LHC run in the third and the relevant signature in the fourth. The signature tops+$\not{E}_T$ refers to the sum of the processes $tt + \not{E}_T$, $t\bar{t} + \not{E}_T$ and $\overline{tt} + \not{E}_T$.

| Scenario | Search | $\sqrt{s}$ | Signatures |
|---|---|---|---|
| Canonic | ATLAS-SUSY-2013-02 [266] | 8 TeV | jets+$\not{E}_T$ |
| | ATLAS-SUSY-2016-07 [267] | 13 TeV | jets+$\not{E}_T$ |
| | ATLAS-SUSY-2016-15 [268] | 13 TeV | tops+$\not{E}_T$ |
| | ATLAS-SUSY-2018-12 [269] | 13 TeV | tops+$\not{E}_T$ |
| | ATLAS-SUSY-2018-22 [270] | 13 TeV | jets+$\not{E}_T$ |
| | CMS-SUS-16-033 [271] | 13 TeV | jets+$\not{E}_T$ |
| | CMS-SUS-16-036 [272] | 13 TeV | jets+$\not{E}_T$ |
| | CMS-SUS-19-006 [273] | 13 TeV | jets+$\not{E}_T$ |
| | CMS-SUS-19-009 [274] | 13 TeV | tops+$\not{E}_T$ |
| | CMS-SUS-20-002 [275] | 13 TeV | tops+$\not{E}_T$ |
| $C_\chi 1_u$ | ATLAS-SUSY-2013-02 [266] | 8 TeV | jets+$\not{E}_T$ |
| | ATLAS-SUSY-2013-21 [276] | 8 TeV | $cc + \not{E}_T$ |
| | ATLAS-SUSY-2014-03 [277] | 8 TeV | $cc + \not{E}_T$ |
| | ATLAS-SUSY-2016-07 [267] | 13 TeV | jets+$\not{E}_T$ |
| | ATLAS-SUSY-2016-15 [268] | 13 TeV | tops+$\not{E}_T$ |
| | ATLAS-SUSY-2016-26 [278] | 13 TeV | $cc + \not{E}_T$ |
| | CMS-SUS-16-033 [271] | 13 TeV | jets+$\not{E}_T$ |
| | CMS-SUS-16-036 [272] | 13 TeV | jets+$\not{E}_T$ |
| | CMS-SUS-16-049 [279] | 13 TeV | tops+$\not{E}_T$ |
| | CMS-SUS-19-006 [273] | 13 TeV | jets+$\not{E}_T$ |
| | CMS-SUS-20-002 [275] | 13 TeV | tops+$\not{E}_T$ |
| $C_\phi 1_u$ | ATLAS-SUSY-2016-32 [280] | 13 TeV | stable R-hadron |
| | CMS-PAS-EXO-16-036 [281] | 13 TeV | stable R-hadron |
| $C_\phi 2_u$ | ATLAS-SUSY-2013-02 [266] | 8 TeV | jets+$\not{E}_T$ |
| | ATLAS-SUSY-2016-32 [280] | 13 TeV | stable R-hadron |
| | CMS-PAS-EXO-16-036 [281] | 13 TeV | stable R-hadron |
| | CMS-SUS-16-032 [282] | 13 TeV | $cc + \not{E}_T$ |
| | CMS-SUS-16-036 [272] | 13 TeV | jets+$\not{E}_T$ |
| | CMS-SUS-16-049 [279] | 13 TeV | tops+$\not{E}_T$ |

masses of $m_\phi \simeq 1200$ GeV and $m_{\chi_3} \simeq 600$ GeV. However, we find several points that are still allowed in the region that is excluded by the simplified models as well as excluded points in the region that is allowed by the simplified models.

For the points that are allowed in the usual excluded region of small dark matter and mediator masses, we find that these points are characterized by a very small mass splitting between the different $\chi_i$ particles. This leads to at least one metastable heavier state which has a lifetime that falls between the prompt and detector stable regime. In this case, it is not clear if the respective $\not{E}_T$ searches are sensitive to these points and thus SModelS conservatively discards them. However, a dedicated reinterpretation for these scenarios could potentially exclude some of these points if the acceptance for non-prompt decays is known.

Now we discuss the excluded points in the region that is usually allowed by the simplified models. These points all have the same characteristic that the production cross section of $\phi$ pairs of the same sign via a $\chi_i$ in the $t$-channel is enhanced. This is because these points have large couplings of the involved $\chi_i$ as well as a large up quark parton density in the relevant momentum range, see as an example [283]. Because of this, a larger amount of pairs of top quarks or jets is produced in the final state because of the subsequent decay of $\phi$. This becomes more relevant for larger dark matter masses as the same-sign pair-production of the mediator is proportional to the Majorana mass $m_{\chi_i}$ which is not the case for opposite-sign pair-production.

To summarize, we still find a large viable parameter space in the canonical freeze-out scenarios that is not excluded by LHC searches or other constraints. In the future, upcoming LHC searches could potentially probe the remaining parameter space because of the large associated production cross sections.

Next, we discuss the constraints from LHC searches on the conversion-driven freeze-out scenarios. The upper right panel of fig. 3.7 shows the constraints on the $C_\phi 1_u$ (turquoise) and $C_\phi 2_u$ (purple) sub-scenarios in the $m_\phi$-$c\tau_\phi$ plane where $\tau_\phi$ is the decay rate of the mediator. Because in these scenarios the mediator can only decay through weak interactions, $\phi$ becomes metastable and therefore the LHC searches for long-lived particles become relevant which is why we chose to show the constraints in this plane. The excluded parameter points are again shown in lighter shading.

We find that typical decay lengths of the mediator are in the range of $c\tau_\phi \sim 10^{-3}$ to $10^1$ m which is consistent with the results for the minimal model considered in [247]. In addition, we also find some points with significantly larger decay lengths which result from extremely small mass splittings between $\chi_3$ and $\phi$. In general, we find larger decay lengths for the $C_\phi 1_u$ scenario compared to the $C_\phi 2_u$ scenario. The constraints on the $C_\phi 1_u$ scenario come exclusively from searches for stable R-hadrons. These searches can place constraints up to mediator masses of $m_\phi \simeq 1.3$ TeV for large decay lengths. On the other hand, the searches become less sensitive for smaller decay lengths because of the suppressed amount of $\phi$ particles traveling through the relevant parts of the detector. Decay lengths smaller than about one meter are therefore not constrained by the current searches. Searches for displaced jets and disappearing tracks could potentially probe this region of the parameter space, however, their applicability to our model is not clear as these searches are not targeted at small mass splittings [284] and therefore not considered by SModelS. The $C_\phi 2_u$ scenario can not only be constrained by stable R-hadron searches but also by missing energy searches as listed in table 3.4.

The last scenario we consider is the $C_\chi 1_u$ scenario which is shown in the lower panel of

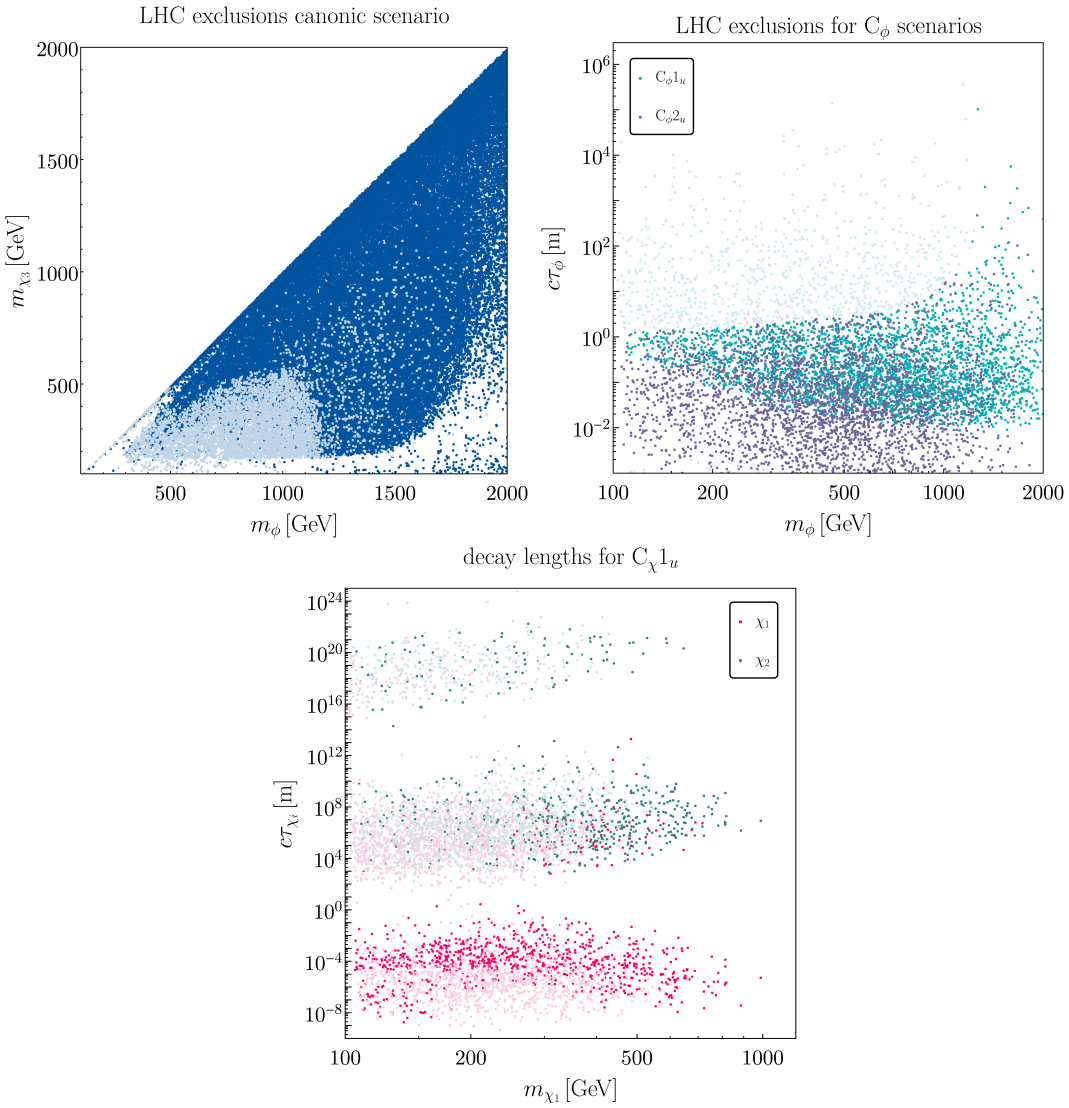


**Figure 3.7:** LHC constraints obtained with SModelS for different freeze-out scenarios. The upper left panel shows the constraints from $\not{E}_T$ searches in the $m_\phi$-$m_{\chi_3}$ plane for the canonical freeze-out scenario. The upper right panel shows the constraints from long-lived particle searches on the $C_\phi 1_u$ (turquoise) and $C_\phi 2_u$ (purple) scenarios in the $m_\phi$-$c\tau_\phi$ plane. The lower panel shows the decay lengths of the $\chi_1$ (pink) and $\chi_2$ (green) particles in the $C_\chi 1_u$ scenario in the $m_{\chi_1}$-$c\tau_{\chi_i}$ plane. In all plots, the darker shaded points are still allowed by all constraints while the lighter shaded points are excluded at 95% CL.

fig. 3.7. Here, we show the decay lengths of the $\chi_1$ (pink) and $\chi_2$ (green) particles in the $m_{\chi_1}$-$c\tau_{\chi_i}$ plane. We find that the $\chi_2$ state is always long-lived with decay lengths bigger than $10^2$ m which is typically longer than the length scale of the detector. The $\chi_1$ state on the other hand can be either (semi-)prompt or long-lived. In contrast to the case of a long-lived mediator however, the existence of a charged track can not be used to constrain this scenario as the $\chi_i$ particles are not charged. In addition to that, displaced vertex searches are not sensitive as the small mass splittings between the different $\chi_i$ particles lead to mostly very soft jets when the $\chi_i$ particles decay. Therefore, this scenario can only be constrained by searches for missing energy that are mostly sensitive to the production of a $\phi$ pair and their subsequent decay into $\chi_1$ and/or $\chi_2$. In the future, new searches for long-lived particles outside the LHC, for example with MATHUSLA [285], could probe the large decay lengths of the $\chi_1$ and $\chi_2$ particles decaying into a quark pair.

In summary, in the conversion-driven freeze-out scenarios we find viable parameter space that is not excluded whenever the mass splitting between the dark matter and the long-lived particle is small as this results in soft decay products which are difficult to test with current searches at the LHC. A new approach with different classes of searches has recently been proposed in [286] to probe the entire range of decay lengths and could potentially be used to probe the remaining parameter space of the conversion-driven freeze-out scenarios.

### 3.5.2 Model-specific signatures

As already discussed in section 3.5.1 and in ref. [41], the cross section for the same-sign production of two mediators $uu \to \phi\phi$ significantly enhances the total cross section for mediator pair production in the Majorana case compared to the Dirac case. This is due to the $t$-channel exchange of the $\chi_i$ states. If the mediator charge is not identified, then this process leads to much stronger exclusion limits for the Majorana case. Dedicated searches for this same-sign signature could however be used to distinguish between Majorana and Dirac flavored dark matter models. The corresponding Dirac case has been studied in [35, 37]. In practice, this distinction exclusively based on the cross section is difficult as the precise measurement of an absolute cross section at a hadron collider is challenging. Additionally, the production of colored particles at the LHC suffers from large higher-order QCD corrections which have not been calculated for our model. Therefore, we propose to look for other model-specific signatures that can be used to distinguish between Majorana and Dirac dark matter. Here, we discuss signatures that rely on both the same-sign production of mediators and the non-trivial flavor structure of the model.

**Same-sign top quark pairs + $\not{E}_T$** The process $uu \to \phi\phi$ can lead to the same-sign signature $tt + \not{E}_T$ in the final state if the mediators both decay into a top and dark matter. The cross section for this process is in the fb range. This process can be distinguished from the more common $t\bar{t} + \not{E}_T$ process by the presence of two positively charged leptons in the final state that are produced in semi-leptonic top decays. Such an analysis has been performed in the context of searches for same-sign tops in CMS in ref. [287]. The authors of this analysis have considered a supersymmetric model with a gluino pair production and subsequent decay into a top or antitop and a stop. The stop then decays into a light quark and a neutralino which leads to the same-sign signatures $ttjj + \not{E}_T$ and $\overline{t}\overline{t}jj + \not{E}_T$. Because in this search a mass splitting between the stop and the neutralino of $\sim 20$ GeV is assumed, the jets in the final state are very

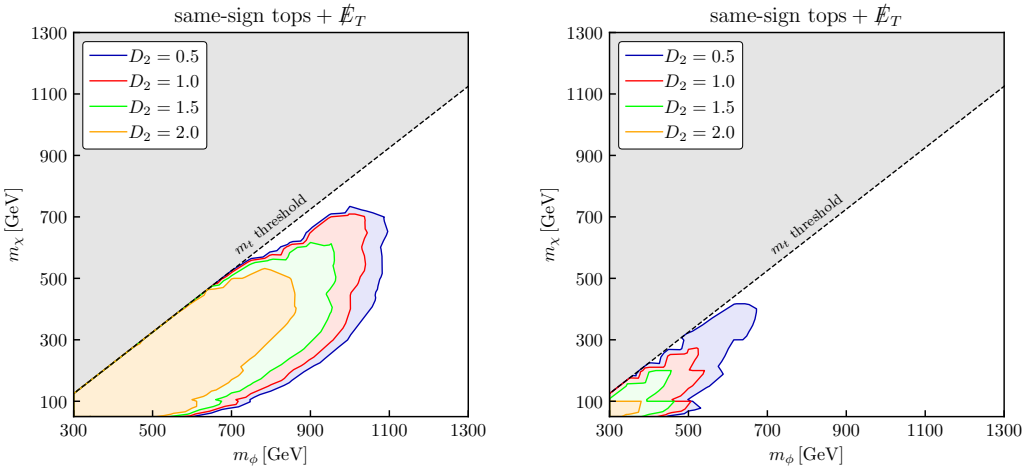


**(a)** $D_1 = D_3 = 2.0$ **(b)** $D_1 = 1$, $D_3 = 2.0$

**Figure 3.8:** Estimated exclusion limits for the mediator and dark matter masses obtained with the same-sign tops + $\not{E}_T$ signature using the CMS analysis in ref. [287]. The results are shown for different values of the coupling $D_1$ where $D_1 = D_3 = 2$ (left) and for $D_1 = 1$ and $D_3 = 2$ (right). The different colors correspond to different values of the $D_2$ coupling. The shaded area under the curves is excluded.

soft. Therefore, in order to estimate the constraints on our model from performing a similar search, we compute the production rates of the signatures $tt + \not{E}_T$ and $\overline{tt} + \not{E}_T$ and disregard the soft jets in the final state. We then use these results and compare them to the upper limits obtained in the CMS analysis in ref. [287]. Also note that in our case the mediator is a scalar and not a fermion as it is the case for the gluino which leads to a different kinematics which arise from the different spin of the mediator. We assume that this will not introduce large differences in the results as we do not expect the efficiency of the search to depend much on the kinematics.

To compute the leading-order cross section for the same-sign final state process, we implement the model in FeynRules [288] to generate a `UFO` file [289], and employ MadGraph5_aMC@NLO [185] to calculate the cross section. For this we assume no flavor- and CP-violation in the model (i.e. $\theta_{ij} = \phi_{ij} = \delta_{ij} = \gamma_i = 0$) since we want to obtain the strongest possible constraints on the model parameters. Allowing for non-vanishing mixing angles would lead to a suppression of the cross section for a flavor-conserving final state as it reduces the branching fraction of such a process. In addition, we assume that the masses of the $\chi_i$ particles are degenerate (i.e. $m_{\chi_i} = m_\chi$) to maximize the cross section. We then place constraints on the remaining parameters which are the three couplings $D_1$, $D_2$ and $D_3$ and the masses of the mediator and dark matter particles.

The results of this analysis are shown in fig. 3.8 where we show the estimated exclusion limits for the mediator and dark matter masses which can be obtained with such a search. We present the results for different values for the coupling $D_2$ indicated by different colors. On the left we set the remaining couplings to $D_1 = D_3 = 2$ and on the right we set $D_1 = 1$ and $D_3 = 2$. We find stronger constraints for $D_1 = D_3 = 2$ as a larger coupling to up quarks ($D_1$) leads to a larger production cross section of a same-sign $\phi\phi$ pair because of the two valence up quarks in the proton. A large

coupling to top quarks ($D_3$) is also required to obtain strong constraints as it results in a large cross section for the decay of the mediator into a top quark and dark matter. Therefore, we also find stronger constraints if the coupling to charm quarks ($D_2$) is suppressed. In the left panel, we find that the strongest constraints reach up to mediator masses of $m_\phi \simeq 1.1$ TeV. In the right panel, we find that the constraints are weaker as the production cross section is suppressed by the smaller coupling $D_1$.

When comparing the constraints obtained in this analysis to the ones obtained with searches for opposite-sign final states with respect to the dark matter mass, we find that the constraints become stronger for larger dark matter masses in the case of same-sign final states while the strongest constraints for opposite-sign final states are obtained for vanishing dark matter masses. This is because of the $t$-channel exchange of two same-sign initial state quarks which is governed by the Majorana mass term that mixes the fields $\chi$ and $\chi^c$. The same-sign final state analysis could therefore exclude dark matter masses up to $m_\chi \simeq 750$ GeV, depending on the couplings and the mediator mass.

When comparing the limits of the same-sign $ttjj + \not{E}_T$ searches to the ones found in ref. [41] using standard supersymmetric squark searches for jets + $\not{E}_T$ and tops + $\not{E}_T$, we find that the constraints are significantly stronger for the squark searches. This is because of the need for two semi-leptonic top decays in the same-sign final state in order to identify the charge of the top quark which suppresses the number of events. Only about 4% of all $tt/\bar{t}\bar{t} + \not{E}_T$ events are expected to have two same-sign leptons in the final state. Therefore, we also investigate the possibility to distinguish between Majorana and Dirac dark matter with single-top final states using the top charge next.

**Single-top charge asymmetry** Another signature that arises in the mediator pair production is the flavor-violating final state $tj + \not{E}_T$ where one mediator decays into $t + \not{E}_T$ and the other into $j + \not{E}_T$. This process has been investigated for the Dirac case in ref. [37] where the authors have shown that the region of testable parameter space is significantly larger for flavor-violating final states compared to the flavor-conserving final states $t\bar{t} + \not{E}_T$ and $jj + \not{E}_T$. It is worth noting that the analysis in [37] is based on a semi-leptonic top decay in the final state which can also be used for charge identification.

The only possible production of a mediator pair in the Dirac case is a pair with opposite sign $\phi^\dagger\phi$. Therefore, the cross sections for top and anti-top final states are equal:

$$\sigma_{\text{Dirac}}(tj + \not{E}_T) = \sigma_{\text{Dirac}}(\bar{t}j + \not{E}_T)\,. \tag{3.35}$$

This is not the case for Majorana dark matter where $\phi\phi$ and $\phi^\dagger\phi^\dagger$ pairs can also be produced. The production of a $\phi\phi$ is significantly enhanced because of the valence up quarks in the proton and therefore the cross section for top production is larger than for anti-top production

$$\sigma_{\text{Majorana}}(tj + \not{E}_T) > \sigma_{\text{Majorana}}(\bar{t}j + \not{E}_T)\,. \tag{3.36}$$

The amount of this enhancement depends on the coupling strength to up quarks as well as the mass of the Majorana dark matter particle. This leads to a charge asymmetry in the final state which we define as

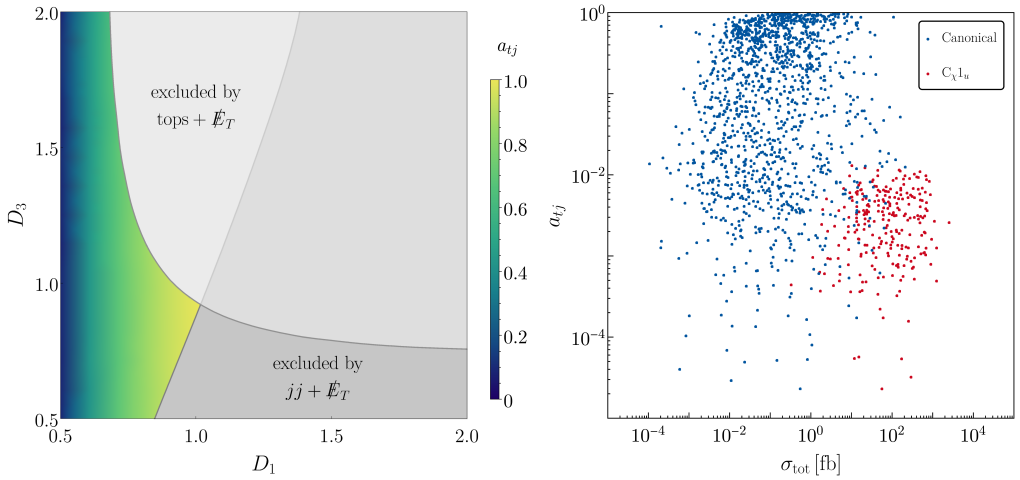


**Figure 3.9:** Prediction for the charge asymmetry $a_{tj}$ in the $tj + \not{E}_T$ final state. The left panel shows the prediction for $a_{tj}$ indicated by the color scale in the $D_1$-$D_3$ plane with $D_2 = 0$, $m_\phi = 1200$ GeV and $m_\chi = 400$ GeV. The light gray region is excluded by tops + $\not{E}_T$ searches and the darker gray region is excluded by jets + $\not{E}_T$ searches. The right panel shows the prediction for $a_{tj}$ depending on the total cross section $\sigma_{\text{tot}} = \sigma(tj + \not{E}_T) + \sigma(\bar{t}j + \not{E}_T)$ for the canonical freeze-out scenario (blue) and the conversion-driven $C_\chi 1_u$ scenario (pink).

$$a_{tj} = \frac{\sigma(tj + \not{E}_T) - \sigma(\bar{t}j + \not{E}_T)}{\sigma(tj + \not{E}_T) + \sigma(\bar{t}j + \not{E}_T)} \,. \tag{3.37}$$

The charge asymmetry $a_{tj}$ is therefore a model-specific signature that can be used to distinguish between Majorana and Dirac dark matter as we expect $a_{tj} > 0$ for Majorana dark matter and $a_{tj} \simeq 0$ for Dirac dark matter[1].

To demonstrate the potential of this signature to distinguish between Majorana and Dirac dark matter in future LHC runs, we compute the $tj + \not{E}_T$ and $\bar{t}j + \not{E}_T$ cross sections using MadGraph5_aMC@NLO and use the result to determine the charge asymmetry $a_{tj}$. Here, we assume a center-of-mass energy of $\sqrt{s} = 14$ TeV. We present the results for the charge asymmetry $a_{tj}$ for Majorana dark matetr in the $D_1$-$D_3$ plane for a benchmark scenario with $D_2 = 0$, $m_\phi = 1200$ GeV and $m_\chi = 400$ GeV in the left panel of fig. 3.9. In gray, we show the regions that are excluded by tops + $\not{E}_T$ searches (light gray) and jets + $\not{E}_T$ searches (darker gray), obtained from the analysis done in ref. [41]. We find that the value of $a_{tj}$ does not depend on the coupling $D_3$ but increases with an increase of the coupling $D_1$. This is expected as a larger coupling to up quarks leads to a larger production cross section of a $\phi\phi$ pair. The charge asymmetry can reach values of $a_{tj} \simeq 1$ for large couplings to up quarks close to the excluded region which makes this signature a promising candidate to test at the LHC.

In the right panel of fig. 3.9, we relate the charge asymmetry $a_{tj}$ to the total cross section $\sigma_{\text{tot}} = \sigma(tj + \not{E}_T) + \sigma(\bar{t}j + \not{E}_T)$ for viable points in the canonical freeze-out scenario (blue points) and the conversion-driven $C_\chi 1_u$ scenario (pink points) that we identified in our scans. In the canonical freeze-out scenario we find values for $a_{tj}$

[1]Note that in the Dirac case, the charge asymmetry is not necessarily exactly zero as processes with the production of a single mediator could contribute to $a_{tj}$. This is however suppressed relative to the production of two mediators and becomes important only for large mediator masses.

of $\mathcal{O}(1)$ for total cross sections up to $\sigma_{\text{tot}} \simeq 100$ fb. This suggests that the charge asymmetry is indeed a promising signature to test. On the other hand, we find that the charge asymmetry is significantly smaller in the conversion-driven scenario with values smaller than $a_{tj} \simeq 10^{-2}$. This is because the production cross section of the $\phi\phi$ pair production is suppressed in this scenario as the coupling to up quarks needs to be small. Here, we do not consider the $\text{C}_\phi$ scenarios as final states with top quarks are kinematically forbidden in these scenarios. Thus, measuring a charge asymmetry larger than zero would strongly constrain the conversion-driven freeze-out scenarios.

## 3.6 Summary

In this chapter, we have discussed the constraints on the Majorana flavored dark matter model in the context of the DMFV framework. This model introduces a new colored scalar mediator and a Majorana flavor triplet that accounts for dark matter and couples to right-handed up-type quarks.

First, we have performed a detailed analysis of the constraints on the model from direct detection, indirect detection, flavor physics and the measured relic abundance. For the latter, we considered the canonical and the conversion-driven freeze-out scenario and performed tailored scans over the 18 free parameters of the model for both scenarios. In all scenarios, we found a large viable parameter space that is not excluded by any of the constraints. More specifically, we found that coannihilation effects between the lightest dark matter triplet state and the heavier ones or the mediator uncovered a large region of parameter space that is not excluded by the relic abundance for mass splittings smaller than about 10 GeV which has not been considered in previous studies. In addition, we found realizations of the conversion-driven freeze-out scenario where dark matter is very weakly coupled and the conversion of dark matter into a coannihilator is semi-efficient. In order to sufficiently dilute the dark matter abundance in this case, a large annihilation cross section of the coannihilator is needed. This is the case for the $\text{C}_\phi 1_u$ and $\text{C}_\phi 2_u$ scenarios where the mediator is the dominant coannihilator. We found a large region of viable parameter space for small mass splittings between the dark matter and the mediator with values smaller than a few percent which is excluded in the canonical freeze-out scenario. Additionally, we found that if $\chi_1$ acts as the dominant coannihilator (scenario $\text{C}_\chi 1_u$), a large coupling of $\chi_1$ to the top is needed as the annihilation cross section of $\chi_1$ is helicity suppressed. Still, we found a large viable parameter space in this scenario that is not excluded by any of the constraints and partly overlaps with the canonical freeze-out scenario.

Next, we have investigated the constraints on the valid parameter space we obtained for the model from LHC searches using SModelS. We found that the canonical freeze-out scenario is mostly constrained by jets + $\not{E}_T$ and tops + $\not{E}_T$ searches which cover a large fraction of the parameter space. However, our model has a more complex phenomenology than the one of simplified models which are used to reinterpret the LHC results. On the one hand, the cross section of same-sign mediator production can be significantly enhanced by a $t$-channel exchange of the $\chi_i$ states which leads to stronger constraints for the Majorana case and excludes some cases with large dark matter and mediator masses. On the other hand, a small mass splitting between the different $\chi_i$ states can lead to metastable $\chi_i$ states which are difficult to test with current $\not{E}_T$ searches and need a dedicated reinterpretation.

For the conversion-driven freeze-out scenarios, searches for long-lived particles become important. The only relevant long-lived particle search that is sensitive in this case

is the search for stable R-hadrons which are formed by pair-produced metastable mediators. These searches can exclude dark matter masses of up to 1.3 TeV in the $C_\phi$ scenarios. Current searches for displaced vertices with hard displaced jets are not sensitive to the small mass splittings in these freeze-out scenarios as they produce very soft jets. Fortunately, conventional $\not{E}_T$ searches can still probe parts of the parameter space in the conversion-driven scenarios, especially in the $C_\chi 1_u$ scenario.

Finally, we have considered two model-specific signatures that can be used to distinguish between Majorana and Dirac dark matter. The first signature is the same-sign production of top quarks in the final state which is enhanced in the Majorana case. To estimate the constraints on the model parameters that can be obtained with this signature, we performed a simplified analysis using the results of a CMS analysis for $ttjj + \not{E}_T$ final states of ref. [287]. We found that the resulting constraints are weaker than for standard jets + $\not{E}_T$ and tops + $\not{E}_T$ searches. This is because of the need for two semi-leptonic top decays in the same-sign final state which suppresses the number of possible events. The second signature is the charge asymmetry $a_{tj}$ in the final state of a single top quark and a jet. A non-zero value of $a_{tj}$ would strongly point towards Majorana dark matter. In parts of the parameter space, we find sizable values of $a_{tj}$ for large single top production cross sections. This signature could therefore be a promising candidate to further investigate at the LHC.

# Chapter 4

# General Framework for Studying Flavored Dark Matter

This chapter is based on work for a publication that is still in preparation. In this chapter, we use the full potential of the DMFV framework and include a variety of possible flavored dark matter models. We consider four different types of dark matter particles (real scalar, complex scalar, Majorana fermion, Dirac fermion) that couple to the SM fermions and discuss their model setups. In order to study the phenomenology of these models, we develop a tool-chain with the ability to calculate constraints from the relic abundance of dark matter, direct and indirect detection experiments, collider searches, and flavor observables for any of the possible flavored dark matter models. To demonstrate the capabilities of the tool-chain, we perform a detailed analysis of the Majorana fermion dark matter model that couples to right-handed SM leptons which has not been studied in the literature yet and discuss the individual constraints on the parameter space of the model.

My contribution to this work was the implementation of all models in FeynRules and the development of the tool-chain to calculate all constraints except for the flavor constraints. Furthermore, I performed the analysis of the Majorana fermion dark matter model that couples to right-handed SM leptons.

## 4.1 Introduction

In the previous chapter, we have discussed the phenomenology of Majorana dark matter coupling to up-type quarks in the context of DMFV. As already mentioned in section 1.5.2, the DMFV scenario is a simple and well-motivated framework which offers a variety of possible flavored dark matter models where the previously considered model is just one example. Therefore, in order to explore the full potential of flavored dark matter, it is necessary to consider other possible models as well. In this chapter, we will discuss different flavored dark matter models and their phenomenology by constructing a general framework that includes a variety of possible models.

## 4.2 Flavored dark matter models

Different flavored dark matter models can be characterized by the type of dark matter particle and the SM fermions it couples to. The dark matter field $\chi$ can be either a real or complex scalar or a Dirac or Majorana fermion. In the DMFV framework, the dark matter candidate will always be part of a flavor triplet $\chi = (\chi_1, \chi_2, \chi_3)^T$ and is a

**Table 4.1:** Possible combinations of dark matter particle type listed in the first column coupling to different SM fermions listed in the first row. The references indicate the models that have been studied in the literature.

| | $u_R$ | $d_R$ | $q_L$ | $e_R$ | $\ell_L$ |
|---|---|---|---|---|---|
| **Real scalar** | – | – | – | – | – |
| **Complex scalar** | – | – | – | [42–44] | [43] |
| **Majorana fermion** | [1, 41] | – | – | – | – |
| **Dirac fermion** | [35–37] | [34, 38] | [37, 39] | [40] | – |

singlet under the SM gauge group $\mathcal{G}_{\text{SM}} = \text{SU}(3)_c \times \text{SU}(2)_L \times \text{U}(1)_Y$. The SM fermions, together with their charge using the short-hand notation $(\text{SU}(3)_c, \text{SU}(2)_L, \text{U}(1)_Y)$, that the dark matter particles can couple to are the following:

- Right-handed up-type quarks $u_R$ with charge $(\mathbf{3}, \mathbf{1}, 2/3)$
- Right-handed down-type quarks $d_R$ with charge $(\mathbf{3}, \mathbf{1}, -1/3)$
- Left-handed quark doublet $q_L$ with charge $(\mathbf{3}, \mathbf{2}, 1/6)$
- Right-handed charged leptons $e_R$ with charge $(\mathbf{1}, \mathbf{1}, -1)$
- Left-handed lepton doublet $\ell_L$ with charge $(\mathbf{1}, \mathbf{2}, -1/2)$

In order to couple to the SM fermions, a mediator particle $\phi$ carrying the same gauge quantum numbers as one of the SM fermions is required. In addition, we introduce a $\mathbb{Z}_2$ symmetry under which the dark matter and mediator fields charged in order to stabilize dark matter[1]. There are three different possibilities for the spin of the mediator particle which can be a complex scalar (spin 0), a vectorlike fermion (spin 1/2) or a complex vector (spin 1). Because considering a complex vector mediator is not straightforward, we will focus on the first two possibilities here. The spin of the mediator particle also determines the spin of the dark matter particle because of Lorentz invariance. This means that if $\phi$ is a complex scalar, then $\chi$ must be a Majorana or Dirac fermion, and if $\phi$ is a vectorlike fermion, then $\chi$ must be a real or complex scalar. Together with the coupling to different SM fermions, this leads to a total of 20 possible flavored dark matter models.

Some of these models have already been studied in the literature (like the one discussed in the previous chapter), while others have not been considered yet. In table 4.1, we summarize the possible combinations of dark matter particle type coupling to different SM fermions and indicate the models that have been studied in the literature. The particle type of dark matter listed in the table also implicitly determines the mediator particle type. Because over half of the possible models have not been studied yet, there is still a lot of unexplored parameter space in the context of flavored dark matter which is why we consider all of the models in this chapter. In order to discuss the details of the different models efficiently, we will consider each dark matter particle type separately in the following.

[1] In case the dark matte flavor triplet is complex and couples to quarks, an additional symmetry is actually not needed as the lightest state is automatically stable, as shown in [34].

### 4.2.1 Real scalar dark matter

In the real scalar dark matter models, we introduce a real scalar dark matter field $\chi$ which is a flavor triplet under the new flavor symmetry group $\mathcal{G}_\chi = \mathrm{O}(3)$ and a mediator $\phi$ which is a Dirac fermion. If $\phi$ couples to the right-handed fermions, then it is a singlet under $\mathrm{SU}(2)_L$. On the other hand, if the mediator couples to the left-handed fermions, then it is a doublet under $\mathrm{SU}(2)_L$ with $\phi = (\phi_0, \phi_1)^T$. The Lagrangian before electroweak symmetry breaking (EWSB) describing all possible interactions of the dark matter flavor triplet with the SM fermions $\psi_{\mathrm{SM}}$ and the mediator is given by

$$\begin{aligned}\mathcal{L} \supset & \frac{1}{2}(\partial_\mu \chi)(\partial^\mu \chi) - \frac{1}{2}\hat{M}_\chi^2 \chi\chi + \bar{\phi}(i\not{D} - m_\phi)\phi + (\lambda_{ij}\bar{\psi}_{\mathrm{SM},i}\phi\chi_j + \mathrm{h.c.}) \\ & + \Lambda_{H\chi,ij}(\chi_i\chi_j)(H^\dagger H) + \Lambda_{\chi\chi,ijkl}\chi_i\chi_j\chi_k\chi_l\,,\end{aligned} \tag{4.1}$$

where $\hat{M}_\chi$ is the mass matrix of the dark matter flavor triplet before EWSB. The complex matrix $\lambda$ describes the coupling of the mediator to the SM fermions and the dark matter flavor triplet. The hermitian coupling matrix $\Lambda_{H\chi}$ describes the interactions of $\chi$ with the Higgs doublet $H$ given by $H = (-i\,G^+, 1/\sqrt{2}\,(v+h+i\,G^0))^T$ after EWSB. The self-interactions of the dark matter flavor triplet are described by the coupling matrix $\Lambda_{\chi\chi}$.

As in the case of Majorana dark matter discussed in section 3.2.2, the coupling matrix $\lambda$ can be parameterized in terms of two diagonal matrices, an orthogonal matrix $O$ given by eq. (3.8) and a unitary matrix $U$ given by eq. (3.7) using the flavor symmetry group O(3):

$$\lambda = U\,\mathrm{diag}(D_1, D_2, D_3)\,O\,\mathrm{diag}(e^{i\gamma_1}, e^{i\gamma_2}, e^{i\gamma_3})\,. \tag{4.2}$$

Therefore, the coupling matrix is described by the same 15 parameters as in the Majorana dark matter case.

According to the DMFV assumption, the coupling matrix $\lambda$ is the only new source of flavor and CP violation in the model. Therefore, we need to parameterize the mass matrix of the real scalar flavor triplet, $\hat{M}_\chi^2$, in terms of $\lambda$ in order to avoid additional sources of flavor and CP violation. This can be done in the most general form by using the spurion ansatz from MFV [31]:

$$\hat{M}_\chi^2 = m_\chi^2 \left[\mathbb{1} + \frac{\eta}{2}(\lambda^\dagger\lambda + \lambda^T\lambda^*) + \mathcal{O}(\lambda^4)\right]. \tag{4.3}$$

Here, $m_\chi$ is the leading order mass parameter, and the $\mathcal{O}(\lambda^2)$ term accounts for the corrections introduced by the effects from the ultraviolet (UV) completion of the model. The parameter $\eta$ accounts for the lack of knowledge about the UV completion of the model.

As it is the case for the previously discussed Majorana dark matter model, it is not guaranteed that the mass matrix $\hat{M}_\chi^2$ is diagonal which leads to a misalignment between the mass and flavor basis of the dark matter flavor triplet. Therefore, we diagonalize the mass matrix by diagonalizing the term $\lambda^\dagger\lambda + \lambda^T\lambda^*$, using an Autonne-Takagi factorization [243, 244]. This results in an expression for the orthogonal matrix $W$

which diagonalizes the $\mathcal{O}(\lambda^2)$ term with $W(\lambda^\dagger\lambda + \lambda^T\lambda^*)W^T$. Using $W$, we can rotate the dark matter flavor triplet $\chi$ to the mass basis with the transformation $\chi \to W\chi$ which transforms the coupling matrix $\lambda$ to

$$\tilde{\lambda} = \lambda W^T \,. \tag{4.4}$$

The diagonalized mass matrix $(\hat{M}_\chi^D)^2$ is then given by

$$(\hat{M}_\chi^D)^2 = \mathrm{diag}(\hat{m}_{\chi_1}^2, \hat{m}_{\chi_2}^2, \hat{m}_{\chi_3}^2) = m_\chi^2 \left[\mathbb{1} + \frac{\eta}{2}(\tilde{\lambda}^\dagger\tilde{\lambda} + \tilde{\lambda}^T\tilde{\lambda}^*) + \mathcal{O}(\tilde{\lambda}^4)\right] . \tag{4.5}$$

Furthermore, we arrange the rows of the orthogonal matrix $W$ in such a way that $\hat{m}_1 > \hat{m}_2 > \hat{m}_3$ which ensures that the mass eigenstates are ordered and $\hat{m}_3$ is the lightest state that forms the dark matter candidate.

Just like the mass matrix, the coupling matrix $\Lambda_{H\chi}$ has to be parameterized in terms of the coupling matrix $\tilde{\lambda}$ in order to avoid additional sources of flavor and CP violation analogous to the mass matrix. Because of the same structure of the mass and Higgs portal coupling matrices in terms of $\tilde{\lambda}$, the matrix $W$ that diagonalizes the mass matrix also diagonalizes the Higgs portal coupling matrix

$$\Lambda_{H\chi}^D = \mathrm{diag}(\lambda_{H\chi_1}, \lambda_{H\chi_2}, \lambda_{H\chi_3}) = \lambda_{H\chi} \left[\mathbb{1} + \frac{\eta_H}{2}(\tilde{\lambda}^\dagger\tilde{\lambda} + \tilde{\lambda}^T\tilde{\lambda}^*) + \mathcal{O}(\tilde{\lambda}^4)\right] . \tag{4.6}$$

Here, $\lambda_{H\chi}$ is a flavor-universal coupling constant, and we account for our ignorance of the UV completion of the theory with $\eta_H$.

Because of the Higgs portal coupling, the dark matter flavor triplet will mix with the Higgs doublet $H$ after EWSB. This mixing leads to a contribution to the dark matter mass term which results in the physical mass eigenstates

$$(M_\chi^D)^2 = \mathrm{diag}(m_{\chi_1}^2, m_{\chi_2}^2, m_{\chi_3}^2) = (\hat{M}_\chi^D)^2 + v^2\Lambda_{H\chi}^D \,, \tag{4.7}$$

where $v$ is the vacuum expectation value of the Higgs. When discussing the phenomenology of the model, we will filter out the points of the parameter space that do not follow the mass hierarchy $m_{\chi_1} > m_{\chi_2} > m_{\chi_3}$ anymore after accounting for the contribution from EWSB. Furthermore, we require the mass of the mediator $m_\phi$ to be larger than the mass of the dark matter candidate $m_{\chi_3}$ in order to avoid dark matter decays into the mediator.

In principle, the dark matter quartic coupling matrix $\Lambda_{\chi\chi}$ can also be parameterized in terms of the coupling matrix $\tilde{\lambda}$ following the DMFV assumption. However, since the dark matter self-interactions are not relevant for the phenomenology of the model, we will set $\Lambda_{\chi\chi,ijkl} = \Lambda_{\chi\chi}\delta_{ijkl}$ for simplicity.

In summary, we are left with the following 21 parameters to describe the real scalar dark matter models:

- 15 parameters to describe the coupling matrix $\lambda$: $\theta_{23}$, $\theta_{13}$, $\theta_{12}$, $\phi_{23}$, $\phi_{13}$, $\phi_{12}$, $\delta_{23}$, $\delta_{13}$, $\delta_{12}$, $\gamma_1$, $\gamma_2$, $\gamma_3$, $D_1$, $D_2$, $D_3$
- 2 parameters to describe the masses of the $\chi_i$: $m_\chi, \eta$

- 2 parameters to describe the Higgs portal coupling matrix $\Lambda_{H\chi}$: $\lambda_{H\chi}, \eta_H$
- 1 parameter to describe the mass of the mediator: $m_\phi$
- 1 parameter to describe the dark matter self-interactions: $\Lambda_{\chi\chi}$

### 4.2.2 Complex scalar dark matter

Some of the complex scalar dark matter models have already been studied in the literature [42–44]. Therefore, we can make use of the model descriptions from these references and extend them to include the other possible models. In the complex scalar dark matter models, we introduce a complex scalar dark matter field $\chi$ which is a flavor triplet under the new flavor symmetry group $\mathcal{G}_\chi = \mathrm{U}(3)$. The mediator $\phi$ is again a Dirac fermion with two possible representations under the $\mathrm{SU}(2)_L$ gauge group depending on whether it couples to the right-handed or left-handed fermions as in the previous case. The Lagrangian before EWSB is very similar to the real scalar dark matter case and is given by

$$\begin{aligned}\mathcal{L} \supset & (\partial_\mu \chi)^\dagger (\partial^\mu \chi) - \hat{M}_\chi^2 \chi^\dagger \chi + \bar{\phi}(i\not{\partial} - m_\phi)\phi + (\lambda_{ij}\bar{\psi}_{\mathrm{SM},i}\phi\chi_j + \mathrm{h.c.}) \\ & + \Lambda_{H\chi,ij}(\chi_i^\dagger \chi_j)(H^\dagger H) + \Lambda_{\chi\chi,ijkl}(\chi_i^\dagger \chi_j)(\chi_k^\dagger \chi_l)\,.\end{aligned} \tag{4.8}$$

The complex matrix $\lambda$ that describes the coupling of the mediator to the SM fermions and the dark matter flavor triplet can be parameterized with two unitary matrices $U$ and $V$ and a diagonal matrix $D = \mathrm{diag}(D_1, D_2, D_3)$ with positive real entries using the singular value decomposition:

$$\lambda = U\,\mathrm{diag}(D_1, D_2, D_3)\,V \tag{4.9}$$

Using that this parameterization is invariant under a diagonal phase transformation of $U$ and $V$, we can remove three complex phases from $U$. Furthermore, we can make use of the flavor symmetry group U(3) to remove the matrix $V$ entirely which is not possible in the real scalar and Majorana dark matter models. This leaves us with

$$\lambda = U\,\mathrm{diag}(D_1, D_2, D_3)\,. \tag{4.10}$$

The matrix $U$ is parameterized in terms of three angles $\theta_{ij}$ and three phases $\phi_{ij}$ with

$$\begin{aligned}U &= U_{23}\,U_{13}\,U_{12} \\ &= \begin{pmatrix}1 & 0 & 0 \\ 0 & c_{23}^\theta & s_{23}^\theta e^{-i\delta_{23}} \\ 0 & -s_{23}^\theta e^{i\delta_{23}} & c_{23}^\theta\end{pmatrix}\begin{pmatrix}c_{13}^\theta & 0 & s_{13}^\theta e^{-i\delta_{13}} \\ 0 & 1 & 0 \\ -s_{13}^\theta e^{i\delta_{13}} & 0 & c_{13}^\theta\end{pmatrix}\begin{pmatrix}c_{12}^\theta & s_{12}^\theta e^{-i\delta_{12}} & 0 \\ -s_{12}^\theta e^{i\delta_{12}} & c_{12}^\theta & 0 \\ 0 & 0 & 1\end{pmatrix},\end{aligned} \tag{4.11}$$

where we use the shorthand notation $c_{ij}^\theta = \cos(\theta_{ij})$ and $s_{ij}^\theta = \sin(\theta_{ij})$. We can therefore describe the coupling matrix $\lambda$ with only 9 physical parameters in contrast to the 15 parameters in the real scalar and Majorana dark matter models. In order to avoid

double-counting in the parameter space, we use the following ranges for the different parameters:

$$\theta_{ij} \in [0, \frac{\pi}{4}], \quad \delta_{ij} \in [0, 2\pi), \quad D_i \in [0, 2]\,. \tag{4.12}$$

The mass matrix $\hat{M}_\chi^2$ in the DMFV framework is again parameterized in terms of the coupling matrix $\lambda$, the flavor-universal mass parameter $m_\chi$ and the expansion parameter $\eta$. Using the DMFV spurion ansatz, we can write the mass matrix as

$$\hat{M}_\chi^2 = m_\chi^2 \left[\mathbb{1} + \eta(\lambda^\dagger\lambda) + \mathcal{O}(\lambda^4)\right] = m_\chi^2 \left[\mathbb{1} + \eta D^2 + \mathcal{O}(D^4)\right]\,. \tag{4.13}$$

Because of the structure of $\lambda$ in this case, the mass matrix $\hat{M}_\chi^2$ is already diagonal and does not require any further diagonalization. Therefore, we can rewrite it in terms of the diagonal matrix $D$. In addition, the second summand in the mass matrix of the real scalar dark matter in eq. (4.3) is absent in the complex scalar dark matter case as it is not required in order to render the mass matrix symmetric.

The next step is again to parameterize the Higgs portal coupling matrix $\Lambda_{H\chi}$ in terms of the coupling matrix $\lambda$, the flavor-universal coupling constant $\lambda_{H\chi}$ and the expansion parameter $\eta_H$. This is done analogously to the mass matrix parameterization and is given by

$$\Lambda_{H\chi} = \lambda_{H\chi} \left[\mathbb{1} + \eta_H(\lambda^\dagger\lambda) + \mathcal{O}(\lambda^4)\right] = \lambda_{H\chi} \left[\mathbb{1} + \eta_H D^2 + \mathcal{O}(D^4)\right]\,. \tag{4.14}$$

Now we can compute the physical mass eigenstates of the dark matter flavor triplet $\chi$ after EWSB by including the contributions that arise from the Higgs portal coupling. Using the expressions for the mass matrix and the Higgs portal coupling matrix in eqs. (4.13) and (4.14), we can express the physical mass eigenstates as

$$\begin{aligned} M_\chi^2 &= \hat{M}_\chi^2 + v^2\Lambda_{H\chi} \\ &= (m_\chi^2 + v^2\lambda_{H\chi}) \left[\mathbb{1} + \left(\eta + \frac{v^2\lambda_{H\chi}(\eta_H - \eta)}{m_\chi^2 + v^2\lambda_{H\chi}}\right) D^2 + \mathcal{O}(D^4)\right]\,. \end{aligned} \tag{4.15}$$

We again order the masses of $M_\chi^2 = \mathrm{diag}(m_{\chi_1}^2, m_{\chi_2}^2, m_{\chi_3}^2)$ in such a way that $m_{\chi_1} > m_{\chi_2} > m_{\chi_3}$. This is done by rearranging the rows of $\lambda$, specifically the order of the $D_i$, such that the mass ordering is fulfilled. Furthermore, we require that the mass of the mediator $m_\phi$ is larger than the mass of the lightest dark matter particle $m_{\chi_3}$.

In analogy to the real scalar dark matter model, we set $\Lambda_{\chi\chi,ijkl} = \Lambda_{\chi\chi}\delta_{ijkl}$ for simplicity as the dark matter self-interactions have no practical relevance for the phenomenology of the model.

All in all, the complex scalar dark matter models are described by the following 15 parameters:

- 9 parameters to describe the coupling matrix $\lambda$: $\theta_{23}$, $\theta_{13}$, $\theta_{12}$, $\delta_{23}$, $\delta_{13}$, $\delta_{12}$, $D_1$, $D_2$, $D_3$
- 2 parameters to describe the masses of the $\chi_i$: $m_\chi, \eta$

- 2 parameters to describe the Higgs portal coupling matrix $\Lambda_{H\chi}$: $\lambda_{H\chi}, \eta_H$
- 1 parameter to describe the mass of the mediator: $m_\phi$
- 1 parameter to describe the dark matter self-interactions: $\Lambda_{\chi\chi}$

### 4.2.3 Majorana fermion dark matter

We have already discussed the Majorana fermion dark matter model where the dark matter flavor triplet couples to up-type quarks in section 3.2.1. In this section, we will extend the model to include the remaining possible interactions with the SM fermions. The Majorana flavor triplet $\chi$ transforms under the fundamental representation of the flavor symmetry group $\mathcal{G}_\chi = \mathrm{O}(3)$ and is given by a four-component Majorana spinor $\chi = (\chi_L, i\sigma_2\chi_L^*)^T$ where $\chi_L$ is a two-component Weyl spinor. The mediator $\phi$ is described by a complex scalar field. Depending on whether the mediator couples to the right-handed or left-handed fermions, the mediator is a singlet or doublet under $\mathrm{SU}(2)_L$. Furthermore, if the mediator couples to the left-handed lepton doublet, then the mediator is parameterized with $\phi = (1/\sqrt{2}(\phi_R + i\phi_I), \phi^+)^T$ as it is the case for scotogenic models [290]. The general Lagrangian before EWSB is given by

$$\begin{aligned}\mathcal{L} \supset & \frac{1}{2}\bar{\chi}(i\partial\!\!\!/ - M_\chi)\chi + (D_\mu\phi)^\dagger(D^\mu\phi) - \hat{m}_\phi^2\phi^\dagger\phi + (\lambda_{ij}\bar{\psi}_{\mathrm{SM},i}\chi_j\phi + \mathrm{h.c.}) + \Lambda_{\phi\phi}(\phi^\dagger\phi)^2 \\ & + \Lambda_{H\phi,1}(\phi^\dagger\phi)(H^\dagger H) + \Lambda_{H\phi,2}(H^\dagger\phi)(\phi^\dagger H) + \frac{1}{2}\Lambda_{H\phi,3}((H_i\varepsilon^{ij}\phi_j)^2 + \mathrm{h.c.})\end{aligned} \tag{4.16}$$

Contrary to the real and complex scalar dark matter models where the dark matter field couples to the Higgs doublet $H$ through the Higgs portal coupling, the Majorana fermion dark matter field does not couple to the Higgs doublet directly. Instead, the mediator $\phi$ couples to the Higgs which is parameterized by the $\Lambda_{H\phi}$ terms. Therefore, the mass term $\hat{m}_\phi$ will receive a contribution after EWSB from the Higgs coupling. Not all terms in the Lagrangian that describe the interactions with the Higgs are present in all Majorana dark matter models. The term $\Lambda_{H\phi,2}(H^\dagger\phi)(\phi^\dagger H)$ only exists if the mediator couples to left-handed SM fields. Furthermore, the $\Lambda_{H\phi,3}/2((H_i\varepsilon^{ij}\phi_j) + \mathrm{h.c.})$ term only exists if the mediator couples specifically to left-handed leptons.

The parameterization of the coupling matrix $\lambda$ and the dark matter mass matrix has been discussed in detail in sections 3.2.2 and 3.2.3. Therefore, we will only summarize the result here. The coupling matrix $\lambda$ is parameterized in terms of two diagonal matrices $D$ and $d$, an orthogonal matrix $O$ (see eq. (3.8)) and a unitary matrix $U$ (see eq. (3.7)) using the flavor symmetry group O(3):

$$\lambda = U\,\mathrm{diag}(D_1, D_2, D_3)\,O\,\mathrm{diag}(d_1, d_2, d_3)\,. \tag{4.17}$$

The coupling matrix is fully described by the 15 parameters given in eq. (3.9). The mass matrix $M_\chi$ is parameterized in terms of the coupling matrix $\lambda$ using the DMFV spurion ansatz with

$$M_\chi = m_\chi\left[\mathbb{1} + \frac{\eta}{2}(\lambda^\dagger\lambda + \lambda^T\lambda^*) + \mathcal{O}(\lambda^4)\right]. \tag{4.18}$$

In order to diagonalize the mass matrix, we use the Autonne-Takagi factorization to find the orthogonal matrix $W$ that diagonalizes the matrix $M_\chi = W^T M_\chi^D W$. The diagonalized mass matrix $(M_\chi^D) = \mathrm{diag}(m_{\chi_1}, m_{\chi_2}, m_{\chi_3})$ is ordered in such a way that $m_{\chi_1} > m_{\chi_2} > m_{\chi_3}$. This diagonalization transforms the coupling matrix $\lambda$ to $\tilde{\lambda} = \lambda W^T$.

In contrast to the model we studied in chapter 3 where we have neglected the interactions of the mediator with the Higgs doublet, we will include these interactions in the general Majorana fermion dark matter models. The charge of the mediator under the SM gauge group $\mathcal{G}_{\mathrm{SM}}$ determines the possible interactions with the Higgs doublet and therefore the correction to the mass term after EWSB. If the mediator is a singlet under $\mathrm{SU}(2)_L$, then the mediator only couples to the Higgs doublet through the $\Lambda_{H\phi,1}(\phi^\dagger\phi)(H^\dagger H)$ term. This leads to a physical mass of the mediator after EWSB given by

$$m_\phi^2 = \hat{m}_\phi^2 + \frac{v^2}{2}\Lambda_{H\phi,1}\,. \tag{4.19}$$

If the mediator is a doublet under $\mathrm{SU}(2)_L$ and couples to the left-handed quark doublet, then the mediator also couples to the Higgs doublet through the $\Lambda_{H\phi,2}(H^\dagger\phi)(\phi^\dagger H)$ term. The fields in the mediator doublet $\phi = (\phi_u, \phi_d)^T$ will receive different contributions to their masses after EWSB. The physical masses of the mediator fields are given by

$$m_{\phi_u}^2 = \hat{m}_\phi^2 + \frac{v^2}{2}\Lambda_{H\phi,1}\,, \quad m_{\phi_d}^2 = \hat{m}_\phi^2 + \frac{v^2}{2}(\Lambda_{H\phi,1} + \Lambda_{H\phi,2})\,. \tag{4.20}$$

Lastly, if the mediator is a doublet under $\mathrm{SU}(2)_L$ and couples to the left-handed lepton doublet, then we parameterize the mediator as $\phi = (1/\sqrt{2}(\phi_R + i\phi_I), \phi^+)^T$ where we decomposed the neutral component of the doublet into its real and imaginary parts $\phi_R$ and $\phi_I$ as it is done in scotogenic models. Additionally, we include the $\Lambda_{H\phi,3}/2((H_i\varepsilon^{ij}\phi_j) + \mathrm{h.c.})$ term in the Lagrangian as another possible interaction of the mediator with the Higgs doublet. The masses of the physical neutral scalar bosons are given by

$$m_{\phi_R}^2 = \hat{m}_\phi^2 + \frac{v^2}{2}(\Lambda_{H\phi,1} + \Lambda_{H\phi,3})\,, \quad m_{\phi_I}^2 = \hat{m}_\phi^2 + \frac{v^2}{2}(\Lambda_{H\phi,1} - \Lambda_{H\phi,3})\,, \tag{4.21}$$

and the mass of the charged scalar boson is given by

$$m_{\phi^+}^2 = \hat{m}_\phi^2 + \frac{v^2}{2}(\Lambda_{H\phi,1} + \Lambda_{H\phi,2})\,. \tag{4.22}$$

In a nutshell, the Majorana fermion dark matter models are described by 20 parameters for all models with the mediator coupling to the right-handed fermions, 21 parameters in case the mediator couples to the left-handed quarks and 22 parameters if the mediator couples to the left-handed leptons:

- 15 parameters to describe the coupling matrix $\lambda$: $\theta_{23}$, $\theta_{13}$, $\theta_{12}$, $\phi_{23}$, $\phi_{13}$, $\phi_{12}$, $\delta_{23}$, $\delta_{13}$, $\delta_{12}$, $\gamma_1$, $\gamma_2$, $\gamma_3$, $D_1$, $D_2$, $D_3$
- 2 parameters to describe the masses of the $\chi_i$: $m_\chi, \eta$
- 1 parameter to describe the mass term of the mediator before EWSB: $\hat{m}_\phi$

- 1 parameter to describe the mediator self-interactions: $\Lambda_{\phi\phi}$
- 1 parameter to describe the mediator coupling to the Higgs doublet: $\Lambda_{H\phi,1}$
- 1 parameter to describe the mediator doublet coupling to the Higgs doublet: $\Lambda_{H\phi,2}$ (only if the mediator couples to left-handed fermions)
- 1 parameter to describe the mediator doublet coupling to the Higgs doublet: $\Lambda_{H\phi,3}$ (only if the mediator couples to left-handed leptons)

### 4.2.4 Dirac fermion dark matter

The Dirac fermion dark matter models have been studied the most in the literature [34–40] with the only exception being the models with coupling to the left-handed lepton doublet. Therefore, we can relate the models that have already been studied to the general framework we are discussing here and introduce a Dirac fermion dark matter flavor triplet transforming under the new flavor symmetry group $\mathcal{G}_\chi = \mathrm{U}(3)$. The scalar mediator $\phi$ can be described analogously to the Majorana fermion dark matter models depending on whether the mediator couples to the right-handed or left-handed fermions. The Lagrangian closely resembles the one of the Majorana fermion dark matter models and is given by

$$\begin{aligned}\mathcal{L} \supset & \bar{\chi}(i\partial\!\!\!/ - M_\chi)\chi + (D_\mu\phi)^\dagger(D^\mu\phi) - \hat{m}_\phi^2\phi^\dagger\phi + (\lambda_{ij}\bar{\psi}_{\mathrm{SM},i}\chi_j\phi + \mathrm{h.c.}) + \Lambda_{\phi\phi}(\phi^\dagger\phi)^2 \\ & + \Lambda_{H\phi,1}(\phi^\dagger\phi)(H^\dagger H) + \Lambda_{H\phi,2}(H^\dagger\phi)(\phi^\dagger H) + \frac{1}{2}\Lambda_{H\phi,3}((H_i\varepsilon^{ij}\phi_j)^2 + \mathrm{h.c.})\,.\end{aligned} \tag{4.23}$$

As in the case of Majorana fermion dark matter, the term $\Lambda_{H\phi,2}(H^\dagger\phi)(\phi^\dagger H)$ only exists if the mediator couples to left-handed SM fields and the $\Lambda_{H\phi,3}/2((H_i\varepsilon^{ij}\phi_j)+\mathrm{h.c.})$ term only exists if the mediator couples to left-handed leptons.

Because of the U(3) flavor symmetry group, we can parameterize the coupling matrix $\lambda$ analogously to the complex scalar dark matter models with

$$\lambda = U\,\mathrm{diag}(D_1, D_2, D_3)\,, \tag{4.24}$$

where $U$ is given by eq. (4.11). We can then use the same expression for the mass matrix $M_\chi$ as in the complex scalar dark matter models in eq. (4.13) to describe the mass matrix of the Dirac fermion dark matter flavor triplet

$$M_\chi = \mathrm{diag}(m_{\chi_1}, m_{\chi_2}, m_{\chi_3}) = m_\chi\left[\mathbb{1} + \eta D^2 + \mathcal{O}(D^4)\right]\,, \tag{4.25}$$

using again, that the mass matrix is already diagonal when expressed in terms of $\lambda$. In order to assign the lightest dark matter particle, we order the masses of the dark matter flavor triplet in such a way that $m_{\chi_1} > m_{\chi_2} > m_{\chi_3}$ as in all other models by rearranging the rows of $\lambda$.

The coupling of the mediator to the Higgs doublet is completely analogous to the Majorana fermion dark matter models. The masses of the mediator are given by eq. (4.19) if the mediator is a singlet under $\mathrm{SU}(2)_L$, by eq. (4.20) if the mediator is charged with $(\mathbf{3}, \mathbf{2}, 1/6)$ under the SM gauge group, and by eqs. (4.21) and (4.22) if

the mediator is charged with $(\mathbf{1}, \mathbf{2}, -1/2)$. This leaves us with 14 parameters in total to describe the model for the first case, 15 parameters for the second case, and 16 parameters for the third case:

- 9 parameters to describe the coupling matrix $\lambda$: $\theta_{23}$, $\theta_{13}$, $\theta_{12}$, $\delta_{23}$, $\delta_{13}$, $\delta_{12}$, $D_1$, $D_2$, $D_3$
- 2 parameters to describe the masses of the $\chi_i$: $m_\chi, \eta$
- 1 parameter to describe the mass term of the mediator before EWSB: $\hat{m}_\phi$
- 1 parameter to describe the mediator self-interactions: $\Lambda_{\phi\phi}$
- 1 parameter to describe the mediator coupling to the Higgs doublet: $\Lambda_{H\phi,1}$
- 1 parameter to describe the mediator doublet coupling to the Higgs doublet: $\Lambda_{H\phi,2}$ (only if the mediator couples to left-handed fermions)
- 1 parameter to describe the mediator doublet coupling to the Higgs doublet: $\Lambda_{H\phi,3}$ (only if the mediator couples to left-handed leptons)

## 4.3 Flavored dark matter phenomenology

All flavored dark matter models can be and partially have been strongly constrained by various experimental data. In this section, we will discuss the different constraints that apply to the models we have introduced in the previous section. We will focus on the constraints that arise from the relic density, direct and indirect detection, collider experiments, and flavor physics.

In order to efficiently study the phenomenology of the models, we develop a tool-chain that allows us to easily generate the model files for the different models and calculate the constraints. To do this, we first implement all models in the MATHEMATICA-based package FEYNRULES [288] by including the description of all new fields and the Lagrangian that describes the possible interactions of the model. This allows us to generate the `CalcHEP` model files [291] which are needed by MICROMEGAS [260]. The tool is used to calculate the relic density of the dark matter particle and the direct and indirect detection cross sections, as well as provides a link to SMODELS [264, 265, 292] which is used to calculate the collider constraints. In order to automate the computation of the flavor physics constraints, we use the MATHEMATICA package MATCHETE [293] to compute matching of the flavored dark matter model to the Standard Model Effective Field Theory (SMEFT) [294] and the SMELLI tool [295] to calculate the likelihood of the model based on the Wilson coefficients of the EFT given the data from flavor observables. In the following, we will discuss the different constraints in more detail.

### 4.3.1 Relic density

In all our models we assume that the dark matter particle is a thermal relic and that the relic abundance is determined by the freeze-out mechanism. The relic density of the dark matter particle then needs to be in agreement with the measured value of $\Omega h^2 = 0.12$ by the PLANCK satellite [6].

The approach of most references mentioned in table 4.1 to analyze the phenomenology of the freeze-out of the dark matter particles was to assume some simplification for the model i.e. neglecting the mass splittings between the different dark matter particles or assuming that the heavier dark matter mass states are much heavier than the lightest one. It was then assumed that the correct relic density is obtained when the thermally averaged dark matter annihilation cross section is equal to the one required to obtain the measured relic density through a single particle freeze-out which is given by $\langle \sigma v \rangle = 2.2 \times 10^{-26}\,\mathrm{cm}^3/\mathrm{s}$ [296]. This approach does not take into account the full model by considering the mass splittings between the different dark matter masses and the possible co-annihilation processes that can occur in the models.

Therefore, in order to take all possible effects into account, here we will use the full model to calculate the relic density directly by solving the Boltzmann equation instead of just computing the annihilation cross section. This is done by using the micrOMEGAs tool which automatically solves the Boltzmann equation numerically. This also includes coannihilation effects between the different particles. The relic density is then compared to the measured value and the points in the parameter space that are not within a 10% range of the measured value are excluded. This analysis is more accurate than the one done in the previous references and allows us to study the phenomenology of the models more precisely. Compared to our analysis in chapter 3, we will not consider the conversion-driven freeze-out mechanism and only focus on the canonical freeze-out scenario.

### 4.3.2 Direct detection

The direct detection of dark matter particles is done by detecting the effects of the dark matter particle scattering off a nucleus in a detector, as discussed in section 1.4.1. The constraints on the scattering cross section of the dark matter particle with a nucleus are given in terms of the SI and SD cross sections. Because the dark matter particle needs to interact with the nucleus, the constraints on the parameter space of dark matter models that couple to the quarks are stronger than for the models that couple to the leptons as there is no direct tree-level coupling to the nucleus for the latter. The only possible interaction for lepton-flavored dark matter models is through loop-induced interactions with the nucleon through a photon or $Z$ boson exchange.

We compute the SI and SD cross sections for interactions with the proton and the neutron in the nucleus using micrOMEGAs and use its built-in routine to exclude points in the parameter space that are not within the 90% exclusion limits of the cross sections obtained with experimental data. The experiments together with their limits considered in the analysis are LZ [80], XENON1T [297, 298], DarkSide-50 [72] PandaX-4t [81], PICO-60 [78], and CRESST-III [76].

### 4.3.3 Indirect detection

Constraints from indirect detection experiments are not as strong as the other constraints discussed in this section but are still relevant for the phenomenology of the models. Model independent constraints are usually given in terms of the thermally averaged annihilation cross section $\langle \sigma v \rangle$ of the dark matter particle annihilating into a particle-antiparticle pair of a specific SM particle and are obtained using data from $\gamma$-ray, $\bar{p}$, $e^+$, and neutrino experiments that measure the flux of these particles as discussed in section 1.4.3. We use the following references with constraints on the

annihilation cross section of possible annihilation channels using mostly the constraints published by the respective collaborations of the experiment:

- $\boldsymbol{b\bar{b}}$: [150] using $\bar{p}$ data, [299] using $\gamma$-ray data
- $\boldsymbol{c\bar{c}}$: [300] using $\gamma$-ray data
- $\boldsymbol{e^+e^-}$: [300, 301] using $\gamma$-ray data, [302] using $e^+$ data
- $\boldsymbol{hh}$: [150] using $\bar{p}$ data
- $\boldsymbol{\mu^+\mu^-}$: [5] using $\gamma$-ray and neutrino data, [302] using $e^+$ data
- $\boldsymbol{\nu\bar{\nu}}$ (not flavor-specific): [303, 304] using neutrino data
- $\boldsymbol{q\bar{q}}$ (includes $u$, $d$, $s$ quarks): [150] using $\bar{p}$ data
- $\boldsymbol{t\bar{t}}$: [300, 305] using $\gamma$-ray data
- $\boldsymbol{\tau^+\tau^-}$: [306, 307] using $\gamma$-ray data, [302] using $e^+$ data
- $\boldsymbol{W^+W^-}$: [150] using $\bar{p}$ data, [5, 308] using $\gamma$-ray data
- $\boldsymbol{ZZ}$: [300, 309] using $\gamma$-ray data

Note that all references used a NFW profile for the dark matter halo except for refs. [305] and [309] which used an Einasto profile (see section 1.1 for more details on the dark matter halo profiles).

We use MICROMEGAs to calculate the total annihilation cross section $\langle\sigma v\rangle$ and the branching fractions of the different primary annihilation channels $\mathrm{BR}_{\mathrm{prim}}$ in order to constrain our models. We compare the annihilation cross section of different annihilation channels $\langle\sigma v\rangle_{\mathrm{prim}} = \mathrm{BR}_{\mathrm{prim}}\langle\sigma v\rangle$ to upper limits on the cross section from the references. The points in the parameter space result in a cross section that is larger than the upper limit in at least one of the annihilation channels are then excluded.

Because the dark matter particle couples to a SM flavor triplet in each model, the final states of the annihilation process via $t$- or $u$-channel exchanges of the mediator do not necessarily have the same flavor. This leads to mixed final states that have not been constrained in the literature yet. Therefore, in order to place constraints on the annihilation cross section with a mixed final state with particles $A$ and $B$ $\langle\sigma v\rangle_{AB}$, we combine the constraints on the cross sections of the individual final states $\langle\sigma v\rangle_{AA}$ and $\langle\sigma v\rangle_{BB}$ using

$$\langle\sigma v\rangle_{AB} = \frac{1}{2}\left(\langle\sigma v\rangle_{AA} + \langle\sigma v\rangle_{BB}\right) , \tag{4.26}$$

which is equivalent to the approach used in MICROMEGAs for mixed final states. This approach however is only possible if the dark matter mass is larger than the mass of both final state particles $m_\chi > m_A, m_B$. In reality, the dark matter particle can also annihilate into the mixed final state if $2m_\chi > m_A + m_B$ which can not be considered in the analysis. For different neutrino flavors in the final state, we ignore the actual flavor of the neutrino and sum over all flavors to obtain a total annihilation cross section for all neutrinos as the constraints in this case are not flavor-specific.

### 4.3.4 Collider constraints

The production of matter particles at colliders can lead to missing energy signatures in the detector which can be used to constrain the parameter space of the models. We explore these constraints using the SModelS v3 interface of micrOMEGAs which is able to calculate the constraints using many current LHC searches. The tool decomposes the signatures of each model into simplified model components (called topologies) that are then compared to experimental constraints. The result is given in terms of so-called $r$-values which correspond to the ratio of the signal cross section to the upper limit on the cross section from the experimental data for each analysis in the database. The database that is used in SModelS includes constraints from ATLAS and CMS searches based on specific models. These searches are particularly sensitive to models with a mediator that carries QCD charge as this leads to a large production cross section in proton-proton collisions.

We compute the constraints on our models by selecting the largest $r$-value computed by SModelS and excluding points in the parameter space where the $r$-value is equal to or larger than 1. Furthermore, we can make use of the computation of missing topologies in SModelS to check if there are any topologies that are not covered by the database yet. The missing topologies are divided into three categories: topologies with displaced decays, topologies with prompt decays, and topologies which are outside the experimental results grid. This allows us to identify regions in the parameter space that are not constrained by the current LHC data and can be used to guide future searches.

### 4.3.5 Flavor constraints

The constraints on the models placed by flavor observables are among the most important constraints as the flavor structure of the models can lead to processes with a large amount of flavor and CP violation that are strongly constrained by experimental data. In order to study the flavor constraints on the models, we need to compute the flavor-violating processes that arise from the flavor structure of the models and confront them with the experimental data. Because computing each flavor-violating process for each model and identifying the relevant flavor observables individually is cumbersome, we use established tools to automate the process. Specifically, we first match the Lagrangian of the models to the SMEFT which is a model-independent framework that describes the effects of high-scale new physics on the low-energy interactions of the SM particles. We then use the SMEFT to compute the flavor observables which we can then compare to the experimental data.

To match the Lagrangian of the models to the dimension 5 and 6 operators in the Warsaw basis [310] of the SMEFT at one-loop, we use the Mathematica package Matchete. The numerical values of Wilson coefficients of the SMEFT operators which are provided by the output of Matchete are then rewritten in terms of the `WCxf` data exchange format [311]. This serves as an input for the smelli tool that computes the flavor observables and compares them to the experimental data. smelli is based on two separate packages: The first one is flavio [312] which computes the flavor observables as a function of the Wilson coefficients and contains a database of the relevant experimental data. The second one is Wilson [313] which computes the matching of the Wilson coefficients to the Weak Effective Theory (WET) [314, 315] and the running of the Wilson coefficients down to the low-energy scale where the flavor observables are measured, employing the renormalization group evolution

of the SMEFT [316–318] and of the WET [319]. The output of SMELLI provides the log-likelihood ratio $\Delta\mathcal{L} = \log(\mathcal{L}_{\rm DM}/\mathcal{L}_{\rm SM})$ of the global likelihood of the dark matter model $\mathcal{L}_{\rm DM}$ and the likelihood of the SM $\mathcal{L}_{\rm SM}$ in terms of the Wilson coefficients given the experimental data of the flavor observables. We exclude points in the parameter space where $\Delta\mathcal{L} \leq -2$ which corresponds to parameter points with a pull of at least approximately $2\sigma$ with respect to the SM.

## 4.4 Example: Majorana dark matter coupling to right-handed leptons

In this section, we demonstrate the capabilities of the tool-chain we have developed to study the phenomenology of the flavored dark matter models by considering a specific example. Here, we will focus on the Majorana dark matter model that couples to the right-handed leptons and study the constraints on the parameter space of the model. As shown in table 4.1, this model has not been studied in the literature yet and is therefore a good example. In addition, we can compare this case to the Dirac and complex scalar dark matter models coupling to the right-handed leptons that have been studied in [42] and [40], respectively. We will first introduce our setup for the scan of the parameter space and then discuss the results of the scan.

### 4.4.1 Scan setup

In order to identify the parameter space that is not yet excluded by any of the constraints, we perform a random scan over the parameter space of the model and apply the constraints discussed in section 4.3. Because of the coupling to right-handed leptons, the lepton flavor violation (LFV) decay process $\ell_i \to \ell_j\gamma$ as shown in fig. 4.1 can get large contributions. Especially the decay $\mu \to e\gamma$ is strongly constrained by the experimental data and can lead to strong constraints on the parameter space of the model. The contribution is proportional to the off-diagonal elements of the coupling matrix $\tilde{\lambda}$. Therefore, we will not scan over the full parameter space of the model in order to avoid points that are already excluded by the LFV decay constraints and will focus on the parameter points where the off-diagonal elements of the coupling matrix entering the $\mu \to e\gamma$ decay are suppressed.

We perform the random scan over the parameters in the following way: The parameters $D_1$, $D_2$ and $D_3$ are randomly generated in the range $[0, 2]$. In order to keep the contribution to the LFV decay process $\mu \to e\gamma$ small, we scan the mixing angles

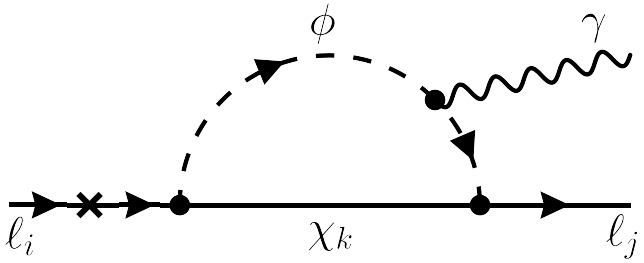


**Figure 4.1:** Feynman diagram of the LFV decay $\ell_i \to \ell_j\gamma$ in the Majorana dark matter model that couples to right-handed leptons. Drawn with FeynGame [320–322].

$\theta_{12}$ and $\phi_{12}$ logarithmically in the range $[10^{-6}, 10^{-2}]$. The remaining mixing angles are scanned logarithmically starting from $10^{-4}$ up to their maximum value of $\pi/4$. The complex phases $\delta_{ij}$ and $\gamma_i$ are scanned linearly over the whole range of $[0, 2\pi)$. The mass term of the dark matter flavor triplet $m_\chi$ is scanned linearly in the range $[100, 1500]$ GeV and the mass term of the mediator is then randomly chosen in the range $[m_{\chi_3}, m_{\chi_3} + 2000]$ GeV for every dark matter mass. Note that because of the mass matrix that is computed from the coupling matrix and the parameter $\eta$ which can be negative, the generated mass of $\chi_3$ can be below 100 GeV and even be negative. We therefore discard the points where the mass of $\chi_3$ is smaller or equal to 0 GeV. Lastly, the coupling to the Higgs doublet $\lambda_{H\phi,1}$ and the parameter $\eta$ are sampled logarithmically in the range $[10^{-3}, 1]$ with a random sign.

We generate roughly 350,000 random points in the defined parameter space of the model and first apply the constraints from the relic density, direct and indirect searches, and collider experiments by using micrOMEGAs and SModelS as these constraints already exclude a large fraction of the generated points. We then apply the flavor constraints to the points that are not excluded by the other constraints using Matchete and smelli.

### 4.4.2 Results

All points in the parameter space of our scan that are still allowed by all constraints are shown in the different panels of fig. 4.2 in blue. The upper left panel shows the parameter points in the $m_{\chi_3}$-$m_\phi$ plane where the gray dashed line corresponds to $m_{\chi_3} = m_\phi$ which is the lower bound on the mass of the mediator in our scans. The upper right panel shows the mass splitting parameter $\eta$ as a function of $m_{\chi_3}$. For $\eta > 0$, the smallest possible mass for $m_{\chi_3}$ is 100 GeV which is the lower bound on the mass parameter $m_\chi$ in our scan as the mass corrections for positive values of $\eta$ will always increase the mass of the dark matter particle. For $\eta < 0$, the mass of the dark matter particle can be smaller than 100 GeV which is why we find points with $m_{\chi_3} < 100$ GeV in the scan for this case. The lower panels show the constraints on the dark matter coupling in the $|\tilde{\lambda}_{e3}|$-$|\tilde{\lambda}_{\mu 3}|$ and $|\tilde{\lambda}_{e3}|$-$|\tilde{\lambda}_{\tau 3}|$ planes. In the following, we will discuss the impact of the different constraints on the parameter space of the model individually, shown in red, green and orange for collider (SMS), indirect detection (ID) and flavor observables constraints, respectively.

**Relic density constraints:** Using first the results obtained with micrOMEGAs, we find that the majority of the points are excluded because they do not reproduce the correct relic density with 97% of all points being excluded. This makes the relic abundance constraint the most constraining for the model. Because of the amount of points that are excluded by the relic abundance constraints, we do not show the points that are excluded explicitly in the plots. The dominant annihilation processes that contribute to the relic density are the coannihilations between the different $\chi_i$ states into leptons through $t$- and $u$-channel exchanges of the mediator.

We find that the relic abundance constraints place a lower bound on the mass of the dark matter particle for a given mediator mass as shown in the upper left panel of fig. 4.2. This is because the annihilation cross section is proportional to $m_{\chi_3}^2$ and if the mass becomes too small, the upper limit we set for the coupling matrix elements $D_i$ inhibits the compensation for the small mass. In addition, we find that the relic abundance constraints allow for large positive values of $\eta$ in the entire mass range of

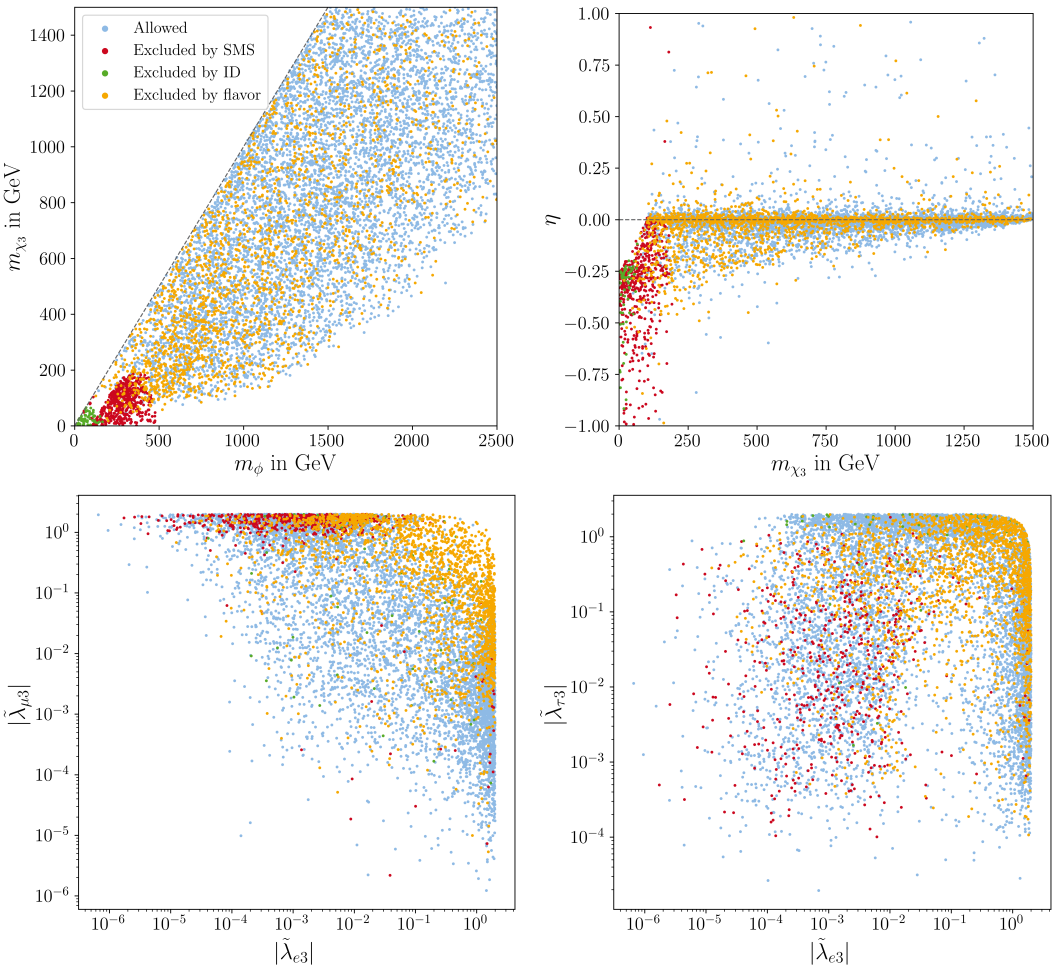


**Figure 4.2:** Allowed parameter space and constraints of the Majorana dark matter model that couples to right-handed leptons. The points in the parameter space that pass all considered constraints are shown in blue. In red, the points that are excluded by only the collider constraints (SMS) are shown. The green points are excluded only by the indirect detection constraints (ID) and the orange points pass all constraints except for the constraints from flavor observables. The upper left panel shows the parameter points in the $m_{\chi_3}$-$m_\phi$ plane where the gray dashed line corresponds to $m_{\chi_3} = m_\phi$. In the upper right panel, we show the mass splitting parameter $\eta$ as a function of $m_{\chi_3}$. The lower panels show the parameter points in the $|\tilde{\lambda}_{e3}|$-$|\tilde{\lambda}_{\mu 3}|$ plane on the left and $|\tilde{\lambda}_{e3}|$-$|\tilde{\lambda}_{\tau 3}|$ plane on the right.

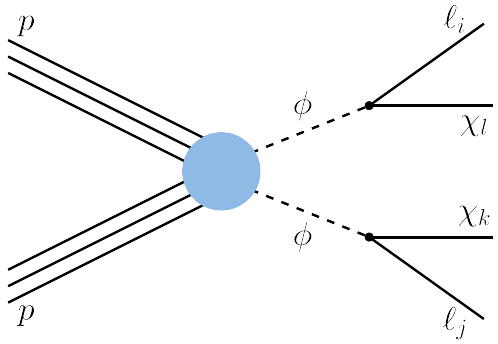


**Figure 4.3:** Feynman diagram of the Drell-Yan production of the mediator pair at the LHC which then decays into two leptons and two dark matter particles. Drawn with FeynGame [320–322].

$m_{\chi_3}$ which is shown in the upper right panel. Large absolute values for a negative $\eta$ are only allowed for small dark matter masses. The allowed absolute value of negative $\eta$ decreases with increasing dark matter mass. This means that significant mass splittings are allowed in case the lightest flavor has the weakest coupling to the SM leptons but are disfavored if the lightest flavor has the strongest coupling to the SM leptons.

**Collider constraints:** Next, we discuss constraints on the parameter space placed by LHC searches using SModelS where only 0.15% of all points are excluded by these searches. The points that are excluded only by LHC searches are shown in red in fig. 4.2 and form a bell-shaped area in the parameter space of the $m_{\chi_3}$-$m_\phi$ plane that extends up to $m_{\chi_3} \approx 200$ GeV and $m_\phi \approx 500$ GeV. This is consistent with the results found in ref. [42] where the authors have considered complex scalar dark matter coupling to right-handed leptons. In the upper right panel of fig. 4.2 we find that collider constraints mostly exclude points with negative $\eta$ and small $m_{\chi_3}$. On the one hand, this is because for positive $\eta$, the mediator coupling to the heavier $\chi_i$ states is stronger than to $\chi_3$ which means that the mediator will decay primarily into the heavier $\chi_i$. The heavier $\chi_i$ states will then further decay into a lepton and a $\chi_3$ which leads to more than one lepton in the final state of the mediator decay. This is not constrained because current searches do not look for this signature. On the other hand, if $\eta$ is negative, then $\chi_3$ has the largest coupling to the SM leptons which leads to stronger constraints from the LHC searches.

For hadron colliders, the most important signal comes from the Drell-Yan production of a mediator pair which then decays into two leptons and missing energy, as shown in fig. 4.3. Because we consider Majorana dark matter in this model, the two leptons can in principle be of the same charge. This is however unlikely as this requires two same-sign leptons in the initial state which is heavily suppressed in proton colliders [323]. In addition, there are no searches that specifically look for this signal at the LHC. Final states with mixed flavors can also be produced in our model but because the SM background for this signal is dominated by the production of $\bar{t}t$ and $W^+W^-$ pairs, the signal is not expected to be large enough to be detected by the LHC [42] and in addition to that, the signal is not considered in SModelS.

The most constraining search implemented in SModelS is a CMS search for supersymmetry which searches for two light oppositely charged same-flavor leptons and missing

energy ($e^+e^- + \not{E}_T$ or $\mu^+\mu^- + \not{E}_T$) [324]. This search excludes almost exclusively points with a large $\chi_3 - \mu$ couplings which can be seen in the lower left panel of fig. 4.2. Furthermore, we find the implementation of the search in SModelS has no sensitivity to the $\chi_3 - e$ coupling. The remaining relevant ATLAS [325–329] and CMS [330] searches which look for either two oppositely charged light leptons with the same flavor plus missing energy or two oppositely charged electrons plus missing energy are much less constraining and only exclude a few points, most of them with a large $\chi_3 - e$ coupling. Searches for two $\tau$ final states are less constraining than searches for light leptons which is why we find no excluded parameter points through a search for a $\tau\bar{\tau} + \not{E}_T$ final state. This is the reason why large $\chi_3 - \tau$ couplings are still allowed in contrast to large $\chi_3 - \mu$ couplings as shown in the lower right panel of fig. 4.2.

Because the model couples to the right-handed leptons, lepton colliders like LEP can also be used to constrain the parameter space of the model. This can be done by using for example the search for the process $e^+e^- \to \chi_i\chi_j\gamma$ which results in a mono-photon plus missing energy signal. As we only consider the searches implemented in SModelS, we do not take the constraints from lepton colliders into account in our analysis. However, we expect that the constraints from LEP will restrict the dark matter and the mediator mass to be larger than $\sim 100$ GeV [331].

**Indirect detection constraints:** The constraints placed by indirect detection experiments are not very strong for this model with only 0.02% of all points being excluded. The indirect detection constraints only exclude points in the parameter space where both the mass of $\chi_3$ and the mediator are small with $m_{\chi_3} \lesssim 65$ GeV and $m_\phi \lesssim 170$ GeV as the constraints on the annihilation cross section become weaker for larger dark matter masses. The excluded points are shown in green in fig. 4.2.

The amount of points excluded by the indirect detection constraints is so small because in our analysis, we only considered the constraints on the annihilation cross section into $\ell^+\ell^-$ which is $p$-wave suppressed and therefore less likely to be the dominant annihilation channel. The dominant annihilation channel for indirect detection is $\chi_3\chi_3 \to \gamma\ell^+\ell^-$ which lifts the $p$-wave suppression but is not considered in the constraints that we used. Including this contribution by taking the sum of the two-body and three-body final state annihilation cross sections as it is done in [42] would lead to stronger constraints on the parameter space of the model. These constraints could however be too tight as the different kinematics of the leptons in the three-body final state are not taken into account correctly. Studying the validity of applying the constraints to the sum of the two- and three-body final state annihilation cross sections will be the subject of future work.

**Direct detection constraints:** As already mentioned in section 4.3.2, lepton-flavored dark matter does not interact with the nucleus at tree-level and therefore constraints from direct detection are not as strong as for models in which dark matter couples directly to quarks. Therefore, in our case, possible interactions are either with the electrons of the target or through loop-induced interactions with the nucleus as shown in fig. 4.4. The interaction with the electrons is however highly suppressed meaning that the only relevant interaction is the loop-induced interaction [332]. Unfortunately, this process is not considered in micrOMEGAs and the interaction cross sections are therefore not calculated. This is why we find no points that are excluded by the direct detection constraints in our analysis and leave the analysis including the loop-induced interactions for future work.

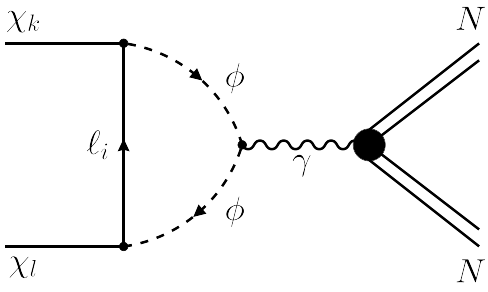


**Figure 4.4:** Feynman diagram of a possible loop-induced interaction of the dark matter particle with the nucleus for direct detection. Other possibilities are exchanging the leptons and the mediator in the diagram or replacing the photon by a $Z$ boson. Drawn with FeynGame [320–322].

**Flavor constraints:** Lastly, we apply the flavor constraints to the points that are not excluded by the relic abundance, collider, and indirect detection constraints. We find that the flavor constraints exclude another $\sim 25\%$ of the points that pass the other constraints which are shown in orange in fig. 4.2. As expected, the most constraining flavor observable is the LFV decay $\mu \to e\gamma$ as shown in fig. 4.1 which excludes most points. Another related and also very relevant observable is the LFV decay $\mu \to eee$ which can happen if the photon in the $\mu \to e\gamma$ decay process, or a $Z$ boson instead of the photon, further decays into an electron positron pair. This process is however suppressed so the relevant contribution to $\mu \to eee$ comes from box diagrams with $\phi$ and $\chi_i$ particles in the loop. This observable has not been considered in the analyses for the Dirac lepton flavored dark matter [40] and the complex scalar lepton flavored dark matter [42].

We find that the flavor observables give stronger constraints on smaller dark matter and mediator masses as the contribution to the LFV decays from our model are suppressed for larger masses. Furthermore, the upper right panel of fig. 4.2 displays that the flavor constraints exclude most points with very small absolute value of $\eta$ and are less constraining for larger values of $\eta$. This is however just a consequence of the fact that we chose a logarithmic prior on $\eta$ for our scan and used a linear plotting for $\eta$. Thus, we find that the fraction of excluded points by the flavor observables does not depend on the absolute value of $\eta$.

The flavor constraints are however very relevant for constraining the coupling matrix $\tilde{\lambda}$ as this directly determines the size of the LFV contribution. The constraints on the elements of the coupling matrix describing the coupling strength of dark matter to the different leptons are shown in the lower panels of fig. 4.2. We find that, as expected, large dark matter couplings to the electron and the muon are excluded by the flavor constraints, especially if both couplings are large as this results in large LFV effects. If only one of the couplings is dominant and the other is a few orders of magnitude smaller, then the points are not excluded by the flavor constraints as can be seen for example in the lower left panel of fig. 4.2 for large $\tilde{\lambda}_{e3}$ and small $\tilde{\lambda}_{\mu 3}$. There is however a very small amount of points with relatively large electron and muon couplings that are not excluded. These points all have very large mediator masses which suppresses the LFV decay contribution. The LFV decays of the $\tau$ however are not as constraining as the LFV decays of the muon which leads to larger allowed regions in the parameter space for the $\tau$ coupling. Large couplings to the $\tau$ are however still excluded by the flavor constraints if the coupling to the electron or muon is also large, as shown in the

lower right panel of fig. 4.2.

## 4.5 Summary

In this chapter, we have introduced a general framework to study the phenomenology of different flavored dark matter models. First, we have listed and discussed 20 different flavored dark matter models that can be realized in the context of the DMFV framework. This included four different types of dark matter particles (Majorana fermion, Dirac fermion, complex scalar, and real scalar) that couple to the different fermions in the SM (left- or right-handed quarks or leptons). For each model, we have discussed the different 15 to 22 parameters that fully describe the individual particle properties and their interactions with the SM particles.

We have then developed a tool-chain that allows us to generate the model files using FeynRules for the different models and use the model files to calculate the constraints on the parameter space of the models. We have included the constraints from the relic density, direct and indirect detection using micrOMEGAs, collider constraints using SModelS, and flavor constraints using Matchete and smelli.

As an example for the performance of our tool-chain, we have studied the Majorana dark matter model that couples to right-handed leptons. In order to identify regions in the parameter space that are not yet excluded by any of the constraints, we have performed a random scan over the parameter space of the model, taking into account that the LFV decay $\mu \to e\gamma$ can place strong constraints on the parameter space and do not allow for large couplings to the electron and muon at the same time. Using the points we have generated in the scan, we have first applied the constraints from the relic density, direct and indirect detection, and collider experiments and later on constrained the remaining points with the flavor observables.

We have found that the relic density constraints which are driven by coannihilations of the different $\chi_i$ states are the most constraining for the model with 97% of all points being excluded. Furthermore, the relic abundance constraints place a lower bound on the mass of the dark matter particle for a given mediator mass due to our upper limit on the coupling matrix elements. Large mass splittings generated by large absolute values of $\eta$ are also disfavored by the relic abundance constraints if the lightest flavor has the strongest coupling to the SM leptons. This is not the case when the lightest flavor has the weakest coupling.

The collider constraints exclude only 0.15% of all points and are most constraining for dark matter masses up to $\sim 200$ GeV and mediator masses up to $\sim 500$ GeV. The parameter space is fully constrained by LHC searches for $e^+e^- + \not{E}_T$ and $\mu^+\mu^- + \not{E}_T$ final states. This leads to the exclusion of most points with large $\chi_3 - \mu$ couplings. The dark matter coupling to the $\tau$ on the other hand is less constrained by the collider searches as the searches for $\tau\bar{\tau} + \not{E}_T$ final states are less constraining.

Indirect detection constraints are rather weak for our model with only 0.02% of all points being excluded. This is because of the $p$-wave suppression of the annihilation cross section in our model. The constraints only affect points with very small dark matter and mediator masses. Here, we have only considered the constraints on the annihilation cross section into $\ell^+\ell^-$ and have neglected the contribution from the three-body final state $\gamma\ell^+\ell^-$ which are the dominant annihilation channel for indirect detection. Including this contribution would lead to stronger constraints on the parameter space of the model and will be the subject of future work as the different

kinematics of the leptons in the three-body final state need to be taken into account correctly.

Because the dark matter particle couples to the right-handed leptons, direct detection constraints are not as strong as for models that couple to the quarks in the SM. The only relevant interaction for our model is the loop-induced interaction with the nucleus through a photon or a $Z$ boson exchange. This interaction is however not considered in micrOMEGAs which leads to no excluded points by the direct detection constraints in this analysis. We expect that including the loop-induced interactions will further constrain large couplings and small dark matter and mediator masses which can be as constraining as the constraints from collider searches as shown in [42].

Lastly, flavor observables exclude another $\sim 25\%$ of the points that are not excluded by the other constraints. The most constraining flavor observable is the LFV decay $\mu \to e\gamma$ which excludes most points. The LFV decays of the tau are not as constraining as the LFV decays of the muon which leads to larger allowed regions in the parameter space for the $\tau$ coupling. As expected, we have found that the flavor constraints are the most relevant for constraining the coupling matrix $\tilde{\lambda}$ as this directly influences the size of the LFV contribution. Hence, large dark matter couplings to the electron and the muon are excluded by the flavor constraints, especially if both couplings are large. If on the other hand only one of the couplings is dominant and the other is significantly smaller, then the points are not excluded. Additionally, large couplings to the tau are also excluded if the coupling to the electron or muon is also large, but the exclusion is less strong than for the electron and muon couplings.

In summary, we have shown that our tool-chain is capable of studying the phenomenology of flavored dark matter models and can easily be used to identify the parameter space that is not yet excluded by the constraints. In the future, this tool chain can be used to study the phenomenology of the other flavored dark matter models that have not been considered in the literature so far and to guide future searches for dark matter at colliders and in direct and indirect detection experiments. Furthermore, the tool-chain can be used to identify similarities and differences between the different flavored dark matter models and makes combining different models to study the phenomenology of more complex models possible.

# Part III

# Conclusions and Appendices

# Chapter 5

# Conclusions

The nature of dark matter is one of the most pressing questions in modern physics. The existence of dark matter is well established through a variety of astrophysical observations, but its properties remain largely unknown. In order to shed light on the nature of dark matter, a variety of experimental and theoretical approaches are being pursued. Searches for dark matter particles are being conducted at colliders as well as direct and indirect detection experiments, while theoretical models are being developed to explain the observed dark matter abundance and its interactions with the Standard Model particles. In this thesis, we have directed our efforts toward contributing to solving the mystery of dark matter by studying two different aspects of investigating dark matter: indirect detection with cosmic ray antideuterons and the phenomenology of flavored dark matter models.

In part I, we first focused on the indirect detection of dark matter with cosmic ray antideuterons. While established searches for antiparticles like antiprotons and positrons have the disadvantage of a very high astrophysical background compared to a possible dark matter signal, antideuterons are expected to have a much lower background in the relevant energy range. Furthermore, the upcoming GAPS experiment is expected to be sensitive to low-energy antideuterons, which are particularly interesting for dark matter searches as this enables a practically background-free search. In order to investigate the sensitivity of current and future experiments to a dark matter signal, we have computed the antideuteron injection spectrum using Monte Carlo simulations, taking into account the uncertainties that arise from the modeling of the production of antideuterons. This included the uncertainty on the coalescence momentum $p_c$ used to model the formation of antideuterons from antiprotons and antineutrons, as well as the rescaling of the $b \to \Lambda_b$ transition ratio. Furthermore, we modeled the propagation of antideuterons through the Galaxy using two different propagation models and accounted for the uncertainties in the propagation parameters.

We then developed a neural network emulator called $\bar{\text{D}}$arkRayNet to predict the antideuteron flux for a given dark matter model and propagation setup. The emulator was trained on the results of the Monte Carlo and propagation simulations and is able to predict the antideuteron flux for any dark matter model and propagation setup within the parameter space covered by the training data. We have shown that the emulator is able to predict the antideuteron flux with high accuracy. This allows for a quick computation of the antideuteron flux for a large number of dark matter masses and propagation parameters which enables us to take into account the uncertainties from cosmic ray propagation models by marginalizing over the propagation parameters of a given propagation model. Therefore, we conclude that the emulator is a powerful tool for the interpretation of future antideuteron data in the context of dark matter searches.

Using the $\bar{\text{D}}$arkRayNet, we investigated the sensitivity of AMS-02, GAPS and AMS-100 to a dark matter signal for two different dark matter models, namely dark matter annihilating purely into $b\bar{b}$ and the singlet scalar Higgs portal (SSHP) model. We furthermore include the uncertainties from the modeling of the antideuteron propagation by marginalizing over the propagation parameters and presenting the results for the two considered propagation models. Assuming an annihilation cross section obtained from the limit using AMS-02 data for antiprotons, we found that AMS-02 is only sensitive to antideuterons produced by dark matter annihilation into $b\bar{b}$ for dark matter masses below $m_\chi \lesssim 20$ GeV. The sensitivity to the SSHP model is however more promising, with AMS-02 being able to probe dark matter masses at around 200 GeV. For GAPS, we find only one mass range where the experiment is potentially sensitive to a dark mater signal for the $b\bar{b}$ model, which is below 10 GeV. In this region, AMS-02 and GAPS are complementary to each other and offer an independent confirmation of a possible dark matter signal. Furthermore, we find that AMS-100 will be able to probe the entire mass range for both dark matter models. We conclude that antideuteron searches offer an innovative detection method that opens up new avenues of discovery and that our tool will be quick and useful for the interpretation of future data in terms of different dark matter models.

In the second part of the thesis, we have studied the phenomenology of flavored dark matter models in the context of DMFV. While the viable parameter space of popular WIMP models is becoming increasingly constrained by experiments, models with multiple generations of dark matter particles with couplings to SM particles that are flavor-dependent offer a rich phenomenology that can evade current constraints and allow for a more dynamic freeze-out phenomenology. Therefore, we have specifically studied the phenomenology of a flavored Majorana dark matter model with couplings to up-type quarks in chapter 3. Building on an existing phenomenological study, we have extended the analysis to include more general freeze-out scenarios. These included considering all possible mass splittings between the dark matter particles and the mediator, as well as the possibility of coannihilations with the mediator, in the canonical freeze-out scenario. Furthermore, we showed that the conversion-driven freeze-out scenario can be realized in the model, which allows for very weakly coupled dark matter particles.

To study the impact of more general freeze-out scenarios on the viable parameter space of the model, we performed detailed scans over the parameter space and computed the relic density and constraints from direct and indirect detection experiments as well as flavor constraints. We found that the possibilities of coannihilations and conversion-driven freeze-out significantly impact the viable parameter space of the model and uncover new regions that are consistent with all constraints. In particular, we found that small mass splittings between the dark matter particle and the mediator are allowed in the conversion-driven freeze-out scenario while this was not the case in the canonical freeze-out scenario. Furthermore, if the heavier dark matter states act as a coannihilator to the lightest one in the conversion-driven freeze-out scenario, the viable parameter space is significantly extended to small dark matter masses and mass splittings compared to the canonical freeze-out scenario.

In order to extend the analysis of constraints placed by LHC searches, we used the full data set of LHC searches implemented in SModelS and confronted the viable parameter space from the performed scans with the constraints from the LHC. We found that most of the parameter space for the canonical freeze-out scenarios can be probed by the LHC which excludes mostly the regions with mediator masses below $\sim 1200$ GeV and dark matter masses below $\sim 600$ GeV. There are however regions in

our parameter space that are not covered by the LHC searches because of the more complex phenomenology of the model. In particular, small mass splittings between the dark matter particles can lead to metastable states which are not straightforward to search for at the LHC which leads to a few allowed points in the excluded region of the parameter space. Regarding the conversion-driven freeze-out scenario, we found that long-lived particle searches become relevant because of possible long lifetimes of the mediator. This is the case if the mediator is the dominant coannihilator which leads to an exclusion of the parameter space of dark matter masses up to $\sim 1.5$ TeV. The scenarios where the heavier dark matter states act as coannihilators are not constrained by long-lived particle searches but can be probed by the conventional missing energy searches.

Lastly, we discussed two possible signatures to distinguish the Majorana dark matter model from the Dirac case, namely the same-sign production of top quarks and the charge asymmetry in the production of a top quark and a jet. We found that the same-sign top production is not a promising signature as it is suppressed by the small number of events that produce two semi-leptonic top decays in order to identify the charge of the top quark. The charge asymmetry on the other hand is a promising signature as we find sizable values for the charge asymmetry in parts of the parameter space which point towards the Majorana nature of the dark matter particle.

In chapter 4, we have extended the study of flavored dark matter models and considered a wide range of possible models that can be realized in the context of DMFV. In order to study the phenomenology of these models, we have first discussed the model descriptions and parameters that are relevant for the phenomenology of the models and then developed a framework to compute the constraints on the different models. For this, we have implemented the models in FeynRules and used micrOMEGAs to compute the relic density and constraints from direct and indirect detection experiments. We have addressed the constraints from collider searches by using SModelS and the flavor constraints by using Matchete and smelli.

As an example for demonstrating the capabilities of our tool-chain, we have studied the phenomenology of a model with a Majorana dark matter particle coupling to the right-handed leptons of the SM. We have performed a general scan of the parameter space of the model and used the tool-chain to compute the constraints on the parameter space. We found that the model is mostly constrained by the relic abundance constraints, followed by the flavor constraints. From the relic abundance constraints, we have identified a lower bound on the dark matter mass as a function of the mediator mass that comes from the upper bound we have placed on the coupling strength in our scan. Furthermore, the correct relic abundance can be obtained for large $m_{\chi_i}$ mass splittings if the lightest $\chi_i$ has the weakest coupling to the SM leptons. If the lightest $\chi_i$ has the largest coupling, then the mass splittings have to be small in order to obtain the correct relic abundance, especially if the mediator mass is large.

The flavor constraints are mostly relevant for constraining the couplings of the dark matter particles to the SM leptons where the strongest constraints come from the $\mu \to e\gamma$ decay. The observable is very sensitive to the couplings of the dark matter particles to the electron and muon and therefore places strong constraints on large $\chi_3 - e$ and $\chi_3 - \mu$ couplings, especially if both couplings are large. The constraints become less stringent if one of the couplings becomes very small compared to the other one. The coupling strength to the tau lepton is less constrained by flavor observables as the limits on the LFV decay processes of the tau lepton are less stringent than the ones for the muon.

The remaining constraints from direct and indirect detection experiments and collider searches are much less stringent than the ones from the relic abundance and flavor observables. We found that the collider constraints are mostly relevant for constraining the mediator mass and the dark matter mass below $m_\phi \lesssim 500$ GeV and $m_{\chi_3} \lesssim 200$ GeV, as well as for large couplings to the muon. The indirect detection constraints affect a very small region of the parameter space with very small dark matter and mediator masses. The only relevant interaction of the dark matter particles with a nucleus which is necessary to obtain direct detection constrants is through a loop-induced interaction. As this interaction is not implemented in micrOMEGAs, we have not been able to compute the constraints from direct detection experiments and postpone this to future work. We conclude that discovering potential models that are not yet excluded is essential for guiding experimental efforts and for developing new search strategies. Our framework is therefore very powerful as it allows for studying the phenomenology of flavored dark matter models and can be used to study a wide range of models that can be realized in the context of DMFV.

# Appendix A

# Sensitivity Factor for the SSHP Model

Here, we provide the sensitivity factor for the singlet scalar Higgs portal (SSHP) model for GAPS and AMS-100 in analogy to the results shown chapter 2 for the analysis of the indirect detection of dark matter with cosmic ray antideuterons. We show the results in fig. A.1 for the propagation models INJ.BRK and DIFF.BRK, as well as for two different assumptions for the annihilation cross section.

We find that the sensitivity factor looks almost identical to the one for the $b\bar{b}$ annihilation model shown in fig. 2.12 for dark matter masses below 50 GeV. This is due to the fact that the antideuteron flux in the SSHP model is dominated by the annihilation into $b\bar{b}$ for low dark matter masses. Therefore, we can draw the same conclusions as for the $b\bar{b}$ annihilation model presented in section 2.4. The result starts to deviate as the dark matter mass increases and other annihilation channels become kinematically accessible. In both propagation models we find an increase of the sensitivity factor for the SSHP model compared to the $b\bar{b}$ annihilation model for dark matter masses above $\sim 100$ GeV assuming the annihilation cross section limit obtained with antiprotons. This increase is however not enough to make the SSHP model detectable with GAPS. For AMS-100, the sensitivity is again sufficient to be able to detect a dark matter signal for the entire mass range considered.

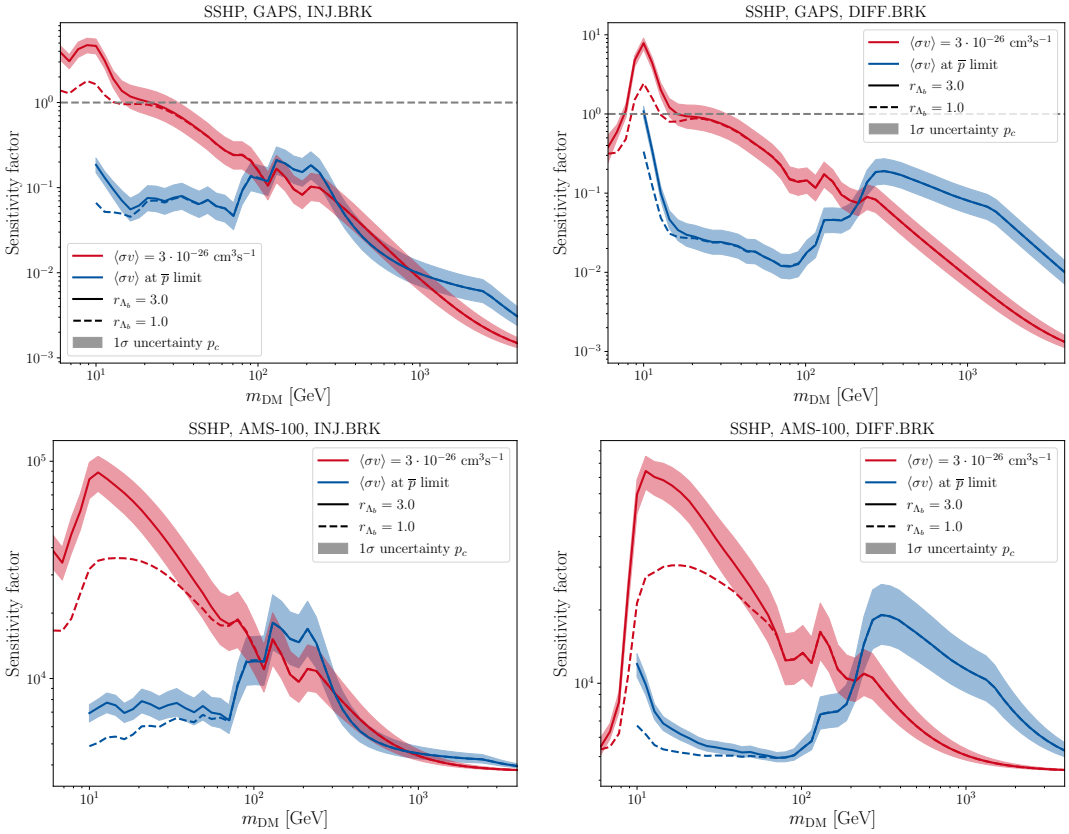


**Figure A.1:** Sensitivity factor for GAPS (upper panels) and AMS-100 (lower panels) within the propagation models INJ.BRK (left panels) and DIFF.BRK (right panels). Here we consider the singlet scalar Higgs portal model. The solid lines and shaded bands denote the results for $r_{\Lambda_b} = 3$ and the $1\sigma$ coalescence momentum uncertainty, respectively, while the dashed curves correspond to $r_{\Lambda_b} = 1$.

# Appendix B

# Cross Sections and Rates for Flavored Majorana Dark Matter

In this appendix chapter, we provide analytic expressions for the relevant annihilation and conversion processes used in our analysis of the flavored Majorana dark matter model coupling to up-type quarks in chapter 3. We computed the matrix elements of the processes using FeynCalc [333–335] and FeynArts [336]. The thermal average for the $2 \to 2$ cross sections for the process $ij \to kl$ is obtained by [246]

$$\langle \sigma v \rangle_{ij} = \sum_{kl} \frac{g_i g_j \, T}{8\pi^4 \, n_i^{\mathrm{eq}} n_j^{\mathrm{eq}}} \int \mathrm{d}s \, \sqrt{s} \; p_{\mathrm{COM}}(s, m_i, m_j)^2 \, \sigma_{ij \to kl}(s) \, K_1\left(\frac{\sqrt{s}}{T}\right) , \tag{B.1}$$

where the center-of-mass momentum is given by

$$p_{\mathrm{COM}}(s, m_i, m_j) = \frac{\sqrt{s - (m_i + m_j)^2}\sqrt{s - (m_i - m_j)^2}}{2\sqrt{s}} . \tag{B.2}$$

Note that in this appendix, $s$ and $t$ denote the respective Mandelstam variables. For all cross sections the lower and upper integration limits of the Mandelstam variable $t$, $t_{\mathrm{min}}$ and $t_{\mathrm{max}}$, respectively, are given by:

$$\begin{aligned} &t_{\mathrm{min}}(s, m_1, m_2, m_3, m_4) \\ &\quad = m_1^2 + m_3^2 - 2\sqrt{p_{\mathrm{COM}}(s, m_1, m_2)^2 + m_1^2}\sqrt{p_{\mathrm{COM}}(s, m_3, m_4)^2 + m_3^2} \\ &\qquad - 2 p_{\mathrm{COM}}(s, m_1, m_2) \, p_{\mathrm{COM}}(s, m_3, m_4) \end{aligned} \tag{B.3}$$

$$\begin{aligned} &t_{\mathrm{max}}(s, m_1, m_2, m_3, m_4) \\ &\quad = m_1^2 + m_3^2 - 2\sqrt{p_{\mathrm{COM}}(s, m_1, m_2)^2 + m_1^2}\sqrt{p_{\mathrm{COM}}(s, m_3, m_4)^2 + m_3^2} \\ &\qquad + 2 p_{\mathrm{COM}}(s, m_1, m_2) \, p_{\mathrm{COM}}(s, m_3, m_4) \end{aligned} \tag{B.4}$$

## B.1 Cross sections for annihilation processes

Here we provide the cross sections for the annihilation processes of the flavored Majorana dark matter particles and the mediator. We consider the following processes:

• $\phi\,\phi^\dagger \to gg$:

$$\sigma_{\phi\phi^\dagger\to gg}(s) = \frac{g_s^4}{54\pi s^2(4m_\phi^2 - s)}\left[\left(62m_\phi^2 + 5s\right)\sqrt{s(s-4m_\phi^2)} + 8\left(4m_\phi^2 s + m_\phi^4\right)\,\log\left(\frac{\sqrt{s(s-4m_\phi^2)} - s}{\sqrt{s(s-4m_\phi^2)} + s}\right)\right] \tag{B.5}$$

• $\phi\,\phi^\dagger \to q_i\bar{q}_i$ for up-type quarks:

$$\begin{aligned}
&\sigma_{\phi\phi^\dagger\to q_i\bar{q}_i}(s)\\
=&\frac{1}{144\pi s^3(s-4m_\phi^2)}\int_{t_{\min}(s)}^{t_{\max}(s)}\mathrm{d}t\Bigg(16s\left(m_q^4 + 2tm_\phi^2 - m_\phi^4 - t(s+t)\right)\sum_j\frac{g_s^2|\lambda_{ij}|^2}{(t-m_{\chi_j}^2)}\\
&-16g_s^4\left(-m_q^2(-2m_\phi^2 + s + 2t) + m_q^4 - 2tm_\phi^2 + m_\phi^4 + t(s+t)\right)\\
&-9s^2\left(-2m_q^2m_\phi^2 + m_q^4 - 2tm_\phi^2 + m_\phi^4 + t(s+t)\right)\\
&\times\frac{\left(|\lambda_{i1}|^2(t-m_{\chi_2}^2)(t-m_{\chi_3}^2) + |\lambda_{i2}|^2(t-m_{\chi_1}^2)(t-m_{\chi_3}^2) + |\lambda_{i3}|^2(t-m_{\chi_1}^2)(t-m_{\chi_2}^2)\right)^2}{(t-m_{\chi_1}^2)(t-m_{\chi_2}^2)(t-m_{\chi_3}^2)}\Bigg),
\end{aligned} \tag{B.6}$$

where $t_{\min/\max}(s) = t_{\min/\max}(s, m_\phi, m_\phi, m_{q_i}, m_{q_i})$.

• $\phi\,\phi^\dagger \to q_i\bar{q}_i$ for down-type quarks:

$$\sigma_{\phi\phi^\dagger\to q_i\bar{q}_i}(s) = -\int_{t_{\min}(s)}^{t_{\max}(s)}\mathrm{d}t\,\frac{g_s^4\left[m_q^2\left(2m_\phi^2 - s - 2t\right) + m_q^4 - 2tm_\phi^2 + m_\phi^4 + t(s+t)\right]}{9\pi s^3\left(s-4m_\phi^2\right)}, \tag{B.7}$$

where $t_{\min/\max}(s) = t_{\min/\max}(s, m_\phi, m_\phi, m_{q_i}, m_{q_i})$.

• $\phi\,\phi^\dagger \to q_i\bar{q}_j$, $i \neq j$:

$$\begin{aligned}
\sigma_{\phi\phi^\dagger\to q_i\bar{q}_j}(s) =& -\int_{t_{\min}(s)}^{t_{\max}(s)}\mathrm{d}t\left(-2m_\phi^2\left(m_{q_i}^2 + t\right) + tm_{q_i}^2 + m_{q_i}^4 - tm_{q_j}^2 + m_\phi^4 + t(s+t)\right)\\
&\times\frac{|\lambda_{i1}\lambda_{j1}(t-m_{\chi_2}^2)(t-m_{\chi_3}^2) + \lambda_{i2}\lambda_{j2}(t-m_{\chi_1}^2)(t-m_{\chi_3}^2) + \lambda_{i3}\lambda_{j3}(t-m_{\chi_1}^2)(t-m_{\chi_2}^2)|^2}{16\pi s(s-4m_\phi^2)(t-m_{\chi_1}^2)^2(t-m_{\chi_2}^2)^2(t-m_{\chi_3}^2)^2},
\end{aligned} \tag{B.8}$$

where $t_{\min/\max}(s) = t_{\min/\max}(s, m_\phi, m_\phi, m_{q_i}, m_{q_j})$.

• $\phi\,\phi \to q_i q_j$, $i \neq j$:

$$\sigma_{\phi\phi\to q_i q_j}(s) = \sum_{k,l} \frac{\lambda_{ik}^* \lambda_{il} \lambda_{jk}^* \lambda_{jl} m_{\chi_k} m_{\chi_l} \left(-m_{q_i}^2 - m_{q_j}^2 + s\right)}{48\pi s \left(s - 4m_\phi^2\right)} \int_{t_{\min}(s)}^{t_{\max}(s)} \mathrm{d}t \, \frac{1}{(t - m_{\chi_k}^2)(t - m_{\chi_l}^2)}$$
$$\times \left( \frac{3(m_{q_i}^2 + m_{q_j}^2)^2 - (2m_{q_i}^2 + 2m_{q_j}^2)(2m_{\chi_k}^2 + 2m_{\chi_l}^2 - 6m_\phi^2 + 3s + 2t)}{(-m_{q_i}^2 - m_{q_j}^2 + m_{\chi_k}^2 - 2m_\phi^2 + s + t)(-m_{q_i}^2 - m_{q_j}^2 + m_{\chi_l}^2 - 2m_\phi^2 + s + t)} \right.$$
$$\left. + \frac{4\big[ -2m_\phi^2(m_{\chi_k}^2 + m_{\chi_l}^2 + \frac{3}{2}s + t) + m_{\chi_l}^2 \left(2m_{\chi_k}^2 + s\right) + s m_{\chi_k}^2 + 3m_\phi^4\big] + 3s^2 + 4t(s+t)}{(-m_{q_i}^2 - m_{q_j}^2 + m_{\chi_k}^2 - 2m_\phi^2 + s + t)(-m_{q_i}^2 - m_{q_j}^2 + m_{\chi_l}^2 - 2m_\phi^2 + s + t)} \right), \tag{B.9}$$

where $t_{\min/\max}(s) = t_{\min/\max}(s, m_\phi, m_\phi, m_{q_i}, m_{q_j})$.

• $\phi\,\phi \to q_i q_i$:

$$\sigma_{\phi\phi\to q_i q_i}(s) = \frac{1}{2} \sigma_{\phi\phi\to q_i q_j}(s)\big|_{i=j} \tag{B.10}$$

• $\phi\,\chi_i \to q_j g$:

$$\sigma_{\phi\chi_i\to q_j g}(s) = \frac{g_s^2 |\lambda_{ji}|^2}{48\pi s (s - m_{q_j}^2)^2 \, p_{\mathrm{COM}}(s, m_\phi, m_{\chi_i})^2}$$
$$\times \int_{t_{\min}(s)}^{t_{\max}(s)} \mathrm{d}t \left( m_{q_j}^2 \Big\{ -t\left(-4s m_{\chi_i}^2 + 2m_{\chi_i}^4 + 2s^2 + 4st + t^2\right) \right.$$
$$- m_\phi^4 \left(4m_{\chi_i}^2 + 4s + 5t\right) + m_\phi^2 \left[4t m_{\chi_i}^2 + 2m_{\chi_i}^4 + t(4s+3t)\right] + 3m_\phi^6 \Big\}$$
$$+ m_{q_j}^4 \Big\{ t\left(-2m_{\chi_i}^2 + 2s + t\right) + 2s m_\phi^2 + m_\phi^4 \Big\} - 2m_{q_j}^6 m_\phi^2$$
$$\left. + s \Big\{ \left(m_\phi^4 + t^2\right)\left(-m_\phi^2 + s + t\right) + 2m_{\chi_i}^2 \left(m_\phi^4 - t(s+t)\right) + 2m_{\chi_i}^4 \left(t - m_\phi^2\right) \Big\} \right), \tag{B.11}$$

where $t_{\min/\max}(s) = t_{\min/\max}(s, m_{\chi_i}, m_\phi, m_{q_j}, 0)$.

• $\chi_i\,\chi_j \to q_k q_l$:

$$\sigma_{\chi_i\chi_j\to q_k q_l}(s) = \frac{3}{256\pi s \, p_{\mathrm{COM}}(s, m_{\chi_i}, m_{\chi_j})^2}$$
$$\times \int_{t_{\min}(s)}^{t_{\max}(s)} \mathrm{d}t \left( - \frac{2\mathrm{Re}(\lambda_{ki}\lambda_{kj}\lambda_{li}\lambda_{lj})\, m_{\chi_i} m_{\chi_j} (s - m_{q_k}^2 - m_{q_l}^2)}{(t - m_\phi^2)(m_{q_k}^2 + m_{q_l}^2 + m_{\chi_i}^2 + m_{\chi_j}^2 - m_\phi^2 - s - t)} \right.$$
$$+ \frac{|\lambda_{ki}|^2 |\lambda_{lj}|^2 (-m_{q_k}^2 - m_{\chi_i}^2 + t)(-m_{q_l}^2 - m_{\chi_j}^2 + t)}{(t - m_\phi^2)^2}$$
$$\left. + \frac{|\lambda_{kj}|^2 |\lambda_{li}|^2 (-m_{q_k}^2 - m_{\chi_j}^2 + s + t)(-m_{q_l}^2 - m_{\chi_i}^2 + s + t)}{(m_{q_k}^2 + m_{q_l}^2 + m_{\chi_i}^2 + m_{\chi_j}^2 - m_\phi^2 - s - t)^2} \right), \tag{B.12}$$

where $t_{\min/\max}(s) = t_{\min/\max}(s, m_{\chi_i}, m_{\chi_j}, m_{q_k}, m_{q_l})$.

## B.2 Cross sections for conversion processes (scatterings)

For the conversion via scattering we take into account the leading diagrams in $\alpha_s$ neglecting sub-leading electroweak contributions.

• $\phi, q_j \to \chi_i g$:

$$\begin{aligned}\sigma_{\phi q_j \to \chi_i g}(s) =& \frac{g_s^2 |\lambda_{ji}|^2}{72\pi s\, p_{\rm COM}(s, m_\phi, m_{q_j})^2} \int_{t_{\min}(s)}^{t_{\max}(s)} \mathrm{d}t \left( \frac{2m_{q_j}^4 (s - m_{\chi_i}^2)}{(t - m_\phi^2)\big( - m_{\chi_i}^2 - m_\phi^2 + s + t\big)^2} \right. \\ &+ \frac{2m_{q_j}^2 \{2m_{\chi_i}^2 (t m_\phi^2 - m_\phi^4 + st) + s[m_\phi^4 - t(s+t)] - t m_{\chi_i}^4\}}{(t - m_\phi^2)^2\big( - m_{\chi_i}^2 - m_\phi^2 + s + t\big)^2} \\ &\left. + \frac{t[st - m_{\chi_i}^2(2s+t)] + m_\phi^4 (s - 3m_{\chi_i}^2) + 2m_{\chi_i}^2 m_\phi^2 (m_{\chi_i}^2 + t)}{(t - m_\phi^2)^2\big( - m_{\chi_i}^2 - m_\phi^2 + s + t\big)} \right),\end{aligned} \tag{B.13}$$

where $t_{\min/\max}(s) = t_{\min/\max}(s, m_{q_j}, m_\phi, m_{\chi_i}, 0)$.

• $\phi\, g \to \chi_i q_j$:

$$\begin{aligned}\sigma_{\phi g \to \chi_i q_j}(s) =& \frac{g_s^2 |\lambda_{ji}|^2}{192\pi s (s - m_\phi^2)^2\, p_{\rm COM}(s, m_\phi, 0)^2} \\ &\times \int_{t_{\min}(s)}^{t_{\max}(s)} \mathrm{d}t \left( - \frac{m_{q_j}^4 \left[s\left(-2m_{\chi_i}^2 + s + 2t\right) + 2t m_\phi^2 + m_\phi^4\right]}{(t - m_{q_j}^2)^2} \right. \\ &+ \frac{m_{q_j}^2 \left[s\left(2m_{\chi_i}^4 - 4t m_{\chi_i}^2 + s^2 + 4st + 2t^2\right) - m_\phi^2\left(4s m_{\chi_i}^2 + 2m_{\chi_i}^4 + 3s^2 + 4st\right)\right]}{(t - m_{q_j}^2)^2} \\ &+ \frac{m_{q_j}^2 \left[m_\phi^4\left(4m_{\chi_i}^2 + 5s + 4t\right) - 3m_\phi^6\right] + 2m_{q_j}^6 m_\phi^2}{(t - m_{q_j}^2)^2} \\ &\left. + \frac{t\{(m_\phi^4 + s^2)(m_\phi^2 - s - t) + 2m_{\chi_i}^2 [s(s+t) - m_\phi^4] + 2m_{\chi_i}^4 (m_\phi^2 - s)\}}{(t - m_{q_j}^2)^2} \right),\end{aligned} \tag{B.14}$$

where $t_{\min/\max}(s) = t_{\min/\max}(s, m_\phi, 0, m_{\chi_i}, m_{q_j})$. Note that we regularized the soft divergence in the cross section for $\phi\, g \to \chi_i q_j$ by introducing a thermal mass for the gluon.

• $\chi_i\, q_k \to \chi_j q_l$:

$$\begin{aligned}\sigma_{\chi_i q_k\to\chi_j q_l}(s) = &\ \frac{1}{128\pi s\, p_{\rm COM}(s,m_{\chi_i},m_{q_k})^2}\\ &\times\int_{t_{\rm min}(s)}^{t_{\rm max}(s)}{\rm d}t\left(\frac{|\lambda_{ki}|^2|\lambda_{lj}|^2(-m_{q_k}^2-m_{\chi_i}^2+s)(-m_{q_l}^2-m_{\chi_j}^2+s)}{(\Gamma_\phi^2-2s)m_\phi^2+m_\phi^4+s^2}\right.\\ &+\frac{|\lambda_{kj}|^2|\lambda_{li}|^2(-m_{q_k}^2-m_{\chi_j}^2+t)(-m_{q_l}^2-m_{\chi_i}^2+t)}{(\Gamma_\phi^2-2t)m_\phi^2+m_\phi^4+t^2}\\ &\left.+\frac{2{\rm Re}(\lambda_{ki}\lambda_{kj}\lambda_{li}\lambda_{lj})\,m_{\chi_i}m_{\chi_j}\left[m_\phi^2\Gamma_\phi^2+(m_\phi^2-s)(m_\phi^2-t)\right](-m_{\chi_i}^2-m_{\chi_j}^2+s+t)}{\left[(\Gamma_\phi^2-2s)m_\phi^2+m_\phi^4+s^2\right]\left[(\Gamma_\phi^2-2t)m_\phi^2+m_\phi^4+t^2\right]}\right),\end{aligned} \tag{B.15}$$

where $t_{\rm min/max}(s) = t_{\rm min/max}(s, m_{\chi_i}, m_{q_k}, m_{q_l}, m_{\chi_j})$.

## B.3 Decay rates

Finally, we provide the decay rates for the heavier flavored Majorana dark matter particles ($\chi_1$ and $\chi_2$) and the mediator $\phi$.

• $\phi \to \chi_i q_j$:

$$\Gamma_{\phi\to\chi_i q_j} = \frac{|\lambda_{ji}|^2}{8\pi m_\phi^2}(m_\phi^2-m_{q_i}^2-m_{\chi_j}^2)\,p_{\rm COM}(m_\phi^2,m_{q_i},m_{\chi_j}) \tag{B.16}$$

• $\chi_i \to \chi_j q_k q_l$:

$$\begin{aligned}\Gamma_{\chi_i\to\chi_j q_k q_l} = &\ \frac{3}{128\pi m_{\chi_i}^3}\int_{m_{12}^{\rm min}}^{m_{12}^{\rm max}}{\rm d}m_{12}\int_{m_{23}^{\rm min}(m_{12})}^{m_{23}^{\rm max}(m_{12})}{\rm d}m_{23}\\ &\times\left(\frac{2{\rm Re}(\lambda_{ki}\lambda_{kj}\lambda_{li}\lambda_{lj})\,m_{\chi_i}m_{\chi_j}(m_{q_k}^2+m_{q_l}^2-m_{12})}{(m_{23}-m_\phi^2)(-m_{q_k}^2-m_{q_l}^2-m_{\chi_i}^2-m_{\chi_j}^2+m_\phi^2+m_{12}+m_{23})}\right.\\ &-\frac{|\lambda_{ki}|^2|\lambda_{lj}|^2(-m_{q_k}^2-m_{\chi_i}^2+m_{23})(-m_{q_l}^2-m_{\chi_j}^2+m_{23})}{(m_{23}-m_\phi^2)^2}\\ &\left.+\frac{|\lambda_{kj}|^2|\lambda_{li}|^2(-m_{q_k}^2-m_{\chi_j}^2+m_{12}+m_{23})(m_{q_l}^2+m_{\chi_i}^2-m_{12}-m_{23})}{(m_{q_k}^2+m_{q_l}^2+m_{\chi_i}^2+m_{\chi_j}^2-m_\phi^2-m_{12}-m_{23})^2}\right),\end{aligned} \tag{B.17}$$

where $m_{12}^{\min} = (m_{q_k} + m_{q_l})^2$, $m_{12}^{\max} = (m_{\chi_i} - m_{\chi_j})^2$, and

$$m_{23}^{\min}(m_{12}) = \frac{(m_{q_l}^2 - m_{q_k}^2 + m_{\chi_i}^2 - m_{\chi_j}^2)^2}{4m_{12}} - \left( \sqrt{\frac{(m_{12} - m_{q_k}^2 + m_{q_l}^2)^2}{4m_{12}} - m_{q_l}^2} + \sqrt{\frac{(m_{\chi_i}^2 - m_{12} - m_{\chi_j}^2)^2}{4m_{12}} - m_{\chi_j}^2} \right)^2, \tag{B.18}$$

$$m_{23}^{\max}(m_{12}) = \frac{(m_{q_l}^2 - m_{q_k}^2 + m_{\chi_i}^2 - m_{\chi_j}^2)^2}{4m_{12}} + \left( \sqrt{\frac{(m_{12} - m_{q_k}^2 + m_{q_l}^2)^2}{4m_{12}} - m_{q_l}^2} + \sqrt{\frac{(m_{\chi_i}^2 - m_{12} - m_{\chi_j}^2)^2}{4m_{12}} - m_{\chi_j}^2} \right)^2. \tag{B.19}$$

# Bibliography


[1] Harun Acaroğlu et al. "Flavoured Majorana Dark Matter then and now: from freeze-out scenarios to LHC signatures". In: *JHEP* 06 (2024), p. 179. DOI: 10.1007/JHEP06(2024)179. arXiv: 2312.09274 [hep-ph].

[2] Jan Heisig et al. "$\bar{\text{D}}$arkRayNet: emulation of cosmic-ray antideuteron fluxes from dark matter". In: *Journal of Cosmology and Astroparticle Physics* 2024.11 (Nov. 2024), p. 017. ISSN: 1475-7516. DOI: 10.1088/1475-7516/2024/11/017. URL: http://dx.doi.org/10.1088/1475-7516/2024/11/017.

[3] A. Arbey and F. Mahmoudi. "Dark matter and the early Universe: A review". In: *Progress in Particle and Nuclear Physics* 119 (July 2021), p. 103865. ISSN: 0146-6410. DOI: 10.1016/j.ppnp.2021.103865. URL: http://dx.doi.org/10.1016/j.ppnp.2021.103865.

[4] Gianfranco Bertone, Dan Hooper, and Joseph Silk. "Particle dark matter: Evidence, candidates and constraints". In: *Phys. Rept.* 405 (2005), pp. 279–390. DOI: 10.1016/j.physrep.2004.08.031. arXiv: hep-ph/0404175.

[5] Marco Cirelli, Alessandro Strumia, and Jure Zupan. *Dark Matter*. 2024. arXiv: 2406.01705 [hep-ph]. URL: https://arxiv.org/abs/2406.01705.

[6] N. Aghanim et al. "Planck 2018 results. VI. Cosmological parameters". In: *Astron. Astrophys.* 641 (2020). [Erratum: Astron.Astrophys. 652, C4 (2021)], A6. DOI: 10.1051/0004-6361/201833910. arXiv: 1807.06209 [astro-ph.CO].

[7] Jonathan L. Feng. "Dark Matter Candidates from Particle Physics and Methods of Detection". In: *Ann. Rev. Astron. Astrophys.* 48 (2010), pp. 495–545. DOI: 10.1146/annurev-astro-082708-101659. arXiv: 1003.0904 [astro-ph.CO].

[8] M. Bauer and T. Plehn. *Yet Another Introduction to Dark Matter*. Springer Cham, 2019.

[9] Pablo Villanueva-Domingo, Olga Mena, and Sergio Palomares-Ruiz. "A Brief Review on Primordial Black Holes as Dark Matter". In: *Frontiers in Astronomy and Space Sciences* 8 (May 2021). ISSN: 2296-987X. DOI: 10.3389/fspas.2021.681084. URL: http://dx.doi.org/10.3389/fspas.2021.681084.

[10] Stefano Profumo, Leonardo Giani, and Oliver F. Piattella. *An Introduction to Particle Dark Matter*. 2019. arXiv: 1910.05610 [hep-ph].

[11] Carlos Pérez de los Heros. "Status, Challenges and Directions in Indirect Dark Matter Searches". In: *Symmetry* 12.10 (Oct. 2020), p. 1648. ISSN: 2073-8994. DOI: 10.3390/sym12101648. URL: http://dx.doi.org/10.3390/sym12101648.

[12] Rebecca K. Leane. *Indirect Detection of Dark Matter in the Galaxy*. 2020. arXiv: 2006.00513 [hep-ph]. URL: https://arxiv.org/abs/2006.00513.

[13] Tracy R. Slatyer. *TASI Lectures on Indirect Detection of Dark Matter*. 2017. arXiv: 1710.05137 [hep-ph]. URL: https://arxiv.org/abs/1710.05137.

[14] Fiorenza Donato, Nicolao Fornengo, and Pierre Salati. "Anti-deuterons as a signature of supersymmetric dark matter". In: *Phys. Rev. D* 62 (2000), p. 043003. DOI: 10.1103/PhysRevD.62.043003. arXiv: hep-ph/9904481.

[15] Fiorenza Donato, Nicolao Fornengo, and David Maurin. "Antideuteron fluxes from dark matter annihilation in diffusion models". In: *Phys. Rev. D* 78 (2008), p. 043506. DOI: 10.1103/PhysRevD.78.043506. arXiv: 0803.2640 [hep-ph].

[16] T. Aramaki et al. "Review of the theoretical and experimental status of dark matter identification with cosmic-ray antideuterons". In: *Phys. Rept.* 618 (2016), pp. 1–37. DOI: 10.1016/j.physrep.2016.01.002. arXiv: 1505.07785 [hep-ph].

[17] Michael Korsmeier, Fiorenza Donato, and Nicolao Fornengo. "Prospects to verify a possible dark matter hint in cosmic antiprotons with antideuterons and antihelium". In: *Phys. Rev. D* 97.10 (2018), p. 103011. DOI: 10.1103/PhysRevD.97.103011. arXiv: 1711.08465 [astro-ph.HE].

[18] Diego-Mauricio Gomez-Coral et al. "Deuteron and Antideuteron Production Simulation in Cosmic-Ray Interactions". In: *Phys. Rev. D* 98.2 (2018), p. 023012. DOI: 10.1103/PhysRevD.98.023012. arXiv: 1806.09303 [astro-ph.HE].

[19] Pedro De La Torre Luque, Martin Wolfgang Winkler, and Tim Linden. "Cosmic-Ray Propagation Models Elucidate the Prospects for Antinuclei Detection". In: (Apr. 2024). arXiv: 2404.13114 [astro-ph.HE].

[20] Leszek Roszkowski, Enrico Maria Sessolo, and Sebastian Trojanowski. "WIMP dark matter candidates and searches—current status and future prospects". In: *Reports on Progress in Physics* 81.6 (May 2018), p. 066201. DOI: 10.1088/1361-6633/aab913. URL: https://dx.doi.org/10.1088/1361-6633/aab913.

[21] Giorgio Arcadi et al. "The waning of the WIMP? A review of models, searches, and constraints". In: *The European Physical Journal C* 78.3 (Mar. 2018). ISSN: 1434-6052. DOI: 10.1140/epjc/s10052-018-5662-y. URL: http://dx.doi.org/10.1140/epjc/s10052-018-5662-y.

[22] Jennifer Kile and Amarjit Soni. "Flavored Dark Matter in Direct Detection Experiments and at LHC". In: *Phys. Rev. D* 84 (2011), p. 035016. DOI: 10.1103/PhysRevD.84.035016. arXiv: 1104.5239 [hep-ph].

[23] Jernej F. Kamenik and Jure Zupan. "Discovering Dark Matter Through Flavor Violation at the LHC". In: *Phys. Rev. D* 84 (2011), p. 111502. DOI: 10.1103/PhysRevD.84.111502. arXiv: 1107.0623 [hep-ph].

[24] Prateek Agrawal et al. "Flavored Dark Matter, and Its Implications for Direct Detection and Colliders". In: *Phys. Rev. D* 86 (2012), p. 055002. DOI: 10.1103/PhysRevD.86.055002. arXiv: 1109.3516 [hep-ph].

[25] Brian Batell, Tongyan Lin, and Lian-Tao Wang. "Flavored Dark Matter and R-Parity Violation". In: *JHEP* 01 (2014), p. 075. DOI: 10.1007/JHEP01(2014)075. arXiv: 1309.4462 [hep-ph].

[26] Jennifer Kile. "Flavored Dark Matter: A Review". In: *Mod. Phys. Lett. A* 28 (2013), p. 1330031. DOI: 10.1142/S0217732313300310. arXiv: 1308.0584 [hep-ph].

[27] Prateek Agrawal et al. "Flavored Dark Matter and the Galactic Center Gamma-Ray Excess". In: *Phys. Rev. D* 90.6 (2014), p. 063512. DOI: 10.1103/PhysRevD.90.063512. arXiv: 1404.1373 [hep-ph].

[28] Jennifer Kile, Andrew Kobach, and Amarjit Soni. "Lepton-Flavored Dark Matter". In: *Phys. Lett. B* 744 (2015), pp. 330–338. DOI: 10.1016/j.physletb.2015.04.005. arXiv: 1411.1407 [hep-ph].

[29] Can Kilic, Matthew D. Klimek, and Jiang-Hao Yu. "Signatures of top flavored dark matter". In: *Physical Review D* 91.5 (Mar. 2015). ISSN: 1550-2368. DOI: 10.1103/physrevd.91.054036. URL: http://dx.doi.org/10.1103/PhysRevD.91.054036.

[30] A. J. Buras et al. "Universal unitarity triangle and physics beyond the standard model". In: *Phys. Lett. B* 500 (2001), pp. 161–167. DOI: 10.1016/S0370-2693(01)00061-2. arXiv: hep-ph/0007085.

[31] G. D'Ambrosio et al. "Minimal flavor violation: An Effective field theory approach". In: *Nucl. Phys. B* 645 (2002), pp. 155–187. DOI: 10.1016/S0550-3213(02)00836-2. arXiv: hep-ph/0207036.

[32] R. Sekhar Chivukula and Howard Georgi. "Composite Technicolor Standard Model". In: *Phys. Lett. B* 188 (1987), pp. 99–104. DOI: 10.1016/0370-2693(87)90713-1.

[33] L. J. Hall and Lisa Randall. "Weak scale effective supersymmetry". In: *Phys. Rev. Lett.* 65 (1990), pp. 2939–2942. DOI: 10.1103/PhysRevLett.65.2939.

[34] Prateek Agrawal, Monika Blanke, and Katrin Gemmler. "Flavored dark matter beyond Minimal Flavor Violation". In: *JHEP* 10 (2014), p. 072. DOI: 10.1007/JHEP10(2014)072. arXiv: 1405.6709 [hep-ph].

[35] Monika Blanke and Simon Kast. "Top-Flavoured Dark Matter in Dark Minimal Flavour Violation". In: *JHEP* 05 (2017), p. 162. DOI: 10.1007/JHEP05(2017)162. arXiv: 1702.08457 [hep-ph].

[36] Thomas Jubb, Matthew Kirk, and Alexander Lenz. "Charming Dark Matter". In: *JHEP* 12 (2017), p. 010. DOI: 10.1007/JHEP12(2017)010. arXiv: 1709.01930 [hep-ph].

[37] Monika Blanke et al. "Single-top final states as a probe of top-flavoured dark matter models at the LHC". In: *JHEP* 01 (2021), p. 194. DOI: 10.1007/JHEP01(2021)194. arXiv: 2010.10530 [hep-ph].

[38] Wafia Bensalem and Daniel Stolarski. "Flavor and CP violation from a QCD-like hidden sector". In: *JHEP* 02 (2022), p. 011. DOI: 10.1007/JHEP02(2022)011. arXiv: 2111.05515 [hep-ph].

[39] Monika Blanke, Satrajit Das, and Simon Kast. "Flavoured Dark Matter Moving Left". In: *JHEP* 02 (2018), p. 105. DOI: 10.1007/JHEP02(2018)105. arXiv: 1711.10493 [hep-ph].

[40] Mu-Chun Chen, Jinrui Huang, and Volodymyr Takhistov. "Beyond Minimal Lepton Flavored Dark Matter". In: *JHEP* 02 (2016), p. 060. DOI: 10.1007/JHEP02(2016)060. arXiv: 1510.04694 [hep-ph].

[41] Harun Acaroğlu and Monika Blanke. "Tasting flavoured Majorana dark matter". In: *JHEP* 05 (2022), p. 086. DOI: 10.1007/JHEP05(2022)086. arXiv: 2109.10357 [hep-ph].

[42] Harun Acaroğlu, Prateek Agrawal, and Monika Blanke. "Lepton-flavoured scalar dark matter in Dark Minimal Flavour Violation". In: *JHEP* 05 (2023), p. 106. DOI: 10.1007/JHEP05(2023)106. arXiv: 2211.03809 [hep-ph].

[43] Harun Acaroğlu, Prateek Agrawal, and Monika Blanke. "Flavoured $(g-2)_\mu$ with dark lepton seasoning". In: *SciPost Phys.* 15.4 (2023), p. 176. DOI: 10.21468/SciPostPhys.15.4.176. arXiv: 2212.08142 [hep-ph].

[44] Harun Acaroğlu, Monika Blanke, and Mustafa Tabet. "Opening the Higgs portal to lepton-flavoured dark matter". In: *JHEP* 11 (2023), p. 079. DOI: 10.1007/JHEP11(2023)079. arXiv: 2309.10700 [hep-ph].

[45] Katherine Freese. "Status of dark matter in the universe". In: *International Journal of Modern Physics D* 26.06 (Mar. 2017), p. 1730012. ISSN: 1793-6594. DOI: 10.1142/s0218271817300129. URL: http://dx.doi.org/10.1142/S0218271817300129.

[46] Gianfranco Bertone and Dan Hooper. "History of dark matter". In: *Reviews of Modern Physics* 90.4 (Oct. 2018). ISSN: 1539-0756. DOI: 10.1103/revmodphys.90.045002. URL: http://dx.doi.org/10.1103/RevModPhys.90.045002.

[47] F. Zwicky. "Die Rotverschiebung von extragalaktischen Nebeln". In: *Helvetica Physica Acta* 6 (Jan. 1933), pp. 110–127.

[48] K. G. Begeman, A. H. Broeils, and R. H. Sanders. "Extended rotation curves of spiral galaxies : dark haloes and modified dynamics." In: *mnras* 249 (Apr. 1991), p. 523. DOI: 10.1093/mnras/249.3.523.

[49] Julio F. Navarro, Carlos S. Frenk, and Simon D. M. White. "The Structure of Cold Dark Matter Halos". In: *The Astrophysical Journal* 462 (May 1996), p. 563. ISSN: 1538-4357. DOI: 10.1086/177173. URL: http://dx.doi.org/10.1086/177173.

[50] A. Burkert. "The Structure of Dark Matter Halos in Dwarf Galaxies". In: *The Astrophysical Journal* 447.1 (July 1995). ISSN: 0004-637X. DOI: 10.1086/309560. URL: http://dx.doi.org/10.1086/309560.

[51] J. Einasto. "On the Construction of a Composite Model for the Galaxy and on the Determination of the System of Galactic Parameters". In: *Trudy Astrofizicheskogo Instituta Alma-Ata* 5 (Jan. 1965), pp. 87–100.

[52] Thomas Siegert, Francesca Calore, and Pasquale Dario Serpico. "Sub-GeV Dark Matter Annihilation: Limits from Milky Way observations with INTEGRAL". In: (Jan. 2024). arXiv: 2401.03795 [astro-ph.HE].

[53] M. Milgrom. "A modification of the Newtonian dynamics as a possible alternative to the hidden mass hypothesis." In: *The Astrophysical Journal* 270 (July 1983), pp. 365–370. DOI: 10.1086/161130.

[54] Keiichi Umetsu. "Cluster–galaxy weak lensing". In: *The Astronomy and Astrophysics Review* 28.1 (Nov. 2020). ISSN: 1432-0754. DOI: 10.1007/s00159-020-00129-w. URL: http://dx.doi.org/10.1007/s00159-020-00129-w.

[55] Maxim Markevitch. *Chandra observation of the most interesting cluster in the Universe*. 2005. arXiv: astro-ph/0511345 [astro-ph].

[56] Douglas Clowe et al. "A Direct Empirical Proof of the Existence of Dark Matter". In: *The Astrophysical Journal* 648.2 (Aug. 2006), pp. L109–L113. ISSN: 1538-4357. DOI: 10.1086/508162. URL: http://dx.doi.org/10.1086/508162.

[57] David Harvey et al. "The nongravitational interactions of dark matter in colliding galaxy clusters". In: *Science* 347.6229 (Mar. 2015), pp. 1462–1465. ISSN: 1095-9203. DOI: 10.1126/science.1261381. URL: http://dx.doi.org/10.1126/science.1261381.

[58] Alistair O. Hodson and Hongsheng Zhao. "Generalizing MOND to explain the missing mass in galaxy clusters". In: *Astronomy & Astrophysics* 598 (Feb. 2017), A127. ISSN: 1432-0746. DOI: 10.1051/0004-6361/201629358. URL: http://dx.doi.org/10.1051/0004-6361/201629358.

[59] Donald G. York et al. "The Sloan Digital Sky Survey: Technical Summary". In: *The Astronomical Journal* 120.3 (Sept. 2000), pp. 1579–1587. ISSN: 0004-6256. DOI: 10.1086/301513. URL: http://dx.doi.org/10.1086/301513.

[60] Volker Springel et al. "Simulations of the formation, evolution and clustering of galaxies and quasars". In: *Nature* 435 (June 2005). DOI: 10.1038/nature03597.

[61] R. L. Workman et al. "Review of Particle Physics". In: *PTEP* 2022 (2022), p. 083C01. DOI: 10.1093/ptep/ptac097.

[62] Samuel D. McDermott, Hai-Bo Yu, and Kathryn M. Zurek. "Turning off the lights: How dark is dark matter?" In: *Physical Review D* 83.6 (Mar. 2011). ISSN: 1550-2368. DOI: 10.1103/physrevd.83.063509. URL: http://dx.doi.org/10.1103/PhysRevD.83.063509.

[63] Benjamin R. Safdi. *TASI Lectures on the Particle Physics and Astrophysics of Dark Matter*. 2023. arXiv: 2303.02169 [hep-ph].

[64] Daniel Baumann. *Cosmology*. Cambridge University Press, July 2022. DOI: 10.1017/9781108937092.

[65] Paolo Gondolo and Graciela Gelmini. "Cosmic Abundances of Stable Particles: improved analysis". In: *Nuclear Physics B - NUCL PHYS B* 360 (Aug. 1991), pp. 145–179. DOI: 10.1016/0550-3213(91)90438-4.

[66] Nicolás Bernal et al. "The dawn of FIMP Dark Matter: A review of models and constraints". In: *International Journal of Modern Physics A* 32.27 (Sept. 2017), p. 1730023. ISSN: 1793-656X. DOI: 10.1142/s0217751x1730023x. URL: http://dx.doi.org/10.1142/S0217751X1730023X.

[67] Marcin Misiaszek and Nicola Rossi. "Direct Detection of Dark Matter: A Critical Review". In: *Symmetry* 16.2 (Feb. 2024), p. 201. ISSN: 2073-8994. DOI: 10.3390/sym16020201. URL: http://dx.doi.org/10.3390/sym16020201.

[68] Julien Billard et al. "Direct detection of dark matter—APPEC committee report*". In: *Reports on Progress in Physics* 85.5 (Apr. 2022), p. 056201. ISSN: 1361-6633. DOI: 10.1088/1361-6633/ac5754. URL: http://dx.doi.org/10.1088/1361-6633/ac5754.

[69] XENON Collaboration et al. *The XENONnT Dark Matter Experiment*. 2024. arXiv: 2402.10446 [physics.ins-det]. URL: https://arxiv.org/abs/2402.10446.

[70] D.S. Akerib et al. "The LUX-ZEPLIN (LZ) experiment". In: *Nuclear Instruments and Methods in Physics Research Section A: Accelerators, Spectrometers, Detectors and Associated Equipment* 953 (Feb. 2020), p. 163047. ISSN: 0168-9002. DOI: 10.1016/j.nima.2019.163047. URL: http://dx.doi.org/10.1016/j.nima.2019.163047.

[71] HongGuang Zhang et al. "Dark matter direct search sensitivity of the PandaX-4T experiment". In: *Science China Physics, Mechanics & Astronomy* 62.3 (Aug. 2018). ISSN: 1869-1927. DOI: 10.1007/s11433-018-9259-0. URL: http://dx.doi.org/10.1007/s11433-018-9259-0.

[72] P. Agnes et al. "Low-Mass Dark Matter Search with the DarkSide-50 Experiment". In: *Physical Review Letters* 121.8 (Aug. 2018). ISSN: 1079-7114. DOI: 10.1103/physrevlett.121.081307. URL: http://dx.doi.org/10.1103/PhysRevLett.121.081307.

[73] Mark Stringer. "The DEAP-3600 Experiment". In: *Proceedings of 37th International Cosmic Ray Conference — PoS(ICRC2021)*. Vol. 395. 2021, p. 527. DOI: 10.22323/1.395.0527.

[74] Ioannis Manthos. "DarkSide-20k: Next generation Direct Dark Matter searches with liquid Argon". In: *Proceedings of The European Physical Society Conference on High Energy Physics — PoS(EPS-HEP2023)*. EPS-HEP2023. Sissa Medialab, Feb. 2024, p. 113. DOI: 10.22323/1.449.0113. URL: http://dx.doi.org/10.22323/1.449.0113.

[75] R. Agnese et al. "Search for low-mass dark matter with CDMSlite using a profile likelihood fit". In: *Physical Review D* 99.6 (Mar. 2019). ISSN: 2470-0029. DOI: 10.1103/physrevd.99.062001. URL: http://dx.doi.org/10.1103/PhysRevD.99.062001.

[76] A. H. Abdelhameed et al. "First results from the CRESST-III low-mass dark matter program". In: *Physical Review D* 100.10 (Nov. 2019). ISSN: 2470-0029. DOI: 10.1103/physrevd.100.102002. URL: http://dx.doi.org/10.1103/PhysRevD.100.102002.

[77] R. Bernabei et al. "The DAMA project: Achievements, implications and perspectives". In: *Progress in Particle and Nuclear Physics* 114 (Sept. 2020), p. 103810. ISSN: 0146-6410. DOI: https://doi.org/10.1016/j.ppnp.2020.103810. URL: https://www.sciencedirect.com/science/article/pii/S0146641020300570.

[78] C. Amole et al. "Dark matter search results from the complete exposure of the PICO-60 $C_3F_8$ bubble chamber". In: *Physical Review D* 100.2 (July 2019). ISSN: 2470-0029. DOI: 10.1103/physrevd.100.022001. URL: http://dx.doi.org/10.1103/PhysRevD.100.022001.

[79] E. Aprile et al. "First Dark Matter Search with Nuclear Recoils from the XENONnT Experiment". In: *Physical Review Letters* 131.4 (July 2023). ISSN: 1079-7114. DOI: 10.1103/physrevlett.131.041003. URL: http://dx.doi.org/10.1103/PhysRevLett.131.041003.

[80] J. Aalbers et al. "First Dark Matter Search Results from the LUX-ZEPLIN (LZ) Experiment". In: *Physical Review Letters* 131.4 (July 2023). ISSN: 1079-7114. DOI: 10.1103/physrevlett.131.041002. URL: http://dx.doi.org/10.1103/PhysRevLett.131.041002.

[81] Yue Meng et al. "Dark Matter Search Results from the PandaX-4T Commissioning Run". In: *Physical Review Letters* 127.26 (Dec. 2021). ISSN: 1079-7114. DOI: 10.1103/physrevlett.127.261802. URL: http://dx.doi.org/10.1103/PhysRevLett.127.261802.

[82] Patrick J. Fox et al. "LEP shines light on dark matter". In: *Physical Review D* 84.1 (July 2011). ISSN: 1550-2368. DOI: 10.1103/physrevd.84.014028. URL: http://dx.doi.org/10.1103/PhysRevD.84.014028.

[83] Matthew D. Schwartz. *TASI Lectures on Collider Physics*. 2017. arXiv: 1709.04533 [hep-ph]. URL: https://arxiv.org/abs/1709.04533.

[84] Antonio Boveia and Caterina Doglioni. "Dark Matter Searches at Colliders". In: *Annual Review of Nuclear and Particle Science* 68.1 (Oct. 2018), pp. 429–459. ISSN: 1545-4134. DOI: 10.1146/annurev-nucl-101917-021008. URL: http://dx.doi.org/10.1146/annurev-nucl-101917-021008.

[85] Felix Kahlhoefer. "Review of LHC dark matter searches". In: *International Journal of Modern Physics A* 32.13 (May 2017), p. 1730006. ISSN: 1793-656X. DOI: 10.1142/s0217751x1730006x. URL: http://dx.doi.org/10.1142/S0217751X1730006X.

[86] Juliette Alimena et al. "Searching for long-lived particles beyond the Standard Model at the Large Hadron Collider". In: *Journal of Physics G: Nuclear and Particle Physics* 47.9 (Sept. 2020), p. 090501. ISSN: 1361-6471. DOI: 10.1088/1361-6471/ab4574. URL: http://dx.doi.org/10.1088/1361-6471/ab4574.

[87] Jalal Abdallah et al. "Simplified models for dark matter searches at the LHC". In: *Physics of the Dark Universe* 9–10 (Sept. 2015), pp. 8–23. ISSN: 2212-6864. DOI: 10.1016/j.dark.2015.08.001. URL: http://dx.doi.org/10.1016/j.dark.2015.08.001.

[88] Nassim Bozorgnia et al. *Dark Matter Candidates and Searches*. 2024. arXiv: 2410.23454 [hep-ph]. URL: https://arxiv.org/abs/2410.23454.

[89] Lawrence Lee et al. "Collider searches for long-lived particles beyond the Standard Model". In: *Progress in Particle and Nuclear Physics* 106 (May 2019), pp. 210–255. ISSN: 0146-6410. DOI: 10.1016/j.ppnp.2019.02.006. URL: http://dx.doi.org/10.1016/j.ppnp.2019.02.006.

[90] Marco Cirelli et al. "PPPC 4 DM ID: a poor particle physicist cookbook for dark matter indirect detection". In: *Journal of Cosmology and Astroparticle Physics* 2011.03 (Mar. 2011), pp. 051–051. ISSN: 1475-7516. DOI: 10.1088/1475-7516/2011/03/051. URL: http://dx.doi.org/10.1088/1475-7516/2011/03/051.

[91] Chiara Arina et al. "CosmiXs: cosmic messenger spectra for indirect dark matter searches". In: *JCAP* 03 (2024), p. 035. DOI: 10.1088/1475-7516/2024/03/035. arXiv: 2312.01153 [astro-ph.HE].

[92] F. W. Stecker. "The cosmic gamma -ray background from the annihilation of primordial stable neutral heavy leptons." In: *Astrophysical Journal* 223 (Aug. 1978), pp. 1032–1036. DOI: 10.1086/156336.

[93] W. B. Atwood et al. "The Large Area Telescope on the Fermi Gamma-ray Space Telescope Mission". In: *The Astrophysical Journal* 697.2 (May 2009), pp. 1071–1102. ISSN: 1538-4357. DOI: 10.1088/0004-637x/697/2/1071. URL: http://dx.doi.org/10.1088/0004-637X/697/2/1071.

[94] E. Lorenz. "Status of the 17-m MAGIC telescope". In: *New Astron. Rev.* 48 (2004), pp. 339–344. DOI: 10.1016/j.newar.2003.12.059.

[95] J. Aleksić et al. "The major upgrade of the MAGIC telescopes, Part II: A performance study using observations of the Crab Nebula". In: *Astroparticle Physics* 72 (Jan. 2016), pp. 76–94. ISSN: 0927-6505. DOI: 10.1016/j.astropartphys.2015.02.005. URL: http://dx.doi.org/10.1016/j.astropartphys.2015.02.005.

[96] T.C Weekes et al. "VERITAS: the Very Energetic Radiation Imaging Telescope Array System". In: *Astroparticle Physics* 17.2 (May 2002), pp. 221–243. ISSN: 0927-6505. DOI: 10.1016/s0927-6505(01)00152-9. URL: http://dx.doi.org/10.1016/S0927-6505(01)00152-9.

[97] H.E.S.S. Collaboration. *H.E.S.S. First Public Test Data Release*. en. 2018. DOI: 10.5281/ZENODO.1421098. URL: https://zenodo.org/record/1421098.

[98] J.A Hinton. "The status of the HESS project". In: *New Astronomy Reviews* 48.5–6 (Apr. 2004), pp. 331–337. ISSN: 1387-6473. DOI: 10.1016/j.newar.2003.12.004. URL: http://dx.doi.org/10.1016/j.newar.2003.12.004.

[99] A. Albert et al. "3HWC: The Third HAWC Catalog of Very-high-energy Gamma-Ray Sources". In: *The Astrophysical Journal* 905.1 (Dec. 2020), p. 76. ISSN: 1538-4357. DOI: 10.3847/1538-4357/abc2d8. URL: http://dx.doi.org/10.3847/1538-4357/abc2d8.

[100] Zhen Cao et al. "The First LHAASO Catalog of Gamma-Ray Sources". In: *The Astrophysical Journal Supplement Series* 271.1 (Feb. 2024), p. 25. ISSN: 1538-4365. DOI: 10.3847/1538-4365/acfd29. URL: http://dx.doi.org/10.3847/1538-4365/acfd29.

[101] Esra Bulbul et al. "Detection of An Unidentified Emission Line in the Stacked X-ray spectrum of Galaxy Clusters". In: *The Astrophysical Journal* 789.1 (June 2014), p. 13. ISSN: 1538-4357. DOI: 10.1088/0004-637x/789/1/13. URL: http://dx.doi.org/10.1088/0004-637X/789/1/13.

[102] A. Boyarsky et al. "Unidentified Line in X-Ray Spectra of the Andromeda Galaxy and Perseus Galaxy Cluster". In: *Physical Review Letters* 113.25 (Dec. 2014). ISSN: 1079-7114. DOI: 10.1103/physrevlett.113.251301. URL: http://dx.doi.org/10.1103/PhysRevLett.113.251301.

[103] Winkler, C. et al. "The INTEGRAL mission". In: *A&A* 411.1 (2003), pp. L1–L6. DOI: 10.1051/0004-6361:20031288. URL: https://doi.org/10.1051/0004-6361:20031288.

[104] Daniel A. Schwartz. "Invited Review Article: The Chandra X-ray Observatory". In: *Review of Scientific Instruments* 85.6, 061101 (June 2014), p. 061101. DOI: 10.1063/1.4881695.

[105] Kazuhisa Mitsuda et al. "The X-Ray Observatory Suzaku". In: *pasj* 59 (Jan. 2007), pp. 1–7. DOI: 10.1093/pasj/59.sp1.S1.

[106] Fiona A. Harrison et al. "The Nuclear Spectroscopic Telescope Array (NuSTAR) High-energy X-Ray Mission". In: *The Astrophysical Journal* 770.2 (May 2013), p. 103. ISSN: 1538-4357. DOI: 10.1088/0004-637x/770/2/103. URL: http://dx.doi.org/10.1088/0004-637X/770/2/103.

[107] Andrew Gould. "Resonant Enhancements in Weakly Interacting Massive Particle Capture by the Earth". In: *Astrophysical Journal* 321 (Oct. 1987), p. 571. DOI: 10.1086/165653.

[108] Francis Halzen and Spencer R. Klein. "Invited Review Article: IceCube: An instrument for neutrino astronomy". In: *Review of Scientific Instruments* 81.8 (Aug. 2010). ISSN: 1089-7623. DOI: 10.1063/1.3480478. URL: http://dx.doi.org/10.1063/1.3480478.

[109] M. Ageron et al. "ANTARES: The first undersea neutrino telescope". In: *Nuclear Instruments and Methods in Physics Research Section A: Accelerators, Spectrometers, Detectors and Associated Equipment* 656.1 (Nov. 2011), pp. 11–38. ISSN: 0168-9002. DOI: 10.1016/j.nima.2011.06.103. URL: http://dx.doi.org/10.1016/j.nima.2011.06.103.

[110] S. Fukuda et al. "The Super-Kamiokande detector". In: *Nuclear Instruments and Methods in Physics Research Section A: Accelerators, Spectrometers, Detectors and Associated Equipment* 501.2 (2003), pp. 418–462. ISSN: 0168-9002. DOI: https://doi.org/10.1016/S0168-9002(03)00425-X. URL: https://www.sciencedirect.com/science/article/pii/S016890020300425X.

[111] Grigory Safronov. *Baikal-GVD: status and first results*. 2020. arXiv: 2012.03373 [astro-ph.HE]. URL: https://arxiv.org/abs/2012.03373.

[112] John Ellis et al. "Cosmic ray constraints on the annihilations of relic particles in the galactic halo". In: *Physics Letters B* 214.3 (1988), pp. 403–412. ISSN: 0370-2693. DOI: https://doi.org/10.1016/0370-2693(88)91385-8. URL: https://www.sciencedirect.com/science/article/pii/0370269388913858.

[113] Roberto Battiston. "The antimatter spectrometer (AMS-02): A particle physics detector in space". In: *Nuclear Instruments and Methods in Physics Research Section A: Accelerators, Spectrometers, Detectors and Associated Equipment* 588.1 (2008). Proceedings of the First International Conference on Astroparticle Physics, pp. 227–234. ISSN: 0168-9002. DOI: https://doi.org/10.1016/j.nima.2008.01.044. URL: https://www.sciencedirect.com/science/article/pii/S0168900208000727.

[114] O. Adriani et al. "The PAMELA Mission: Heralding a new era in precision cosmic ray physics". In: *Phys. Rept.* 544 (2014), pp. 323–370. DOI: 10.1016/j.physrep.2014.06.003.

[115] J. Chang et al. "The DArk Matter Particle Explorer mission". In: *Astroparticle Physics* 95 (Oct. 2017), pp. 6–24. ISSN: 0927-6505. DOI: 10.1016/j.astropartphys.2017.08.005. URL: http://dx.doi.org/10.1016/j.astropartphys.2017.08.005.

[116] N. Cannady et al. "Characteristics and Performance of the CALorimetric Electron Telescope (CALET) Calorimeter for Gamma-Ray Observations". In: *The Astrophysical Journal Supplement Series* 238.1 (Sept. 2018), p. 5. DOI: 10.3847/1538-4365/aad6a3. URL: https://dx.doi.org/10.3847/1538-4365/aad6a3.

[117] M. Aguilar et al. "First Result from the Alpha Magnetic Spectrometer on the International Space Station: Precision Measurement of the Positron Fraction in Primary Cosmic Rays of 0.5-350 GeV". In: *Phys. Rev. Lett.* 110 (2013), p. 141102. DOI: 10.1103/PhysRevLett.110.141102.

[118] L. Accardo et al. "High Statistics Measurement of the Positron Fraction in Primary Cosmic Rays of 0.5-500 GeV with the Alpha Magnetic Spectrometer on the International Space Station". In: *Phys. Rev. Lett.* 113 (2014), p. 121101. DOI: 10.1103/PhysRevLett.113.121101.

[119] O. Adriani et al. "An anomalous positron abundance in cosmic rays with energies 1.5–100 GeV". In: *Nature* 458.7238 (Apr. 2009), pp. 607–609. ISSN: 1476-4687. DOI: 10.1038/nature07942. URL: http://dx.doi.org/10.1038/nature07942.

[120] O. Adriani et al. "A statistical procedure for the identification of positrons in the PAMELA experiment". In: *Astroparticle Physics* 34.1 (Aug. 2010), pp. 1–11. ISSN: 0927-6505. DOI: 10.1016/j.astropartphys.2010.04.007. URL: http://dx.doi.org/10.1016/j.astropartphys.2010.04.007.

[121] Lars Bergström, Torsten Bringmann, and Joakim Edsjö. "New positron spectral features from supersymmetric dark matter: A way to explain the PAMELA data?" In: *Physical Review D* 78.10 (Nov. 2008). ISSN: 1550-2368. DOI: 10.1103/physrevd.78.103520. URL: http://dx.doi.org/10.1103/PhysRevD.78.103520.

[122] M. Cirelli et al. "Model-independent implications of the e+, e-, anti-proton cosmic ray spectra on properties of Dark Matter". In: *Nuclear Physics B* 813.1–2 (May 2009), pp. 1–21. ISSN: 0550-3213. DOI: 10.1016/j.nuclphysb.2008.11.031. URL: http://dx.doi.org/10.1016/j.nuclphysb.2008.11.031.

[123] M. Di Mauro et al. "Interpretation of AMS-02 electrons and positrons data". In: *Journal of Cosmology and Astroparticle Physics* 2014.04 (Apr. 2014), pp. 006–006. ISSN: 1475-7516. DOI: 10.1088/1475-7516/2014/04/006. URL: http://dx.doi.org/10.1088/1475-7516/2014/04/006.

[124] Joseph Silk and Mark Srednicki. "Cosmic Ray anti-Protons as a Probe of a Photino Dominated Universe". In: *Phys. Rev. Lett.* 53 (1984). Ed. by M. A. Srednicki, p. 624. DOI: 10.1103/PhysRevLett.53.624.

[125] Andrew W. Strong and Igor V. Moskalenko. "Propagation of Cosmic-Ray Nucleons in the Galaxy". In: *The Astrophysical Journal* 509.1 (Dec. 1998), pp. 212–228. ISSN: 1538-4357. DOI: 10.1086/306470. URL: http://dx.doi.org/10.1086/306470.

[126] Kenichi Yoshimura et al. "BESS-Polar II experiment". In: *Proceedings of the 30th International Cosmic Ray Conference, ICRC 2007* 2 (Jan. 2007), pp. 91–94.

[127] S.A.I. Mognet et al. "The prototype GAPS (pGAPS) experiment". In: *Nuclear Instruments and Methods in Physics Research Section A: Accelerators, Spectrometers, Detectors and Associated Equipment* 735 (Jan. 2014), pp. 24–38. ISSN: 0168-9002. DOI: 10.1016/j.nima.2013.08.030. URL: http://dx.doi.org/10.1016/j.nima.2013.08.030.

[128] Vanda Silveira and A. Zee. "Scalar Phantoms". In: *Physics Letters B* 161.1 (1985), pp. 136–140. ISSN: 0370-2693. DOI: https://doi.org/10.1016/0370-2693(85)90624-0. URL: https://www.sciencedirect.com/science/article/pii/0370269385906240.

[129] John McDonald. "Gauge singlet scalars as cold dark matter". In: *Physical Review D* 50.6 (Sept. 1994), pp. 3637–3649. ISSN: 0556-2821. DOI: 10.1103/physrevd.50.3637. URL: http://dx.doi.org/10.1103/PhysRevD.50.3637.

[130] C.P. Burgess, Maxim Pospelov, and Tonnis ter Veldhuis. "The Minimal Model of nonbaryonic dark matter: a singlet scalar". In: *Nuclear Physics B* 619.1–3 (Dec. 2001), pp. 709–728. ISSN: 0550-3213. DOI: 10.1016/s0550-3213(01)00513-2. URL: http://dx.doi.org/10.1016/S0550-3213(01)00513-2.

[131] James M. Cline et al. "Update on scalar singlet dark matter". In: *Physical Review D* 88.5 (Sept. 2013). ISSN: 1550-2368. DOI: 10.1103/physrevd.88.055025. URL: http://dx.doi.org/10.1103/PhysRevD.88.055025.

[132] Peter Athron et al. "Global analyses of Higgs portal singlet dark matter models using GAMBIT". In: *The European Physical Journal C* 79.1 (Jan. 2019). ISSN: 1434-6052. DOI: 10.1140/epjc/s10052-018-6513-6. URL: http://dx.doi.org/10.1140/epjc/s10052-018-6513-6.

[133] Peter Athron et al. "Impact of vacuum stability, perturbativity and XENON1T on global fits of $\mathbb{Z}_2$ and $\mathbb{Z}_3$ scalar singlet dark matter". In: *The European Physical Journal C* 78.10 (Oct. 2018). ISSN: 1434-6052. DOI: 10.1140/epjc/s10052-018-6314-y. URL: http://dx.doi.org/10.1140/epjc/s10052-018-6314-y.

[134] Xiao-Gang He and Jusak Tandean. "New LUX and PandaX-II results illuminating the simplest Higgs-portal dark matter models". In: *Journal of High Energy Physics* 2016.12 (Dec. 2016). ISSN: 1029-8479. DOI: 10.1007/jhep12(2016)074. URL: http://dx.doi.org/10.1007/JHEP12(2016)074.

[135] Mattia Di Mauro et al. "Dark matter in the Higgs resonance region". In: *Phys. Rev. D* 108.9 (2023), p. 095008. DOI: 10.1103/PhysRevD.108.095008. arXiv: 2305.11937 [hep-ph].

[136] Alessandro Cuoco et al. "A global fit of the $\gamma$-ray galactic center excess within the scalar singlet Higgs portal model". In: *JCAP* 06 (2016), p. 050. DOI: 10.1088/1475-7516/2016/06/050. arXiv: 1603.08228 [hep-ph].

[137] Alessandro Cuoco et al. "Probing dark matter annihilation in the Galaxy with antiprotons and gamma rays". In: *Journal of Cosmology and Astroparticle Physics* 2017.10 (Oct. 2017), pp. 053–053. ISSN: 1475-7516. DOI: 10.1088/1475-7516/2017/10/053. URL: http://dx.doi.org/10.1088/1475-7516/2017/10/053.

[138] Vernon Barger et al. "CERN LHC phenomenology of an extended standard model with a real scalar singlet". In: *Physical Review D* 77.3 (Feb. 2008). ISSN: 1550-2368. DOI: 10.1103/physrevd.77.035005. URL: http://dx.doi.org/10.1103/PhysRevD.77.035005.

[139] Seungwon Baek, P. Ko, and Wan-Il Park. *Local $Z_2$ scalar dark matter model confronting galactic GeV-scale $\gamma$-ray*. 2015. arXiv: 1407.6588 [hep-ph]. URL: https://arxiv.org/abs/1407.6588.

[140] Ankit Beniwal et al. "Combined analysis of effective Higgs portal dark matter models". In: *Physical Review D* 93.11 (June 2016). ISSN: 2470-0029. DOI: 10.1103/physrevd.93.115016. URL: http://dx.doi.org/10.1103/PhysRevD.93.115016.

[141] Brian Batell, Josef Pradler, and Michael Spannowsky. "Dark Matter from Minimal Flavor Violation". In: *JHEP* 08 (2011), p. 038. DOI: 10.1007/JHEP08(2011)038. arXiv: 1105.1781 [hep-ph].

[142] Laura Lopez-Honorez and Luca Merlo. "Dark matter within the minimal flavour violation ansatz". In: *Phys. Lett. B* 722 (2013), pp. 135–143. DOI: 10.1016/j.physletb.2013.04.015. arXiv: 1303.1087 [hep-ph].

[143] Abhishek Kumar and Sean Tulin. "Top-flavored dark matter and the forward-backward asymmetry". In: *Phys. Rev. D* 87.9 (2013), p. 095006. DOI: 10.1103/PhysRevD.87.095006. arXiv: 1303.0332 [hep-ph].

[144] Chao-Jung Lee and Jusak Tandean. "Lepton-Flavored Scalar Dark Matter with Minimal Flavor Violation". In: *JHEP* 04 (2015), p. 174. DOI: 10.1007/JHEP04(2015)174. arXiv: 1410.6803 [hep-ph].

[145] Prateek Agrawal et al. "A Couplet from Flavored Dark Matter". In: *JHEP* 08 (2015), p. 072. DOI: 10.1007/JHEP08(2015)072. arXiv: 1503.03057 [hep-ph].

[146] M. Aguilar et al. "The Alpha Magnetic Spectrometer (AMS) on the international space station: Part II — Results from the first seven years". In: *Physics Reports* 894 (2021). The Alpha Magnetic Spectrometer (AMS) on the International Space Station: Part II - Results from the First Seven Years, pp. 1–116. ISSN: 0370-1573. DOI: https://doi.org/10.1016/j.physrep.2020.09.003. URL: https://www.sciencedirect.com/science/article/pii/S0370157320303434.

[147] Alessandro Cuoco et al. "Constraining heavy dark matter with cosmic-ray antiprotons". In: *JCAP* 04 (2018), p. 004. DOI: 10.1088/1475-7516/2018/04/004. arXiv: 1711.05274 [hep-ph].

[148] Ilias Cholis, Tim Linden, and Dan Hooper. "A Robust Excess in the Cosmic-Ray Antiproton Spectrum: Implications for Annihilating Dark Matter". In: *Phys. Rev. D* 99.10 (2019), p. 103026. DOI: 10.1103/PhysRevD.99.103026. arXiv: 1903.02549 [astro-ph.HE].

[149] Felix Kahlhoefer et al. "Constraining dark matter annihilation with cosmic ray antiprotons using neural networks". In: *JCAP* 12.12 (2021), p. 037. DOI: 10.1088/1475-7516/2021/12/037. arXiv: 2107.12395 [astro-ph.HE].

[150] Francesca Calore et al. "AMS-02 antiprotons and dark matter: Trimmed hints and robust bounds". In: *SciPost Phys.* 12.5 (2022), p. 163. DOI: 10.21468/SciPostPhys.12.5.163. arXiv: 2202.03076 [hep-ph].

[151] Sowmiya Balan et al. "Fast and accurate AMS-02 antiproton likelihoods for global dark matter fits". In: *JCAP* 08 (2023), p. 052. DOI: 10.1088/1475-7516/2023/08/052. arXiv: 2303.07362 [hep-ph].

[152] Pedro De la Torre Luque, Martin Wolfgang Winkler, and Tim Linden. "Antiproton bounds on dark matter annihilation from a combined analysis using the DRAGON2 code". In: *JCAP* 05 (2024), p. 104. DOI: 10.1088/1475-7516/2024/05/104. arXiv: 2401.10329 [astro-ph.HE].

[153] Annika Reinert and Martin Wolfgang Winkler. "A Precision Search for WIMPs with Charged Cosmic Rays". In: *JCAP* 01 (2018), p. 055. DOI: 10.1088/1475-7516/2018/01/055. arXiv: 1712.00002 [astro-ph.HE].

[154] Alessandro Cuoco et al. "Scrutinizing the evidence for dark matter in cosmic-ray antiprotons". In: *Phys. Rev. D* 99.10 (2019), p. 103014. DOI: 10.1103/PhysRevD.99.103014. arXiv: 1903.01472 [astro-ph.HE].

[155] L. Derome et al. "Fitting B/C cosmic-ray data in the AMS-02 era: A cookbook". In: *Astron. Astrophys.* 627 (2019), A158. DOI: 10.1051/0004-6361/201935717. arXiv: 1904.08210 [astro-ph.HE].

[156] Mathieu Boudaud et al. "AMS-02 antiprotons' consistency with a secondary astrophysical origin". In: *Phys. Rev. Res.* 2.2 (2020), p. 023022. DOI: 10.1103/PhysRevResearch.2.023022. arXiv: 1906.07119 [astro-ph.HE].

[157] Jan Heisig, Michael Korsmeier, and Martin Wolfgang Winkler. "Dark matter or correlated errors: Systematics of the AMS-02 antiproton excess". In: *Phys. Rev. Res.* 2.4 (2020), p. 043017. DOI: 10.1103/PhysRevResearch.2.043017. arXiv: 2005.04237 [astro-ph.HE].

[158] Jan Heisig. "Cosmic-ray antiprotons in the AMS-02 era: A sensitive probe of dark matter". In: *Mod. Phys. Lett. A* 36.05 (2021), p. 2130003. DOI: 10.1142/S0217732321300032. arXiv: 2012.03956 [astro-ph.HE].

[159] Pascal Chardonnet, Jean Orloff, and Pierre Salati. "The Production of antimatter in our galaxy". In: *Phys. Lett. B* 409 (1997), pp. 313–320. DOI: 10.1016/S0370-2693(97)00870-8. arXiv: astro-ph/9705110.

[160] R. P. Duperray, K. V. Protasov, and A. Yu. Voronin. "Anti-deuteron production in proton proton and proton nucleus collisions". In: *Eur. Phys. J. A* 16 (2003), pp. 27–34. DOI: 10.1140/epja/i2002-10074-0. arXiv: nucl-th/0209078.

[161] R. Duperray et al. "Flux of light antimatter nuclei near Earth, induced by cosmic rays in the Galaxy and in the atmosphere". In: *Phys. Rev. D* 71 (2005), p. 083013. DOI: 10.1103/PhysRevD.71.083013. arXiv: astro-ph/0503544.

[162] Alejandro Ibarra and David Tran. "Antideuterons from Dark Matter Decay". In: *JCAP* 06 (2009), p. 004. DOI: 10.1088/1475-7516/2009/06/004. arXiv: 0904.1410 [hep-ph].

[163] Carolin B. Brauninger and Marco Cirelli. "Anti-deuterons from heavy Dark Matter". In: *Phys. Lett. B* 678 (2009), pp. 20–31. DOI: 10.1016/j.physletb.2009.05.059. arXiv: 0904.1165 [hep-ph].

[164] Marco Cirelli et al. "Anti-helium from Dark Matter annihilations". In: *JHEP* 08 (2014), p. 009. DOI: 10.1007/JHEP08(2014)009. arXiv: 1401.4017 [hep-ph].

[165] Eric Carlson et al. "Antihelium from Dark Matter". In: *Phys. Rev. D* 89.7 (2014), p. 076005. DOI: 10.1103/PhysRevD.89.076005. arXiv: 1401.2461 [hep-ph].

[166] Mario Kadastik, Martti Raidal, and Alessandro Strumia. "Enhanced anti-deuteron Dark Matter signal and the implications of PAMELA". In: *Phys. Lett. B* 683 (2010), pp. 248–254. DOI: 10.1016/j.physletb.2009.12.005. arXiv: 0908.1578 [hep-ph].

[167] Alejandro Ibarra and Sebastian Wild. "Determination of the Cosmic Antideuteron Flux in a Monte Carlo approach". In: *Phys. Rev. D* 88 (2013), p. 023014. DOI: 10.1103/PhysRevD.88.023014. arXiv: 1301.3820 [astro-ph.HE].

[168] N. Fornengo, L. Maccione, and A. Vittino. "Dark matter searches with cosmic antideuterons: status and perspectives". In: *JCAP* 09 (2013), p. 031. DOI: 10.1088/1475-7516/2013/09/031. arXiv: 1306.4171 [hep-ph].

[169] Johannes Herms et al. "Antideuterons in cosmic rays: sources and discovery potential". In: *JCAP* 02 (2017), p. 018. DOI: 10.1088/1475-7516/2017/02/018. arXiv: 1610.00699 [astro-ph.HE].

[170] L. A. Dal and A. R. Raklev. "Antideuteron Limits on Decaying Dark Matter with a Tuned Formation Model". In: *Phys. Rev. D* 89.10 (2014), p. 103504. DOI: 10.1103/PhysRevD.89.103504. arXiv: 1402.6259 [hep-ph].

[171] Torbjörn Sjöstrand et al. "An introduction to PYTHIA 8.2". In: *Comput. Phys. Commun.* 191 (2015), pp. 159–177. DOI: 10.1016/j.cpc.2015.01.024. arXiv: 1410.3012 [hep-ph].

[172] Johannes Bellm et al. "Herwig 7.0/Herwig++ 3.0 release note". In: *Eur. Phys. J. C* 76.4 (2016), p. 196. DOI: 10.1140/epjc/s10052-016-4018-8. arXiv: 1512.01178 [hep-ph].

[173] Sergey Ostapchenko. "Monte Carlo treatment of hadronic interactions in enhanced Pomeron scheme: I. QGSJET-II model". In: *Phys. Rev. D* 83 (2011), p. 014018. DOI: 10.1103/PhysRevD.83.014018. arXiv: 1010.1869 [hep-ph].

[174] S. Ostapchenko. "QGSJET-II: physics, recent improvements, and results for air showers". In: *EPJ Web Conf.* 52 (2013). Ed. by U. Gensch and M. Walter, p. 02001. DOI: 10.1051/epjconf/20125202001.

[175] M. Kachelrieß, S. Ostapchenko, and J. Tjemsland. "Revisiting cosmic ray antinuclei fluxes with a new coalescence model". In: *JCAP* 08 (2020), p. 048. DOI: 10.1088/1475-7516/2020/08/048. arXiv: 2002.10481 [hep-ph].

[176] T. Pierog et al. "EPOS LHC: Test of collective hadronization with data measured at the CERN Large Hadron Collider". In: *Physical Review C* 92.3 (Sept. 2015). ISSN: 1089-490X. DOI: 10.1103/physrevc.92.034906. URL: http://dx.doi.org/10.1103/PhysRevC.92.034906.

[177] S. Agostinelli et al. "Geant4—a simulation toolkit". In: *Nuclear Instruments and Methods in Physics Research Section A: Accelerators, Spectrometers, Detectors and Associated Equipment* 506.3 (2003), pp. 250–303. ISSN: 0168-9002. DOI: https://doi.org/10.1016/S0168-9002(03)01368-8. URL: https://www.sciencedirect.com/science/article/pii/S0168900203013688.

[178] M. Kachelrieß, S. Ostapchenko, and J. Tjemsland. "Alternative coalescence model for deuteron, tritium, helium-3 and their antinuclei". In: *Eur. Phys. J. A* 56.1 (2020), p. 4. DOI: 10.1140/epja/s10050-019-00007-9. arXiv: 1905.01192 [hep-ph].

[179] M. Kachelriess, S. Ostapchenko, and J. Tjemsland. "Effect of nonequal emission times and space-time correlations on (anti-) nuclei production". In: *Phys. Rev. C* 108.2 (2023), p. 024903. DOI: 10.1103/PhysRevC.108.024903. arXiv: 2303.08437 [hep-ph].

[180] Kfir Blum and Masahiro Takimoto. "Nuclear coalescence from correlation functions". In: *Phys. Rev. C* 99.4 (2019), p. 044913. DOI: 10.1103/PhysRevC.99.044913. arXiv: 1901.07088 [nucl-th].

[181] Mattia Di Mauro et al. *Nailing down the theoretical uncertainties of* $\overline{\mathrm{D}}$ *spectrum produced from dark matter*. 2024. arXiv: 2411.04815 [astro-ph.HE]. URL: https://arxiv.org/abs/2411.04815.

[182] S. Schael et al. "Deuteron and anti-deuteron production in e+ e- collisions at the Z resonance". In: *Phys. Lett. B* 639 (2006), pp. 192–201. DOI: 10.1016/j.physletb.2006.06.043. arXiv: hep-ex/0604023.

[183] ALICE Collaboration. *Rapidity dependence of antideuteron coalescence in pp collisions at* $\sqrt{s}$ *= 13 TeV with ALICE*. 2024. arXiv: 2407.10527 [nucl-ex]. URL: https://arxiv.org/abs/2407.10527.

[184] Martin Wolfgang Winkler and Tim Linden. "Dark Matter Annihilation Can Produce a Detectable Antihelium Flux through $\bar{\Lambda}_b$ Decays". In: *Phys. Rev. Lett.* 126.10 (2021), p. 101101. DOI: 10.1103/PhysRevLett.126.101101. arXiv: 2006.16251 [hep-ph].

[185] J. Alwall et al. "The automated computation of tree-level and next-to-leading order differential cross sections, and their matching to parton shower simulations". In: *JHEP* 07 (2014), p. 079. DOI: 10.1007/JHEP07(2014)079. arXiv: 1405.0301 [hep-ph].

[186] Federico Ambrogi et al. "MadDM v.3.0: a Comprehensive Tool for Dark Matter Studies". In: *Phys. Dark Univ.* 24 (2019), p. 100249. DOI: 10.1016/j.dark.2018.11.009. arXiv: 1804.00044 [hep-ph].

[187] Alejandro Ibarra and Sebastian Wild. "Prospects of antideuteron detection from dark matter annihilations or decays at AMS-02 and GAPS". In: *JCAP* 02 (2013), p. 021. DOI: 10.1088/1475-7516/2013/02/021. arXiv: 1209.5539 [hep-ph].

[188] Andrew W. Strong, Igor V. Moskalenko, and Vladimir S. Ptuskin. "Cosmic-Ray Propagation and Interactions in the Galaxy". In: *Annual Review of Nuclear and Particle Science* 57.1 (Nov. 2007), pp. 285–327. ISSN: 1545-4134. DOI: 10.1146/annurev.nucl.57.090506.123011. URL: http://dx.doi.org/10.1146/annurev.nucl.57.090506.123011.

[189] Elena Amato and Pasquale Blasi. "Cosmic ray transport in the Galaxy: A review". In: *Advances in Space Research* 62.10 (Nov. 2018), pp. 2731–2749. ISSN: 0273-1177. DOI: 10.1016/j.asr.2017.04.019. URL: http://dx.doi.org/10.1016/j.asr.2017.04.019.

[190] Stefano Gabici et al. "The origin of Galactic cosmic rays: Challenges to the standard paradigm". In: *International Journal of Modern Physics D* 28.15 (Nov. 2019), p. 1930022. ISSN: 1793-6594. DOI: 10.1142/s0218271819300222. URL: http://dx.doi.org/10.1142/S0218271819300222.

[191] Jaehong Park, Damiano Caprioli, and Anatoly Spitkovsky. "Simultaneous Acceleration of Protons and Electrons at Nonrelativistic Quasiparallel Collisionless Shocks". In: *Physical Review Letters* 114.8 (Feb. 2015). ISSN: 1079-7114. DOI: 10.1103/physrevlett.114.085003. URL: http://dx.doi.org/10.1103/PhysRevLett.114.085003.

[192] Andrea Vittino et al. "Breaks in interstellar spectra of positrons and electrons derived from time-dependent AMS data". In: *Physical Review D* 100.4 (Aug. 2019). ISSN: 2470-0029. DOI: 10.1103/physrevd.100.043007. URL: http://dx.doi.org/10.1103/PhysRevD.100.043007.

[193] Pasquale Blasi, Elena Amato, and Pasquale D. Serpico. "Spectral Breaks as a Signature of Cosmic Ray Induced Turbulence in the Galaxy". In: *Physical Review Letters* 109.6 (Aug. 2012). ISSN: 1079-7114. DOI: 10.1103/physrevlett.109.061101. URL: http://dx.doi.org/10.1103/PhysRevLett.109.061101.

[194] Carmelo Evoli et al. "Origin of the Cosmic Ray Galactic Halo Driven by Advected Turbulence and Self-Generated Waves". In: *Physical Review Letters* 121.2 (July 2018). ISSN: 1079-7114. DOI: 10.1103/physrevlett.121.021102. URL: http://dx.doi.org/10.1103/PhysRevLett.121.021102.

[195] M. Aguilar et al. "Observation of New Properties of Secondary Cosmic Rays Lithium, Beryllium, and Boron by the Alpha Magnetic Spectrometer on the International Space Station". In: *Phys. Rev. Lett.* 120 (2 Jan. 2018), p. 021101. DOI: 10.1103/PhysRevLett.120.021101. URL: https://link.aps.org/doi/10.1103/PhysRevLett.120.021101.

[196] Yoann Génolini et al. "Indications for a High-Rigidity Break in the Cosmic-Ray Diffusion Coefficient". In: *Physical Review Letters* 119.24 (Dec. 2017). ISSN: 1079-7114. DOI: 10.1103/physrevlett.119.241101. URL: http://dx.doi.org/10.1103/PhysRevLett.119.241101.

[197] Michael Korsmeier and Alessandro Cuoco. "Implications of Lithium to Oxygen AMS-02 spectra on our understanding of cosmic-ray diffusion". In: *Phys. Rev. D* 103.10 (2021), p. 103016. DOI: 10.1103/PhysRevD.103.103016. arXiv: 2103.09824 [astro-ph.HE].

[198] E. S. Seo and V. S. Ptuskin. "Stochastic Reacceleration of Cosmic Rays in the Interstellar Medium". In: *Astrophysical Journal* 431 (Aug. 1994), p. 705. DOI: 10.1086/174520.

[199] Vladimir Ptuskin, Vladimir Zirakashvili, and Eun-Suk Seo. "Spectra of Cosmic Ray Protons and Helium Produced in Supernova Remnants". In: *The Astrophysical Journal* 763.1 (Jan. 2013), p. 47. ISSN: 1538-4357. DOI: 10.1088/0004-637x/763/1/47. URL: http://dx.doi.org/10.1088/0004-637X/763/1/47.

[200] Nicola Tomassetti. "Testing universality of cosmic-ray acceleration with proton/helium data from AMS and Voyager-1". In: *Advances in Space Research* 60.4 (Aug. 2017), pp. 815–825. ISSN: 0273-1177. DOI: 10.1016/j.asr.2016.10.024. URL: http://dx.doi.org/10.1016/j.asr.2016.10.024.

[201] A A Lagutin et al. "Origin of hardening and universality of cosmic rays spectra in GV–PV rigidity region". In: *Journal of Physics: Conference Series* 1181 (Feb. 2019), p. 012023. ISSN: 1742-6596. DOI: 10.1088/1742-6596/1181/1/012023. URL: http://dx.doi.org/10.1088/1742-6596/1181/1/012023.

[202] Damiano Caprioli, Dennis T. Yi, and Anatoly Spitkovsky. "Chemical Enhancements in Shock-Accelerated Particles: Ab-initio Simulations". In: *Physical Review Letters* 119.17 (Oct. 2017). ISSN: 1079-7114. DOI: 10.1103/physrevlett.119.171101. URL: http://dx.doi.org/10.1103/PhysRevLett.119.171101.

[203] Adrian Hanusch, Tatyana V. Liseykina, and Mikhail Malkov. "Acceleration of Cosmic Rays in Supernova Shocks: Elemental Selectivity of the Injection Mechanism". In: *The Astrophysical Journal* 872.1 (Feb. 2019), p. 108. ISSN: 1538-4357. DOI: 10.3847/1538-4357/aafdae. URL: http://dx.doi.org/10.3847/1538-4357/aafdae.

[204] D. Maurin et al. "Cosmic Rays below Z=30 in a Diffusion Model: New Constraints on Propagation Parameters". In: *The Astrophysical Journal* 555.2 (July 2001), pp. 585–596. ISSN: 1538-4357. DOI: 10.1086/321496. URL: http://dx.doi.org/10.1086/321496.

[205] Giuseppe Di Bernardo et al. "Unified interpretation of cosmic ray nuclei and antiproton recent measurements". In: *Astroparticle Physics* 34.5 (Dec. 2010), pp. 274–283. ISSN: 0927-6505. DOI: 10.1016/j.astropartphys.2010.08.006. URL: http://dx.doi.org/10.1016/j.astropartphys.2010.08.006.

[206] G. Jóhannesson et al. "Bayesian analysis of cosmic-ray propagation: evidence against homogeneous diffusion". In: *The Astrophysical Journal* 824.1 (June 2016), p. 16. ISSN: 1538-4357. DOI: 10.3847/0004-637x/824/1/16. URL: http://dx.doi.org/10.3847/0004-637X/824/1/16.

[207] Michael Korsmeier and Alessandro Cuoco. "Galactic cosmic-ray propagation in the light of AMS-02: Analysis of protons, helium, and antiprotons". In: *Physical Review D* 94.12 (Dec. 2016). ISSN: 2470-0029. DOI: 10.1103/physrevd.94.123019. URL: http://dx.doi.org/10.1103/PhysRevD.94.123019.

[208] P. De La Torre Luque et al. "Markov chain Monte Carlo analyses of the flux ratios of B, Be and Li with the DRAGON2 code". In: *Journal of Cosmology and Astroparticle Physics* 2021.07 (July 2021), p. 010. ISSN: 1475-7516. DOI: 10.1088/1475-7516/2021/07/010. URL: http://dx.doi.org/10.1088/1475-7516/2021/07/010.

[209] Vladimir S. Ptuskin et al. "Dissipation of Magnetohydrodynamic Waves on Energetic Particles: Impact on Interstellar Turbulence and Cosmic-Ray Transport". In: *The Astrophysical Journal* 642.2 (May 2006), pp. 902–916. ISSN: 1538-4357. DOI: 10.1086/501117. URL: http://dx.doi.org/10.1086/501117.

[210] N. Weinrich et al. "Combined analysis of AMS-02 (Li,Be,B)/C, N/O, 3He, and 4He data". In: *A&A* 639 (July 2020), A131. ISSN: 1432-0746. DOI: 10.1051/0004-6361/202037875. URL: http://dx.doi.org/10.1051/0004-6361/202037875.

[211] Carmelo Evoli et al. "AMS-02 beryllium data and its implication for cosmic ray transport". In: *Phys. Rev. D* 101.2 (2020), p. 023013. DOI: 10.1103/PhysRevD.101.023013. arXiv: 1910.04113 [astro-ph.HE].

[212] N. Weinrich et al. "Galactic halo size in the light of recent AMS-02 data". In: *Astron. Astrophys.* 639 (2020), A74. DOI: 10.1051/0004-6361/202038064. arXiv: 2004.00441 [astro-ph.HE].

[213] D. Maurin, E. Ferronato Bueno, and L. Derome. "A simple determination of the halo size from 10Be/9Be data". In: *Astron. Astrophys.* 667 (2022), A25. DOI: 10.1051/0004-6361/202243546. arXiv: 2203.07265 [astro-ph.HE].

[214] Yoann Genolini et al. "Current status and desired precision of the isotopic production cross sections relevant to astrophysics of cosmic rays: Li, Be, B, C, and N". In: *Phys. Rev. C* 98.3 (2018), p. 034611. DOI: 10.1103/PhysRevC.98.034611. arXiv: 1803.04686 [astro-ph.HE].

[215] Yoann Génolini et al. "New minimal, median, and maximal propagation models for dark matter searches with Galactic cosmic rays". In: *Phys. Rev. D* 104.8 (2021), p. 083005. DOI: 10.1103/PhysRevD.104.083005. arXiv: 2103.04108 [astro-ph.HE].

[216] Carmelo Evoli et al. "Cosmic ray nuclei, antiprotons and gamma rays in the galaxy: a new diffusion model". In: *Journal of Cosmology and Astroparticle Physics* 2008.10 (Oct. 2008), p. 018. ISSN: 1475-7516. DOI: 10.1088/1475-7516/2008/10/018. URL: http://dx.doi.org/10.1088/1475-7516/2008/10/018.

[217] Carmelo Evoli et al. "Cosmic-ray propagation with DRAGON2: II. Nuclear interactions with the interstellar gas". In: *Journal of Cosmology and Astroparticle Physics* 2018.07 (July 2018), pp. 006–006. ISSN: 1475-7516. DOI: 10.1088/1475-7516/2018/07/006. URL: http://dx.doi.org/10.1088/1475-7516/2018/07/006.

[218] R. Kissmann. "PICARD: A novel code for the Galactic Cosmic Ray propagation problem". In: *Astroparticle Physics* 55 (Mar. 2014), pp. 37–50. ISSN: 0927-6505. DOI: 10.1016/j.astropartphys.2014.02.002. URL: http://dx.doi.org/10.1016/j.astropartphys.2014.02.002.

[219] David Maurin. "usine: Semi-analytical models for Galactic cosmic-ray propagation". In: *Computer Physics Communications* 247 (Feb. 2020), p. 106942. ISSN: 0010-4655. DOI: 10.1016/j.cpc.2019.106942. URL: http://dx.doi.org/10.1016/j.cpc.2019.106942.

[220] Andrew W. Strong, Igor V. Moskalenko, and Olaf Reimer. "Diffuse continuum gamma-rays from the galaxy". In: *Astrophys. J.* 537 (2000). [Erratum: Astrophys.J. 541, 1109 (2000)], pp. 763–784. DOI: 10.1086/309038. arXiv: astro-ph/9811296.

[221] Michael Korsmeier, Fiorenza Donato, and Mattia Di Mauro. "Production cross sections of cosmic antiprotons in the light of new data from the NA61 and LHCb experiments". In: *Phys. Rev. D* 97.10 (2018), p. 103019. DOI: 10.1103/PhysRevD.97.103019. arXiv: 1802.03030 [astro-ph.HE].

[222] Rolf Kappl. "SOLARPROP: Charge-sign dependent solar modulation for everyone". In: *Computer Physics Communications* 207 (Oct. 2016), pp. 386–399. ISSN: 0010-4655. DOI: 10.1016/j.cpc.2016.05.025. URL: http://dx.doi.org/10.1016/j.cpc.2016.05.025.

[223] Andrea Vittino, Carmelo Evoli, and Daniele Gaggero. "Cosmic-ray transport in the heliosphere with HELIOPROP". In: *Proceedings of 35th International Cosmic Ray Conference — PoS(ICRC2017)*. ICRC2017. Sissa Medialab, Aug. 2017, p. 024. DOI: 10.22323/1.301.0024. URL: http://dx.doi.org/10.22323/1.301.0024.

[224] M.J. Boschini et al. "Propagation of cosmic rays in heliosphere: The HelMod model". In: *Advances in Space Research* 62.10 (Nov. 2018), pp. 2859–2879. ISSN: 0273-1177. DOI: 10.1016/j.asr.2017.04.017. URL: http://dx.doi.org/10.1016/j.asr.2017.04.017.

[225] E. Fiandrini et al. "Numerical modeling of cosmic rays in the heliosphere: Analysis of proton data from AMS-02 and PAMELA". In: *Physical Review D* 104.2 (July 2021). ISSN: 2470-0029. DOI: 10.1103/physrevd.104.023012. URL: http://dx.doi.org/10.1103/PhysRevD.104.023012.

[226] L. A. Fisk. "Solar modulation and a galactic origin for the anomalous component observed in low-energy cosmic rays." In: *Astrophysical Journal* 206 (May 1976), pp. 333–341. DOI: 10.1086/154387.

[227] Sergey A. Koldobskiy et al. "Validation of the Neutron Monitor Yield Function Using Data From AMS-02 Experiment, 2011-2017". In: *Journal of Geophysical Research (Space Physics)* 124.4 (Apr. 2019), pp. 2367–2379. DOI: 10.1029/2018JA026340. arXiv: 1904.01929 [physics.space-ph].

[228] Kerstin Perez et al. *Astro 2020 Science White Paper: Cosmic-ray Antinuclei as Messengers for Dark Matter*. 2021. arXiv: 1904.05938 [astro-ph.HE]. URL: https://arxiv.org/abs/1904.05938.

[229] F. Cadoux et al. "The Electromagnetic Calorimeter Trigger System for the AMS-02 Experiment". In: *Nuclear Science, IEEE Transactions on* 55 (May 2008), pp. 817–821. DOI: 10.1109/TNS.2008.918517.

[230] T. Aramaki et al. "Antideuteron Sensitivity for the GAPS Experiment". In: *Astropart. Phys.* 74 (2016), pp. 6–13. DOI: 10.1016/j.astropartphys.2015.09.001. arXiv: 1506.02513 [astro-ph.HE].

[231] V. Choutko and F. Giovacchini. "Cosmic Rays Antideuteron Sensitivity for AMS-02 Experiment". In: *International Cosmic Ray Conference*. Vol. 4. International Cosmic Ray Conference. Jan. 2008, pp. 765–768.

[232] S. Schael et al. "AMS-100: The next generation magnetic spectrometer in space – An international science platform for physics and astrophysics at Lagrange point 2". In: *Nuclear Instruments and Methods in Physics Research Section A: Accelerators, Spectrometers, Detectors and Associated Equipment* 944 (Nov. 2019), p. 162561. ISSN: 0168-9002. DOI: 10.1016/j.nima.2019.162561. URL: http://dx.doi.org/10.1016/j.nima.2019.162561.

[233] Samuel Ting. "Latest Results from AMS on the International Space Station". In: *CERN Colloquium* (2023). URL: https://indico.cern.ch/event/1275785/.

[234] T. Aramaki et al. "Reconstruction of antinucleus-annihilation events in the GAPS experiment". In: *PoS* ICRC2021 (2021), p. 504. DOI: 10.22323/1.395.0504.

[235] Francois Chollet et al. *Keras*. 2015. URL: https://github.com/fchollet/keras.

[236] Martín Abadi et al. "TensorFlow: Large-Scale Machine Learning on Heterogeneous Systems". In: (2015). Software available from tensorflow.org. eprint: 1603.04467. URL: https://www.tensorflow.org/.

[237] Robin M. Schmidt. *Recurrent Neural Networks (RNNs): A gentle Introduction and Overview*. 2019. arXiv: 1912.05911 [cs.LG]. URL: https://arxiv.org/abs/1912.05911.

[238] P.J. Werbos. "Backpropagation through time: what it does and how to do it". In: *Proceedings of the IEEE* 78.10 (1990), pp. 1550–1560. DOI: 10.1109/5.58337.

[239] Sepp Hochreiter and Jürgen Schmidhuber. "Long Short-Term Memory". In: *Neural Computation* 9.8 (Nov. 1997), pp. 1735–1780. ISSN: 0899-7667. DOI: 10.1162/neco.1997.9.8.1735. eprint: https://direct.mit.edu/neco/article-pdf/9/8/1735/813796/neco.1997.9.8.1735.pdf. URL: https://doi.org/10.1162/neco.1997.9.8.1735.

[240] Kyunghyun Cho et al. "Learning Phrase Representations using RNN Encoder–Decoder for Statistical Machine Translation". In: *Proceedings of the 2014 Conference on Empirical Methods in Natural Language Processing (EMNLP)*. Ed. by Alessandro Moschitti, Bo Pang, and Walter Daelemans. Doha, Qatar: Association for Computational Linguistics, Oct. 2014, pp. 1724–1734. DOI: 10.3115/v1/D14-1179. URL: https://aclanthology.org/D14-1179.

[241] Hartmut Führ and Ziemowit Rzeszotnik. "A note on factoring unitary matrices". In: *Linear Algebra and its Applications* 547 (2018), pp. 32–44. ISSN: 0024-3795. DOI: https://doi.org/10.1016/j.laa.2018.02.017. URL: https://www.sciencedirect.com/science/article/pii/S0024379518300843.

[242] Monika Blanke et al. "Another look at the flavour structure of the Littlest Higgs model with T-parity". In: *Physics Letters B* 646.5–6 (Mar. 2007), pp. 253–257. ISSN: 0370-2693. DOI: 10.1016/j.physletb.2007.01.037. URL: http://dx.doi.org/10.1016/j.physletb.2007.01.037.

[243] Teiji Takagi. "On an algebraic problem reluted to an analytic theorem of carathéodory and fejér and on an allied theorem of Landau". In: *Japanese journal of mathematics: transactions and abstracts* 1 (1924), pp. 83–93.

[244] L.C. Autonne. *Sur les matrices hypohermitiennes et sur les matrices unitaires*. Annales de l'Université de Lyon: Sciences, médecine Bd. 38. J.-B. Baillière et fils, 1915. URL: https://books.google.de/books?id=7JxbrgEACAAJ.

[245] Kim Griest and David Seckel. "Three exceptions in the calculation of relic abundances". In: *Phys. Rev. D* 43 (10 May 1991), pp. 3191–3203. DOI: 10.1103/PhysRevD.43.3191. URL: https://link.aps.org/doi/10.1103/PhysRevD.43.3191.

[246] Joakim Edsjö and Paolo Gondolo. "Neutralino relic density including coannihilations". In: *Physical Review D* 56.4 (Aug. 1997), pp. 1879–1894. ISSN: 1089-4918. DOI: 10.1103/physrevd.56.1879. URL: http://dx.doi.org/10.1103/PhysRevD.56.1879.

[247] Mathias Garny et al. "Coannihilation without chemical equilibrium". In: *Physical Review D* 96.10 (Nov. 2017). ISSN: 2470-0029. DOI: 10.1103/physrevd.96.103521. URL: http://dx.doi.org/10.1103/PhysRevD.96.103521.

[248] Raffaele Tito D'Agnolo, Duccio Pappadopulo, and Joshua T. Ruderman. "Fourth Exception in the Calculation of Relic Abundances". In: *Phys. Rev. Lett.* 119.6 (2017), p. 061102. DOI: 10.1103/PhysRevLett.119.061102. arXiv: 1705.08450 [hep-ph].

[249] Julian Heeck, Jan Heisig, and Anil Thapa. "Dark matter and radiative neutrino masses in conversion-driven scotogenesis". In: *Phys. Rev. D* 107.1 (2023), p. 015028. DOI: 10.1103/PhysRevD.107.015028. arXiv: 2211.13013 [hep-ph].

[250] Mathias Garny et al. "Top-philic dark matter within and beyond the WIMP paradigm". In: *Phys. Rev. D* 97.7 (2018), p. 075002. DOI: 10.1103/PhysRevD.97.075002. arXiv: 1802.00814 [hep-ph].

[251] M. Aguilar et al. "Antiproton Flux, Antiproton-to-Proton Flux Ratio, and Properties of Elementary Particle Fluxes in Primary Cosmic Rays Measured with the Alpha Magnetic Spectrometer on the International Space Station". In: *Phys. Rev. Lett.* 117 (9 Aug. 2016), p. 091103. DOI: 10.1103/PhysRevLett.117.091103. URL: https://link.aps.org/doi/10.1103/PhysRevLett.117.091103.

[252] M. Aguilar et al. "Precision Measurement of the Proton Flux in Primary Cosmic Rays from Rigidity 1 GV to 1.8 TV with the Alpha Magnetic Spectrometer on the International Space Station". In: *Phys. Rev. Lett.* 114 (17 Apr. 2015), p. 171103. DOI: 10.1103/PhysRevLett.114.171103. URL: https://link.aps.org/doi/10.1103/PhysRevLett.114.171103.

[253] M. Aguilar et al. "Precision Measurement of the Helium Flux in Primary Cosmic Rays of Rigidities 1.9 GV to 3 TV with the Alpha Magnetic Spectrometer on the International Space Station". In: *Phys. Rev. Lett.* 115 (21 Nov. 2015), p. 211101. DOI: 10.1103/PhysRevLett.115.211101. URL: https://link.aps.org/doi/10.1103/PhysRevLett.115.211101.

[254] Y. S. Yoon et al. "Cosmic-Ray Proton and Helium Spectra from the First CREAM Flight". In: *The Astrophysical Journal* 728.2 (Jan. 2011), p. 122. ISSN: 1538-4357. DOI: 10.1088/0004-637x/728/2/122. URL: http://dx.doi.org/10.1088/0004-637X/728/2/122.

[255] E. C. Stone et al. "Voyager 1 Observes Low-Energy Galactic Cosmic Rays in a Region Depleted of Heliospheric Ions". In: *Science* 341.6142 (2013), pp. 150–153. DOI: 10.1126/science.1236408. eprint: https://www.science.org/doi/pdf/10.1126/science.1236408. URL: https://www.science.org/doi/abs/10.1126/science.1236408.

[256] S. Aoki et al. "FLAG Review 2019: Flavour Lattice Averaging Group (FLAG)". In: *Eur. Phys. J. C* 80.2 (2020), p. 113. DOI: 10.1140/epjc/s10052-019-7354-7. arXiv: 1902.08191 [hep-lat].

[257] N. Carrasco et al. "$D^0 - \bar{D}^0$ mixing in the standard model and beyond from $N_f$ =2 twisted mass QCD". In: *Phys. Rev. D* 90.1 (2014), p. 014502. DOI: 10.1103/PhysRevD.90.014502. arXiv: 1403.7302 [hep-lat].

[258] Andrzej J. Buras, Sebastian Jager, and Jorg Urban. "Master formulae for Delta F=2 NLO QCD factors in the standard model and beyond". In: *Nucl. Phys. B* 605 (2001), pp. 600–624. DOI: 10.1016/S0550-3213(01)00207-3. arXiv: hep-ph/0102316.

[259] Yasmine Sara Amhis et al. "Averages of $b$-hadron, $c$-hadron, and $\tau$-lepton properties as of 2018". In: (2019). updated results and plots available at https://hflav.web.cern.ch/. arXiv: 1909.12524 [hep-ex].

[260] Geneviève Bélanger et al. "micrOMEGAs5.0 : Freeze-in". In: *Comput. Phys. Commun.* 231 (2018), pp. 173–186. DOI: 10.1016/j.cpc.2018.04.027. arXiv: 1801.03509 [hep-ph].

[261] Tobias Binder et al. "Excited bound states and their role in dark matter production". In: *Phys. Rev. D* 108.9 (2023), p. 095030. DOI: 10.1103/PhysRevD.108.095030. arXiv: 2308.01336 [hep-ph].

[262] Mathias Garny and Jan Heisig. "Bound-state effects on dark matter coannihilation: Pushing the boundaries of conversion-driven freeze-out". In: *Phys. Rev. D* 105.5 (2022), p. 055004. DOI: 10.1103/PhysRevD.105.055004. arXiv: 2112.01499 [hep-ph].

[263] Michele Papucci, Alessandro Vichi, and Kathryn M. Zurek. "Monojet versus the rest of the world I: t-channel models". In: *JHEP* 11 (2014), p. 024. DOI: 10.1007/JHEP11(2014)024. arXiv: 1402.2285 [hep-ph].

[264] Gaël Alguero et al. "Constraining new physics with SModelS version 2". In: *JHEP* 08 (2022), p. 068. DOI: 10.1007/JHEP08(2022)068. arXiv: 2112.00769 [hep-ph].

[265] Mohammad Mahdi Altakach et al. "SModelS v2.3: Enabling global likelihood analyses". In: *SciPost Phys.* 15.5 (2023), p. 185. DOI: 10.21468/SciPostPhys.15.5.185. arXiv: 2306.17676 [hep-ph].

[266] Georges Aad et al. "Search for squarks and gluinos with the ATLAS detector in final states with jets and missing transverse momentum using $\sqrt{s} = 8$ TeV proton–proton collision data". In: *JHEP* 09 (2014), p. 176. DOI: 10.1007/JHEP09(2014)176. arXiv: 1405.7875 [hep-ex].

[267] Morad Aaboud et al. "Search for squarks and gluinos in final states with jets and missing transverse momentum using 36 fb$^{-1}$ of $\sqrt{s} = 13$ TeV pp collision data with the ATLAS detector". In: *Phys. Rev. D* 97.11 (2018), p. 112001. DOI: 10.1103/PhysRevD.97.112001. arXiv: 1712.02332 [hep-ex].

[268] Morad Aaboud et al. "Search for a scalar partner of the top quark in the jets plus missing transverse momentum final state at $\sqrt{s}$=13 TeV with the ATLAS detector". In: *JHEP* 12 (2017), p. 085. DOI: 10.1007/JHEP12(2017)085. arXiv: 1709.04183 [hep-ex].

[269] Georges Aad et al. "Search for a scalar partner of the top quark in the all-hadronic $t\bar{t}$ plus missing transverse momentum final state at $\sqrt{s} = 13$ TeV with the ATLAS detector". In: *Eur. Phys. J. C* 80.8 (2020), p. 737. DOI: 10.1140/epjc/s10052-020-8102-8. arXiv: 2004.14060 [hep-ex].

[270] Georges Aad et al. "Search for squarks and gluinos in final states with jets and missing transverse momentum using 139 fb$^{-1}$ of $\sqrt{s}$ =13 TeV $pp$ collision data with the ATLAS detector". In: *JHEP* 02 (2021), p. 143. DOI: 10.1007/JHEP02(2021)143. arXiv: 2010.14293 [hep-ex].

[271] Albert M Sirunyan et al. "Search for supersymmetry in multijet events with missing transverse momentum in proton-proton collisions at 13 TeV". In: *Phys. Rev. D* 96.3 (2017), p. 032003. DOI: 10.1103/PhysRevD.96.032003. arXiv: 1704.07781 [hep-ex].

[272] Albert M Sirunyan et al. "Search for new phenomena with the $M_{T2}$ variable in the all-hadronic final state produced in proton–proton collisions at $\sqrt{s} = 13$ TeV". In: *Eur. Phys. J. C* 77.10 (2017), p. 710. DOI: 10.1140/epjc/s10052-017-5267-x. arXiv: 1705.04650 [hep-ex].

[273] The Cms Collaboration et al. "Search for supersymmetry in proton-proton collisions at 13 TeV in final states with jets and missing transverse momentum". In: *JHEP* 10 (2019), p. 244. DOI: 10.1007/JHEP10(2019)244. arXiv: 1908.04722 [hep-ex].

[274] Albert M Sirunyan et al. "Search for direct top squark pair production in events with one lepton, jets, and missing transverse momentum at 13 TeV with the CMS experiment". In: *JHEP* 05 (2020), p. 032. DOI: 10.1007/JHEP05(2020)032. arXiv: 1912.08887 [hep-ex].

[275] Armen Tumasyan et al. "Combined searches for the production of supersymmetric top quark partners in proton–proton collisions at $\sqrt{s} = 13$ TeV". In: *Eur. Phys. J. C* 81.11 (2021), p. 970. DOI: 10.1140/epjc/s10052-021-09721-5. arXiv: 2107.10892 [hep-ex].

[276] Georges Aad et al. "Search for pair-produced third-generation squarks decaying via charm quarks or in compressed supersymmetric scenarios in *pp* collisions at $\sqrt{s} = 8$ TeV with the ATLAS detector". In: *Phys. Rev. D* 90.5 (2014), p. 052008. DOI: 10.1103/PhysRevD.90.052008. arXiv: 1407.0608 [hep-ex].

[277] Georges Aad et al. "Search for Scalar Charm Quark Pair Production in *pp* Collisions at $\sqrt{s} = 8$ TeV with the ATLAS Detector". In: *Phys. Rev. Lett.* 114.16 (2015), p. 161801. DOI: 10.1103/PhysRevLett.114.161801. arXiv: 1501.01325 [hep-ex].

[278] Morad Aaboud et al. "Search for supersymmetry in final states with charm jets and missing transverse momentum in 13 TeV *pp* collisions with the ATLAS detector". In: *JHEP* 09 (2018), p. 050. DOI: 10.1007/JHEP09(2018)050. arXiv: 1805.01649 [hep-ex].

[279] Albert M Sirunyan et al. "Search for direct production of supersymmetric partners of the top quark in the all-jets final state in proton-proton collisions at $\sqrt{s} = 13$ TeV". In: *JHEP* 10 (2017), p. 005. DOI: 10.1007/JHEP10(2017)005. arXiv: 1707.03316 [hep-ex].

[280] Morad Aaboud et al. "Search for heavy charged long-lived particles in the ATLAS detector in 36.1 fb$^{-1}$ of proton-proton collision data at $\sqrt{s} = 13$ TeV". In: *Phys. Rev. D* 99.9 (2019), p. 092007. DOI: 10.1103/PhysRevD.99.092007. arXiv: 1902.01636 [hep-ex].

[281] *Search for heavy stable charged particles with* 12.9 fb$^{-1}$ *of 2016 data*. Tech. rep. Geneva: CERN, 2016. URL: https://cds.cern.ch/record/2205281.

[282] Albert M Sirunyan et al. "Search for the pair production of third-generation squarks with two-body decays to a bottom or charm quark and a neutralino in proton–proton collisions at $\sqrt{s} = 13$ TeV". In: *Phys. Lett. B* 778 (2018), pp. 263–291. DOI: 10.1016/j.physletb.2018.01.012. arXiv: 1707.07274 [hep-ex].

[283] Mathias Garny et al. "Internal bremsstrahlung signatures in light of direct dark matter searches". In: *JCAP* 12 (2013), p. 046. DOI: 10.1088/1475-7516/2013/12/046. arXiv: 1306.6342 [hep-ph].

[284] G. Brooijmans et al. "Les Houches 2019 Physics at TeV Colliders: New Physics Working Group Report, Contribution No. 7". In: *11th Les Houches Workshop on Physics at TeV Colliders: PhysTeV Les Houches*. Feb. 2020. arXiv: 2002.12220 [hep-ph].

[285] David Curtin et al. "Long-Lived Particles at the Energy Frontier: The MATHUSLA Physics Case". In: *Rept. Prog. Phys.* 82.11 (2019), p. 116201. DOI: 10.1088/1361-6633/ab28d6. arXiv: 1806.07396 [hep-ph].

[286] Jan Heisig, Andre Lessa, and Lucas Magno D. Ramos. "Probing conversion-driven freeze-out at the LHC". In: *Physical Review D* 110.1 (July 2024). ISSN: 2470-0029. DOI: 10.1103/physrevd.110.015031. URL: http://dx.doi.org/10.1103/PhysRevD.110.015031.

[287] Albert M Sirunyan et al. "Search for physics beyond the standard model in events with jets and two same-sign or at least three charged leptons in proton-proton collisions at $\sqrt{s} = 13$ TeV". In: *Eur. Phys. J. C* 80.8 (2020), p. 752. DOI: 10.1140/epjc/s10052-020-8168-3. arXiv: 2001.10086 [hep-ex].

[288] Adam Alloul et al. "FeynRules 2.0 - A complete toolbox for tree-level phenomenology". In: *Comput. Phys. Commun.* 185 (2014), pp. 2250–2300. DOI: 10.1016/j.cpc.2014.04.012. arXiv: 1310.1921 [hep-ph].

[289] Luc Darmé et al. "UFO 2.0: the 'Universal Feynman Output' format". In: *The European Physical Journal C* 83.7 (July 2023). ISSN: 1434-6052. DOI: 10.1140/epjc/s10052-023-11780-9. URL: http://dx.doi.org/10.1140/epjc/s10052-023-11780-9.

[290] Ernest Ma. "Verifiable radiative seesaw mechanism of neutrino mass and dark matter". In: *Physical Review D* 73.7 (Apr. 2006). ISSN: 1550-2368. DOI: 10.1103/physrevd.73.077301. URL: http://dx.doi.org/10.1103/PhysRevD.73.077301.

[291] Alexander Belyaev, Neil D. Christensen, and Alexander Pukhov. "CalcHEP 3.4 for collider physics within and beyond the Standard Model". In: *Computer Physics Communications* 184.7 (July 2013), pp. 1729–1769. ISSN: 0010-4655. DOI: 10.1016/j.cpc.2013.01.014. URL: http://dx.doi.org/10.1016/j.cpc.2013.01.014.

[292] Mohammad Mahdi Altakach et al. "SModelS v3: going beyond $\mathcal{Z}_2$ topologies". In: *JHEP* 11 (2024), p. 074. DOI: 10.1007/JHEP11(2024)074. arXiv: 2409.12942 [hep-ph].

[293] Javier Fuentes-Martín et al. "A proof of concept for matchete: an automated tool for matching effective theories". In: *The European Physical Journal C* 83.7 (July 2023). ISSN: 1434-6052. DOI: 10.1140/epjc/s10052-023-11726-1. URL: http://dx.doi.org/10.1140/epjc/s10052-023-11726-1.

[294] W. Buchmuller and D. Wyler. "Effective Lagrangian Analysis of New Interactions and Flavor Conservation". In: *Nucl. Phys. B* 268 (1986), pp. 621–653. DOI: 10.1016/0550-3213(86)90262-2.

[295] Jason Aebischer et al. "A global likelihood for precision constraints and flavour anomalies". In: *The European Physical Journal C* 79.6 (June 2019). ISSN: 1434-6052. DOI: 10.1140/epjc/s10052-019-6977-z. URL: http://dx.doi.org/10.1140/epjc/s10052-019-6977-z.

[296] Gary Steigman, Basudeb Dasgupta, and John F. Beacom. "Precise relic WIMP abundance and its impact on searches for dark matter annihilation". In: *Physical Review D* 86.2 (July 2012). ISSN: 1550-2368. DOI: 10.1103/physrevd.86.023506. URL: http://dx.doi.org/10.1103/PhysRevD.86.023506.

[297] E. Aprile et al. "Dark Matter Search Results from a One Ton-Year Exposure of XENON1T". In: *Physical Review Letters* 121.11 (Sept. 2018). ISSN: 1079-7114. DOI: 10.1103/physrevlett.121.111302. URL: http://dx.doi.org/10.1103/PhysRevLett.121.111302.

[298] E. Aprile et al. "Constraining the Spin-Dependent WIMP-Nucleon Cross Sections with XENON1T". In: *Physical Review Letters* 122.14 (Apr. 2019). ISSN: 1079-7114. DOI: 10.1103/physrevlett.122.141301. URL: http://dx.doi.org/10.1103/PhysRevLett.122.141301.

[299] Celine Armand et al. *Combined dark matter searches towards dwarf spheroidal galaxies with Fermi-LAT, HAWC, H.E.S.S., MAGIC, and VERITAS*. 2021. arXiv: 2108.13646 [hep-ex]. URL: https://arxiv.org/abs/2108.13646.

[300] S. Archambault et al. "Dark matter constraints from a joint analysis of dwarf Spheroidal galaxy observations with VERITAS". In: *Physical Review D* 95.8 (Apr. 2017). ISSN: 2470-0029. DOI: 10.1103/physrevd.95.082001. URL: http://dx.doi.org/10.1103/PhysRevD.95.082001.

[301] A. Acharyya et al. *An indirect search for dark matter with a combined analysis of dwarf spheroidal galaxies from VERITAS*. 2024. arXiv: 2407.16518 [astro-ph.HE]. URL: https://arxiv.org/abs/2407.16518.

[302] Isabelle John and Tim Linden. "Cosmic-ray positrons strongly constrain leptophilic dark matter". In: *Journal of Cosmology and Astroparticle Physics* 2021.12 (Dec. 2021), p. 007. ISSN: 1475-7516. DOI: 10.1088/1475-7516/2021/12/007. URL: http://dx.doi.org/10.1088/1475-7516/2021/12/007.

[303] The IceCube Collaboration et al. *Search for neutrino lines from dark matter annihilation and decay with IceCube*. 2023. arXiv: 2303.13663 [astro-ph.HE]. URL: https://arxiv.org/abs/2303.13663.

[304] A. Albert et al. "Search for dark matter towards the Galactic Centre with 11 years of ANTARES data". In: *Physics Letters B* 805 (June 2020), p. 135439. ISSN: 0370-2693. DOI: 10.1016/j.physletb.2020.135439. URL: http://dx.doi.org/10.1016/j.physletb.2020.135439.

[305] H. Abdallah et al. "Search for Dark Matter Annihilations towards the Inner Galactic Halo from 10 Years of Observations with H.E.S.S." In: *Physical Review Letters* 117.11 (Sept. 2016). ISSN: 1079-7114. DOI: 10.1103/physrevlett.117.111301. URL: http://dx.doi.org/10.1103/PhysRevLett.117.111301.

[306] A. Albert et al. "Searching for Dark Matter Annihilation in Recently Discovered Milky Way Satellites with Fermi-LAT". In: *The Astrophysical Journal* 834.2 (Jan. 2017), p. 110. ISSN: 1538-4357. DOI: 10.3847/1538-4357/834/2/110. URL: http://dx.doi.org/10.3847/1538-4357/834/2/110.

[307] MAGIC collaboration. "Limits to dark matter annihilation cross-section from a combined analysis of MAGIC and Fermi-LAT observations of dwarf satellite galaxies". In: *Journal of Cosmology and Astroparticle Physics* 2016.02 (Feb. 2016), pp. 039–039. ISSN: 1475-7516. DOI: 10.1088/1475-7516/2016/02/039. URL: http://dx.doi.org/10.1088/1475-7516/2016/02/039.

[308] M. Ackermann et al. "Searching for Dark Matter Annihilation from Milky Way Dwarf Spheroidal Galaxies with Six Years of Fermi Large Area Telescope Data". In: *Physical Review Letters* 115.23 (Nov. 2015). ISSN: 1079-7114. DOI: 10.1103/physrevlett.115.231301. URL: http://dx.doi.org/10.1103/PhysRevLett.115.231301.

[309] J. Aleksić et al. "Optimized dark matter searches in deep observations of Segue 1 with MAGIC". In: *Journal of Cosmology and Astroparticle Physics* 2014.02 (Feb. 2014), pp. 008–008. ISSN: 1475-7516. DOI: 10.1088/1475-7516/2014/02/008. URL: http://dx.doi.org/10.1088/1475-7516/2014/02/008.

[310] B. Grzadkowski et al. "Dimension-Six Terms in the Standard Model Lagrangian". In: *JHEP* 10 (2010), p. 085. DOI: 10.1007/JHEP10(2010)085. arXiv: 1008.4884 [hep-ph].

[311] Jason Aebischer et al. "WCxf: An exchange format for Wilson coefficients beyond the Standard Model". In: *Computer Physics Communications* 232 (Nov. 2018), pp. 71–83. ISSN: 0010-4655. DOI: 10.1016/j.cpc.2018.05.022. URL: http://dx.doi.org/10.1016/j.cpc.2018.05.022.

[312] David M. Straub. *flavio: a Python package for flavour and precision phenomenology in the Standard Model and beyond*. 2018. arXiv: 1810.08132 [hep-ph]. URL: https://arxiv.org/abs/1810.08132.

[313] Jason Aebischer, Jacky Kumar, and David M. Straub. "Wilson: a Python package for the running and matching of Wilson coefficients above and below the electroweak scale". In: *The European Physical Journal C* 78.12 (Dec. 2018). ISSN: 1434-6052. DOI: 10.1140/epjc/s10052-018-6492-7. URL: http://dx.doi.org/10.1140/epjc/s10052-018-6492-7.

[314] Elizabeth E. Jenkins, Aneesh V. Manohar, and Peter Stoffer. "Low-Energy Effective Field Theory below the Electroweak Scale: Operators and Matching". In: *JHEP* 03 (2018). [Erratum: JHEP 12, 043 (2023)], p. 016. DOI: 10.1007/JHEP03(2018)016. arXiv: 1709.04486 [hep-ph].

[315] Wouter Dekens and Peter Stoffer. "Low-energy effective field theory below the electroweak scale: matching at one loop". In: *JHEP* 10 (2019). [Erratum: JHEP 11, 148 (2022)], p. 197. DOI: 10.1007/JHEP10(2019)197. arXiv: 1908.05295 [hep-ph].

[316] Elizabeth E. Jenkins, Aneesh V. Manohar, and Michael Trott. "Renormalization Group Evolution of the Standard Model Dimension Six Operators I: Formalism and lambda Dependence". In: *JHEP* 10 (2013), p. 087. DOI: 10.1007/JHEP10(2013)087. arXiv: 1308.2627 [hep-ph].

[317] Elizabeth E. Jenkins, Aneesh V. Manohar, and Michael Trott. "Renormalization Group Evolution of the Standard Model Dimension Six Operators II: Yukawa Dependence". In: *JHEP* 01 (2014), p. 035. DOI: 10.1007/JHEP01(2014)035. arXiv: 1310.4838 [hep-ph].

[318] Rodrigo Alonso et al. "Renormalization Group Evolution of the Standard Model Dimension Six Operators III: Gauge Coupling Dependence and Phenomenology". In: *JHEP* 04 (2014), p. 159. DOI: 10.1007/JHEP04(2014)159. arXiv: 1312.2014 [hep-ph].

[319] Elizabeth E. Jenkins, Aneesh V. Manohar, and Peter Stoffer. "Low-Energy Effective Field Theory below the Electroweak Scale: Anomalous Dimensions". In: *JHEP* 01 (2018). [Erratum: JHEP 12, 042 (2023)], p. 084. DOI: 10.1007/JHEP01(2018)084. arXiv: 1711.05270 [hep-ph].

[320] R.V. Harlander, S.Y. Klein, and M. Lipp. "FeynGame". In: *Computer Physics Communications* 256 (Nov. 2020), p. 107465. ISSN: 0010-4655. DOI: 10.1016/j.cpc.2020.107465. URL: http://dx.doi.org/10.1016/j.cpc.2020.107465.

[321] Robert Harlander, Sven Yannick Klein, and Magnus C. Schaaf. "FeynGame-2.1 – Feynman diagrams made easy". In: *PoS* EPS-HEP2023 (2024), p. 657. DOI: 10.22323/1.449.0657. arXiv: 2401.12778 [hep-ph].

[322] L. Bündgen et al. "FeynGame 3.0". In: (Jan. 2025). arXiv: 2501.04651 [hep-ph].

[323] Luca Buonocore et al. "Leptons in the proton". In: *Journal of High Energy Physics* 2020.8 (Aug. 2020). ISSN: 1029-8479. DOI: 10.1007/jhep08(2020)019. URL: http://dx.doi.org/10.1007/JHEP08(2020)019.

[324] A. M. Sirunyan et al. "Search for supersymmetry in final states with two oppositely charged same-flavor leptons and missing transverse momentum in proton-proton collisions at $\sqrt{s} = 13$ TeV". In: *Journal of High Energy Physics* 2021.4 (Apr. 2021). ISSN: 1029-8479. DOI: 10.1007/jhep04(2021)123. URL: http://dx.doi.org/10.1007/JHEP04(2021)123.

[325] Georges Aad et al. "Searches for electroweak production of supersymmetric particles with compressed mass spectra in $\sqrt{s} = 13$ TeV *pp* collisions with the ATLAS detector". In: *Phys. Rev. D* 101.5 (2020), p. 052005. DOI: 10.1103/PhysRevD.101.052005. arXiv: 1911.12606 [hep-ex].

[326] Georges Aad et al. "Search for direct production of charginos, neutralinos and sleptons in final states with two leptons and missing transverse momentum in *pp* collisions at $\sqrt{s} = 8$ TeV with the ATLAS detector". In: *JHEP* 05 (2014), p. 071. DOI: 10.1007/JHEP05(2014)071. arXiv: 1403.5294 [hep-ex].

[327] M. Aaboud et al. "Search for electroweak production of supersymmetric particles in final states with two or three leptons at $\sqrt{s} = 13\,\text{TeV}$ with the ATLAS detector". In: *Eur. Phys. J. C* 78.12 (2018), p. 995. DOI: 10.1140/epjc/s10052-018-6423-7. arXiv: 1803.02762 [hep-ex].

[328] Georges Aad et al. "Search for direct pair production of sleptons and charginos decaying to two leptons and neutralinos with mass splittings near the W-boson mass in $\sqrt{s} = 13$ TeV pp collisions with the ATLAS detector". In: *JHEP* 06 (2023), p. 031. DOI: 10.1007/JHEP06(2023)031. arXiv: 2209.13935 [hep-ex].

[329] Georges Aad et al. "Search for electroweak production of charginos and sleptons decaying into final states with two leptons and missing transverse momentum in $\sqrt{s} = 13$ TeV *pp* collisions using the ATLAS detector". In: *Eur. Phys. J. C* 80.2 (2020), p. 123. DOI: 10.1140/epjc/s10052-019-7594-6. arXiv: 1908.08215 [hep-ex].

[330] Albert M. Sirunyan et al. "Search for supersymmetric partners of electrons and muons in proton-proton collisions at $\sqrt{s} = 13$ TeV". In: *Phys. Lett. B* 790 (2019), pp. 140–166. DOI: 10.1016/j.physletb.2019.01.005. arXiv: 1806.05264 [hep-ex].

[331] J. Abdallah et al. "Searches for supersymmetric particles in e + e- collisions up to 208 GeV and interpretation of the results within the MSSM". In: *The European Physical Journal C* 31.4 (Dec. 2003), pp. 421–479. ISSN: 1434-6052. DOI: 10.1140/epjc/s2003-01355-5. URL: http://dx.doi.org/10.1140/epjc/s2003-01355-5.

[332] Joachim Kopp et al. "DAMA/LIBRA data and leptonically interacting dark matter". In: *Physical Review D* 80.8 (Oct. 2009). ISSN: 1550-2368. DOI: 10.1103/physrevd.80.083502. URL: http://dx.doi.org/10.1103/PhysRevD.80.083502.

[333] Vladyslav Shtabovenko, Rolf Mertig, and Frederik Orellana. "FeynCalc 9.3: New features and improvements". In: *Computer Physics Communications* 256 (Nov. 2020), p. 107478. ISSN: 0010-4655. DOI: 10.1016/j.cpc.2020.107478. URL: http://dx.doi.org/10.1016/j.cpc.2020.107478.

[334] Vladyslav Shtabovenko, Rolf Mertig, and Frederik Orellana. "New developments in FeynCalc 9.0". In: *Computer Physics Communications* 207 (Oct. 2016), pp. 432–444. ISSN: 0010-4655. DOI: 10.1016/j.cpc.2016.06.008. URL: http://dx.doi.org/10.1016/j.cpc.2016.06.008.

[335] R. Mertig, M. Böhm, and A. Denner. "Feyn Calc - Computer-algebraic calculation of Feynman amplitudes". In: *Computer Physics Communications* 64.3 (1991), pp. 345–359. ISSN: 0010-4655. DOI: https://doi.org/10.1016/0010-4655(91)90130-D. URL: https://www.sciencedirect.com/science/article/pii/001046559190130D.

[336] Thomas Hahn. "Generating Feynman diagrams and amplitudes with FeynArts 3". In: *Computer Physics Communications* 140.3 (Nov. 2001), pp. 418–431. ISSN: 0010-4655. DOI: 10.1016/s0010-4655(01)00290-9. URL: http://dx.doi.org/10.1016/S0010-4655(01)00290-9.